Electronic and Superconducting Properties of the Two-dimensional Electron System at the LaAlO$_3$/SrTiO$_3$(111) Interface

by

Inge Groen

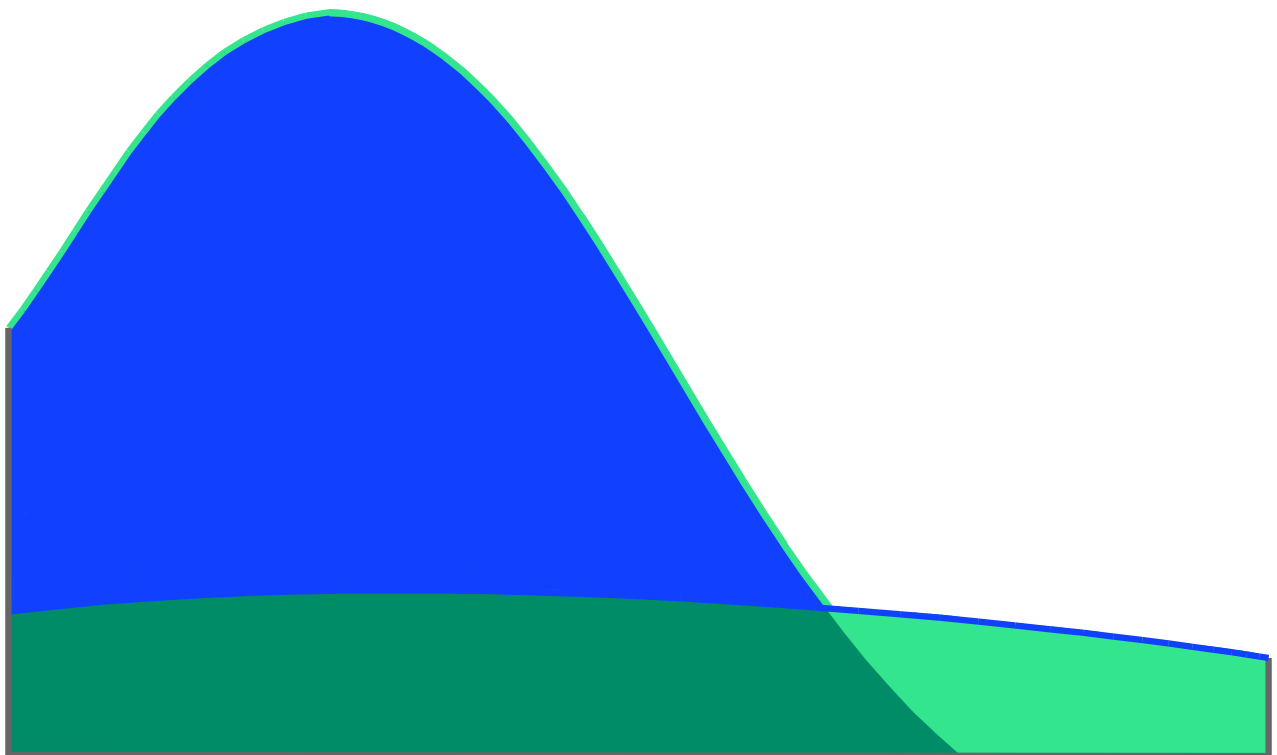# Electronic and superconducting properties of the two-dimensional electron system at the LaAlO₃/SrTiO₃(111) interface

by

Inge Groen

in partial fulfilment of the requirements for the degree of

Master of Science

in Applied Physics & Materials Science and Engineering
at the Delft University of Technology
Faculty of Applied Sciences
Kavli Institute of Nanoscience
Caviglia lab: Designer Quantum Materials

to be defended publicly on Tuesday May 17, 2016 at 16:00

Graduation Committee
Applied Physics:

      Dr. A.D. Caviglia,

      Prof. dr. H. S. J. van der Zant,

      Prof. dr. Y. M. Blanter

Materials Science and Engineering:

      Prof. dr. B. J. Thijsse

      Prof. dr. J. Sietsema

      Dr. M. Sluiter

Daily supervisor

      Dr. A.D. Caviglia

      M.S.c. A.M.R.V.L. Monteiro

TUDelft

Abstract

The (100)-oriented $LaAlO_3$/$SrTiO_3$ (LAO/STO) interface has been subject of intense study since the discovery of the two-dimensional electron system (2DES) in this heterostructure. Recently, it has been observed that the LAO/STO(111) interface also hosts a 2DES but its physical properties are relatively unexplored. This work presents a systematic magnetotransport study on the 2DES of this structure. We report on superconductivity in a patterned interface with a 10 uc LAO thin film. The evolution of the superconducting phase at the LAO/STO(111) interface is under investigation. The superconducting phase is observed to be gate tunable and, at optimal doping, the BKT temperature, the maximum critical current and the critical magnetic field are observed to be ~70 mK, ~ 200 nA and ~21 mT, respectively. Furthermore, we observe that interface conduction can be modelled by a random array of Josephson junctions formed by superconducting puddles due to the inhomogeneous character of the interface.

Table of Contents

This thesis describes research that was executed as a combined Master Research Project in Applied Physics and Materials Science and Engineering, leading up to a double MSc degree. In a research subject such as this it is difficult (and sometimes impossible) to separately identify Physics and Materials aspects. Nevertheless, there are certain parts of this thesis that focus mainly on Physics and some that focus mainly on Materials Science. For the convenience of the reader the following list has been compiled.

Main focus on Applied Physics

Section 2.3   Magnetotransport at the $LaAlO_3$/$SrTiO_3$ interface
Section 2.4   Superconductivity at the $LaAlO_3$/$SrTiO_3$ interface
Section 3.6   Magnetotransport
Chapter 5.   Magnetotransport Measurements
Chapter 6.   Superconductivity

Main focus on Materials Science

Section 2.1   Material properties
Section 3.1   Surface treatment
Section 3.3   Pulsed Laser Deposition
Section 3.4   Reflection High-Energy Electron Diffraction
Chapter 4.   Surface Treatment

1. Introduction

Nowadays, the demand for new and more advanced technology in order to improve the quality of life in this fast changing society is large. The developments in information and communication technology would not be possible, if it was not for the progress in physics and materials science that enables these advancements. An important class of novel materials is the transition metal oxides (TMOs) where, due to the strongly correlated electrons, outstanding electronic properties such as ferroelectricity, superconductivity and colossal magnetoresistance are observed. The crystalline structure of TMOs, consisting of layered ionic planes, allows for the creation of artificial crystals consisting of a combination of different TMOs characterized by sharp interfaces. These heterostructures result in physical properties which are not found in bulk constituents due to the interplay between charge, spin, orbit and lattice degrees of freedom. One of the most studied complex oxide heterostructures is the $LaAlO_3/SrTiO_3$ (LAO/STO) which is also be the subject of this thesis.

The discovery of the high mobility two-dimensional electron system (2DES) at the interface of the two band insulators LAO and STO has generated a lot of interest in the field of complex oxide interfaces.[1] Furthermore, it motivated the investigation of the electronic properties at the interface of the LAO/STO(100) heterostructure. The interface was found to exhibit exotic properties such as ferromagnetism[2], giant negative magnetoresistance[3], and two-dimensional superconductivity[4]. Recently, is was discovered that the (110)- and (111)-oriented LAO/STO heterostructures also host a 2DES with comparable values for the sheet carrier density and electron mobility.[5] This was unexpected since the polar character of the three crystallographic orientations is different. Therefore, the origin of the 2DES is still a hot topic of debate. Additionally, superconductivity was observed in the LAO/STO(110) structure. Now the remaining question is: does the 2DES of the LAO/STO(111) structure condense into a superconducting phase? In this thesis, we will explore the electronic and superconducting properties at the interface of the LAO/STO(111) heterostructure.

In chapter 2 of this thesis, we will present the theoretical background of TMOs, with focus on the parent constituents LAO and STO. The origin of the two-dimensional electron system at the interface of an $LaAlO_3/SrTiO_3$ heterostructures is discussed, followed by a description of the electronic and superconducting transport properties of the system. Chapter 3 describes the preparation methods of the samples, including surface treatment, pulsed laser deposition, reflection high energy electron diffraction and the cleanroom processing. Furthermore, the working principle of the devices used to characterize the sample properties, like atomic force microscopy and the cryogenic devices, are explained. Chapter 4 discusses different etching and heat treatments which are performed on STO substrates in order to achieve single termination. In chapter 5, the results of the magnetotransport measurements on the 2DES in LAO/STO(111) heterostructures are presented together with an interpretation in terms of electronic properties. Chapter 6 shows that the 2DES at the interface of a LAO/STO(111) condenses into a superconducting ground state. Thereafter, the temperature, electric field and magnetic field dependence of the superconducting phase are investigated. Chapter 7 presents a summary of the work performed in this thesis and discusses recommendations for future research.

2. Theoretical Background

2.1 Material properties

2.1.1 Perovskites

Perovskite is a class of materials with a crystal structure which takes its name from the atomic arrangements found in the mineral calcium titanate ($CaTiO_3$). The general chemical formula of perovskite type of materials is ABX_3, where A and B are cations and X is an anion. Cations A are mostly rare earth or alkaline earth metal, cations B are a 3d, 4d or 5d transition metal and anion X is an oxygen atom. Figure 2.1 shows the ideal crystal structure of a perovskite which belongs to the space group $Pm\overline{3}m$.[6] Generally, the radius of cations A is larger than the radius of the cations B. Therefore, cations B are 6-fold coordinated while cations A are 12-fold coordinated.[7] Many transition metals oxides (TMOs) have adopted the perovskite structure with the chemical formula ABO_3.

Site A
Site X
Site B
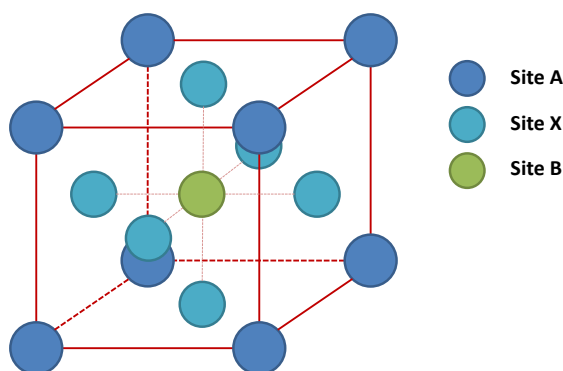
Figure 2.1: The perovskite structure, ABX_3 where A and B are cations and X is an anion.

The physical properties of TMOs are determined by the d-orbital electrons of the transition metal. The s-orbital electrons of the transition metal are transferred to the oxygen ion. The remaining electrons are the highly correlated d-orbital electrons, which determine the electronic and magnetic properties of the system. These electron correlations constrain the number of electrons at a given lattice site and induce a local entanglement of the charge, spin and orbital degrees of freedom.[8]

The ideal structure of perovskites can display a variety of structural instabilities. These instabilities involve rotations and distortions of the oxygen octahedra as well as displacements of atoms from the ideal sites of the cations (site A and B).[9] In 1926, Goldschmidt introduced a tolerance factor based on the radii of the atoms at room temperature.[10] The tolerance factor is defined by

$$t = (r_A + r_O)/\sqrt{2}(r_B + r_O), \tag{2.1}$$

where r_A, r_B and r_O are the radii of cation A, cation B and anion O, respectively. In the ideal case, the tolerance factor is 1, i.e., the atoms form a perfect cubic symmetric perovskite structure. The atomic structure is still called a perovskite structure for values of t between 0.75 - 1. These structures obtain a slight distortion in comparison to the ideal perovskite structure, e.g., orthorhombic symmetry. Therefore a large variety of A and B cation combination are allowed. As a consequence, perovskites show a large variety in magnetic, electric and optical properties.

2.1.2 SrTiO$_3$ & LaAlO$_3$

The materials of interest in this study are SrTiO$_3$ (STO) and LaAlO$_3$ (LAO). Both are TMOs with a perovskite structure. These materials have insulating properties when considering bulk. However, a conducting interface between LAO and STO can be constructed. The lattice constant and the bandgap energy of bulk LAO are 3.790 Å and 5.4 eV, respectively.[1]

Bulk SrTiO$_3$

STO will be the key element of the system considered in the remainder of this research. In the {100} orientation the unit cell is cubic and its lattice constant is a_{STO} =3.905 Å.[1] During a cool down, STO undergoes a second order, anti-ferrodistortive (AFD), phase transition around 105 K. An ADF is a non-polar instability consisting of a rotation of the oxygen octrahedra by a small angle along the c-axis, alternating from one unit cell to the neighbouring one. This can be related to the tolerance factor where t<1 is anti-ferromagnetic distorted and t>1 is ferromagnetic distorted. Furthermore, Koonce et al.[11] studied the superconducting phase transition temperature of STO for different carrier concentrations, as depicted in figure 2.2. The graph shows that despite the fact that STO has a low charge density, a superconducting ground state is observed in a range of electron carrier concentrations from 8.5x10^{18} to 3.0x10^{20} cm^{-3}. The transition temperature achieves a maximum value near 9x10^{-19} cm^{-3} of 0.27 K.[12]
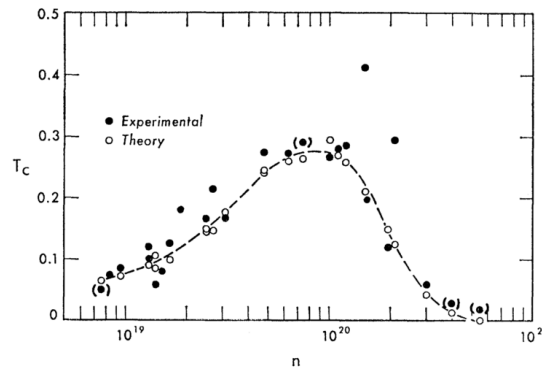
Figure 2.2: The transition temperature, T_c (K), as a function of the carrier concentration. The solid circles are the experimentally obtained data, the open circles show the result from calculations.[11]

2.1.3 Surface Structure

Crystallographic orientation

The perovskite structure (figure 2.1) can be considered along different crystallographic orientations. Perovskite materials can be regarded as a layered structure of ionic planes. The stoichiometry of these planes depends on the crystallographic orientation of the system. Figure 2.3 shows the perovskite structure where the crystallographic planes of the three main orientations {100}, {110} and {111} are indicated by the purple planes where naming of the crystallographic planes follows from Miller indices. The ionic arrangement of a plane is given by the ions intersecting the crystallographic plane. Due to the differences in the arrangements of the planes, each orientation has a different unit cell and therefore different surface properties. Preferentially, the surface will be constructed by the orientation with the lowest surface energy, i.e., the most stable structure. However, it is also possible that less stable orientations can exist.

For the three orientations considered, the LAO and STO crystal structures are constructed from alternating layers parallel to the surface of termination.[5] For STO, the elements and ionic charges are: Sr^{2+}, Ti^{4+}, O^{2-} and it is constructed by the following planes:

- {100} consists of layers of [SrO] and [TiO$_2$]   (cubic structure)
- {110} consists of layers of [SrTiO]$^{4+}$ and [O$_2$]$^{4-}$ (orthorhombic structure)
- {111} consists of layers of [SrO$_3$]$^{4-}$ and [Ti]$^{4+}$ (hexagonal structure)

The structures mentioned on the right are the unit cell structures in the associated orientation. The most stable STO surface is the {100}-orientated surface due to zero net excess charge. This makes STO(100) a widely used substrate. On the other hand, the {110} and {111} orientations both have polar surfaces displaying an excess charge of +4 or -4.

Figure 2.3: The {100}, {110} and {111} oriented crystallographic planes of a perovskite structure material.
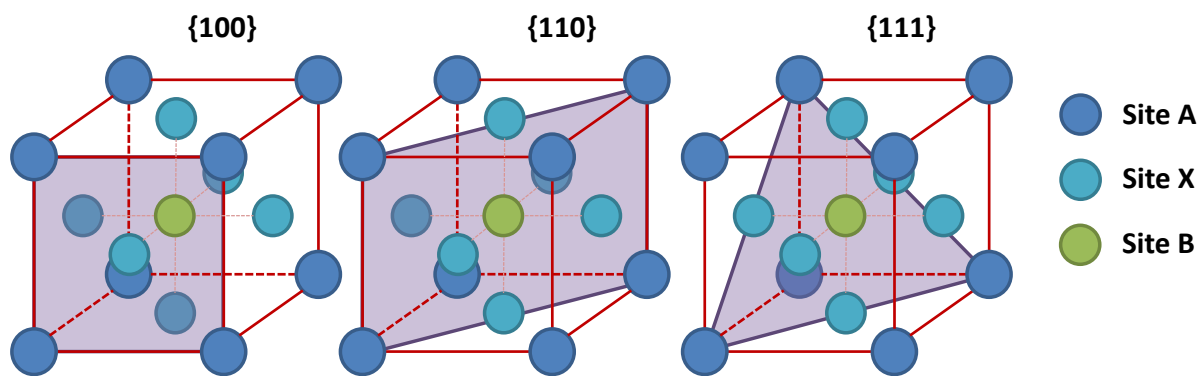
The elements and the electronic charge of LAO are: La^{3+}, Al^{3+}, O^{2-} and the ionic planes for each orientation in LAO structures are:
- {100} consists of layers of [LaO]$^{1+}$ and [AlO$_2$]$^{1-}$ (cubic structure)
- {110} consists of layers of [LaAlO]$^{4+}$ and [O$_2$]$^{4-}$ (orthorhombic structure)
- {111} consists of layers of [LaO$_3$]$^{3-}$ and [Al]$^{3+}$ (hexagonal structure)

In this case, all the orientations show an surface excess charge resulting in a polar surface in every orientation.

Reconstruction of a polar surface

A polar surface yields an unstable termination due to the presence of a perpendicular dipole which induces an infinite surface energy. A polar surface can only exist if the dipole is removed. In 2007, Russel et al.[13] studied the surface reconstruction of single crystal Nb-doped STO(111) annealed in Ultra High Vacuum (UHV) at 850°C for 30 min with use of Scanning Tunnelling Microscope (STM) and Auger Electron Spectroscopy (AES). They explain that reconstruction can be achieved by the following 4 mechanisms:

1) **Changing the surface stoichiometry** will produce different phases in the first few layers of the surface. The charge distribution in these layers will be different from the bulk termination and can quench the dipole.

2) **Redistribution of electrons** near the surface as a response to the polar electrostatic field thereby removing the polarity.

3) **Adsorption of atoms or molecules** from the residual atmosphere compensating the excess charge.

4) **Microfaceting** will increase the surface area and reduce the surface energy of nonpolar facets. Faceting only occur if the other three methods did not lower the energy sufficiently.

Figure 2.4 presents a scans of the surface of a Nb-doped STO(111) surface. Two distinct ordered domains can be identified, phase α indicating (√13×√13)R13.9° reconstruction and phase β indicating (√7×√7)R19.1° reconstruction. Their co-existence indicates that both reconstructions have similar energies. No evidence of microfaceting can be identified in the images. Furthermore, the AES spectra do not indicate absorption of foreign species, but however do show non-stoichiometry in the surface region. Both ordered phases are enriched in Ti and Sr and deficient in O. The reconstructions are most likely to be a kinetic phase of the STO(111) surface.[13]
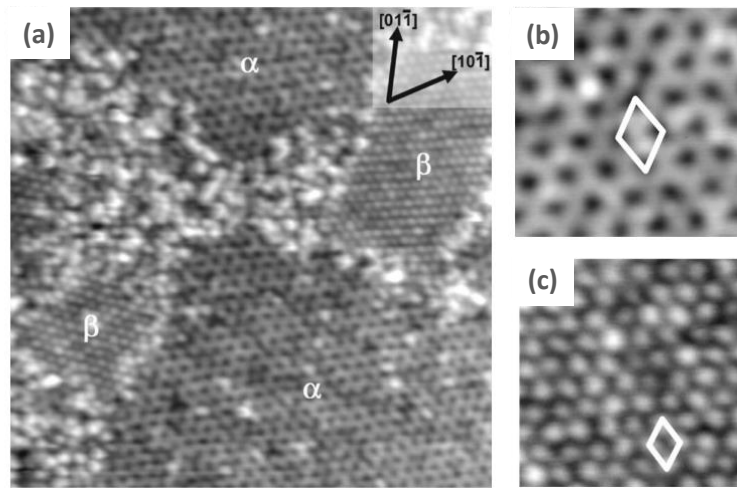
Figure 2.4: STM images of the thermally treated Nb-doped STO(111) samples. a) 65x65 nm^2 scan of the surface containing ordered domains where two different domain orientations can be identified by α and β being $\left(\sqrt{13} \times \sqrt{13}\right)R13.9°$ and $\left(\sqrt{7} \times \sqrt{7}\right)R19.1°$, respectively. Boundaries between the domains appear disordered. b) 12x12 nm^2 scan of the $\left(\sqrt{13} \times \sqrt{13}\right)R13.9°$ reconstruction and c) of the $\left(\sqrt{7} \times \sqrt{7}\right)R19.1°$ reconstruction where the unit cells are indicated by the white lines. [13]

Marks et al.[14] performed a theoretical study on the reconstruction of STO(111) surfaces using density functional theory (DFT) calculations. Their analysis suggest that the surface spontaneously disproportionate into SrO and TiO$_2$ rich domains. Note, these domains obey the compositions of the ionic planes of STO(100). In 2008, Russel et al.[15] performed a similar study on Nb-doped STO(110) samples using STM and AES analysis to investigate the reconstruction of the polar surface of the samples. They found that in this system the reconstruction of the dipole takes place by a change in stoichiometry. The analysis shows that the upper layers of the STO surface are Ti and Sr enriched and O deficient compared to the bulk stoichiometry, similarly to the Nb-doped STO(111).

2.1.4 Band Structure and Fermi Surface

The band structure of bulk STO(100) is constructed as follows: the top of the valance band is mainly composed of 2p-orbitals of oxygen in nonbonding states whereas the lower part of the valance band is formed by bonding states between 3d-orbitals of titanium and 2p-orbitals of oxygen. The conduction band mainly consist of 3d, 4s and 4p states of titanium and 3d and 4s states of strontium.

The fundamental gap of STO, separates the 3d bands of titanium from the 2p band of oxygen which determine the energy gap to be 3.2 eV at the Γ-point.[9,16]

The properties of the conduction band can be discussed by considering the titanium atoms in the crystal field. Figure 2.5 shows the energy level of the titanium 3d-orbitals and the splitting of the energy level due to the change of symmetry in the system. In absence of a crystal field (spherical symmetry), the energy levels are degenerate. The perovskite structure creates crystal field in which the transition metal ion (titanium) is surrounded by 6 oxygen ions. The oxygen ions produce a crystal field acting on the titanium with cubic symmetry. Wave functions pointing towards the oxygen ions have higher energy in comparison to the wave functions pointing between the oxygen ions , owing to the repulsion between the d-orbital electrons and the surrounding charge, i.e., the oxygen ions. As a consequence, the original 5-fold degenerate 3d-orbitals of the transition metal are split into three-fold degenerate T$_{2g}$ orbitals (d_{xy}, d_{xz} and d_{yz}) and two-fold degenerate E$_g$ orbitals ($d_{x^2-y^2}$ and $d_{3z^2-r^2}$). The energy difference between the two states is determined to be ∼2 eV.[17] This means that the bottom of the conduction band consists of the T$_{2g}$ states in the 3d-orbitals of titanium.
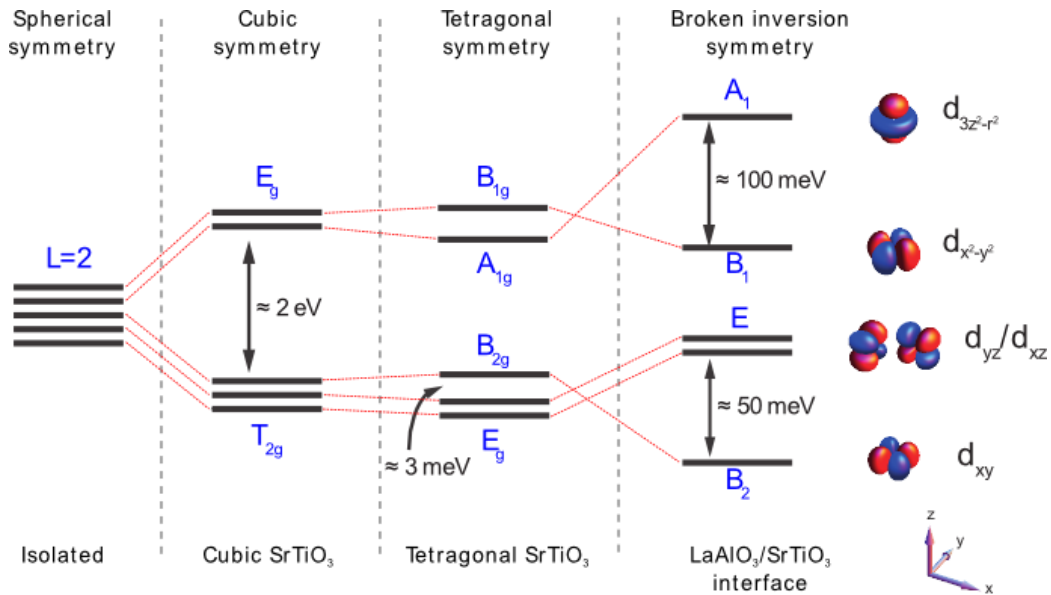
Figure 2.5: The 3d-orbital energy levels of titanium atoms in STO(100) structures with spherical, cubic, tetragonal and broken inversion symmetry due to the different symmetries, the energy level split and become non-degenerate.[18]

The AFD transition of STO(100) at 105 K changes the symmetry from cubic to tetragonal due to the rotation of the oxygen octrahedra, this results in a splitting within the T$_{2g}$ and E$_g$ energy levels. The extension of the c-axis hinders the planar orbitals therefore shifting the energy of the d_{xy} orbital by ∼3 meV relative to the d_{xz} and d_{yz} orbitals.[19] The creation of an interface with LAO(100) results in a confined potential that breaks the inversion symmetry. This reverses the order of the energy levels in the E$_g$ and T$_{2g}$ states as shown in figure 2.5. At the interface, the d_{xy} orbitals will be located at the bottom of the conduction band. The average energy of the level splitting between d_{xy} states and d_{xz} and d_{yz} states, at LAO/STO(100) interfaces, is experimentally observed to be ∼50 meV.[20] Salluzzo et al.[21] used x-ray absorption spectroscopy to determine the average energy splitting of $d_{x^2-y^2}$ states and $d_{3z^2-r^2}$ states to be ∼100 meV.[9,22,23]

Figure 2.6a depicts the band structure of the dominate energy bands in the conduction band of STO(100) near the LAO/STO interface. Below at critical carrier density, the electrons will most probably reside in the d_{xy} bands, leaving the system with one type of charge carrier. The Fermi level enters the d_{xz} and d_{yz} bands when the density exceeds the critical carrier density and the system will undergo a so-called Lifshitz transition. This indicates that above the critical carrier density the d_{xz} and d_{yz} bands start to be populated and new types of carriers are predicted to contribute to the conduction.

The atomic surface structure of STO(111) is different from STO(100). In an {111}-oriented bilayer of cubic symmetric TMOs, the transition metal forms a honeycomb lattice. Figure 2.6b shows the perovskite structured STO with the {111} plane highlighted in grey. Figure 2.6c displays the honeycomb lattice constructed of three consecutive titanium layers. The titanium ions in the different layers are indicated by red, blue and green. This lattice structure gives rise to exotic, potentially topological, electronic states at the interface such that the electronic states at the surface of the STO(111) with the corresponding Fermi surface, subband masses and orbital ordering are different from the STO(100) surface.
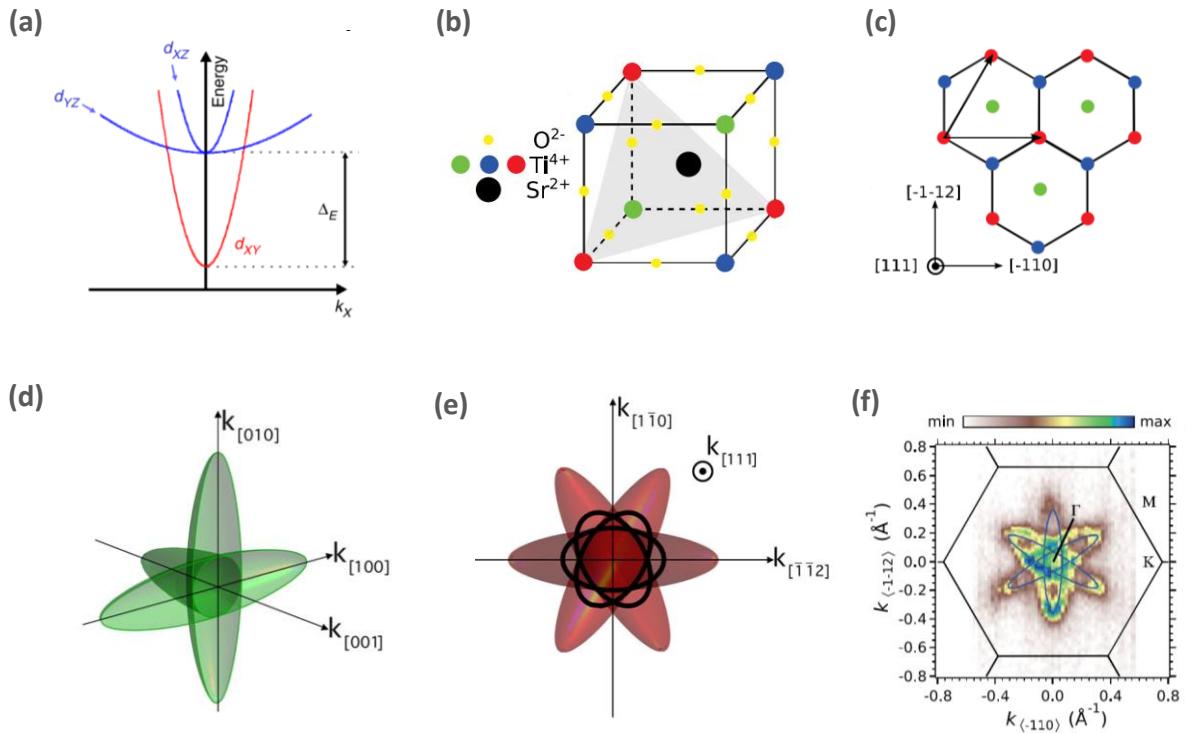
Figure 2.6: a) The dominate 3d-orbitals energy bands in the conduction band of LAO/STO(100). The d_{xy} band and the d_{xz} and d_{yz} bands are split by an energy $\Delta_E \sim 50$ meV.[20] b) The STO perovskite structure with a grey plane indicating the (111) plane. c) The honeycomb lattice constructed from titanium atoms resulting from a bilayer of the STO(111) structure. The different colours indicate the titanium atoms in the different layers.[24] d) The projection of the Fermi surface and the Γ point surface cut through the [001] axis of bulk STO. e) The projection of the Fermi surface of bulk STO cut through the [111] axis. The black lines are the cut though the Γ point of the (111) plane.[25] f) An ARPES Fermi surface map of STO(111) surface prepared in-situ. The blue lines give the projection of the Fermi surface.[24]

The two major differences between STO(100) and STO(111) are the symmetry and the polar character of the atomic planes. The STO(100) has a four-fold symmetry and is non-polar whereas the STO(111) has a six-fold symmetry and consists of atomic planes having a charge ± 4. Figure 2.6d

displays the four-fold Fermi surface of bulk STO cut by the (100) plane. The black lines in figure 2.6e show the six-fold Fermi surface of bulk STO cut through the (111) plane. However, in a 2D system all values of the momenta perpendicular to the surface ($k_\perp$) collapse on the surface. Consequently the electronic states have the same energy for all values of momenta. The Fermi surface of the 2DES can be approximated by the projection of the 3D bulk Fermi surface onto the surface plane, i.e., the contour of the green area in figure 2.6d and red area in figure 2.6e for STO(100) and STO(111), respectively.[25] Rödel et al.[24] imaged with ARPES the electronic structure of in-situ cleaved STO(111) in vacuum. Figure 2.6f is the obtained surface map of the STO(111) sample where the blue lines indicate the projection of the Fermi surface of the unreconstructed surface plane. The measured Fermi surface is comparable to the unreconstructed surface. Therefore, they state that reconstructions and defects at the interface do not influence the electronic states of the 2DES which could indicate that the 2DES is living a in a subsurface layer of the STO.

2.2 The 2D Electron System at the LaAlO$_3$/SrTiO$_3$ Interface

In 2004, Ohtomo and Hwang[1] where the first to experimentally realize a LAO(100)/STO(100) heterointerface. Figure 2.7 shows the two possible arrangements of ionic planes at the interface, [LaO]$^{1+}$/[TiO$_2$] and [AlO$_2$]$^{1-}$/[SrO]. In both arrangements a polar discontinuity is created at the interface due to the polar character of LAO and the non-polar character of STO. Unusual states, not found in bulk materials, can be realized if the polar discontinuities can be atomically controlled. In this study, the interfaces were created by growth of an LAO thin film using pulsed laser deposition (PLD) on top of a single crystal STO substrates characterized by well-defined terminations. The sheet resistance and Hall effect have been studied and a Two-Dimensional Electron System (2DES) was observed at the [LaO]$_{1+}$/[TiO$_2$] interface of LAO/STO(100) heterostructures.

(a) (AlO$_2$)$^-$ (LaO)$^+$ (AlO$_2$)$^-$ (LaO)$^+$ (TiO$_2$)^0 (SrO)^0 (TiO$_2$)^0 (SrO)^0

(b) (LaO)$^+$ (AlO$_2$)$^-$ (LaO)$^+$ (AlO$_2$)$^-$ (SrO)^0 (TiO$_2$)^0 (SrO)^0 (TiO$_2$)^0
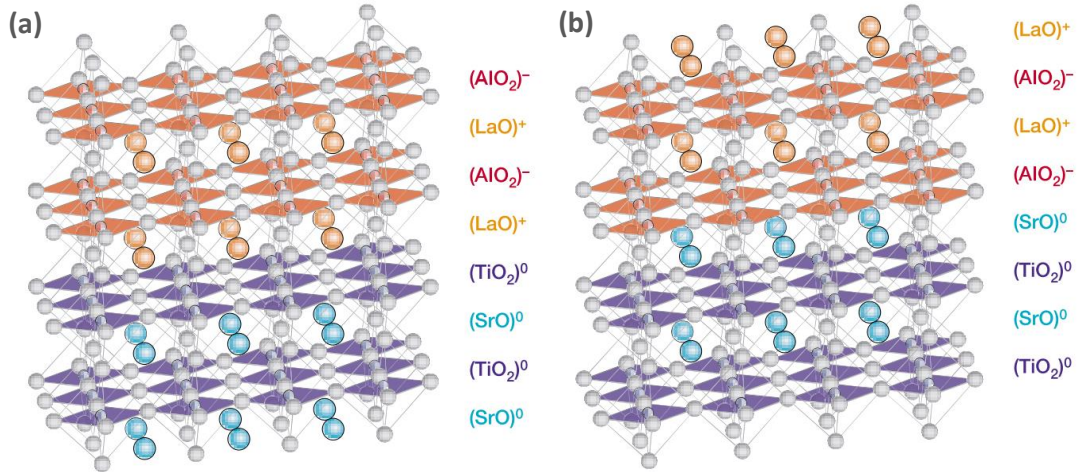
Figure 2.7: The two possible interfaces between LAO(100) and STO(100). a) Ti-rich terminated STO with interface planes [LaO]$^{1+}$/[TiO$_2$] and b) Sr-rich terminated STO with interface planes [AlO$_2$]$^{1-}$/[SrO].[1]

2.2.1 Origin of the two-dimensional electron system

There are several mechanisms proposed in literature for the existence of a 2DES at the LAO/STO(100) interface, namely polar discontinuity, vacancy doping and cation interdiffusion, which will be discussed in the following sections.

- **Polar discontinuity**

As mentioned before, the LAO/STO interface consists of a layered structure of ionic planes. If the heterointerface is constructed from polar LAO and nonpolar STO planes (or any type of planes from different charge families) a charge discontinuity is present, creating dangling bonds and incomplete atomic coordinations at an atomically abrupt interfaces. In TMOs, electrons can move even when atoms are not hence energy reconstruction can be achieved by redistribution of electronic charge. This reconstruction scenario allows electrons from the LAO surface layer to travel to the LAO/STO interface, creating a more gradual charge discontinuity.

Figure 2.8 shows the atomic arrangements of the unreconstructed and reconstructed LAO/STO(100) heterostructures. Furthermore, the net charge (ρ), electric field (E), and the electrical potential (V) in the system are presented. Figure 2.8a and b show the arrangements of the ionic planes of the unreconstructed heterostructures for the two different terminations. Both terminations have a polar/nonpolar interface configuration and the net charge in the film is alternating ±1. Consequently, the electric field at the interface induces a diverging potential with increasing film thickness. Theoretically, the diverging potential can be avoided if half an electron is added (removed) to the top Ti (Sr) interface layer hence charge reconstruction can avoid a polar catastrophe.

Figure 2.8c shows the electron-doped heterostructure with the interface planes $[LaO]^{1+}/[TiO_2]^0$. Half an electron per unit cell is transferred from the LAO surface layer to the interface and the mixed valance Ti state obtains a charge +3.5, creating an overall neutral structure. The interface dipole that arises due to this reconstruction, results in an electric field which oscillates around zero and subsequently induces a finite potential. This interface is hosting a 2DES with an electron mobility and sheet carrier density of $\sim10^3$ cm^2/Vs and $\sim10^{13}$ electrons/cm^2, respectively.[1] Figure 2.8d displays the hole-doped $[AlO_2]^{1-}/[SrO]^0$ interface. It is experimentally observed that such an interface is insulating.[1] This is ascribed to the fact that there are no mixed-valence states available to compensate for half a hole such that atomic reconstruction is more favourable in this case.[26] This indicates the importance of the termination of the STO substrate.

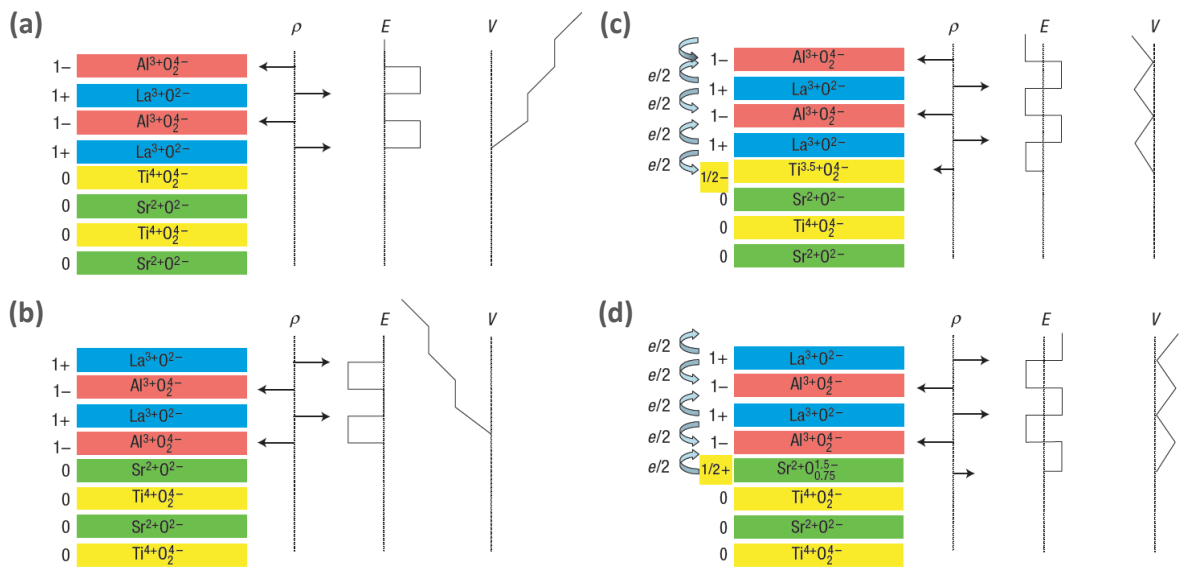**Figure 2.8: The polar catastrophe for atomically abrupt LAO/STO(100) interfaces with the accompanying net charge (ρ), electric field (E), and the electrical potential (V). a) unreconstructed $[LaO]^{1+}/[TiO_2]^0$ interface, b) unreconstructed $[AlO_2]^{1-}/[SrO]^0$ interface, c) reconstructed electron doped $[LaO]^{1+}/[TiO_2]^0$ interface, d) reconstructed hole doped $[AlO_2]^{1-}/[SrO]^0$ interface.[26]**

This last phenomenon is emphasized by Nishimura et al.[27] who carried out a study on the influence of a interlayer of SrO between LAO/STO(100) interface. One fractional atomic layer of SrO is deposited on a TiO_2 terminated substrate before deposition of the LAO film. Figure 2.9 shows the influence of the different partial coverages of SrO (θ_{SrO}) on the properties of the system. Figure 2.9a displays a metal-to-insulator transition as the coverage of SrO became complete (from 0.83 to 1.0). Figure 2.9b presents the Hall coefficient as a function of SrO coverage. At zero SrO coverage the density is 0.5 electrons per Ti site where full SrO coverage results in zero electrons per Ti site, supporting the theory of polar discontinuity.
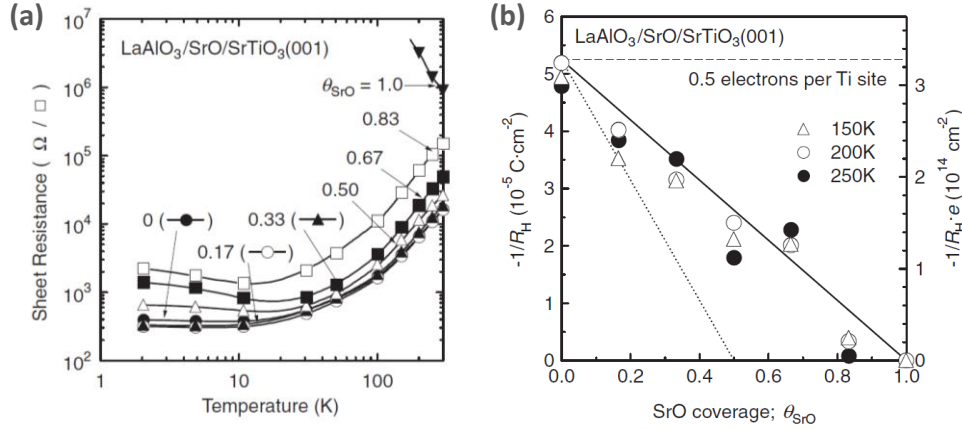

Figure 2.9: a) Temperature dependence of the sheet resistance LaAlO₃/SrO/SrTiO₃ heterointerfaces with different fractional SrO coverages. b) The inverse Hall coeffiecient dependence of the SrO coverage.[27]

Thiel et al.[28] have experimentally verified that the thickness of the LAO layer plays an important role in the transport properties of the system. Figure 2.10 shows the critical thickness (d_c) for the {100} orientation of the LAO/STO system to be 4 unit cells (uc). An LAO layer with a thickness below 4 uc results in an insulating interface with a sheet conductance below their measurement limit for all temperatures. Samples with a thickness above 3 uc obtain a conducting interface with the sheet conductance varying between 4×10^{-3} Ω^{-1} and 2×10^{-5} Ω^{-1} for temperatures between 4.2 K and 300 K. The critical thickness can be understood by considering the band bending due to the electric field in the LAO film. The energy gap between the conduction band of the STO and the valance band on the LAO is ~3.3 eV. At the critical thickness, the potential build-up causes the valance band of LAO to reach the energy of the conduction band of STO and a Zener breakdown occurs.[29]

The two dimensional carrier density at the interface predicted by the polar catastrophe is one half electron per unit cell, i.e., 3.5 x 10^{14} cm⁻².[1,30] The carrier density that is commonly measured is 1-2 x 10^{13} cm⁻² which is lower than predicted by the polar discontinuity theory.[30–32] According to the density functional study of Popović et al.[33], this can be explained by a model assuming the presence of localized and delocalized electron states in the system. For the purpose of their study the conduction band structure of the LAO/STO(100) system resulting from the first four Ti layers is considered. The d_{xz} and d_{yz} band have the same band structure for all layers whereas the d_{xy} bands show an increase in energy when moving away from the interface. Though, the first four layers of these bands are lower in energy than the d_{xz} and d_{yz} bands because of larger hopping integrals in the xy-plane (parallel to the interface). The lowest d_{xy} subband (Ti_1) is localized because of its lower interface potential. The higher energy d_{xy} subbands, i.e., Ti_2, Ti_3 and Ti_4, have similar energies. The first kind of electrons reside in the lowest conduction band, consisting of mostly Ti_1 (d_{xy}) subbands. These

electrons have a strong 2D character and are Anderson localized by disorder, thus do not participate in the electronic transport. The second type of electrons residing in the Ti_2, Ti_3 and Ti_4 d_{xy} subbands have a low mass and are difficult to localize by disorder. The number of these mobile electrons is estimated to be 8×10^{13} cm^{-2}. Although, higher than the measured carrier densities, it is 5 times smaller than the one need to satisfy the polar catastrophe.

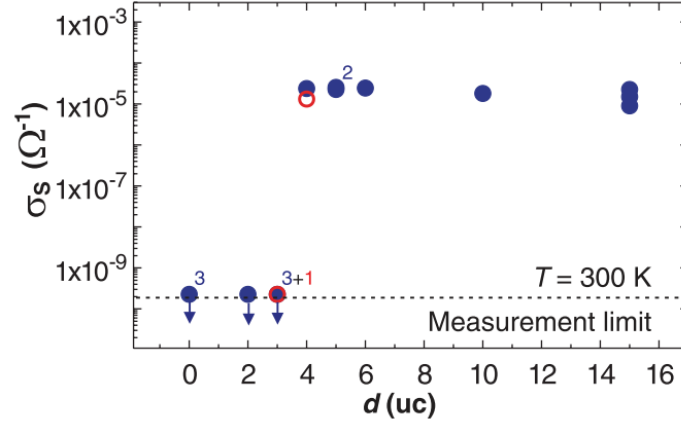**Figure 2.10: Influence of the LaAlO₃ layer thickness (*d*) on the sheet conductance of the LaAlO₃/SrTiO₃ heterostructure at the (100) interface. (Blue dots indicate the samples grown at 770°C and the red at 815°C.)**[28]

- **Vacancy doping**

Several studies have shown that atomic defects arising from the growth condition during the deposition of an LAO thin film play an essential role in the electronic properties of the system.[30–32] Oxygen vacancies are created due to the high kinetic energy of the incoming atoms and low oxygen pressure ($<10^{-6}$ mbar) during the deposition. An environment with low oxygen pressure prevents oxygen vacancies to be refilled. After the completion of an LAO monolayer, the vacancies are trapped in the system. The removal of an neutral oxygen atom from an O^{-2} site leaves two electrons in the vicinity of the vacancy. The formation of vacancies at the interface are energetically more favourable as bulk vacancy formation because at the interface the electrons can accommodate and compensate holes that are intrinsic to this charge-imbalanced interface.[34]

Liu et al.[35] have studied the effect of the oxygen vacancy concentration on the conductivity in the LAO/STO(100) interface by varying the oxygen pressure during deposition of amorphous and crystalline LAO films. Figure 2.11 shows the temperature dependence of the sheet resistance of amorphous LAO/STO interfaces prepared under different oxygen pressures. For each oxygen pressure, the heterostructures exhibit metallic behaviour in the whole temperature range. Though, the room temperature sheet resistance increases with increasing oxygen partial pressure. Post-annealing for 1 hour at 600°C in 1 bar oxygen flow removes the conductivity of the amorphous heterostructures, indicating that oxygen vacancies are the source of the interface conductivity. Heterostructures with crystalline LAO films result in conducting interface for unannealed as well as post-annealed structures. Though, after post-annealing the room temperature sheet resistance is increased by a factor 7. This indicates that for crystalline LAO/STO(100) systems oxygen vacancies are only partially responsible for the interface conductivity. Furthermore, the crystallinity of the LAO film is essential for the polar catastrophe mechanism.

Cancellieri et al.[36] also studied the effect of the oxygen pressure during the deposition of crystalline LAO films on a STO(100) substrate. They showed that while depositing LAO films at different oxygen pressures ranging from 10^{-6} mbar to 10^{-2} mbar, subsequent post-annealing at 530 °C for 1 hours with an oxygen pressure of 0.2 bar result in similar electrical transport properties. Indicating that post-annealing successfully refills the oxygen vacancies and removes the conducting effect related to the oxygen vacancies. Concluding again that the conductivity of unannealed heterostructures is dependent on both oxygen vacancies and the polar discontinuity whereas the conducting interface of the annealed heterostructures are determined by the polar discontinuity only.

In Ohtomo and Hwang's work[1], the influence of the oxygen vacancies on the conductivity is discussed. An extra atomic layer of SrO is introduced before the growth of the LAO layer, resulting in a non-conducting interface. In line with the observations of Nishimura et al..[27] They discuss that if oxygen vacancies would be the dominant mechanism, both interface terminations ($[LaO]^{1+}/[TiO_2]^0$ and $[AlO_2]^{1-}/[SrO]^0$) should display conductivity, however this was not observed.
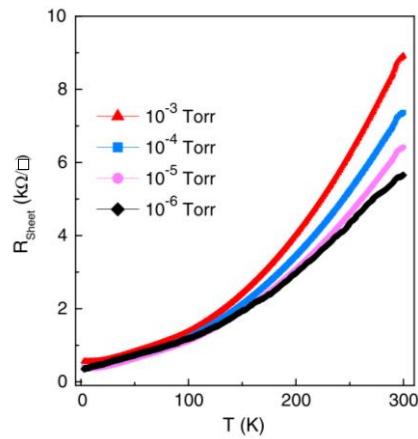
Figure 2.11: The temperature dependence of the sheet resistivity of the amorphous LAO/STO interface for different oxygen pressures.[35]

- **Cation interdiffusion**

One of the explanations mentioned in literature for the conductivity at the LAO/STO interface is redistribution of the cations in the vicinity of the interface. In 2010, Chambers et al.[37] investigated the possibility of intermixing of atoms at the LAO/STO(100) heterostructures by means of DFT calculations. According to their calculations, it is energetically more favourable to form an intermixed interface when taking into account classical and quantum mechanical potentials. The diffusion takes place at temperatures of 1000 K, which is comparable to the growth temperature used in the PLD. During the growth, A-site cations (La and Sr) are exchanged with each other and the same for B-site cations (Al and Ti). A claim is made that there is a preference of La interdiffusion into STO, leading to n-type doping, i.e., formation of mobile electrons in the STO. The correct band offset can be estimated by the calculations when including intermixing into the physical model.

Willmot et al.[38] studied the formation of metallic $La_{1-x}Sr_xTiO_3$ caused by cation intermixing at the interface of LAO/STO(100) heterostructures by surface x-ray diffraction. The measured interface is not atomically abrupt hence diffusion of the cations has occurred. They have experimentally observed that Sr and La have the larger probability for intermixing resulting in a 1 or 2 monolayer thick metallic $La_{1-x}Sr_xTiO_3$ layer. These observations are supported by DFT calculations.

2.2.2 Other crystallographic orientations

The (100)-oriented LAO/STO interface has been the subject of intense study. The 2DES can host superconductivity, Shubnikov - de Haas oscillations and even incipient magnetism, illustrating how electron correlations can be enhanced in 2D confined systems. Not much attention has been devoted to alternative orientations, which could be related to the ongoing discussion about the different scenarios explaining the origin of the 2DES. Recently, {110}-oriented LAO/STO interface and the {111}-oriented interface are gaining more attention due to the fact that high mobility conductivity is observed at the interface of these heterostructures.[5]

The nature of the charge transfer is supposedly dependent on the crystallographic orientation of the interface. Figure 2.12 shows a schematic of the LAO/STO interfaces in the {100}, {110} and {111} orientation which give raise to a high mobility 2DES with the corresponding configuration of ionic planes of the STO substrates and the LAO film. The LAO/STO(100) configuration is the same as shown in figure 2.7a. The {110}-oriented interface is created by surface planes of $[LaAlO]^{4+}/[O2]^{4-}$ which do not create a polar discontinuity. The {111}-orientated interface is constructed by $[LaO_3]^{3-}/[Ti]^{4+}$ surface planes displaying a polar discontinuity. Note that in this orientation the discontinuity is caused by a polar/polar interface whereas the discontinuity in the {100}-orientated interface is caused by a polar/non-polar interface. Surface reconstruction of the Ti^{4+} toplayer will occur before growth of the LAO film.
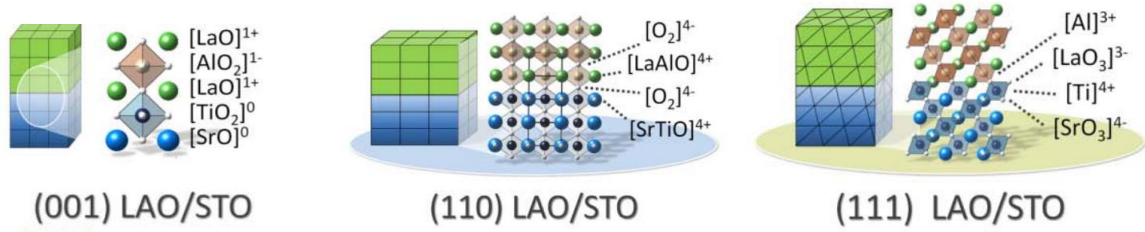
Figure 2.12: The LAO/STO interface in the (100), (110) and (111) orientations where STO is presented by the blue blocks and LAO by the green blocks. The composition of the ionic planes in given on the right of the blocks.[5]
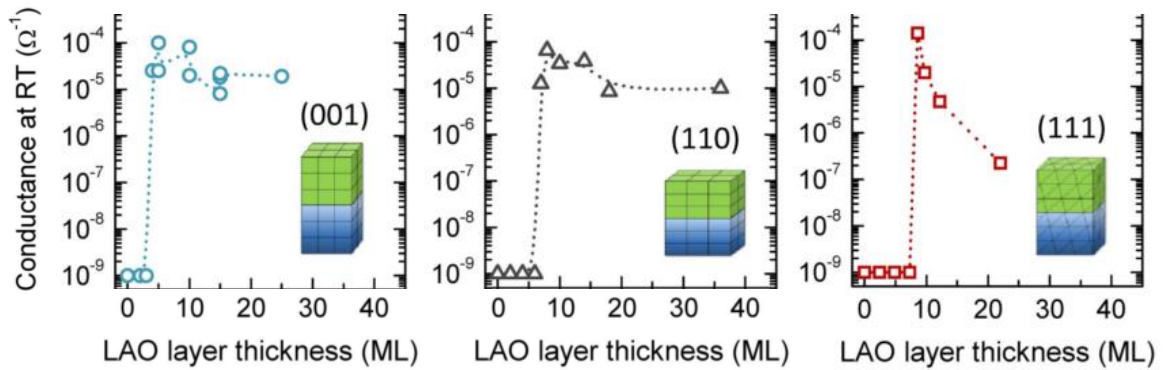
Figure 2.13: The LAO film thickness dependence of the conductance in the LAO/STO heterostructure for the (100), (110) and the (111) oriented interfaces. An abrupt jump is observed at a critical thickness indicating a metal-to-insulator transition.[39]

In 2012, Herranz et al.[5] conducted a research on the electronic properties of the {110} and {111} orientations of the LAO/STO system with the goal to broaden the scope of the origin and the behaviour of interfaces containing a 2DES. It appears that both orientations show conductivity, thereby obtaining values for the electron mobility and sheet carrier density up to 2500 cm^2/Vs and 10^{14} cm^{-2}, respectively. As discussed before, the {110} orientation has no polar discontinuity and in contrast to experimental observations, no metallic behaviour was expected according to the polar

discontinuity theory.[40] The conducting interface for the {111} orientation was predicted due to the polar mismatch of the interface layers. In the same study, Herranz et al. also observed a critical thickness of the LAO film for {110}- and {111}-oriented LAO/STO interfaces, similar to the {100} interface. Figure 2.13 shows the abrupt jump from an insulating to a metallic state at a critical thickness observed in the {100}, {110} and {111} orientations. The critical thickness at the {110}-oriented interfaces and the {111}-oriented interfaces is measured to be 7 uc and 9 uc, respectively. Furthermore, the it can be seen that the conductance of the {110} orientation is reaching a constant value while the conductance at the {111} orientation shows a significant decrease with increasing film thickness.

Although the conducting interfaces of all three crystal orientation show similar properties, the {110} orientation does not have the same polar nature as {100} and {111} orientation, suggesting that polar discontinuity is not the proper explanation for the 2DEG at the interface. However, Annadi et al.[41] used measurements and DFT calculations to show that the explanation of electronic reconstruction at the LAO/STO interface for the appearance of the 2DEG can be the valid. The characteristics of the transport properties at the interface of the {110} orientation are similar to the other two orientations but strong anisotropic properties along the in-plane directions are observed. The DFT calculations show that the atomic surface structure in the {110} crystal orientation is not a parallel interface but the preferable interface structure is buckled. Figure 2.14 displays a schematic of the atomic arrangement for the buckled surface structure. This structure can explain the anisotropic characteristic and supports electronic reconstruction because such an interface will induce a polarization discontinuity at the interface of the {110} orientation.
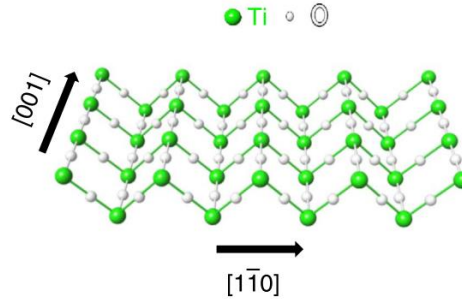
Figure 2.14: A buckled structure is the preferred interface structure in the {110} orientation of LAO/STO heterostructures (green: Ti atoms, white: oxygen atoms) [41]

2.3 Magnetotransport at the LaAlO₃/SrTiO₃ interface

2.3.1 Hall characteristics

An accurate method to determine the sheet carrier density and the electron mobility in a system is the Hall effect. The Hall effect is based on a voltage difference across an electrical conductor perpendicular to the applied electrical current induced by an out-of-plane magnetic field. An applied magnetic field produces a Lorentz force that acts on the charge carrier. The path of the carriers will be bend and therefore a Hall voltage is induced. The drift velocity of the electrons can be obtained by the relaxation time approximation,

$$m^* \left[\frac{d\boldsymbol{v}}{dt} + \frac{\boldsymbol{v}}{\tau} \right] = q\boldsymbol{E} + q\boldsymbol{v} \times \boldsymbol{B}, \tag{2.2}$$

with τ^{-1} being the relaxation scattering time, q is the electronic charge and m^* is the effective mass. We consider the interface to be in the xy-plane such that the magnetic field is applied in the z-direction, $\boldsymbol{B} = (0,0,B)$. Furthermore, we assume the electric field to be in-plane, i.e., $\boldsymbol{E} = (E_x, E_y, 0)$. The Hall effect represents a steady state of the system, i.e., $d\boldsymbol{v}/dt = 0$ such that the components of the time relaxation approximation become:

$$v_x = \mu E_x + \omega_c \tau v_y \tag{2.3}$$

and

$$v_y = \mu E_y - \omega_c \tau v_x, \tag{2.4}$$

where the carrier mobility, $\mu = \frac{e\tau}{m^*}$ and the cyclotron frequency, $\omega_c \equiv eB/m^*$. The Hall effect is the influence of the magnetic field on the resistivity perpendicular to the applied current. If the response of the Hall resistivity is linear, one type of charge carrier is present in de system. In this case, it is imposed that no current will flow in the y-direction, i.e., $v_y = 0$ such that the current in the x-direction, $v_x = E_y/B$. Furthermore, the current density is in x-direction of the interface is given by $J_x = -n_s^{2D} e v_x$ where n_s^{2D} is the sheet carrier density. The definition of the Hall coefficient is:

$$R_{\mathrm{H}} \equiv \frac{E_y}{J_x B}. \tag{2.5}$$

The sheet carrier density can be obtained from the Hall coefficient via

$$n_s^{2D} = -\frac{1}{eR_{\mathrm{H}}} \tag{2.6}$$

Furthermore, the mobility of the charge carriers can be extracted using:

$$\mu_e = \frac{1}{n_s^{2D} e \rho_{xy}^{2D}} \tag{2.7}$$

In a system with multiple charge carriers, e.g. light and heavy electrons with different effective mass (m^*), scattering rate (τ^{-1}), charge (q) and carrier density (n_s^{2D}), the Hall coefficient becomes non-linear. The magnetic field dependence of the sheet resistance becomes:

$$\rho_{xy}(B) = -\frac{(\sigma_1^0 \mu_1 + \sigma_2^0 \mu_2) + (\sigma_1^0 \mu_2 + \sigma_2^0 \mu_1)\mu_1 \mu_2 B^2}{(\sigma_1^0 + \sigma_2^0)^2 + (\sigma_1^0 \mu_2 + \sigma_1^0 \mu_1)^2 B^2} B, \tag{2.8}$$

where $\sigma_j^0 = n_j q_j \mu_j$ is the zero-field conductivity of the Sommerfeld model for carrier j.[42]

- **Temperature dependent Hall effect**

Veerendra et al.[43] studied the Hall effect at the interface of LAO/STO(100) heterostructures as a function of temperature. The measurements are performed in the van der Pauw configuration with the temperature varying between 4 and 70 K. The out-of-plane applied magnetic field goes up to 30 T. The Hall effect is observed to be linear below 7 K and above 50 K. The sheet carrier densities in the two distinct regions are $n_{4.2\,K} = 8.7{\times}10^{13}$ and $n_{65\,K} = 7{\times}10^{13}$ electrons/cm² and the electron mobilities are $\mu_{4.2\,K} = 10$ cm²/Vs and $\mu_{65\,K} = 120$ cm²/Vs. In these region the conduction is dominated by a single conduction band whereas in between 7 K and 50 K the Hall resistance show non-linear behaviour indicating multiband conduction.

Gariglio et al.[44] measured the Hall effect on LAO/STO(100) heterostructures with a film thickness of 4 uc. Figure 2.15 shows the sheet carrier density which is measured to be $\sim$4-7$\times$10^{13} electrons/cm^2. The inset displays the electron mobility where an increase of the electron mobility is observed when cooling down from 300 K due to the freeze out of the phonon vibrations. At low temperatures, the electron mobility depends only on the inhomogeneities at the interface and saturates at 300 cm^2/Vs.

Herranz et al.[5] studied the Hall effect for LAO/STO(110) heterostructures for different LAO film thicknesses. The sheet carrier density is observed to be between 10^{13}-10^{14} electrons/cm^2. Each film thickness shows a decrease in mobility at high temperature whereas the saturation of the mobility varies from 30 to 2300 cm^2/Vs indicating that the film thickness influences the transport properties of the conducting electrons, even above the critical thickness. Note, the values are in the same order of magnitude as measured at STO(100) interfaces.
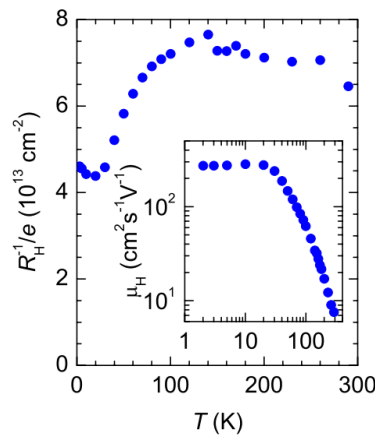

Figure 2.15: The sheet carrier density and the electron mobility of an LAO/STO(100) interface.[44]

- **Gate tunable Hall effect**

In LAO/STO systems, both LAO and STO can be used as a gate dielectric such that back, top or side gates can electrostatically tune the number of mobile carriers at the interface. The conductivity of the 2DES can be modulated through a phase transition from an insulating to a metallic state by applying a gate voltage. Electrostatic doping allows for tuning of the sheet carrier density while preserving the structural features of the interface. Thiel et al.[28] showed that the transport properties of the 2DES at the LAO/STO interface can effectively be modulated by an electric field. They measured that, in LAO/STO(100) heterostructure with a 3 uc film, the back gate can generate a conductance change of seven orders of magnitude inducing a phase transition. A system with a film thickness $\geq$ 4 uc, that has a conducting interface at V_{bg}= 0 V, back gate modulation was possible but a phase transition to an insulating state was not induced.

Joshua et al.[20] measured the back gate voltage dependence of the Hall effect of LAO/STO(100) heterostructures. Figure 2.16 shows the Hall coefficient with the back gate voltage varying from -40 V to 420 V. The Hall coefficient shows a distinct change at the critical voltage, V_C= 40 V. Below V_C, the resistivity is linear such that the Hall coefficient is roughly constant with a decreasing magnitude when reducing V_{bg}. Above V_C, the resistivity is non-linear and the Hall coefficient shows an Bell-like shape. The change in behaviour of the resistivity is attributed to the Fermi level reaching the d_{xz} and d_{yz} bands at a specific electron doping, i.e., the critical voltage, changing the transport form single to multi band conduction.
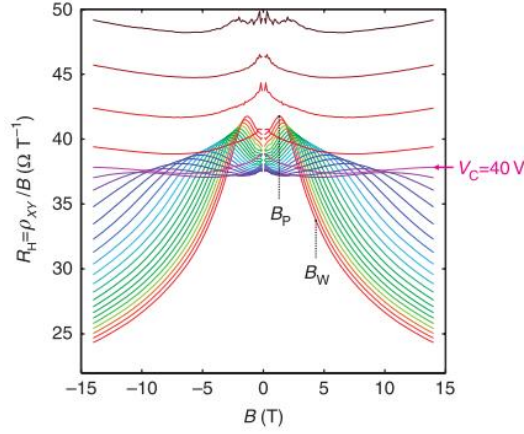
Figure 2.16: a) The Hall coefficient, R_H as a function of magnetic field for different back-gate voltages at 4.2 K. Above the critical voltage (40 V) the resistivity curves are linear and the Hall coefficient is fairly constant while below the critical voltage the resistivity becomes non-linear and the Hall coefficient show a peak at B_P and B_W gives the fall-off field. [20]

2.3.2 Magnetoresistance

The MagnetoResistance (MR) is based on a voltage difference across an electrical conductor parallel to the applied electrical current induced by an out-of-plane magnetic field. The magnetic field is defined in the z-direction such that $\boldsymbol{B} = (0,0,B)$ and the electric field is considered to be only in the x-direction, i.e., $\boldsymbol{E} = (E_x, 0,0)$. In order to find the MR, the current density in response to the electric and magnetic field will be obtained. The velocity of the carriers is determined by the relaxation time approximation, equation (2.2). As for the Hall effect, the MR is also a steady state of the system such that $d\boldsymbol{v}/dt = 0$ hence the resulting component for the velocity are

$$v_x = -\mu E_x + \omega_c \tau v_y \tag{2.9}$$

and

$$v_y = \omega_c \tau v_x, \tag{2.10}$$

where $\mu = e\tau/m^*$ is the carrier mobility and $\omega_c = eB/m^*$ is the cyclotron frequency. Note that the magnetic field creates an anisotropic current flow. Rearranging equation (2.9) and (2.10) and substituting the velocities in the expression for the current density, i.e., $J_{x(y)} = -n_s^{2D} e v_{x(y)}$, we obtain

$$J_x = \frac{\sigma_0}{1 + \omega_c^2 \tau^2} E_x \text{ and } J_y = \frac{\sigma_0 \omega_c \tau}{1 + \omega_c^2 \tau^2} E_x, \tag{2.11}$$

where $\sigma_0 = ne^2\tau/m^*$ is the zero-field conductivity. The sheet conductivity is extracted from equation 2.11, resulting in

$$\sigma_{xx}(B) = \frac{\sigma_0}{1 + \omega_c^2 \tau^2} \tag{2.12}$$

and applying very large magnetic field the sheet conductivity gives

$$\lim_{B\to\infty} \sigma_{xx} = \lim_{\omega_c\to\infty} \left[\frac{\sigma_0}{1 + \omega_c^2 \tau^2} \right] = \frac{\sigma_0}{\omega_c^2 \tau^2} \propto \frac{1}{B^2}. \tag{2.13}$$

The sheet resistivity is determined by $\rho_{xx} = 1/\sigma_{xx}$ indicating that, at large magnetic field, the sheet resistivity has is proportional to B^2 which is observed in the sheet resistivity measurements. Furthermore, the relative magnetoresistance, with $\rho_0 = 1/\sigma_0$ is

$$MR(B) = \frac{\rho_{xx}(B) - \rho_0}{\rho_0}.$$

(2.14)

In the case of multiple carrier transport the total current density will be given by the sum of the different components. Assume two types of carriers with current density J_1 and J_2 and a parallel current flow. When a magnetic field is applied, the current flow of the carriers, due to differences in density, effective mass and scattering rate, will no longer be parallel hence $|J| \leq |J_1 + J_2|$ resulting in an increase in the sheet resistivity with increasing magnetic field.

At low temperature and low magnetic field, the behaviour of the magnetoresistance shows deviations from the B^2-dependence due to weak (anti-)localisation. Weak Localization (WL) is a physical effect which occurs at low temperatures in diffusive systems. It describes the enhanced probability for electrons to return to their initial position after multiple scattering events which result in a positive contribution to the magnetoresistance. In contrast, Weak Anti-Localization (WAL) induces a negative contribution to the magnetoresistance. In a diffusive system with strong spin-orbit coupling, the wave vector of the electron rotates after every scattering event causing fluctuation on the internal magnetic field. Consequently, these fluctuations cause the spin phase to interfere destructively with the phase of the electron wavefunction resulting in a decreasing sheet resistivity. These effects are supressed at high magnetic fields.

For single band conduction, the total evolution of the magnetocondutivity can be described with the Maekawa-Fukuyama formula which is defined as follows

$$
\frac{\Delta\sigma(H)}{\sigma_0} = \Psi\left(\frac{H}{H_i + H_{so}}\right) + \frac{1}{2\sqrt{1-\gamma^2}}\Psi\left(\frac{H}{H_i + H_{so}\left(1 + \sqrt{1-\gamma^2}\right)}\right)
$$
$$
+ \frac{1}{2\sqrt{1-\gamma^2}}\Psi\left(\frac{H}{H_i + H_{so}\left(1 - \sqrt{1-\gamma^2}\right)}\right),
$$

(2.15)

where the function $\Psi(x) = \ln(x) + \psi(0.5 + 1/x)$ with ψ being the digamma function and g is the effective factor of the Zeeman correction, $\gamma = g\mu_B H/4eDH_{so}$. H_i and H_{so} are respectively the inelastic and spin-orbit characteristic field which determine the inelastic and spin-orbit scattering time,

$$\tau_{i,so} = \frac{\hbar}{4eDH_{i,so}},$$

(2.16)

where the diffusion constant is defined as:

$$D = \frac{\hbar^2 \pi}{e^2} \frac{\sigma_{2D}^{B=0}}{m^*}.$$

(2.17)

The zero field sheet conductivity, $\sigma_{2D}^{B=0}$, can be determined from the experiments. The spin-orbit relaxation time is an essential ingredient to describe electrical transport in a 2DES in the presence of a strong electric field. The spin-orbit relaxation time is defined by the rapidly fluctuation of the internal magnetic field due to the rotations of the wave vector after every scattering event. The inelastic scattering time is related to the spin-orbit interaction of the lattice ions with the conduction electrons. This mechanism become relevant in the presence of strong spin-orbit scattering impurities

or whenever the ionic spin-orbit coupling produces a significant correction to the band structure of the material.[45,46]
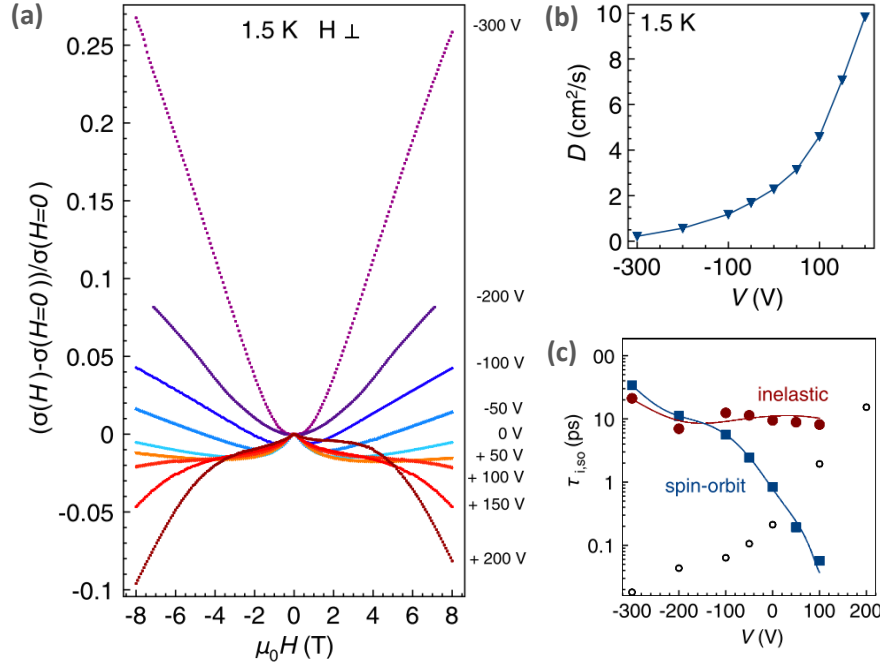

Figure 2.17: a) The evolution of the relative magnetoconductance under influence of magnetic and electric applied fields. b) Field effect modulation of the diffusion constant measured at 1.5 K. c) The inelastic and spin-orbit relaxation times as a function of the gate voltage.[45]

Caviglia et al.[45] studied the spin-orbit interaction in LAO/STO(100) heterostructures by means of magnetoresistance measurements. Figure 2.17a shows the response of the relative magnetoconductance with an applied electric field and in-plane magnetic field. The magnetoconductance is positive for large negative gate voltages whereas the response becomes negative for positive gate voltages. For positive gate voltages at small magnetic field a contribution of the WL (WAL) is observed, indicating spin-orbit coupling. Figure 2.17b displays the change in the diffusion constant with varying gate voltage. An increase in the diffusion constant is observed when the gate voltages is increased. With use of this diffusion constant, equation 2.15 and equation 2.16, the inelastic and spin-orbit scattering time at each applied gate voltage which is determined. Figure 2.17c shows that below a gate voltage of -140 V, the spin-orbit scattering time is shorter than the inelastic scattering time whereas above -140 V the opposite is true. At 100 V, the difference between the two scattering times differs by 3 orders of magnitude. Stornaiuolo et al.[46] studied the same phenomenon with use of a side gate and even though Caviglia et al. used a back gate though the results are comparable.

2.4 Superconductivity at the LaAlO$_3$/SrTiO$_3$ interface

Superconductivity is a quantum phenomenon which describes the sudden disappearance of electrical resistance of certain materials when cooled below a characteristic critical temperature, T_c. The physics behind the superconducting phase is related to an attractive phonon mediated electron-electron interaction. Such a pair of electrons, a Cooper pair, has an energy gap which indicate the minimum amount of energy needed for excitation of the fluid. When the energy gap energy is larger

than the thermal energy ($\Delta > k_B T_c$) of the lattice, the Cooper pairs will not be scattered by the lattice, i.e. flow without energy dissipation.

Two-dimensional superconductivity is observed at the interface of metallic and insulating films (e.g. cuprates) but also between two insulating oxides (e.g. LAO/STO). Reyren et al.[4] were the first to observe superconductivity at the LAO/STO(100) interface with an 8 uc thick film by performing resistivity measurements while the system was cooled down to mK regime. The phase transition is observed at ~190 mK. Gariglio et al.[44] confirmed the superconducting state with a critical transition temperature ~220 mK at the LAO/STO(100) interface with a 4 uc film.

2.4.1 Berezinskii–Kosterlitz–Thouless (BKT) transition

Bulk STO can also undergo a superconducting phase transition at 0.35 K.[11,47] The two-dimensional character of a superconducting state at the LAO/STO heterostructures can be confirmed by the Berezinskii–Kosterlitz–Thouless (BKT) theory of 2D superconductivity. The origin of the two-dimensional phase transition from the superconducting to the normal state are thermally created vortices. A vortex is a magnetic flux tube with a normal vortex core around which a supercurrent circulates. The density of the Cooper pair is zero at the vortex centre and the size of the vortex core is in the order of the superconducting coherence length (ξ).

Below the transition temperature, the thermally created vortices are bound vortex-antivortex pairs. A vortex is characterised by a clockwise rotating supercurrent whereas the antivortex is characterised by a counter-clockwise rotating supercurrent resulting in a zero net current of vortex-antivortex pairs. The density of the vortex pairs will increase while the temperature is raised. At the transition temperature, the vortex pairs start to unbind and free vortices are formed causing dissipation losses. This phase transition is called the Berezinskii-Kosterlitz-Thouless (BKT) transition. There are two methods to characterize BKT phase transitions indicating the two dimensional character of the superconducting phase.[48]

- **Current-voltage characteristics**

IV-characteristics are influenced by the vortices as follows: an external current density and magnetic field applied on a sample induces a Lorentz force on the vortices. This force creates a current gradient perpendicular to the external current. Above T_{BKT} and in the absence of vortex pinning, the Lorentz force produces a steady dissipative vortex motion, which results in a finite resistance. On the other hand, below the BKT transition, the forces acting on the vortex and antivortex are opposite resulting in a zero net force on the vortex-antivortex pairs. Consequently, the vortices do not move and the resistance is zero. However, this ideal case is only reached when the current density and the temperature both approach zero. A non-zero probability for the vortex pairs to unbind exists for finite values of these parameters. The individual vortices are able to move freely and will produce a small resistance until they recombine. This behaviour results in a non-linear response such that below T_{BKT}, the *IV*-characteristics has a power law dependence, i.e., $V \propto I^a$ where $a(T_{BKT}) = 3$. Above T_{BKT}, the behaviour of the *IV*-characteristics is ohmic, i.e., $V \propto I$.[48]

- **Resistance characteristics**

The resistance is related to the correlation length (ξ) which is equal to the vortex core radius. Above T_c, the critical temperature dependence of the correlation length is:

$$\xi(T) = \xi_0 \exp\left(\frac{2\pi}{bt^{\frac{1}{2}}}\right) \text{ where } t = \left|\frac{T - T_c}{T_c}\right|. \tag{2.18}$$

ξ_0 is the classical vortex core radius and b is related to the energy needed to create a vortex ($b = f[E_c/(k_B T)]$). In two dimensions, dynamical scaling invokes the resistance to scale as:

$$R \propto \xi^{-z_{cl}}, \tag{2.19}$$

where z_{cl} is the dynamical critical component of classical dynamics where simple diffusion is described by z_{cl}=2. The combination of equations 2.18 and 2.19 gives:

$$\frac{R(T)}{R_0} = \left(\frac{\xi_o}{\xi(T)}\right)^2 = \exp\left[-b_R(T - T_{\text{BKT}})^{-\frac{1}{2}}\right], \tag{2.20}$$

with $b_R = \left(4\pi T_{\text{BKT}}^{\frac{1}{2}}\right)/b$ and $R_0 \propto 1/(\xi_0^2)$. Accordingly, the compatibility of experimentally observed sheet resistance with the characteristic BKT behaviour can be explored in terms of

$$\left(\frac{d\ln R}{dT}\right)^{-\frac{2}{3}} = \left(\frac{2}{b_R}\right)^{\frac{2}{3}}(T - T_{\text{BKT}}). \tag{2.21}$$

Note that at low temperatures, a deviation of this behaviour is expected due to size effects.[49]
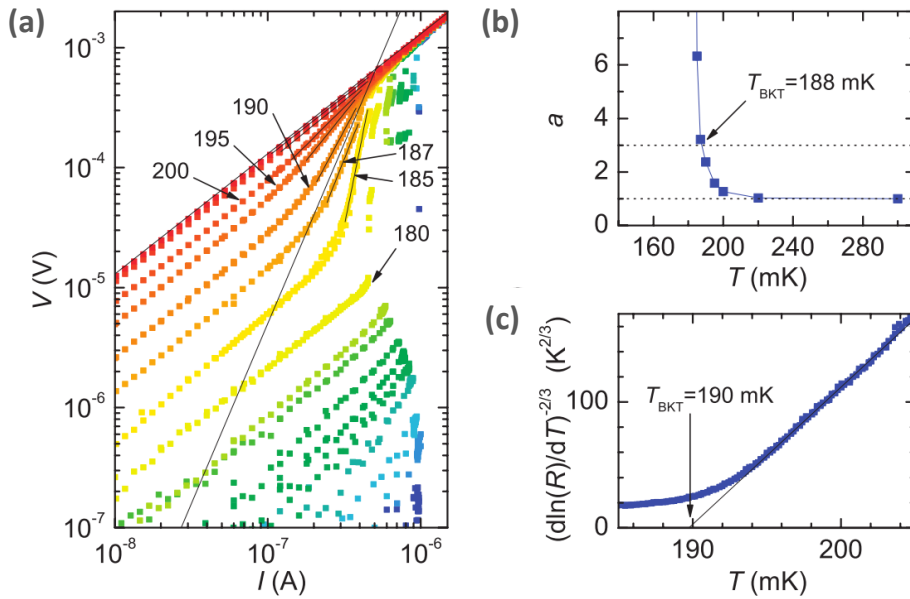
Figure 2.18: Low-temperature transport properties of the 8 uc LAO/STO(100) heterostructure. a) VI-characteristics on a logarithmic scale where the black numbers indicate the measurement temperature in mK. The short black lines are fits of the data in the transition. The two long black lines correspond to $V = IR$ and $V \sim I^3$ dependencies and show that 187 mK < T_{BKT} < 190 mK. b) Temperature dependence of the power-law exponent a, extracted from the $V \sim I^a$ fits shown in (a). c) R(T) dependence of the sample plotted on a [dln(R)/dT]$^{-2/3}$ scale. The solid line is the behaviour expected for a BKT transition with T_{BKT} =190 mK.[4]

In 2007, Reyren et al.[4] reported on superconductivity in the 2DES at the LAO/STO(100) interface with an 8 uc film. The analysis of the superconducting phase transition reveals a clear signature of 2D superconductivity. Figure 2.18a shows the VI-characteristic on a logarithmic scale where each one of the curves represents a different temperature. The most important temperatures are indicated with

black numbers. The long black line represent the voltage-current relation at the BKT transition temperature, i.e. $V(T_{BKT}) \propto I^3$. The shorter black lines fit $V \propto I^{a(T)}$ to the slope of the curve. Figure 2.18b plots the obtained temperature dependence of the exponent a. The value of a = 3 gives the BKT transition temperature, being T_{BKT} = 188 mK. This transition temperature is verified by investigation of the temperature dependence of the resistance. Figure 2.18c shows that the BKT transition temperature is obtained by a linear extrapolation of equation 2.21 and taking the zero value, resulting in a BKT transition temperature, T_{BKT} = 190 mK. This is comparable to the temperature found with the voltage-current characteristic. Gariglio et al.[44] determined, the transition temperature for LAO/STO(100) heterostructure with a 4 uc film by characterizing the resistance. They measured the transition temperature to be T_{BKT}= 222 mK.

2.4.2 Magnetic Field Dependence

An external magnetic field has a large influence on the electronic transport properties. Superconductivity in a system can be completely suppressed by the critical magnetic field. The two-dimensionality of the superconducting phase is characterized by a large anisotropy in the magnetic field dependent transport properties. In a bulk superconductor, the in-plane and out-of-plane critical magnetic field are comparable whereas in 2D superconductors, the out-of-plane magnetic field has larger influence on the bound vortices inducing a lower critical magnetic field as for an in-plane applied magnetic field.

The magnetic field dependence of the electronic transport is used to extract the in-plane correlation length and the thickness of the 2D superconducting layer from the out-of-plane and in-plane critical magnetic field, respectively. The in-plane superconducting coherence length is given by

$$\varepsilon = \left(\Phi_0/2\pi H_{c\perp,0}\right)^{1/2} \tag{2.22}$$

and the superconducting layer thickness, according to the Ginzburg-Landau theory is:

$$d = (\sqrt{3}\Phi_0)/(\pi\varepsilon\mu_{0H_{c\parallel,0}}), \tag{2.23}$$

where the quantum flux: $\Phi_0 = \frac{hc}{2e}$ and μ_0 is the magnetic permeability constant.

There are two ways to determine the critical magnetic field. The first one is by measuring *VI*-characteristics at a specific temperature for varying magnetic fields. Han et al.[50] performed such a measurement and figure 2.19a and d show the *VI*-characteristics for the in-plane and out-of plane magnetic field. In both cases, the zero resistance plateau vanish with increasing magnetic field. The critical field can be determined from the normalized differential, $(dV/dI)_{I=0}/(dV/dI)_{I=b}$ (where b is the value for the current where the differential (figure 2.19b and e) approaches a constant value). Han et al.[50] defined $H_{c,a\,mK}$, the critical magnetic field at a specific temperature as the magnetic field where the normalized differential at *I* = 0 µA recovers to 0.5.

Thereafter, the following formula can be used to determine the critical field at zero temperature:

$$H_{c,0} = H_{c,T}\left[1 + \left(\frac{T}{T_c}\right)^2\right]/\left[1 - \left(\frac{T}{T_c}\right)^2\right], \tag{2.24}$$

where the critical temperature (T_c) can be obtained from the temperature dependence of the sheet resistivity. The critical magnetic field at zero temperature, $H_{c\perp,0}$ and $H_{c\|,0}$, can be deduced by implementing T = a mK and $H_{c\perp,a\,\mathrm{mK}}$ and $H_{c\|,a\,\mathrm{mK}}$ in equation 2.24.

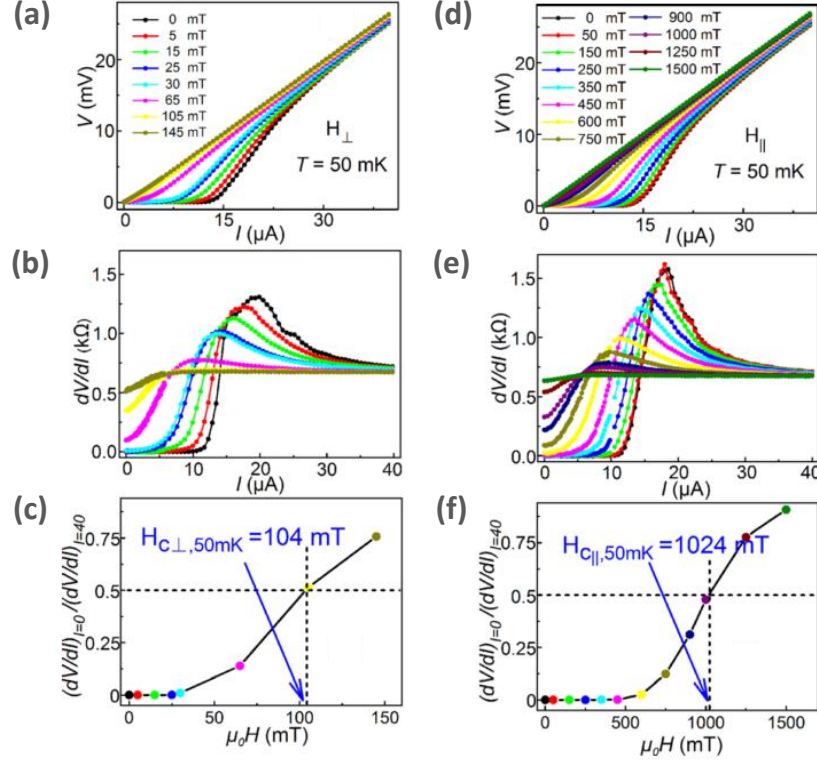**Figure 2.19: a) Magnetic field-dependent *VI*-characteristics of the 5 uc (110) LaAlO3/SrTiO3 heterostructures at 50 mK for various out-of-plane applied magnetic fields. (b) Numerical d*V*/d*I*-*I* curves deduced from the *VI* curves in (a). c) The (d*V*/d*I*)$_{I=0}$/(d*V*/d*I*)$_{I=40}$ at different perpendicular magnetic fields. The magnetic field at which (d*V*/d*I*)$_{I=0}$/(d*V*/d*I*)$_{I=40}$ = 0.5 is defined as the $H_{c\perp,50\,\mathrm{mK}}$,being 104 mT. d)–f) show corresponding results for different in-plane applied magnetic fields applied. The value of $H_{c\|,50\,\mathrm{mK}}$ is measured to be 1024 mT.[50]**

The second way to determine the critical magnetic fields is by measuring the temperature dependence of the sheet resistance with a varying magnetic field. The temperature where the resistance falls to 90% of its normal state is defined as T_c^{onset} with a corresponding sheet resistance $R_s(T_c^{onset})$. The magnetic field which pushes the sheet resistance at zero temperature to $R_s(T_c^{onset})$ is defined as the critical magnetic field.

Reyren et al.[51] measured the temperature dependent sheet resistance at various applied magnetic fields of LAO/STO(100) heterostructures with reproducible data for 4, 8 & 9 u.c. thick films. Figure 2.20 present the in-plane and out-of-plane dependence of the temperature dependent sheet resistance. It can be deduced from this figure that the critical magnetic field for an perpendicular applied field is 150 mT which is in agreement with previous measurements.[4] The critical magnetic field of the parallel applied field is >2 T. Thereafter, the in-plane coherence length is determined to be $\varepsilon \sim 70$ nm and the superconducting layer thickness is d~(11$\pm$3) nm. Previous measurements showed that the superconducting layer thickness at the LAO/STO(100) interface has an upper limit of 10 nm.[4,44]
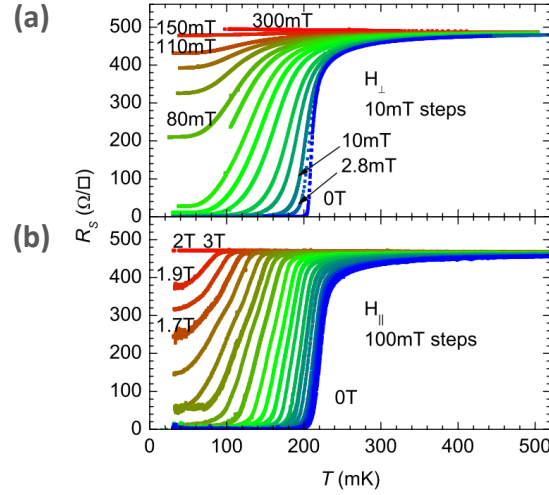
Figure 2.20: Temperature dependent sheet resistance for different magnetic fields applied. a) perpendicular and b) parallel to the interface.[51]

- **Pauli paramagnetic limit**

If magnetic fields is high enough, the paramagnetic susceptibility induces a parallel alignment of the Cooper pair spins that eventually will break them apart, giving a higher limit for the upper critical fields. The Pauli paramagnetic limit is given by:

$$\mu_0 H_c^p = \frac{1.76 k_B T_c}{\sqrt{2}\mu_B} = 1.84\, T_c, \qquad (2.25)$$

where μ_B is the Bohr magnetron. Reyren et al.[51] have observed that the in-plane critical magnetic field exceeds the Pauli paramagnetic limit by a factor 4 to 5 Later Shalom et al.[52] obtained the same result for low carrier densities suggesting an increasing SO coupling.

2.4.3 Gate-tunable superconductivity

It is discussed in section 3.2.1 that the carrier density at the interface of LAO/STO(100) systems can be electrostatically tuned by a gate voltage. The modulation of the carrier density achieved is remarkably close to the total number of free carriers present in the system, indicating that the electric field effect is an excellent tool to probe its phase diagram.[53] Caviglia et al.[54] report that the modulation allows for on/off switching of superconductivity and drives a quantum phase transition. Figure 2.21a displays the evolution of the temperature dependent sheet resistance with back gate voltage varying from -300 to 320 V. At low doping levels, the sheet resistance shows an insulating behaviour. At the critical sheet resistance, $R_c \sim 4.5$ kΩ/cm^2, the system undergoes an insulator-to-metal transition. Figure 2.21b displays the electronic phase diagram of the LAO/STO(100) interface where the blue region presents the two-dimensional superconducting phase. A quantum phase transition is observed at the critical back gate voltage: V_c = -140 V. An increase in back gate voltage raises the BKT transition temperature which reaches a maximum around ~310 mK. Hereafter, the system reaches an overdoped regime such that the T_{BKT} is slowly decreasing. Furthermore, the phase transition line near the quantum critical point goes as: $T_{BKT} \propto (\delta n_{2D})^{z\bar{v}} \propto (\delta V)^{z\bar{v}}$. It is observed that the quantum criticality is well described by $z\bar{v} = 2/3$, in agreement with a classical 3D-xy model, indicative of a weakly disordered 2D system in which quantum fluctuations dominate.[49]
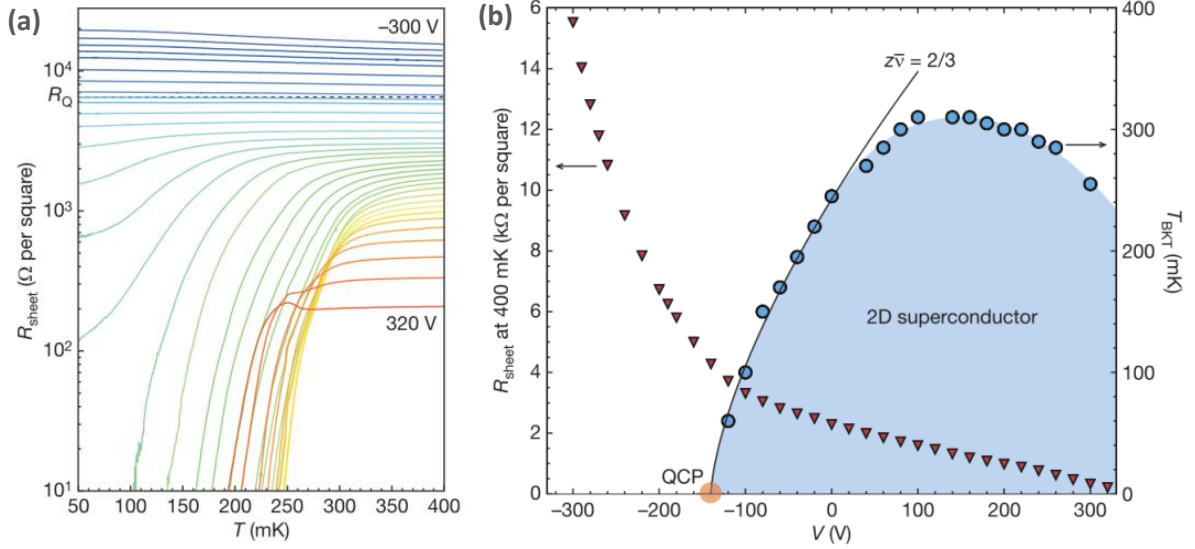
Figure 2.21: a) Field-effect modulation of the sheet resistance at a function of temperature for gate voltages varying between -300 and -260 V with 10 V steps and between -260 V and 300 V with 20 V steps. b) The voltage depended critical temperature T_{BKT} reveals the superconducting region of the phase diagram. The solid line describes the approach to the quantum critical point (QCP) using the scaling relation $T_{BKT} \propto (V - V_c)^{z\bar{\nu}}$ where $z\bar{\nu}=2/3$.

2.4.4 LAO/STO(110) interfaces

In 2014, Han et al.[50] report on 2D superconductivity in the 2DES of the LAO/STO(110) interface with a 5 uc thick film. Figure 2.22 shows the result of the low-temperature transport measurements. Figure 2.22a shows the *VI*-characteristics while figure 2.22b displays the temperature dependence of the exponent extracted from the fit of $V \propto I^a$. The *VI*-characteristics determine the BKT transition temperature to be T_{BKT} = 177 mK whereas the temperature dependence of the resistance (c) results in a BKT transition temperature of T_{BKT} = 182 mK. Herranz et al.[55] found the BKT phase transition temperatures to be 172, 175 and 144 mK for a film thickness of respectively 14, 10 and 8 uc at the (110) interface. These values are slightly lower as the values obtain for the {100} interface.

Herranz et al.[55] studied the anisotropy of the magnetic field on the superconducting phase of the LAO/STO(110). The critical magnetic fields are measured to be $H_{c\perp,0}$=160 mT and $H_{c\|,0}$ = 1000 mT at an interface with a 14 uc film. For film thicknesses 14, 10 and 8 uc, the in-plane coherence length $\varepsilon \approx$ 40-75 nm and the superconducting layer thickness d $\approx$ 24-30 nm at the {110} interfaces. Whereas the coherence lengths are significantly smaller as measured at {100} interfaces ($\varepsilon \approx$ 70 - 100 nm), the superconducting layer thicknesses are larger compared to the superconducting layer thickness of the {100} heterostructures (d $\approx$ 10 nm).

Later, Han et al.[50] performed similar measurements for a sample with a LAO film thickness of 5 uc which result in $H_{c\perp,50}$=104 mT and $H_{c\|,50}$=1024 mT (see figure 2.19). The critical magnetic fields at zero temperature, determined with use of equation 2.24, are $H_{c\perp,0}$=120 mT and $H_{c\|,0}$ = 1187 mT. The critical field gives the in-plane coherence length and the superconducting layer thickness of $\varepsilon \approx$ 52 nm and d $\approx$ 18 nm, respectively. These values are in the same order of magnitude as previously reported. The Pauli paramagnetic limit is $\mu_0 H_c^p = 340$ mT and the limit is exceeded by the in-plane critical magnetic field, though this limit is comparable to the values found at the {100} interface.
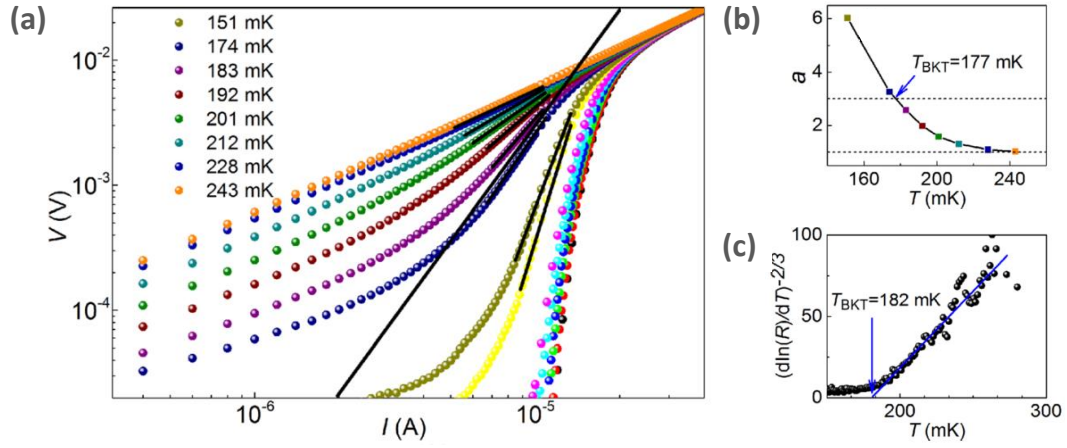
Figure 2.22: Low-temperature transport properties of the 5-uc LaAlO$_3$/SrTiO$_3$(110) heterostructure. a) Temperature-dependent *VI* curves on a logarithmic scale. The short black lines are fits of the data in the transition. The long black line corresponds to $V \propto I^3$ dependence and show that 174 mK < T_{BKT} < 183 mK. b) Temperature dependence of the power-law exponent a, deduced from the fits shown in (a). T_{BKT} ~177 mK was deduced. c) R(T) dependence, plotted on a $[dln(R)/dT]^{-2/3}$ scale. The blue solid line indicates the linear behaviour expected for a BKT transition with T$_{BKT}$ ~182 mK.[50]

3. Experimental Methods

3.1 Surface treatment

The crystal structure of ABO_3 perovskites consists of alternating ionic planes where the ions from covalent bonds. For any given orientation (h, k, l) of a perovskite structure, there are always two distinct types of alternating equally spaced atomic planes having different compositions of the three constituent elements. The stoichiometry of the atomic planes depends on the crystallographic orientation and the surface energy.

A surface of a perovskite structure obtained by cleaving or cutting contains domains of mixed terminations separated in height by steps of half a unit cell. Figure 3.1a shows a simplified schematic of the surface after cutting and polishing. The blue layers (A) and green layers (B) represent the different ionic planes. In the case of STO, depending on the crystallographic orientation {100}, {110} and {111}, these are respectively, $[SrO]^0/[TiO_2]^0$, $[SrTiO]^{4+}/[O_2]^{4-}$ and $[SrO_3]^{4-}/[Ti]^{4+}$. The orange line is the line along which the cutting of the substrate is performed. The angle φ, between the ionic planes and the cutting direction, is called the miscut-angle. Structural features so called step-and-terraces become apparent due to the miscut-angle. 3.1b shows a topview of the substrate surface after cutting, where a mixed termination of A and B domains are present. This preparation method produces an equal amount of A and B domains. However, well-defined single terminated surfaces are essential for thin film growth.

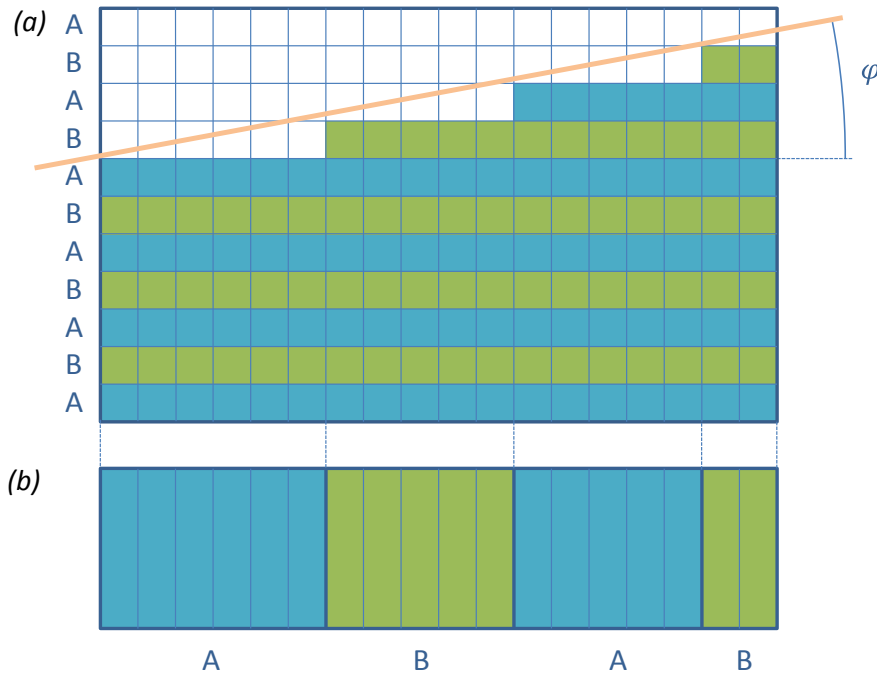**Figure 3.1: Schematic of a perovskite substrate prepared by cutting or cleaving. a) Sideview where the orange line is cutting line, A and B are the ionic planes and φ is the miscut-angle. b) Topview with mixed termination of domains A and B.**

Techniques like annealing in an oxygen atmosphere and bismuth adsorption/desorption are commonly used to improve the surface quality of the substrates and growth reproducibility.

However, these methods do not guarantee a single terminated surface.[56] A powerful tool to obtain single termination is chemical etching. This method removes specific features or domains of undesired material by immersing samples in a chemical bath. Considering 3.1, this procedure would lead to etching of the topmost layers of domain A or B depending on the etch selectivity.

3.1.1 Termination of STO(100) surfaces

In ABO_3 perovskites, the A and B site cations often have different physical and chemical properties. Taking into consideration STO, the SrO will reacts with water and acids at room temperature. In contrast, TiO_2 planes are chemically more stable hence the probability to react with water and most acids is unlikely.[57] By taking into account this difference in solubility of Sr and Ti cations, the SrO surface domains can be etched selectively. The effectiveness of the etching depends on several factors. Namely, the properties of the etching solution, like concentration, composition and the reactivity. The reactivity is the relative capacity of the cations to undergo a chemical reaction with the etchant which is determined by the pH of the etchant. Furthermore the surface properties of the substrate to be etched (like the miscut-angle), the time of etching and temperature influence the efficiency of the chemical treatment. Chemical etching results in single Ti-rich termination of the STO substrates by optimizing the parameters for this process.

In 1994, Kawasaki et al. were the first to introduce a chemical etching procedure for termination of STO(100) surfaces.[58] In this well-established procedure, the chemical treatment is performed with buffered hydrofluoric acid (BHF). The STO(100) polished substrates are immersed in BHF solutions (NH_4F-HF with an NH_4F concentration of 10 M) for 10 min. Subsequent cleaning with deionized water and ethanol was performed, followed by drying with a nitrogen stream. It was found that the pH of the BHF solution has a large influence on the termination. The sample treated with a pH value around 4.5 was measured to have a 100% coverage of TiO_2. A pH > 5 gives rise to a mixed termination of SrO islands whereas a pH < 4 results in etch pits.

Koster et al.[56] introduced an additional step, which is immersing the sample in water before BHF etching. The SrO surface domains immersed in deionised water can selectively form a hydroxide complex due to the difference in solubility of Sr and Ti cations in water. The complex hydroxides can be removed using chemical etching by means of an acid. The chemical reactions of the etching treatment with an acid X are the following[59]:

1. $SrO(s) + 3\,H_2O\,(l) \Rightarrow Sr(OH)_2 \cdot 2\,(H_2O)\,(s)$
2. $HX(aq) \overset{H_2O}{\Longrightarrow} X^-(aq) + H^+(aq)$
3. $Sr(OH)_2 \cdot 2\,(H_2O)\,(s) + 3X^-(aq) \Rightarrow SrX_3 \cdot 3\,(H_2O)\,(aq)$

The $SrX_3 \cdot 3\,(H_2O)$ complex remnants can be removed from the substrate by rinsing the substrates with deionized water after etching. Koster et al. used BHF as the etchant. Moreover, they suggested an heat treatment after the chemical treatment. During the heat treatment, the surface atoms are allowed to diffuse and subsequently decrease the surface roughness. Annealing at 950°C for 1 hour resulted in clear step-and-terrace structures. The height of the step was 3.9 Å, comparable to the lattice constant of the unit cell of STO(100). In the work of Kawasaki et al. the reproducibility of the termination depended severely on the different polishing and annealing procedures prior to the BHF

treatment. The method reported by Koster et al. with intermediate Sr-hydroxide complex formation and subsequent BHF etching gives reproducible, practically perfect TiO_2 terminated surfaces.

The Lippmaa laboratory[60] discusses a different approach to achieve Ti-rich terminated STO(100) substrates. This study is based on multiple etching steps at room temperature, increasing the total etching time with every step. In between each step the morphology of the surface is investigated with use of AFM. In practice, the sample will be immersed in an acid multiple times until a step-and-terrace structure appears. The etchant was BHF and the pH-value was taken between 3.7 and 4.3. After 5 minutes of etching, realised in several etching steps, a step-and-terrace structure started to appear. Increasing the etching times to 8 and 12 minutes the steps become more sharp and the terraces become larger without any annealing.

Recent studies have shown that the BHF chemical treatment results in a non-negligible level of F doping within the terminal surface layers of TiO_2. Chambers et al.[61] determined with use of a combination of x-ray photoelectron spectroscopy and scanned angle x-ray photoelectron diffraction that during BHF treatment ~13% of the oxygen anions sites in the surface layer will be substituted by fluorine anions. Oxygen plasma and annealing were ineffective in removing the F dopants. Though, the doping seems not catastrophic because the dopants do not affect the energy levels. Furthermore, it is suggested to use boiling deionized water for 30 min instead of HF solution to single terminated STO samples. This will reduce the F concentration by a factor ~6.

The discussions about alternative chemical procedures are ongoing.[62] One suggestion for substituting BHF as the etchant is HCl. An etching treatment in HCl-HNO_3 (3:1) of 12 min is proposed.[63] Besides avoiding unintentional F doping, another advantage of this method is the reduction of oxygen vacancies. Zhang et al. studied the occurrence of oxygen vacancies for both acids, HCL and BHF with depth-resolved catholuminesence spectroscopy on TiO_2 terminated STO samples. The intensity of oxygen vacancies with respect to the penetration depth from the surfaces show that when performing HCL etching the oxygen vacancies are observed at distances on the order of 10 nm into the substrate in comparison to BHF where the vacancies are found at depths larger than 200 nm.[64]

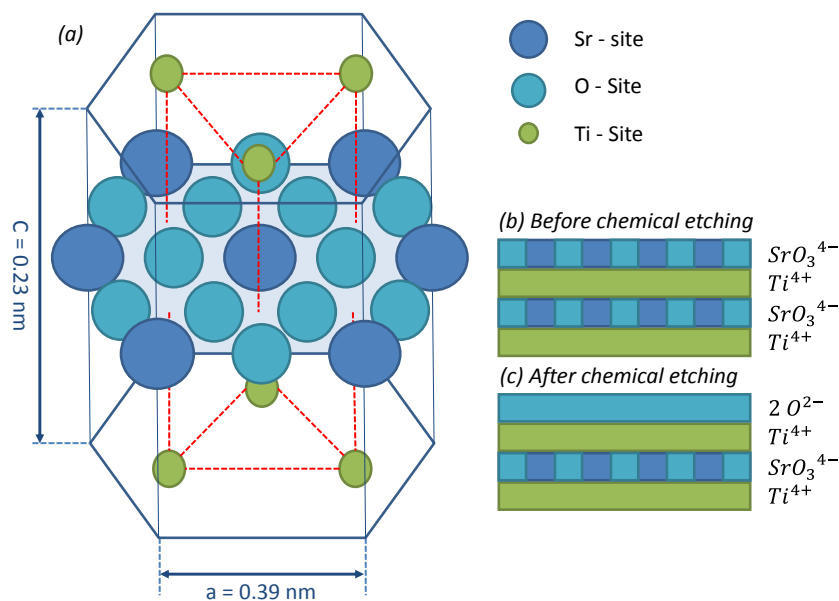**Figure 3.2: a) The hexagonal cell structure**[57] **of the STO(111). The hexagonal unit cell results in a layered structure of atomic planes. (b) The specific planes of the bare substrate and (c) the atomic planes after termination of the STO(111).**

3.1.2 Termination of STO(111) surfaces

In order to obtain single Ti-rich terminated surfaces in the {111} orientation, the same BHF etching procedure as for the {100} orientation can be applied. Even though the STO(111) substrate has a polar surface, it has been reported that such a procedure results in single terminated and atomically flat surfaces.[57,65] Additionally, in comparison to STO(100) which has a cubic structure, the (111) oriented STO has a hexagonal structure. Figure 3.2a shows the hexagonal structure of a STO(111) unit cell. From this schematic it can easily be seen that this orientation consists of a layered structure of alternating $[SrO_3]^{4-}$ and $[Ti]^{4+}$ atomic planes, as shown in figure 3.2b. The domains present after cutting and before etching are $[SrO_3]^{4-}$ and $[Ti]^{4+}$. The expectation is that from the $[SrO_3]^{4-}$ domains, [SrO] dissolves in the water and can be removed in a similar fashion as presented for the STO(100) procedure. The remaining $2[O]^{2-}$ will bond with the $[Ti]^{4+}$ resulting in a non-polar TiO_2-terminated surface, figure 3.2c.[14]

In 2008, a first attempt of terminating the STO(111) surface was reported.[57] This termination was achieved by high temperature ultrasonic agitation in deionized water, dipping in hot ultrasonic agitated BHF solution and the last step was to anneal at 1050°C for 1h. A step-and-terrace structure with a step height of 0.24 nm was observed as expected for STO(111). Later it was found that extending the annealing time leads to more defined step-and-terrace structures with larger terraces.[65,66]

Recently, S. Woo et al.[66] performed a systematic AFM study on the surface treatment of the STO single crystalline and polycrystalline surfaces. The surface treatment consists of soaking in deionized water for 10 seconds, subsequent etching with BHF solution for 15-420 seconds and rinsing with deionized water. After etching, the substrates are annealed for 2-8 hours at 900-1200 °C in air. Figure 3.3 shows the annealing times and temperatures which result in crystalline STO samples with atomically flat step-and-terrace structures (indicated by solid symbols). The etching time has been neglected since it was observed that it has little influence on the surface structure. The {100} orientation covers the largest range of conditions which is related to this orientation having the smallest surface energy. The somewhat smaller ranges of the {110} and {111} orientations suggest that these require longer annealing times and higher temperatures to accomplish the desired structure. The numbers next to the symbols indicate the RMS roughness values of the terraces. In general, a decrease in roughness with increasing annealing times is observed. In the (111) orientation, the heat treatment should be performed in the range of 900-1200 °C and 5-8 hours according to this scheme.

Connell et al.[67] suggest a method with deionized water for termination of STO surfaces. This study is carried out on STO substrates with (100) and (111) orientations. The substrates are prepared by pre-annealing at 1000°C for 1h in air and subsequent rinsing with agitated deionized water at room temperature for 30 seconds. Hereafter, a second annealing step is performed at 1000°C for 1 h in air. Atomically flat surfaces are repeatedly obtained regardless of the miscut-angles. However, SrO segregation is observed within some hours/days after the second annealing step. Introducing another deionized water leaching step of 30 sec removes the segregated SrO and recover stable Ti-rich terminated surfaces. Hatch et al.[62] discuss that for Nb-doped STO substrates the level of disorder of the surface prepared with water leaching is higher in comparison to the methods with BHF and HCl etching. This indicates that rinsing with water might not be the most effective method.
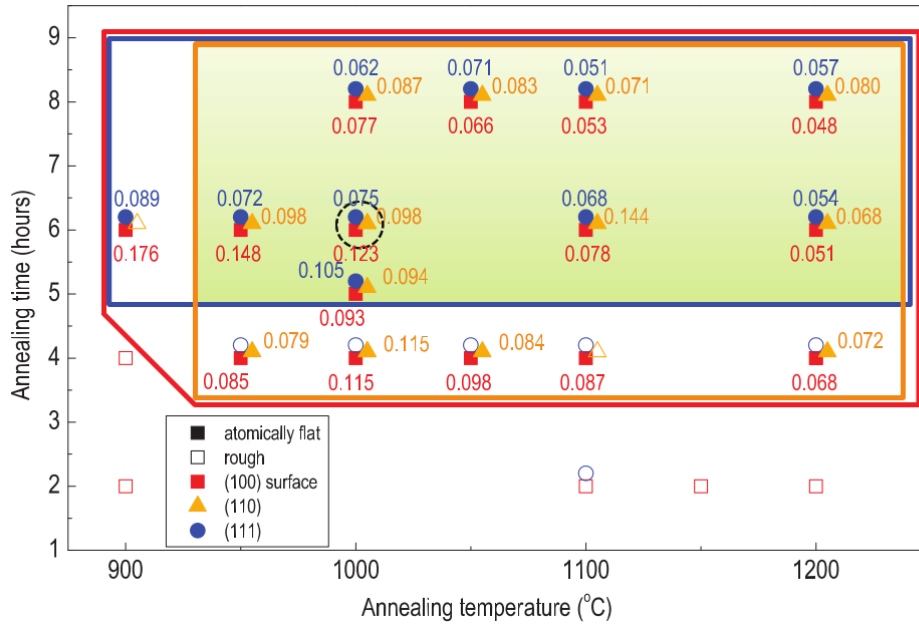
Figure 3.3: Scheme of the surface treatment on crystalline STO sample for three orientations, namely (100), (110) and (111). The solid symbol represent the atomically flat samples with a step-and-terrace structure. The red (100), yellow (110) and the blue (111) blocks indicate per orientation the range of annealing times and temperatures which give atomically flat step-and-terrace structures. The numbers next to the symbols give the RMS roughness values of terraces in nm.[66]

All three discussed procedures, BHF etching, water leaching and HCL etching and subsequent annealing, result in single terminations with a step-and-terrace structure. However, to date there exists no report comparing electronic measurement on STO-based systems obtained by these different methods.

3.2 Atomic Force Microscopy

Atomic Force Microscopy (AFM) is a scanning probe microscopy (SPM) mode. SPM is a technique which uses a physical probe to scan and investigate the surface of a sample at high resolution. Local material properties such as friction, height and magnetism can be measured with such techniques depending on the probe. Most of the SPM modes can image multiple interactions.

The working mechanism of an AFM is based on a sharp tip (probe) which is brought in the proximity of a surface and while scanning over the surface, it can record the surface topology. Figure 3.4 shows a schematic of an AFM. The probe is positioned at the end of a cantilever. The cantilever deflection will change due to (interaction) forces between the probe and the sample surface. A laser focused on the back of the cantilever is reflected onto photodiodes. The reflection angle of the beam will be altered by a change in deflection of the cantilever due to the topology. The change in deflection is registered by the photodiodes. A feedback loop can be implemented such that the height of the cantilever can be adjusted accordingly. The recordings of the height adjustment produces an image of the surface topology. The resolution range is from nanometer to atomic scale depending on the probe size and the parameter settings like scan size, amplitude and gains.

There are three AFM imaging modes:[68]
- Contact mode   : measures the topography by dragging the tip across the surface.
- Tapping Mode   : measures the topography by tapping with a near resonance frequency

oscillating tip across the surface.

- Non-contact mode: measures the topography by sensing the van der Waals attractive forces between the surface and the probe where the probe is held above the surface.

In the non-contact mode, the cantilever has been, as a precautions, kept significantly far from the surface during operation in order to prevent collisions of the probe and the surface, therefore it provides a lower resolution than contact and tapping mode. Since a relative high resolution is necessary to measure the steps in STO(111) substrates, tapping mode is the preferred technique. The contact mode can create shear forces which damage soft samples. This effect is eliminated when using tapping mode.
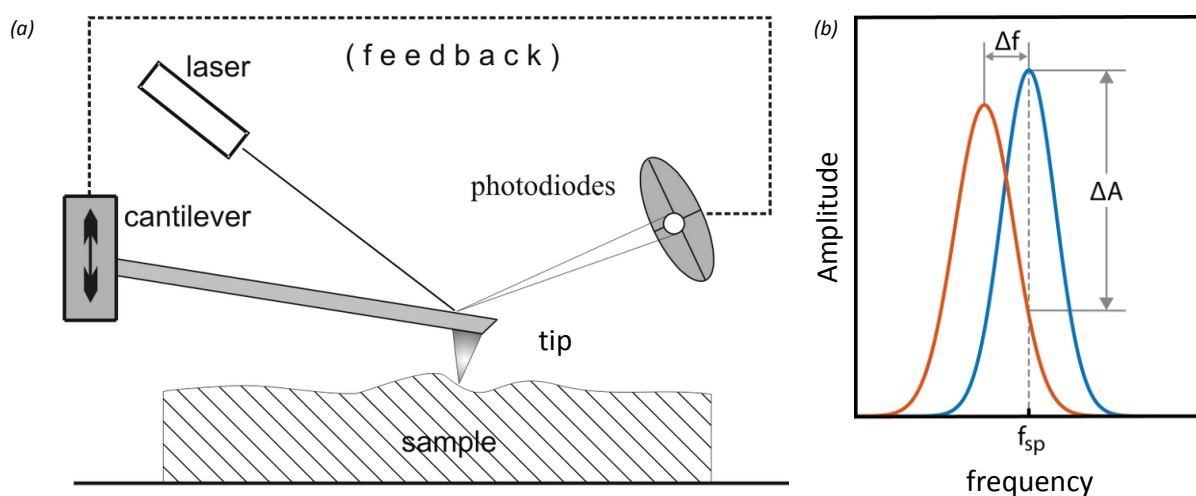

Figure 3.4: a) The set-up of an Atomic Force Microscope (AFM) consisting of a cantilever with a probe at the end which scans the surface of a sample. A laser directed at the back of the cantilever reflects towards photodiodes that registers changes of the scanning probe. A feedback loop can adjust the height of the cantilever.[69] b) The blue line is the response curve of the cantilever in air oscillating at a setpoint frequency (f_{sp}) close to the near resonant frequency. As the tip gets close to the surface, the interaction forces change the response of the cantilever (red line), resulting in a shift of the oscillation frequency (Δf) and a decrease in amplitude (ΔA) at f_{sp} which can be detected by the photodiodes.

In tapping mode AFM, the cantilever is oscillating in free air at an near resonant frequency. Figure 3.4b shows a typical response curve (blue curve) of the cantilever at the frequency setpoint (f_{sp}) close to the resonant frequency, corresponding to the maximum oscillation amplitude. As the tip gets closer to the surface due to surface features, interaction forces (like van der Waals forces, dipole-dipole interactions and electrostatic forces) act on the cantilever. These forces change the response of the cantilever (red curve) and result in a swift of the frequency (Δf) and a decrease of the amplitude (ΔA). The photodiodes measure the variation of the oscillation amplitude and give feedback to the cantilever to maintain the oscillation amplitude. A piezoelectric actuator adjusts the height of the cantilever to bring it back to the original oscillation amplitude determined by the setpoint frequency. The change in height of the cantilever is imaged by registration of the movements of this piezoelectric actuator.

For this research, the AFM images of the terminated STO(111) substrates should display a step-and-terrace structure. The topographic images in this study are made with a tapping mode AFM. The tips used are from BudgetSensors Tap300Al-G with a force constant of 40 N/m. Figure 3.5a shows a typical AFM image of a single Ti-terminated STO(111) surface with a clear step-and-terrace structure.

Figure 3.5b graphs the step height of the structure over the line AB. The height of the steps is measured to be around 0.24 nm, which is consistent with the height of the unit cell of the single terminated STO(111). Therefore, AFM is a good tool to determine if the chemical etching successfully terminates the samples.
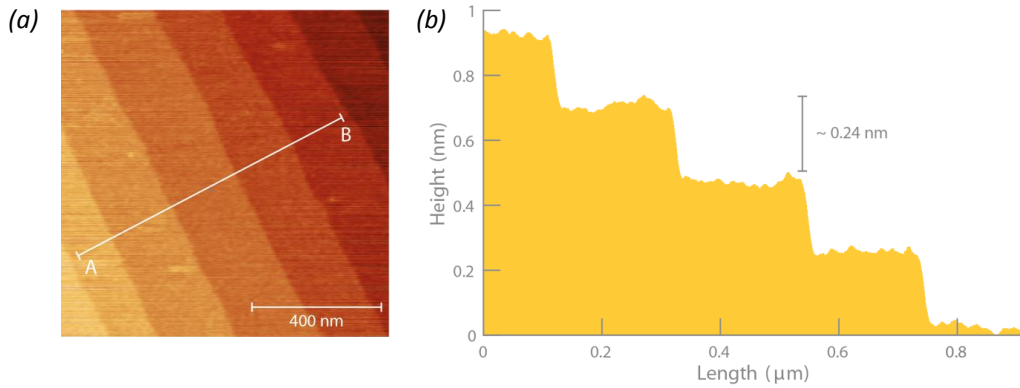

Figure 3.5: a) AFM image of a single Ti-terminated atomically flat STO(111) surface with a step-and-terrace structure after chemical etching (BHF) and heat treatment. b) The height profile of the line AB in the AFM image with a step height close to the size of the unit cell.

3.3 Pulsed Laser Deposition

Pulsed Laser Deposition (PLD) is a physical vapour deposition technique frequently used to grow high quality complex oxide thin films. A high power laser beam strikes a condensed-matter target of the material that is to be deposited. This material is vaporized from the target and deposited as a thin film on a substrate. The main advantage of PLD is the stoichiometric transfer of the target material at high pressure. In this study, PLD is used to grow LAO thin films with varying thicknesses on Ti-rich single terminated STO(111) substrates.

3.3.1 Working principle

Figure 3.6 shows a schematic of the PLD system. A high-power excimer pulsed laser (LPX Pro 305 F, $\lambda = 248$ nm) is aimed at a spinning target inside a ultra-high vacuum chamber. The duration of the laser pulse is in the nanosecond range (~ 20 ns). The laser radiation is absorbed at the surface of the target and the electromagnetic energy of the laser is converted into electronic excitation in the form of plasmons or excitons. The energy of these excitations is transferred into the lattice and induces heating in the thermal absorption layer. The absorption layer will vaporize when the photonic energy of the laser pulse reaches a certain limit. The temperature and pressure will increase such that partial ionization and subsequently expansion of the vapour will occur which results in a so-called plasma plume. The plasma plume contains the material for the film to be deposited and will be oriented perpendicular with respect to the surface of the target due to coulomb repulsion. Furthermore, it is directed towards the substrate. Figure 3.6b is a photo of the plasma plume coming from the target surface pointing towards the substrate. The plasma plume will expand as the ionization and thermal energy are converted into kinetic energy. The energy of the plume can be tuned with use of oxygen background pressure because inelastic collisions of oxygen atoms with the plasma plume reduce the kinetic energy which offers control on the speed of the ablated particles. Additionally, the presence of a gas environment (like oxygen) can induce a chemical reaction with the plasma plume to form for example oxides. The particles in the plasma plume condensate at the substrate surface. The number of ablated particles that will reach surface of the substrate is determined by the distance between

the target and substrate, the background pressure, laser spotsize and the laser energy density. The particles arriving at the substrate surface can nucleate and crystallize. Thereafter a new laser pulse will be emitted and the process is repeated.[70,71]
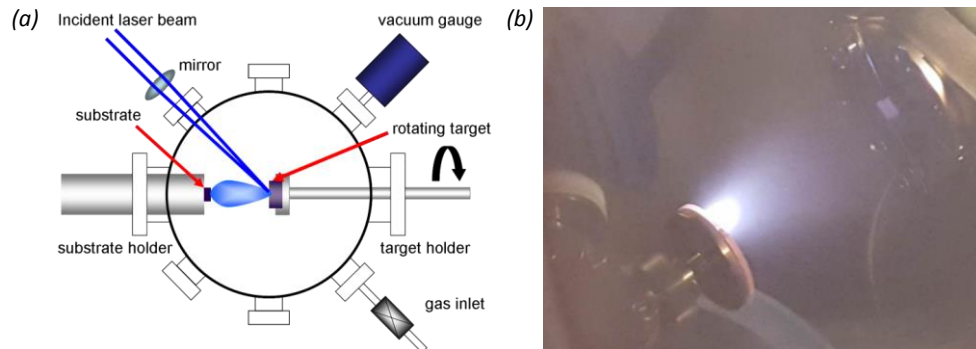

Figure 3.6: a) The Pulsed Laser Deposition set-up with a pulsed laser beam focussed on a spinning target which creates a plasma plume directed towards a substrate. The particles in the plasma plume will be absorbed by the substrate surface. The gas inlet allows for different background gasses and pressures.[72] b) A picture of the PLD set up with on the left the spinning LAO target with the plasma plume ejecting from the target surface and on the right a mounted sample on the sampleholder is visible.

3.3.2 Growth kinetics

An atom or ion which arrives at the surface can diffuse and (1) escape into the vacuum or (2) bond to the surface. An atom which bonds to the substrate will be called an adatom. After the laser pulse, under supersaturated conditions, the adatoms will nucleate on the surface until a critical density of nuclei is attained. Subsequently, the nuclei will grow until they reach a critical cluster size. In a thermodynamic stable system, at small supersaturation, wetting of the adatoms with the surface will determine the growth mode. Figure 3.7 depicts three different growth modes. Good wetting of the adatoms with the substrate, i.e., strong bonding between the film and the substrate, will result in layer-by-layer growth (figure 3.7a). On the other hand, poor wetting between the film and the substrate, i.e., no bonding between the film and the substrate, gives rise to formation of three dimensional islands, 3D growth (figure 3.7b). During heteroepitaxial growth, the growth mode can change from layer-by-layer to 3D growth and vice versa due to lattice mismatch induced strain and/or dislocations (figure 3.7c).
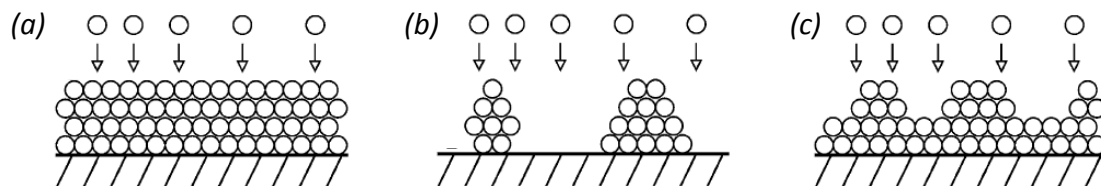

Figure 3.7: The differences in wetting between adatoms and the surface gives rise to three distinct growth modes. a) Good wetting results in layer-by-layer growth (Frank-Van der Merwe growth). b) If the wetting is poor, islands of atoms will grow which is called three-dimensional growth (Volmer-Weber growth). c) Heteroepitaxial growth induces strain and dislocations creating a mixed growth of layer-by-layer and 3D growth (Stranski-Krastanov growth).[70]

Since PLD growth of a thin film is typically not in thermodynamic equilibrium, kinetics effects have to be taken into account. Two kinetic parameters that influence the growth mode, i.e., the morphology of the resulting film, are diffusivity and barrier energy. The barrier energy is an additional energy adatoms need to descend from one terrace to a lower terrace. The diffusivity of the adatoms is determined by the activation energy and temperature. An infrared laser (Compact-Evolution, $\lambda = 980 \, nm$), impinging on the back of the substrate can control the substrate temperature hence

the diffusivity of adatoms. The diffusion coefficient (D) determines the average distance an adatom can travel on a flat surface before being trapped, i.e. $\bar{l}_D = \sqrt{D\bar{\tau}}$, with $\bar{\tau}$ being the average residence time before evaporation. Three different regime can be distinguished when considering the average diffusion length ($\bar{l}_D$) and the average terrace width ($\bar{l}_t$), namely:[70]

1) $\bar{l}_D < \bar{l}_t$, the average diffusion length is smaller than the average terrace width. The adatoms nucleate on top of the terraces. Additional atoms will cluster around the nuclei, resulting in two-dimensional islands which grow until a mono-layer is completed. If the diffusion length is so small that adatoms on the islands cannot diffuse to the edge of the islands, 3D growth will occur and the step-and-terrace structure will be destroyed.

2) $\bar{l}_D \approx \bar{l}_t$, the average diffusion length is similar to the average terrace width hence the thermal energy of the adatom is high enough to reach the edge of the terrace. Therefore, it is energetically favourable for the atoms to nucleate at the step and grow from the step onto the terrace. This is called step flow growth.

3) $\bar{l}_D > \bar{l}_t$, the average diffusion distance is larger than the average terrace width, which means that adatoms are able to diffuse to lower terraces or to the edge of growing islands. This will result in layer-by-layer growth.

3.4 Reflection High-Energy Electron Diffraction

Reflection High-Energy Electron Diffraction (RHEED) is a technique in surface science which uses a high energy electron beam directed at a surface with a grazing angle to investigate the surface characteristics of crystalline materials. This method can be used to monitor the real-time growth of complex oxides with PLD due to the development of high pressure RHEED.
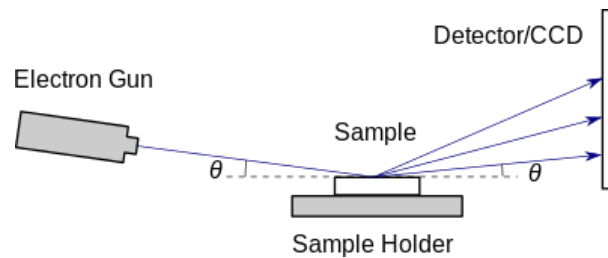

Figure 3.8: Schematic of the Reflection High-Energy Electron Diffraction (RHEED) system. The electron beam incidents at a low angle, θ, on the sample. A crystallographic lattice will reflect the electrons towards a detector screen. The pattern that appears is related to the reciprocal lattice and provides information about the surface structure of the sample.[73]

3.4.1 Working principle

In this research, in-situ RHEED is used to study the growth kinetics. Figure 3.8 shows a schematic of a RHEED set-up where the electron gun, consisting of a tungsten filament, is used to generate an electron beam with an energy of 30 kV and a current of 1.5 A. The electron beam will be directed towards the substrate surface with a low incident angle (0.1°-5°) such that the electrons have a small penetration depth (1-2 nm).[74] This means that the incident electrons can only scatter form the uppermost atomic layers, which makes RHEED a suitable technique for surface analysis. Interactions with the atomic planes will cause constructive and destructive interference creating a Bragg diffraction pattern, a so-called RHEED pattern. Figure 3.9a shows how such patterns can be detected on a fluorescent phosphoric screen. The RHEED pattern is characteristic for the crystal structure and

morphology of the surface. The in-situ RHEED is used during the growth of the thin film in the PLD therefore both the electron gun and detector screen are positioned far from the substrate to minimize interference with the deposition process.

3.4.2 Ewald construction and Laue Zones

The surface of the crystalline STO(111) substrate has a periodic crystal structure where each atom will act as a scatter centre. This periodic structure will produce a set of constructively diffracted beams. The diffraction is determined by the conservation of momentum and energy. Figure 3.9b shows an Ewald sphere and the Laue zones which combines these two parameters and describes the diffraction conditions. For an elastic scattering process, the incident plane wave vector (k_i) and the diffracted plane wave vector (k_d) are of the same length, namely $|2\pi/\lambda|$ where λ is the wavelength of the incident wave. The scattering vector $\Delta k = k_d - k_i$ lies on a sphere with radius $|2\pi/\lambda|$ called the Ewald sphere. The extended reciprocal lattice points (blue lines in figure 3.9) indicate the Laue zones. These lines give the values for the momentum transfer that satisfy the Bragg condition ($2dsin(\theta) = n\lambda$ where d is the interplanar distance and n is a positive integer. The size of the Laue zones are proportional to $E^{-(1/2)}$ such that an increase in energy will decrease the dimension of the Laue zones, i.e., higher incident electron energy will increase the number of zones detected. The allowed diffractions are given by the intersection of the scattering vector (Δk) and a reciprocal lattice vector (G), i.e. the intersection of the Ewald sphere and the Laue zones. RHEED allows for visualization of the points of constructive interference.[75,76]
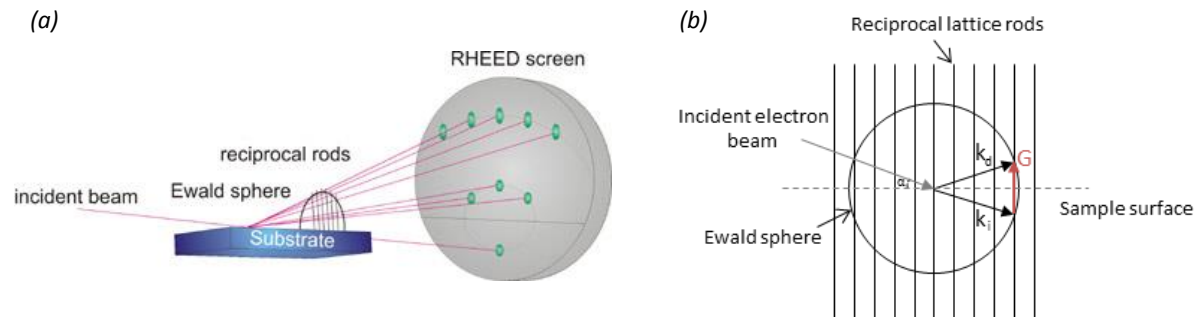

Figure 3.9: a) The formation of the RHEED pattern on a phosphoric screen constructed by the Ewald sphere and reciprocal lattice rods.[77] b) The construction is done by considering the conservation of energy ($|k_d| = |k_i|$) and conservation of momentum ($k_d - k_i = G$) which obey the Bragg condition and lie on the reciprocal lattice rods. The parameter k_i & k_d are the incident and diffracted electron wave vectors and G is the is a reciprocal lattice vector. The angle of incidence is given by α which is small when performing RHEED.

3.4.3 RHEED patterns

In order to obtain a clear RHEED pattern a clean sample surface and low oxygen pressure (10^{-5} bar) are required. A low oxygen pressure avoids significant electron scattering by the background gas. Figure 3.10a is a RHEED image of the surface of a STO(111) sample at 846°C where three intense diffraction spots can be identified. Not all diffracted wavevectors, k_d, can be detected due to the finite size of the detector screen. Therefore, only the diffraction spots within a low angular range of wavevectors will be detected. The zeroth order diffraction spot (indicated by the red arrow) will show the highest intensity.

A perfect crystalline surfaces will produce sharp circular diffraction spots. However, imperfections at the surface, like step edges and crystal defects, will influence the electron scattering and broaden the reciprocal lattice rods resulting in elongated diffraction spots. Therefore, a step-and-terrace structure can create a streaky RHEED pattern. At elevated temperatures, the RHEED pattern will become more

pronounced due to higher diffusivity of the surface atoms which will smoothen the surface. Furthermore, broadening of the diffraction spots can be observed, indicating the presence of small areas of coherence at the surface. This could be induced by the appearance of anisotropic islands at the surface.[75] Besides coherent Bragg diffraction spots, RHEED images often show additional features due to inelastic (multiple) scattering phenomena. Inelastic scattered electrons can obey the Bragg condition and create relatively sharp lines connecting the intense diffractions spots of the RHEED pattern, so-called Kikuchi lines. Figure 3.10b shows a RHEED pattern where the Kikuchi lines are (vaguely) visible. The intersection of the Kikuchi patterns and coherent diffraction spots causes enhancement of the observed intensity.[78]
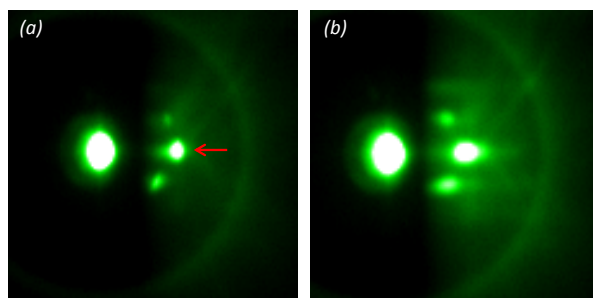

Figure 3.10: a) RHEED pattern for a STO(111) substrate at 846°C. The red arrow indicated the zeroth order diffraction spot and b) RHEED pattern for a STO(111) substrate at 770°C. The spots are a bit streaky and Kikuchi lines are vaguely apparent.

3.4.4 Monitoring the thin film growth

The growth of layer-by-layer thin films can be monitored by observation of the specular intensity of the diffraction spots in the RHEED pattern. This intensity is related to the surface order. A smooth surface (high order) will give rise to intense coherent, diffraction spots whereas a disordered surface will provide weak, incoherent diffraction spots. Figure 3.11 shows the RHEED oscillations of the zeroth order diffraction spot obtained during the growth of an LAO film on an STO(111) substrate. Furthermore, figure 3.11 shows the coverage of the surface where the corresponding numbers in the graph indicate the position in the oscillation. Before deposition, the STO(111) substrate has a smooth surface, i.e. high intensity peak (1). At the beginning of the deposition, ad-atoms on the surface induce roughening hence cause a decrease in the intensity of the diffraction spots (2). The intensity will be minimum when 50% fractional coverage is reached (3). Full coverage will create a smooth surface again and appears as a peak in the spot intensity indicating the growth of a full atomic layer (4). The growth of multiple atomic layers will give rise to periodic RHEED oscillations due to the relative surface coverage where each intensity peak represents the completion of an atomic layer. The number of intensity peaks indicate the thickness of the LAO thin film being 10 atomic layers (10 uc). Furthermore, the overall intensity is decreasing significantly while growing more layers, this is related to interface roughness created during the thin film growth. The growth of a second layer can start while the growth of the first layer has not been completed when the diffusivity of the adatoms is not high enough to reach the vacant atom site in the first layer. This can also happened for subsequent layer resulting in an increase of the interface roughness. Consequently, the overall intensity of the RHEED oscillations decreases. Note, the completion of a full atomic layer is still characterized by a peak in the oscillations.
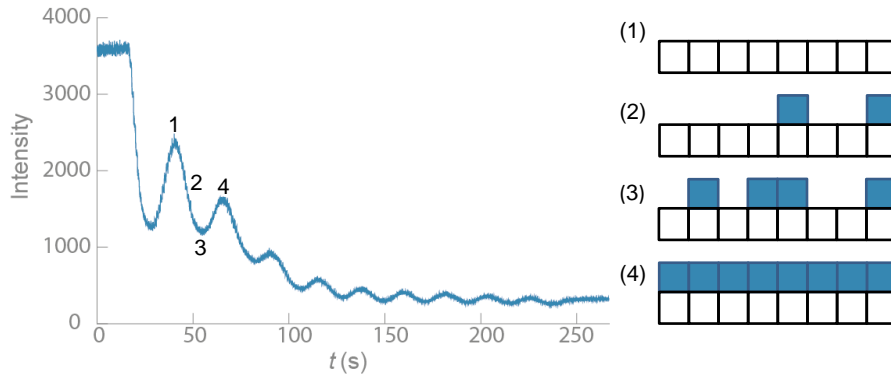
Figure 3.11: The zeroth order diffraction spot RHEED oscillations during the PLD growth of a 10 uc LAO thin film on an STO(111) substrate. The growth temperature was 846°C and O_2 pressure 6×10^{-5} mbar. The magnitude of the intensity is correlated to the coverage of the deposition material on the substrate. The schematic on the right displays the coverage: (1) bare substrate, (2) 25% coverage, (3) 50% coverage and (4) 100% coverage.

3.4.5 Growth conditions for LaAlO$_3$/SrTiO$_3$ heterostructures

The system under investigation is the LAO/STO heterostructure. PLD is commonly used to grow thin films of LAO on top of Ti-rich terminated crystalline STO substrates. The film thickness is important for the formation of the 2DES at the (111)-oriented interface, since it has been experimentally observed that in the range around 9-13 uc a high mobility 2DES is present.[5] Therefore layer-by-layer growth is the preferred growth mode which can be monitored with RHEED. There excists a well-established method for a controllable layer-by-layer growth of LAO films on STO(100) substrates where the target is composed of single crystal LAO. Most research groups use a KrF excimer laser with a repetition rate of 1 Hz and a laser fluency of 1-2 J/cm^{-2}. Typical deposition temperatures and oxygen pressures are 750-850 °C and 10^{-6}-10^{-3} mbar, respectively. In this range of pressures an oxygen deficiency will arise in the system. However, increased pressures (e.g. 10^{-2} mbar) will result in 3D island growth. Post-annealing in high oxygen pressure ($\sim$100 mbar) is performed to refill the oxygen vacancies after the PLD growth.[79]

For the growth of LAO films in this study, a high-power KrF excimer pulsed laser (LPX Pro 305 F, $\lambda = 248$ nm) with a repetition rate of 1 Hz and a laser fluency of 1 J/cm^{-2} is used. The sample is glued with silver paste on a holder to increase the thermal conductance between the holder and the substrate. The growth has been performed at two different temperatures, namely 770 and 850 °C. The oxygen pressure during the growth was set to 6×10^{-5} mbar. Thereafter, the samples are in-situ post-annealed for 1 hour at 600°C and 300 mbar of oxygen pressure and the heterostructure is cooled down to room temperature in the same atmosphere. Appendix C2 contains a list with the growth parameters of the samples under investigation as well as the RHEED oscillations during the PLD growth and the RHEED patterns and AFM images before and after deposition.

3.5 Cryogenic systems

Low temperature measurements need to be performed to observe the electronic properties of the 2DES of LAO/STO heterostructures. In this study, magnetotransport measurements are conducted in a cryostat at temperatures down to 1.5 K. The superconducting properties of a system can only be observed below the superconducting critical temperature which is in the mK regime in the case of LAO/STO heterostructures. A dilution fridge is used to reach a sample temperature of 40 mK.

3.5.1 Cryostat

A cryostat is a cryogenic device which allows for low temperature measurements down to 1.5 K. The performed magnetotransport measurements are done in a bath cryostat which uses liquid cryogenics for cooling. The system is a (Oxford Instruments Spectromag series) low loss cryostat, equipped with a superconducting magnet system. It is a metal construction with vacuum insulation and intermediate temperature radiation shielding. Figure 3.12 is a schematic of the cryostat where the liquid helium is located in the helium jacket (purple) and the sample stick can be mounted into the sample space (green). Radiation shielding reduces boiling of helium (T_B = 4.17 K) and consist of a nitrogen jacket (pink) with a boiling temperature of 77 K. The vacuum space (white) which separates the sample space, the helium jacket and the nitrogen jacket, serves as an isolation shield. At the bottom of the system, immersed in liquid helium, the superconducting magnetic coils (yellow) are located. Appendix A contains a manual for the cool down of the system from room temperature.

The cryostat is equipped with a lambda point refrigerator (λ-fridge) which allows temperatures in the lower region of the helium jacket to be reduced to the lambda point temperature of helium. Figure 3.13 shows the phase diagram of helium with two phases: normal liquid phase (dark green) and superfluid phase (light green). The lambda line is the line indicating the transition from normal liquid helium (helium-1) to superfluid helium (helium-2). The lambda point in a cryostat which contains 100 % ^{4}He (0 % of ^{3}He) is close to 2.18 K.
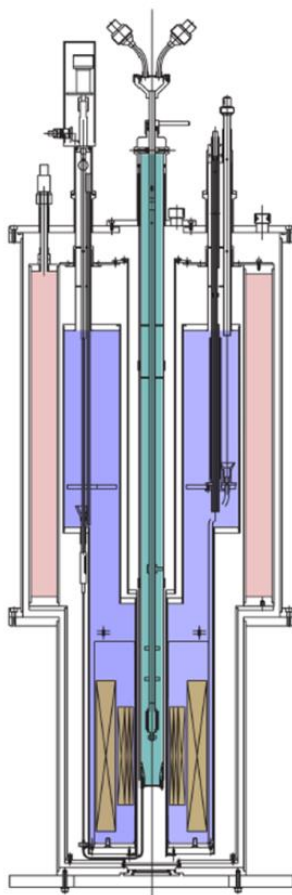

Figure 3.12: A cross-section of a flow cryostat where different colours highlight the main areas: the nitrogen jacket (pink), the helium jacket (purple), the sample space (green), the superconducting magnet coils (yellow) and the vacuum jacket (white).[18]

The λ-fridge consist of a needle valve, a vacuum pump and cooling coils. The needle valve allows for liquid helium from the helium jacket to enter the λ-fridge, creating a (small) helium bath inside. The lambda point temperature is achieved by pumping on the helium bath with the vacuum pump. This results in a reduction of the vapour pressure of helium such that liquid helium molecules evaporate from the helium bath which is a endothermic reaction. This way of cooling is called evaporative cooling. Cooling coils are in thermal contact with the helium bath in the λ-fridge and the helium jacket. A temperature drop to the lambda point temperature in the cooling coils is induced due to the evaporative cooling. Subsequently, the cooling coils will generate a temperature drop in the surrounding liquid helium in the helium jacket by convection. The cold liquid helium will sink to the bottom of the cryostat while the density increases. The thermal conductivity of liquid helium itself is poor, therefore the cold liquid helium is maintained at the bottom of the cryostat and warmer, less dense helium will raise to the top of the helium jacket. This will allow the superconducting magnet to work at temperature below 4.17 K, increasing the maximum working magnetic field which will explained more extensively below.

3.5.2   Dilution refrigerator

A ^{3}He/^{4}He dilution fridge is a cryogenic device which can theoretically provide continuous cooling temperatures to 2 mK. These devices can be divided into two types namely wet dilution refrigerators and dry dilution refrigerators. Wet dilution refrigerators use cryogenic liquids, like nitrogen and helium, to reach temperatures in the mK regime whereas dry dilution refrigerators are cooled by a cryocooler, like pulse tube coolers. The measurements in this study are performed in a wet dilution refrigerator therefore the focus of the section will be on this device.

The thermal isolation of a wet dilution refrigerator is similar to the one in the cryostat described above. The helium jacket is surrounded by a concentric nitrogen jacket and vacuum space. Additionally, the dilution refrigeration has a closed helium system with ^{3}He and ^{4}He saved in external gas containers. The helium is injected in the dilution refrigerator with a capillary. The helium inside the capillary will be pre-cooled to 77 K by the nitrogen jacket and subsequently to 4.2 K by the helium jacket. Figure 3.14 shows the coldest part of the dilution fridge consisting of a 1K bath, the mixing chamber and the still. A 1K bath allows the sample to reach a temperature of 1.2-1.5 K. The 1K bath works on the same principle as the λ-point refrigerator, namely evaporative cooling. Thermal contact between the 1K bath and helium capillary liquefies the ^{3}He gas in the capillary. Further cooling to 500-700 mK is done by the still which contains cold ^{3}He vapour coming from the mixing chamber. The density of the helium will increase and the liquid will move more down the capillary and reach the mixing chamber which is the coldest chamber of the device.

The phase diagram of these isotopes (figure 3.13) shows that the normal liquid phase is a ^{3}He-rich phase and the superfluid phase is a ^{4}He-rich phase. Below 870 mK the composition undergoes a phase separation where the concentration of ^{3}He in the ^{3}He-rich phase is reaching 100% and ^{3}He:^{4}He concentration in the ^{4}He-rich phase is around 6.6%:93.4%. The two phases of helium (^{3}He-rich and ^{4}He-rich) are in equilibrium in the mixing chamber and the cooling mechanism relies on the mixture of these isotopes. The phase separation creates a phase boundary in the mixing chamber. The capillary injects the liquid ^{3}He in the ^{4}He phase which subsequently flows from the dilute phase through the phase boundary into the concentrated ^{3}He phase. The endothermic energy necessary for this process is used to decrease the temperature in the mixing chamber. In this study, the base

temperature of the dilution refrigerator is 20 mK. The sample is in thermal contact with the mixing chambers. We achieved to reach a sample temperature of ~40 mK.
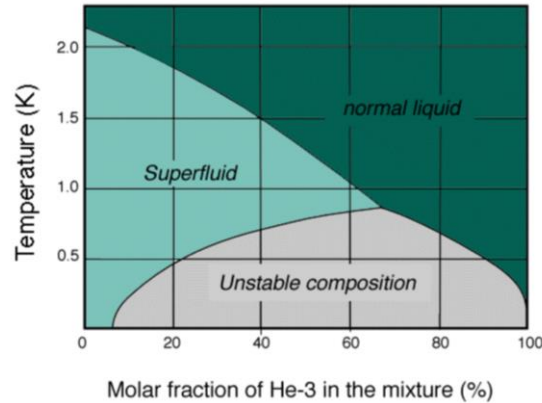

Figure 3.13: ^{3}He/^{4}He phase diagram indicating three different areas which are normal liquid (^{3}He-rich phase), superfluid (^{4}He-rich phase) and unstable region which results in a composition of ^{3}He and ^{4}He.[80]
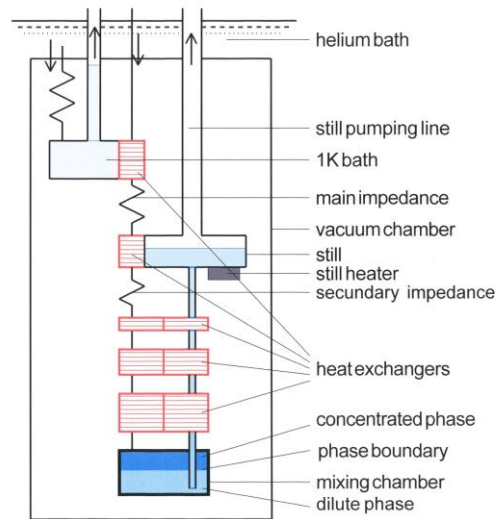

Figure 3.14: Schematic of the lowest temperature part of the ^{3}He/^{4}He dilution refrigerator indicating the important features, namely 1K bath, still and the mixing chamber.[81]

3.5.3 The superconducting magnet system

A superconducting magnet is located in liquid helium at the bottom of both, the flow cryostat and the dilution refrigerator (see figure 3.12), allowing for magnetotransport measurements. It is a high field electromagnet made from two concentric solenoids of superconducting wires. Typically, magnets are composed of an inner coil made from Niobium Tin wires (Nb$_3$Sn: T$_c$ = 18 K and H$_c$(4.2 K) = 25 to 30 T) on a stainless steel former and an outer coil is made from Niobium Titanium wires (NbTi: T$_c$ = 9.2 K and H$_c$(4.2 K) = 15 T) on an aluminium former. To provide mechanical stability the wires are insulated with an epoxy resin and placed inside a copper matrix. The connections to the magnetic current terminals and the cryostat leads are made of flexible strands of superconducting wires (typically NbTi wires). The magnet and the leads are fully immersed in liquid helium which has a boiling temperature lower than the critical temperature of the superconductors. Below the critical temperature, the superconducting phase is more stable with decreasing temperature, i.e., the magnet can withstand higher magnetic fields and current before a phase transition from the superconducting to the normal state occurs.

The superconducting magnet is equipped with a superconducting switch to be able to energize the magnet by a power supply. The switch consist of a superconducting wire which is wound around an electrical heater, positioned parallel to the entire bare magnet. The electrical heater can change the conducting state in the wires of the switch. When no heat is applied, the switch elements are superconducting and the heater is in the closed state. In the open state, the temperature is raised and the switch elements become resistive such that the current will rather flow through the superconducting magnet.

The superconducting magnet can be operated in the persistent mode. This mode allows tuning of the current in the magnet and establishing a required magnetic field which can be maintained. The magnet can be energised in the open state by applying a current to the current leads of the magnet. This current will induce a magnetic field which can be adjusted to the desired magnetic field. In order to obtain a persistent mode, the superconducting switch is changed to the closed state such that the magnet is short circuited. Subsequently, reducing the power supply to zero leaves the magnet in the persistent mode. The current flow will be constant hence a constant magnetic field is induced. The magnet can be taken out of the persistent mode by ramping up the current in the leads to the pre-set current. When the pre-set current is reached, the switch heater is changed to the open state. Then, the magnet current can be adjusted to change the magnitude of the magnetic field and the magnet can be brought back into a persistent mode following the same procedure.

3.6 Magnetotransport

In this thesis, the magnetotransport properties of the 2DES at the LAO/STO(111) interface are studied with varying temperature and electrostatic doping by a back gate voltage. Hall bar configurations are used to conduct accurate transport measurements. Figure 3.15 shows the design of the Hall bar configuration used in this study. Electrical resistance can be determined by measuring the voltage drop between the different contacts. The tensor of resistance is given by Ohm's law:

$$\bar{\bar{\rho}} = \boldsymbol{E}/\boldsymbol{J}, \tag{3.1}$$

where J is the current density per unit length and E is the electric field. The resistance can be measured parallel (Magnetoresistance) and perpendicular (Hall resistance) with respect to the direction of the current. The current density is assumed to be in the x-direction, $\boldsymbol{J} = (J_x, 0, 0)$, such that:

$$\rho_{xx} = E_x/J_x \tag{3.2}$$

and

$$\rho_{xy} = E_y/J_x \tag{3.3}$$

Two dimensional systems have an electric field, $E_{x(y)} = V_{xx(xy)}/L$ and current density, $J_x = I_x/W$, hence the sheet resistance of a conducting layer is given by:

$$R_S^{xx(xy)} = \rho_{xx(xy)}^{2D} = \frac{V_{xx(xy)}}{I_x}\frac{W}{L} = \frac{R_{xx(xy)}}{2} \tag{3.4}$$

where $I_x = I_{\text{Bias}}$ and the ratio $\frac{W}{L} = \frac{1}{2}$ for all the configurations in this study. For accurate magnetotransport measurement, the following design aspects are considered for the Hall bar geometry. The voltage probes have short lateral dimensions such that a possible disturbance of the electrochemical potential in the Hall bar due to scattering in the contact region is minimized. The Hall

bar channel has to be wider than the quantum coherence length. The channel width is chosen to be ≥25 μm while the elastic means free path in two-dimensional LAO/STO is ~10-100 nm.[82] Furthermore, the distance between the current contacts and the voltage contact need to be sufficiently large to prevent the interactions between the contacts that could influence the electronic measurement.[83]
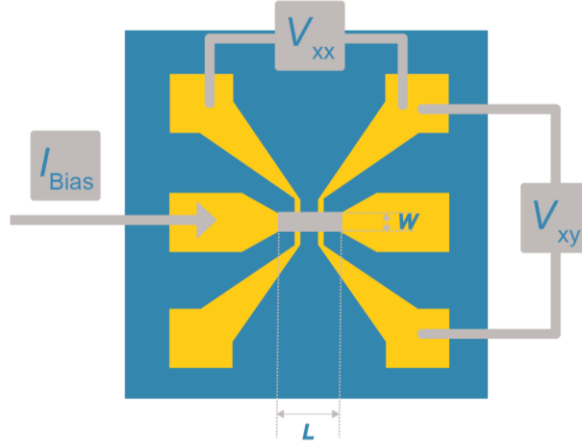

Figure 3.15: Schematic of an Hall bar with an aspect ratio W/L = ½ where W is the width and L is the length. The blue area is the STO substrate, the yellow area is the gold contacts and the grey channel is the LAO film. The voltage drop (V_{xy} and V_{xx}) due to an applied current (I_{Bias}) from the left to right gives the Hall resistance (R_{xy}) and the magnetoresistance (R_{xx}).

3.6.1 Hall resistance

The Hall effect is the influence of the magnetic field on the resistance perpendicular to the applied current. We have seen in section 2.3.1, that when one type of carrier is present in the system, the Hall coefficient is related to the sheet carrier density as

$$n_s^{2D} = -\frac{1}{eR_H} \tag{3.5}$$

Furthermore, implementing equation 3.5 in the definition of the Hall coefficient (equation 2.5), the sheet carrier density can be related to the slope of the Hall measurements by

$$n_s^{2D} = -\frac{B}{eR_s^{xy}}. \tag{3.6}$$

Thereafter, the mobility of the charge carriers can be extracted using:

$$\mu_e = \frac{1}{n_s^{2D}e\rho_{xy}^{2D}}. \tag{3.7}$$

For the two type of carriers system, the sheet carrier density and the carrier mobility can be extracted by fitting the data to the Hall coefficient of the two band model, i.e.,

$$R_H = \frac{1}{|e|}\frac{n_1\mu_1{}^2 - n_2\mu_1{}^2}{(n_1\mu_1 + n_2\mu_2)^2}. \tag{3.8}$$

3.6.2 Magnetoresistance

The magnetoresistance (MR) is related to the change in electrical resistance parallel to the applied current due to an external applied magnetic field, $\boldsymbol{B} = (0,0,B)$. The definition of the relative magnetoresistance is:

$$MR(B) = \frac{\rho_{xx}(B) - \rho_{xx}(0)}{\rho_{xx}(0)} \tag{3.9}$$

with $\rho_{xx}(0)$ is the sheet resistance without any magnetic field applied. The magnetic field dependence of the resistance, $\rho_{xx}(B)$ can be extracted from the magnetotransport measurements.

3.7 Sample fabrication

The LAO/STO heterostructures are patterned into a Hall bar geometry in order to perform accurate magnetotransport measurements. The preparation of the sample is carried out in the cleanroom of the Kavli Nanolab Delft. Electron beam (e-beam) lithography, Argon milling (Ar milling) and Physical Vapour Deposition (PVD) are the methods used to process the samples. Figure 3.16a shows one of the designs used during this study where the red areas are the contacts and the grey are the Hall bar channels. The design contains five Hall bars where the centre Hall bar is equipped with side gates. Figure 3.16b is a zoom-in of the centre Hall bar. The small features at the boundary of the contacts (red) and the channel (grey) are introduced to increase the contact surface area. The cleanroom processing of this pattern is done in two steps: (1) deposition of metal contacts and markers and (2) milling to create the Hall bar channels. Appendix B contains a schematic of all the processing steps described in this section.

The cleanroom processing is done after the PLD growth of the LAO/STO heterostructure. The samples need to be cleaned before starting the processing. This is done by ultra-sonication in acetone and subsequent ultra-sonication in IsoPropanol (IPA), both for 10 minutes. The nitrogen gun is used to blow dry the sample and remove the residual IPA.
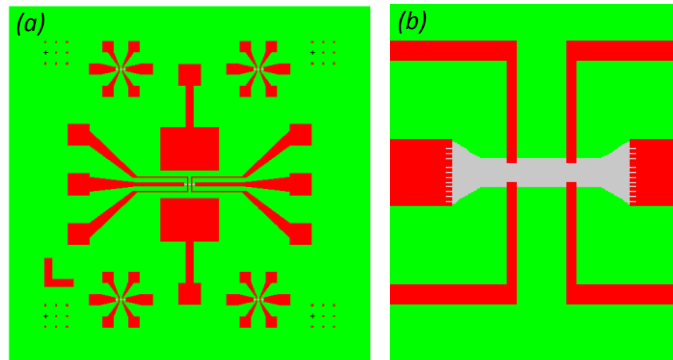

Figure 3.16: a) A pattern for electron beam lithography with five hall bars which is used in this study. The markers are positioned in the corner of the sample. The Hall bar, indicated in grey, are located between the contacts displayed in red. The hall bar in the centre is equipped with side gates. b) A zoom-in of the central hall bar.

3.7.1 Step 1: Metals contacts and markers

A temporary mask is made in order to define where the contact and marker areas should be located. Spin-coating of a positive tone electron-sensitive resist and subsequent e-beam lithography is used to write the mask. When using positive tone resist, the chemical bonds are broken in the e-beam exposed areas. The solubility of the exposed areas is changed with respect to the unexposed areas and the exposed areas can be dissolved in a solvent.

Three layers of polymer resist is spin-coated on the sample and will form the mask. The first two layers consist of positive tone resist called PolyMethylMethAcrylaat (PMMA). The molecular weight

of first and second layer are respectively, 495 kDa and 950 kDa. Both layers, PMMA A3 495 and PMMA A6 950 are spin-coated at 4000 rpm and baked for 10 minutes at 175°C. This results in a layer thickness of ~150 and ~300 nm for PMMA A3 495 and PMMA A6 950, respectively. The samples are baked in order to evaporate residual solvents. In the first layer, the lower molecular weight layer, more bonds are broken during e-beam exposure in comparison to the second layer. The ordering of the layers creates an undercut such that lift-off, the removal of residual resist of the mask, can be performed successfully. A third conducting layer called Elektra is spin-coated because of the insulating character of the LAO/STO samples. The conducting layer prevents charging of the samples during e-beam exposure. The spinning of this layer is done at 4000 rpm after which it is baked for 1 minute at 110°C.

After spin-coating the layers of resist, the sample is exposed to the e-beam in order to define the contacts and markers. The electron beam pattern generator (EBPG) used is the Vistec EBPG5000 PLUS HR 100. The writing in this step will be done with a small spotsize because of the small features at the end of the contacts (see figure 3.16b). The electron beam energy is 100 kV with a 78 nm spotsize and a stepsize of 50 nm using a dose of 850 μC/cm^2. After e-beam lithography and before Ar milling, the written part is dissolved, i.e., development. The first step of the development procedure is removal of the Elektra by immersing the sample in H_2O for 2 minutes. Thereafter, the sample is dipped into MethylIsoButylKeton (MIBK):IPA (1:3) for 90 seconds and 15 seconds in IPA to remove both PMMA layers. The nitrogen gun is used to remove the remaining IPA on the sample.

After development, 6 nm of the heterostructure (the LAO thin film and partially the STO) in the exposed areas is removed by using Ar milling. In this way, the deposited material will be in contact with the interface of the heterostructure, i.e. the 2DES. A set-up inside the loadlock of the MB_AJA is used to accelerate argon atoms and perform Ar milling. The beam current is set to 2 mA which yields an etching rate of 0.4 nm/min for STO. The Ar milling selectivity of STO:PMMA is ~1:10. Hence, 15 min of Ar milling removes 60 nm of the PMMA layer, leaving the PMMA layer thickness to be ~390 nm. This thickness should be at least twice as thick as the metal layer to be deposited, otherwise lift-off is not possible.

The contacts consists of two layers of different metals, namely titanium and gold. The titanium serves as an bonding layer between the STO (dielectric) and the gold (noble metal) because of poor adhesion between latter two. The workfunction of the bonding layer is chosen such that it is in between the workfunction of STO and the gold. This provides good adhesion between the sample and the contacts. The sample is brought into the main chamber of the MB_AJA to deposit 3 nm of titanium and 77 nm of gold. The deposition of the metal is done by PVD. Lift-off is executed after deposition of the metals, which means that residual resist of the mask and residual metal on top of these areas is removed. This is achieved by ultra-sonication for 30 seconds in acetone, cleaning with IPA and blow drying with a nitrogen gun.

3.7.2 Step 2: Hall bar channels

The 2DES has to be confined to a well-defined channel which is achieved by creating hall bar channels in between the metal contacts. E-beam lithography is used to write a mask such that the channels can be defined by Ar milling. Additionally, the mask will protect the metal contacts. Spinning of the positive tone resist and the conducting layer is done with the same procedure as discussed in step 1. The area around the markers, contacts and hall bars is written by the e-beam such that Ar milling will remove all of the LAO thin film, except at the places where the channels are located (see figure 3.16b, grey area). This will confine the 2DES at the interface of these channels.

The spotsize, stepsize and dose used for this step are respectively, 150 nm, 100 nm and 850 μC/cm^2. The development, argon milling and lift-off is done in the same manner as explained for the contacts. This will finish the sample fabrication in the cleanroom.

Thereafter, the sample will be pasted with silver epoxy to a chip carrier. Subsequently, the contacts on the sample need to be bonded to the contacts on the chip carrier. The bonding is done with aluminium wires using a ultra-sonic wire bonder. Hereafter, the samples will be ready to load into the measurement set-up (cryostat or dilution fridge).

4. Surface Treatment

As described in section 3.1, STO substrates need to be single Ti-rich terminated for the formation of a 2DES at LAO/STO interfaces. This termination can be achieved by a surface treatment of the substrates. In this study, the surface treatment, consisting of chemical etching and annealing, is conducted on unterminated STO(111) 5x5mm samples from CrysTec GmbH. The chemical treatment selectively etches away SrO domains whereas annealing is performed to remove the remnants of the previous treatments and facilitate recrystallization, yielding a flat step-and-terrace structure (for a more detailed explanation see section 3.1). The heat treatment is performed in an oxygen environment to prevent formation of oxygen vacancies. A detailed list of all the samples and the corresponding treatment steps can be found in Appendix C.1.

Figure 4.1a shows an AFM image of an as-received substrate which is typical for the STO(111) substrates under investigation. In the case of STO(100), unterminated substrates show signs of a step-and-terrace structure. On the contrary, all the surfaces of the as-received STO(111) samples in this batch appear to be flat, i.e., no clear step-and-terrace structure can be distinguished.
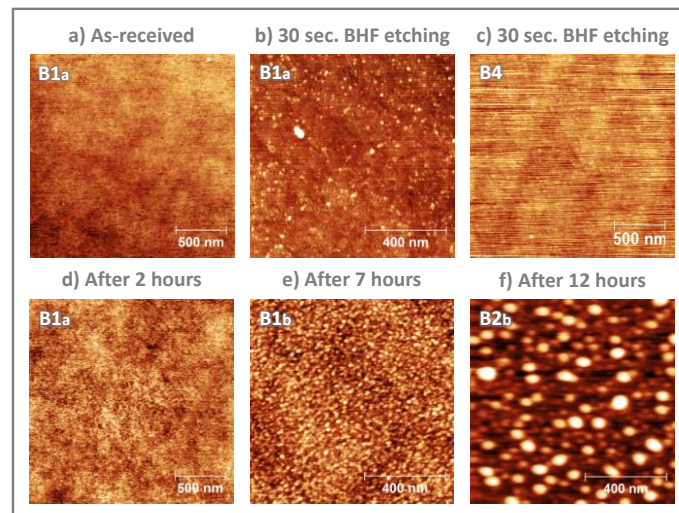

Figure 4.1: AFM images of the STO(111) substrates. a) Sample B1$_a$, as-received unterminated STO(111) from CrysTec GmbH, b) & c) Sample B1 and B4 after chemical etching with BHF for 30 seconds. d) After 2 hours, e) 7 hours and f) 12 hours of annealing at 1000 °C in a tube furnace with the ramp up and ramp down being 5°C/min and 10 °C/min, respectively.

The chemical treatment is performed by following the procedure for single Ti-rich termination of STO(100) substrates introduced by Koster et al.[56]. The samples are immersed in deionized water while sonicating for 20 minutes at room temperature. Subsequently, the samples are dipped in BHF for 30 seconds and rinsed with deionized water to remove the complex hydroxides. Figure 4.1b and 1c display AFM images of samples B1$_a$ and B4 after 30 seconds of BHF etching. These images are representative of the etched STO(111) surfaces in this work. The chemical treatment results in a flat surfaces and no indication of a step-and-terrace structure is observed, i.e., the chemical treatment seems to be ineffective.

Subsequent heat treatment is performed to uncover an underlying structure. A heat treatment allows for diffusion of the surface atoms such that potential step-and-terrace structures become

more pronounced. After the chemical treatment of the STO(111) substrates B1 and B2, a post-annealing step is performed in a tube furnace at 1000°C where the temperature is increased with a constant rate of 5 °C/min and decreased with 20 °C/min and the oxygen flow was set to 2 L/h. Figure 4.1d, 1e and 1f show the surface of the substrates $B1_a$, $B1_b$ and $B2_b$, after undergoing a post annealing of 2, 7 and 12 hours, respectively. It is expected that longer annealing times give rise to more smooth step-and-terrace structures.[66] After 2 hours of annealing, no clear change of the surface is observed in comparison to the surface of the as-received substrate. An additional 5 hours, resulting in a total annealing time of 7 hours, gives rise to spherical features at the surface. Even larger features, with a height of 0.6 nm, are observed after annealing for 12 hours. These features can originate from Sr segregation from the bulk STO to the surface or contamination of the set-up.

An attempt to enhance the formation of the step-and-terrace structure is done by raising the annealing temperature such that the diffusivity of the surface atoms is increased. The temperature is set to 1100 °C where the increase and decrease rate of the temperature is again 5 °C/min and 20 °C/min, respectively and the oxygen flow is kept the same, i.e., 2 L/h. The chemical treatment is unchanged and the annealing times are 6, 12 and 24 hours for sample B3, B4 and B5, respectively. Figure 4.2 shows the AFM images of these substrates after chemical etching and the heat treatment described above. After 6 hours of annealing, it appears that an onset of a step-and-terrace structure is formed, but no improvement of the surface structure is observed when increasing the annealing time to 12 or 24 hours. The longer the annealing time, the more features appear at the surface. When comparing these features to the ones of the samples annealed at 1000°C, the shape is different and the size is larger. The height of these features is ∼1 nm which is not indicative of the observations of the steps (with a step height of 0.24 nm) if present.
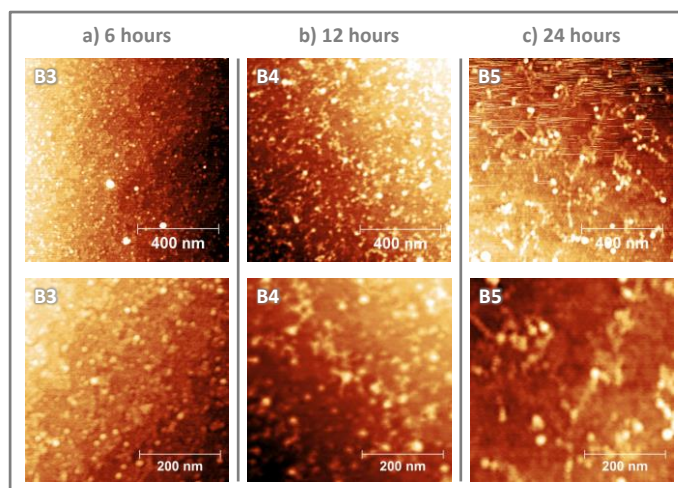

Figure 4.2: AFM images of STO(111) substrates after chemical etching with BHF for 30 seconds and subsequent heat treatment at 1100 °C for a) 6, b) 12 and c) 24 hours. The oxygen flow is 2L/h and the ramp up and ramp down of the temperature are respectively 5°C/min and 20°C/min.

The chemical treatment (30 seconds BHF etching) employed up to this point is not efficiently terminating the surface with the desired composition. In order to investigate the effectiveness of the chemical treatment, a different approach is considered, which involves multiple BHF etching steps. The Lippmaa laboratory carried out such a procedure on STO(100) substrates.[84] The substrate surfaces is etched for a certain amount of time, imaged with the AFM and etched again. This process will be repeated until the step-and-terrace structure appears. The resulting AFM images of the

Lippmaa laboratory are shown in figure 4.3. The surface structure of their substrate shows a clear step-and-terrace structure which becomes more prominent after longer etching times. In our study, we performed a similar procedure on STO(111) substrate. The total BHF etching times considered are 30, 60, 90, 180 and 300 seconds. Figure 4.3 display the AFM images of substrate B7 after the subsequent steps of etching. The first two etching steps, 30 and 60 seconds show the appearance of what could be the onset of a step-and-terrace structure. After 90 seconds a rough, more disordered structures has formed. Subsequent etching steps, achieving total etching times of 180 and 300 seconds, do not result in an atomically flat step-and-terrace structures. The AFM images of the substrate show that chemical treatment is unsuccessful. Note that the images are not taken at the same location at the surface. The effectiveness of the chemical treatment may not be the same over the entire substrate.
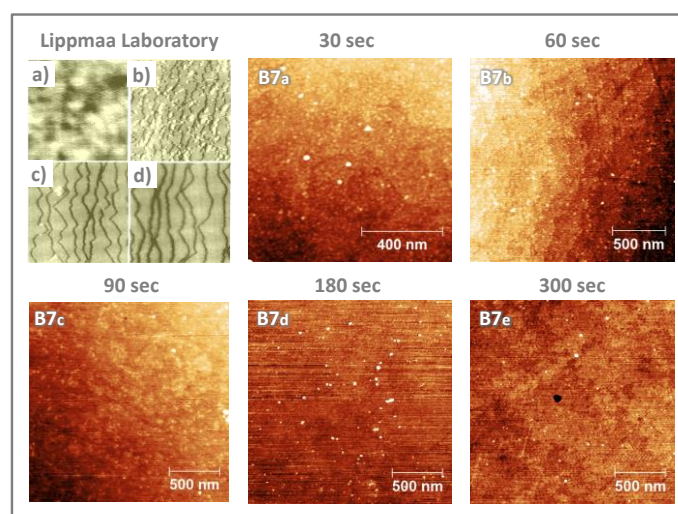

Figure 4.3: The top left panel shows the result of the Lippmaa Laboratory[84] after BHF etching of an STO(100) substrate surface for a) 0, b) 5, c) 8 and d) 12 minutes at room temperature. A distinct step-and-terrace structure can be identified in the AFM images (1000 x 1000 nm^2). The other panels show STO(111) substrate B7 after repeated BHF etching in line with the work of the Lippmaa laboratory. The substrate is etched 30 seconds and subsequently imaged with the AFM to determine the surface structure. Hereafter, the substrate is again immersed in BHF with total etching times of 60, 90, 180 and 300 seconds. The substrate is imaged after each etching step.

It seems that the procedure used for the surface treatment is not resulting in single Ti-rich terminated STO(111) surfaces with an atomically flat step-and-terrace structure. In order to validate the procedure for the surface treatment, the standard procedure for STO(100) is performed on commercially available STO(100) substrates from CrysTec GmbH. The substrates A1, A2, and A3 are BHF etched for 30 seconds and post-annealed for 90 minutes at 950°C under different oxygen conditions, namely 0 L/h, 2 L/h and 10 L/h. Figure 4.4 displays the AFM images of the these substrates after etching and annealing. A heat treatment with an oxygen flow of 0 L/h results in the appearance of structural spherical features at the surface. These surface features are less pronounced when increasing the oxygen flow to 2 L/h, though the desired structure is not observed. Furthermore, sharp distinct lines are identified at the surface of substrate $A2_a$. The sharpness and abruptness of these lines, indicate that these are not step-and-terraces but most probably dislocation lines arising from defect inherent to the substrate. After post-annealing with an oxygen flow set to 10 L/h a rough step-and-terrace structure is obtained. The spherical surface features which are observed at the surface are much smaller than the features observed in substrate $A1_a$. It appears that the higher oxygen flow is reducing the contamination at the surface which could

indicate that the tube of the furnace is contaminated and high oxygen flow prevents contamination particles originating from the tube to be deposited on the surface.
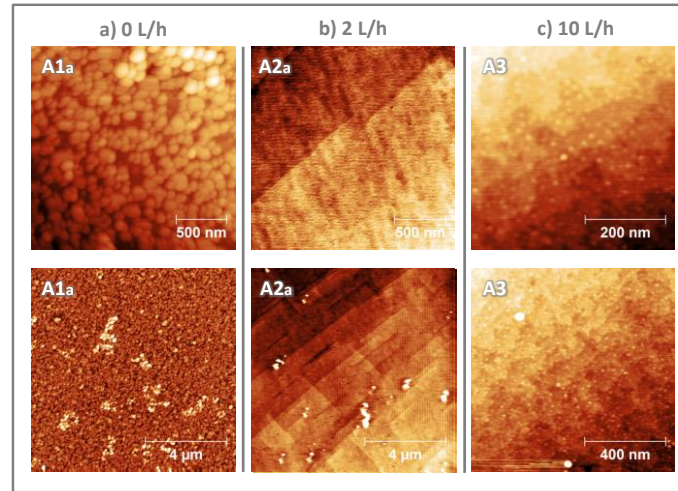

Figure 4.4: STO(100) substrates annealed at 950°C for 90 minutes with varying oxygen flow namely a) 0 L/h (substrate A1$_a$), b) 2L/h (substrate a2$_a$) and c) 10 L/h (substrate A3). The increase in oxygen flow results in a decrease of the appearance of spherical features. In the case of the highest oxygen flow a step-and-terrace structures is present.
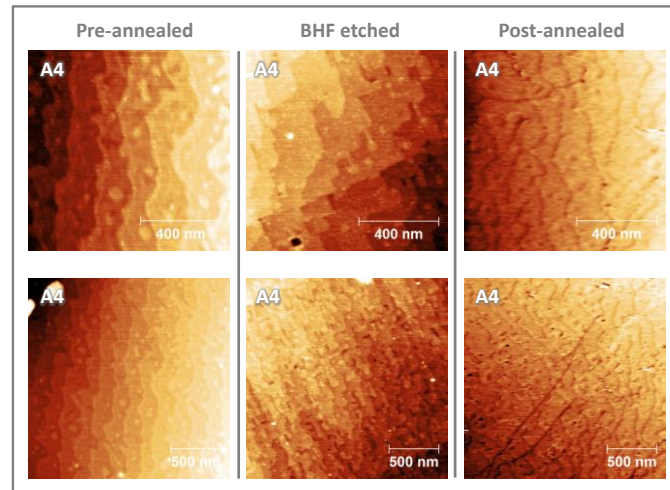

Figure 4.5: The unterminated STO(100) substrate A4 annealed at 950°C for 90 minutes with an oxygen flow of 8 L/h in a clean tube. Pre-annealing of this sample results in a step-and-terrace structure. Subsequent BHF etching removes the islands on the terraces and post-annealing makes the edges of the terraces sharper. The lower AFM images are an enlargement of the upper AFM images.

In order to investigate the formation of these features, a new clean tube for the furnace is used to anneal another STO(100) substrate. The substrate is pre-annealed at 950°C for 90 minutes, BHF etched for 30 seconds and post-annealed at 950°C for 90 minutes. The oxygen flow during the experiment was 8 L/h. Figure 4.5 shows the AFM images after each of the steps. After pre-annealing a step-and-terrace structure with rough terrace edges is present and islands are formed on the terraces which is characteristic of a mixed termination. The chemical treatment removes these islands and results in a step-and-terrace structure indicating that 30 seconds BHF etching is effectively terminating the surface. Subsequent annealing smoothens out the terrace edges and makes the structure even more pronounced. A comparison between substrates A4 and A3 (figure 4.4) shows that the terraces at the surface of substrate A4 are more sharply defined than the terraces observed at the surface of substrate A3. Figure 4.6 displays height profile of the step-and-

terrace structure of sample A4 after chemical treatment. The average height of the step in the structure is ~0.36 nm which is comparable to the size of the unit cell (a_{STO} =0.39 nm) of the STO(100). This suggests that single Ti-rich termination is achieved. The reduction of structural features at the surface indicates that the features most likely originate from contamination in the tube of the furnace.
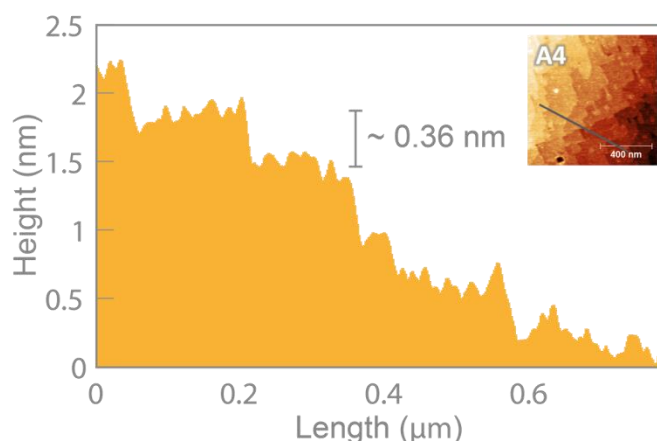

Figure 4.6: A height profile of step-and-terrace structure at the surface of sample 4A. The line along which the profile is taken is given in the inset. The step height ~0.36 nm is close to the height of the STO(100) unit cell.

The same procedure that successfully terminated the STO(100) substrate is performed on an STO(111) substrate. Figure 4.7 shows the AFM images of the subsequent steps of the treatment on substrate B10. After annealing for 90 min at 950°C, the surface does not show any sign of a step-and-terrace structure. BHF etching results in a very disordered structured surface where the features have a size of $\pm$ 0.3 nm which is in the order of the step height. This could hide a potential step-and-terrace structure. Post-annealing does not enhance this disordered structure but also does not give rise to the desired structure. A second chemical treatment is conducted which is not able to terminate the surface of the substrate as shown in figure 4.7. The obtained structure is similar to the surface structure of the first etching step.

Several articles report well-defined single terminated STO(111) surfaces created by BHF etching and annealing in an oxygen environment.[85,86] In this work, we could not reproduce these results. A wide range of different etching times, annealing temperatures, annealing times and the oxygen flows were explored. The variation of the parameters controlling the heat treatment indicated that the tube of the furnace was contaminated, depositing features onto the surface. A successful termination of STO(100) substrates was performed after changing to a new tube but the attempt to terminated STO(111) samples with this new tube failed. The unsuccessful surface treatment may be related to the quality of the substrates of this batch, because all STO(111) substrates in this study are from the same batch. In future work, x-ray diffraction measurements can be performed to give confirmation on the quality of the samples. Furthermore, the same surface treatment can be applied to unterminated STO(111) samples from another batch to confirm the results presented in previous research.
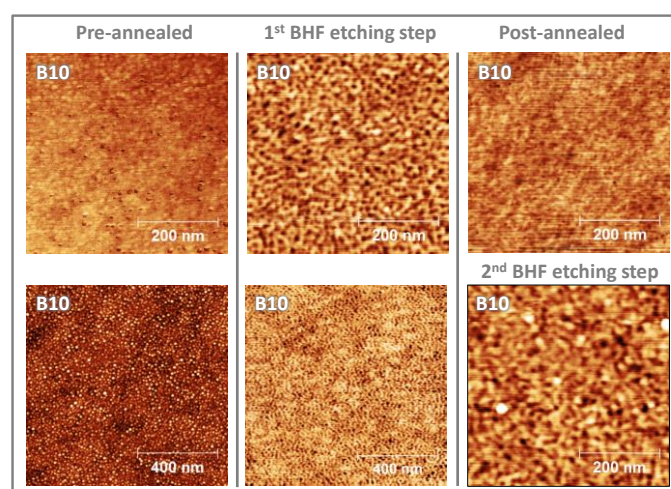
Figure 4.7: The pre-annealed, etched, post-annealed and etched STO(111) substrate B10. The annealing was performed at 950°C for 90 minutes with an oxygen flow of 8 L/h. The surface treatment does not have the desired result, none of the images shows a step-and-terrace structure.

5. Magnetotransport Measurements

In this chapter, the electronic properties of the 2DES at the LAO/STO(111) interface are explored by means of magnetotransport measurement. The LAO film thicknesses is varied to investigate the influence of the film thickness on the electronic properties and determine the critical film thickness in order to obtain conducting interfaces. Additionally, two batches with different growth temperature are fabricated and measured. The samples under investigation are prepared by PLD growth with growth temperatures 770 °C and 840 °C which allows for further investigation of the effect of the growth temperature on the electronic properties at the interface. All the measurements discussed in this work are performed in a Hall bar geometry, as described in section 3.6 and 3.7. Appendix C.2 gives more detailed information about the growth conditions and the surface structure.

5.1 The critical thickness

The most accepted mechanism for the origin of a conducting interface in LAO/STO heterostructures is the polar discontinuity at the interface.[1,26] An increasing amount of LAO monolayers gives rise to a diverging electrostatic potential and intrinsic electronic reconstruction takes place when reaching a critical thickness.

The LAO/STO(111) heterostructure consists of alternating atomic planes of $[Al]^{3+}$ and $[LaO_3]^{3-}$ for LAO and $[Ti]^{4+}$ and $[SrO_3]^{4-}$ for STO. In the purely ionic limit, these atomic planes create a polar discontinuity at the interface. However, in contrast to the {100}-oriented interface, the polar character of the planes in the STO(111) substrate induces in an additional increase of the diverging potential. Electronic reconstruction of the STO(111) substrate is necessary to remove the dipole. It is predicted that $[O]^{2-}$ will bond to the $[Ti]^{4+}$ to compensate for the diverging potential.[14] Figure 5.1a shows a schematic of the charged atomic planes and the oxygen atom which bonds to the outer titanium layer. The charge of the surface layer becomes +2 such that the resulting electric field in the substrate oscillates around zero and the potential becomes finite. However, a diverging potential in the LAO film remains. An intrinsic electronic reconstruction, like in LAO/STO(100) systems, can remove this divergence. Figure 5.1b depicts the addition of half an electron to the interface such that a charge of e/2 is transferred from the LAO surface layer to the interface. Consequently, the charge of the interface layer of the STO(111) changes from +4 to +3.5 due to the flexible valence of titanium. The electronic reconstruction makes the electric field of the LAO film oscillate around zero and the total potential of the heterostructure is finite.

The electronic reconstruction will occur when a certain thickness of the LAO film is reached. The critical thickness of the LAO/STO(100) interfaces is theoretically predicted by a parallel plate capacitor model. The atomic planes with alternating charge are considered to be parallel plate capacitors coupled in series.[29] The potential in a series of capacitors is given by:

$$V = \frac{q}{C} = \sum_i \frac{q_i}{C_i} \tag{5.1}$$

where i is the number of capacitors, q is the charge and the capacitance is given by $C = \varepsilon_r \varepsilon_0 A/d$. A is the surface area of the unit cell, d is the distance between two plates and ε_r and ε_0 are the relative

permittivity and the vacuum permittivity, respectively. This results in the following expression for the potential of a single capacitor:

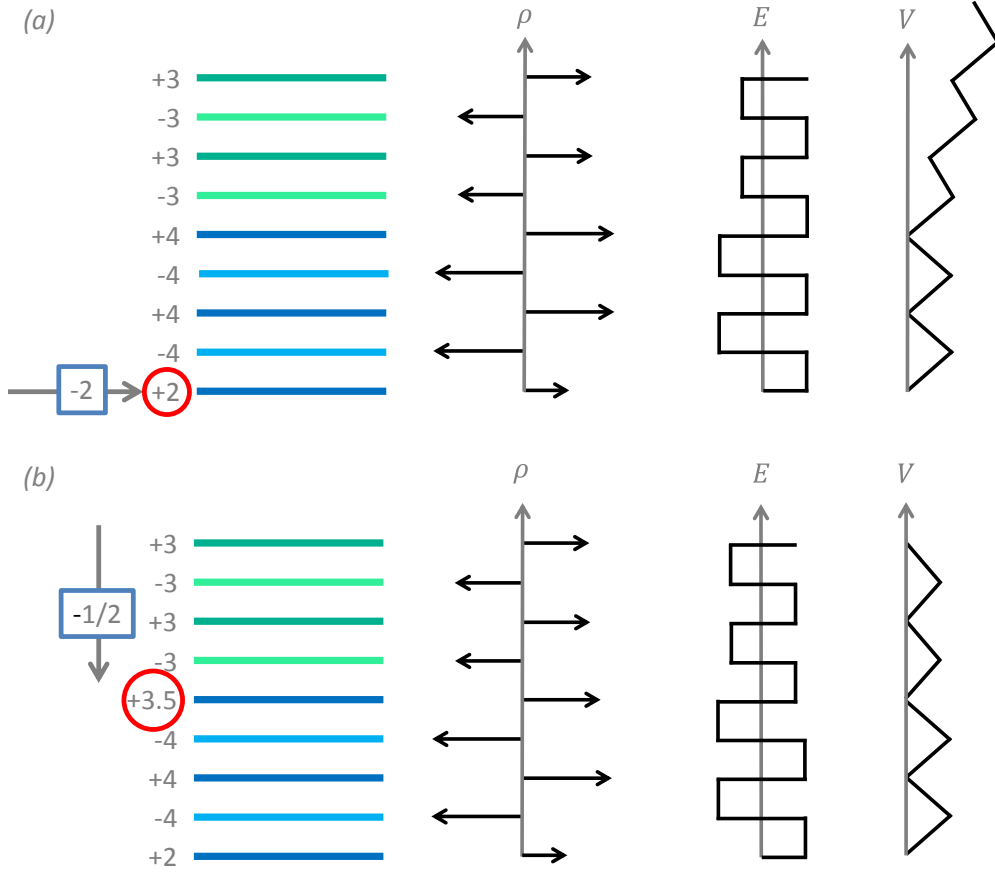$$V_i = \frac{q_i}{C_i} = \frac{q_i d_i}{\varepsilon_{r,i} \varepsilon_0 A_i} \tag{5.2}$$

Figure 5.1: The polar catastrophe explained for atomically abrupt Ti-rich terminated LAO/STO(111) interfaces. For each of the steps the charge (ρ), the electric field (E) and the potential (V) are presented. The unreconstructed LAO/STO(111) interface consists of atomic planes with alternating charge ± 4 in the STO substrate and the atomic planes in LAO(111) film have an alternating charge ± 3. a) The surface reconstruction of the STO(111) substrate considering the surface atoms reacted with oxygen atoms from the environment. The oxygen atoms contribute a charge of -2 to the bottom surface layer, leaving the atomic plane +2. This removes the diverging potential of the substrate. b) Intrinsic electronic reconstruction by the addition of a half electron from the LAO surface to the interface layer avoids the divergence of the electrostatic potential caused by the charged atomic planes in the LAO film.

The capacitance in each monolayer of the LAO thin film is the same, such that for x_c capacitors the total potential in the systems results in:

$$V = x_c \frac{qd}{\varepsilon_r \varepsilon_0 A} \tag{5.3}$$

The electronic reconstruction will happen when the potential reaches the energy difference between the valence band of LAO and the conduction band of STO (energy gap), i.e., $V = \Delta E$. In this case, the critical thickness is:

$$t_c = \frac{\varepsilon_r \varepsilon_0 A \Delta E}{q} \tag{5.4}$$

This equation allows for the determination of the amount of capacitors with thickness d needed for the electronic reconstruction to take place. Each unit cell consists of two plate capacitors with

thickness d. The critical thickness in number of unit cells is: $t_c = \mathrm{x}_{uc} h$ where h is the height of the unit cell. The critical thickness of LAO/STO(100) heterostructures can be determined by taking the charge contribution to the capacitor to be half the charge of the atomic planes, i.e., $q_{(100)}^{\mathrm{LAO}} = 1/2$ and $q_{(100)}^{\mathrm{STO}} = 0$ such that $\left|q_{(100)}\right| = e/2$. The other parameters needed for the calculation are listed in Table 1. Implementing these values into equation 4.3, the critical thickness for LAO/STO(100) heterostructures is found to be 3.5 uc, in good agreement with reported experiments.[5]

Property	{100}	{111}
$\|q\|$	$e/2$	$e/2$
$\varepsilon_r^{\mathrm{LAO}}$	$24^{[87]}$	$24^{[87]}$
h^{LAO} (Å)	$3.79^{[88]}$	2.19
A^{STO} (nm^2)	0.15	0.26
ΔE (eV)	$3.3^{[29]}$	$3.3^{[29]}$
t_c (nm)	1.33	2.31
t_c (uc)	3.5	10.5

Table 1: Physical properties of the LAO/STO {100} and {111} oriented heterostructures. The height of the unit cell for LAO(100) and LAO(111) is given by $h_{(100)}^{\mathrm{LAO}} = a_{(100)}^{\mathrm{LAO}}$ and $h_{(111)}^{\mathrm{LAO}} = a_{(100)}^{\mathrm{LAO}}/\sqrt{3} = c_{(111)}$, respectively where the lattice parameter for STO(100), $a_{(100)}^{\mathrm{LAO}} = 0.39$ nm.[88] The surface area of the ground planes is determined from $A_{(100)}^{\mathrm{STO}} = a_{(100)}^2$ and $A_{(111)}^{\mathrm{STO}} = \sqrt{3}a_{(100)}^2$. The critical thickness t_c are the exact values obtained from equation 5.4.

In the case of LAO/STO(111) heterostructures, the charge contribution of the atomic planes to the capacitor are $q_{(111)}^{\mathrm{LAO}} = 3e/2$ and $q_{(111)}^{\mathrm{STO}} = 4e/2$ such that $\left|q_{(111)}\right| = e/2$. This is similar to the potential in the LAO/STO(100) heterostructure. We assume that the relative permittivity and the energy gap are not influenced by the change of crystallographic orientation. The critical thickness results in 10.5 uc when considering the physical parameters presented in Table 1.

Figure 5.2 combines the polar discontinuity and the parallel plate capacitor model. The blue curve is the potential for the LAO/STO(100) heterostructure whereas the green curve is the potential for the LAO/STO(111) heterostructure. Note that the potential of the (111) orientation starts with a positive offset due to the polar character of the STO(111). The electronic reconstruction takes place when the potential is equal to the energy gap, $\Delta E \approx 3.3$ eV.[29] The critical thicknesses determined from this graph are $t_c^{(100)} = 1.22$ nm and $t_c^{(111)} = 1.73$ nm corresponding to 3.2 uc and 7.9 uc, respectively.

The critical thickness of the LAO film for the {100} orientation, predicted by the linear potential and the non-linear potential defined by the polar discontinuity is 4 uc, in line with experimental observations.[5] In the {111} orientation, the two plate capacitor model results in a critical thickness of 11 uc, whereas the polar discontinuity gives 8 uc. Neither one of the models predicts the experimental value of the critical thickness which is 9 uc.[5] Note, this analysis is valid in the ionic limit. In reality, the structure consists of ionic and covalent bonds which will modify the picture that was sketched above. Furthermore, we have to realize that in both models the relative permittivity and the energy gap are taken to be the same as for the {100} orientation. Thereafter, the two plate capacitor model does not take into account the polar character of the STO and therefore results in a

higher critical thickness as determined with the polar discontinuity model. In the case of the polar discontinuity model, it is assumed that the reconstruction of the polar substrates occurs by a reaction of the surface atoms with oxygen atoms from the environment. During the reconstruction of the STO(111) substrate, different titanate phases can be formed at the polar surface.[14] This will make the reconstruction mechanism more complex and inhomogeneous. A critical thickness of 9 uc can be obtained if such a reconstruction would slightly reduce the potential of the STO(111) substrate.

Furthermore, the mismatch in the lattice parameter of STO and LAO induces tensile strain in the LAO film. The height of the unit cell is reduced due to the strain build up in the LAO film. The height of the LAO unit cell in LAO/STO(100) heterostructure is observed to be 3.74 Å for a LAO film thickness from 5 to 20 uc. Above 20 uc, the unit cell height obtains back the bulk value, 3.79 Å, due to strain relaxation.[42] Therefore, it is highly probable that the unit cell height of LAO in the {111}-oriented heterostructures is reduced by the tensile strain. Assuming the height of the unit cell is strained to 2.10 Å, the discontinuity model induces a slight increase in the exact critical thickness but the general critical thickness predicted by this model remains 8 uc.
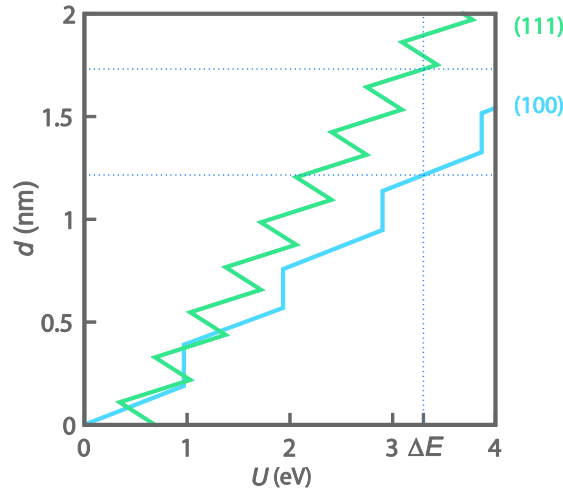

Figure 5.2: Representation of the diverging potential energy with increasing thickness (d) of the LAO film defined by the polar discontinuity for LAO/STO heterostructures in the {100} and {111} orientations (blue line and green line, respectively). The potential is converted to potential energy with the factor $e/2\varepsilon_r\varepsilon_0 A$. The electronic reconstruction takes place when the potential energy reaches the energy gap (ΔE). The points of intersection give the values for the critical thickness which are 1.22 nm and 1.73 nm for the {100} and {111}, respectively.
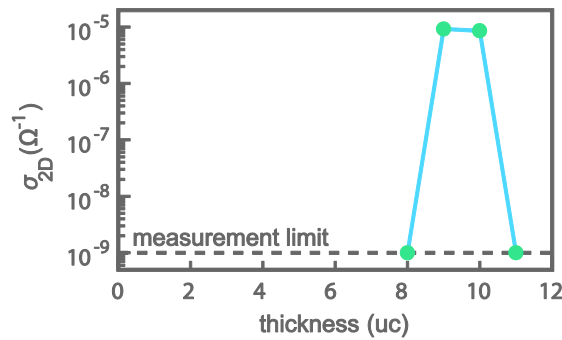

Figure 5.3: The conductivity at room temperature for LAO/STO(111) interfaces with 8, 9, 10 & 11 uc thick LAO films grown at 770 °C. The observed critical thickness for the conducting LAO/STO(111) interface is 9 uc. The conductivity of the heterostructures with 8 uc and 11 uc LAO film are both below the measurement limit.

In order to test the previous calculations, the conductivity of LAO/STO(111) heterostructures is measured for several film thicknesses to experimentally determined the critical thickness. The samples are prepared with LAO film thicknesses of 8, 9, 10 and 11 uc (sample C1, C2, C3 and C4) and the thin films are all grown at 770 °C. Figure 5.3 displays the measured conductivity at the LAO/STO(111) interface as a function of the film thickness at room temperature. The measurement limit is determined by specific characteristics of the measurement setup. The maximum measurable voltage is 2 V and a minimum applied current is 1 nA. Hence, the minimum conductivity which can be measured is 10^{-9} Ω according to Ohm's law. The 8 uc film is observed to be below the measurement limit indicating that the interface is in an insulating state. Changing the layer thickness from 8 uc to 9 uc, the system undergoes a insulator-to-metal transition indicating that the critical film thickness for conduction at this interface is 9 uc, in correspondence with literature.[5] The conductivity for the 9 uc LAO film thickness is $\sim 10^{-5}$ Ω^{-1}. The 10 uc film shows a small decrease in conductivity, whereas the conductivity of the sample with an 11 uc film is below the measurement limit, indicating an insulating interface. This is in contradiction with previous reports[5], where a decrease in conductivity is observed but the interface remains conducting.

Appendix C.2 presents the AFM images taken before and after deposition of the 11 uc thin film as well as the RHEED oscillations of the sample (sample C4). The difference in the measured conductivity at the interface of sample C4 and the conductivity observed in previous studies can be induced by several factors. The STO(111) substrate can be of poor quality, meaning the cutting, polishing and/or termination is not performed properly, inducing defects in the heterostructure. Before deposition of the film, a step-and-terrace structure at the surface of sample C4 can be distinguished in the AFM image, but the terraces are rough. Secondly, the difference can be contributed to the thin film growth. No RHEED oscillations are observed during the PLD growth of the LAO film. The thickness of the thin film is determined by the number of pulses per unit cell which can be extracted from growth of previous LAO films on STO(111) substrates. The AFM images after deposition show an increased roughness of the step-and-terrace structure, indicating that the thin film growth is the most probable cause for the insulating character of the interface of sample C4. Other factors that can reduce the conductance are the PMMA and Argon milling during the processing of the sample. The PMMA (used to create a mask) can degrade with time. If the spinning of the PMMA is performed several days before performing e-beam lithography and/or Argon milling, the performance of the mask can change. Thereafter, it can be that the Argon milling, which defines the electrical contacts, is not sufficient such that the contacts will not or poorly be in contact with the 2DES. A new sample should be fabricated and measured to determine the actual conductance of LAO/STO heterostructures with an 11 uc thick LAO film.

5.2 Sheet resistivity

The sheet resistivity of three different samples (C2, C3 and D2) is measured during the cool down from room temperature to 1.6 K. Figure 5.4a depicts the temperature dependence of the sheet resistivity at the LAO/STO(111) interface for LAO films grown at 770 °C with thicknesses of 9 and 10 uc (sample C2 and sample C3, respectively). Sample C2 exhibits metallic behaviour over the entire temperature range while sample C3 shows metallic behaviour at high temperatures and a low temperature resistivity upturn. The overall resistivity of the 10 uc film is larger than the resistivity of

the 9 uc film, in agreement with previous research that observed a decrease in conductance after reaching the critical film thickness.[5] For the sample grown at a temperature of 840 °C with a 9 uc thick film (sample D2), the resistivity shows metallic behaviour over the whole range of temperatures during the cool down.

The shape of the resistivity curve of sample D2 is similar to the curve of sample C2 while the magnitude of the resistivity is lower. Thin films grown at lower temperatures have a reduced thermal energy, i.e., diffusivity during the growth. This results in an increased amount of inhomogeneities in the heterostructure, inducing an increase in the resistivity. However, in the (100) orientation the opposite is observed. The interface with the lowest growth temperature exhibit the highest electron mobility.[89] We will come back to this point one the mobility is determined. Furthermore, Herranz et al.[5] showed a resistivity at the LAO/STO(111) interface for different film thicknesses grown at 850 °C comparable to the sheet resistivity of our samples.
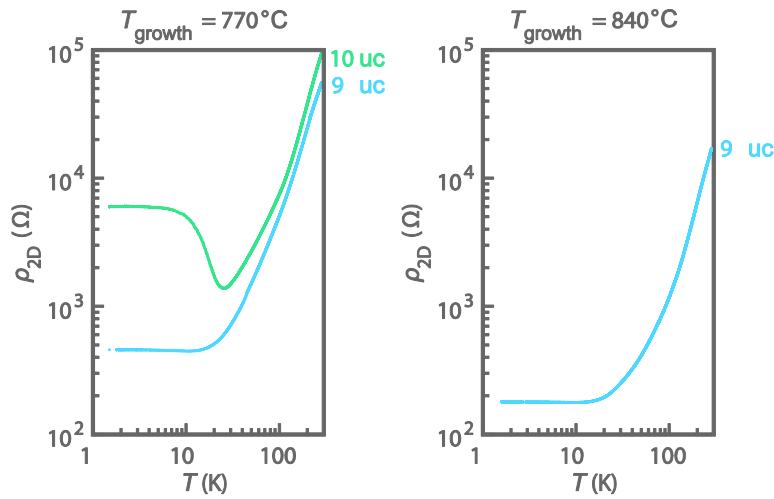

Figure 5.4: The temperature dependence of the sheet resistance at LAO/STO(111) interfaces patterned with Hall bars. a) Heterostructures with an LAO film thickness of 9 (sample C2) & 10 uc (sample C3), grown at 770 °C. b) A heterostructure with an LAO film thickness of 9 uc (sample D2), grown at 840 °C.

In general, the temperature dependent resistivity is given by Matthiessen's rule, $\rho(T) = \rho_0 + \rho_{BG}(T)$ which takes into account the temperature independent residual resistivity, ρ_0 and the resistivity caused by the electron-phonon scattering, ρ_{BG}. The latter is described by the Bloch-Gruneisen law:

$$\rho_{BG} = \beta_{BG} T \left(\frac{T}{\theta_D}\right)^4 \int_0^{T/\theta_D} \frac{x^5 dx}{(e^x-1)(1-e^{-x})}, \tag{5.5}$$

where β_{BG} is a material-dependent electron-phonon coupling parameter and θ_D is the Debye temperature.[90]

At low temperatures, the resistivity at the interface of sample C3 shows an upturn. This upturn can be related to electron localization (electron-electron scattering) or the Kondo effect (magnetic impurity scattering). The saturation of the upturn is a strong indication that the loss of conductance is due to magnetic impurity scattering. The relation for the sheet resistivity, taking into account all the interaction terms results in:

$$\rho_{2D} = \rho_0 + AT^2 + \rho_k(T) + \rho_{BG}(T), \tag{5.6}$$

where the T^2 contribution is resulting from electron-electron scattering and the Kondo term is:

$$\rho_k = C \left(1 - \frac{\ln(T/T_k)}{\ln(T/T_k)^2 + \pi^2 S(S+1)}\right),$$ (5.7)

with T_k is the effective Kondo temperature and S is the effective spin of the magnetic scatters.[91]

Figure 5.5 shows again the temperature dependent sheet resistivity for sample C3. The red line presents the best fit of equation 5.6 with the experimental data. At high temperature the fit is in good agreement with the experimental data, while at the low temperatures slight deviations are observed. The fitting parameters are displayed in figure 5.5, Table 2. The Debye temperature is a measure of the energy necessary to excited all phonon modes. According to this fit, the heterostructures with a 10 uc film needs an thermal energy $\sim 1390 k_B$ to excited the all phonon vibrations where k_B is the Boltzmann constant. Furthermore, the electron-electron scattering, given by AT^2, is predicted to give a small contribution to the total resistivity whereas the magnetic impurity scattering, given by the Kondo term, is predicted to result a more significant contribution. The Kondo temperature, which defines the limiting energy scale for which the Kondo theory holds, is similar to Kondo temperatures determined before in titanates.[91,92]

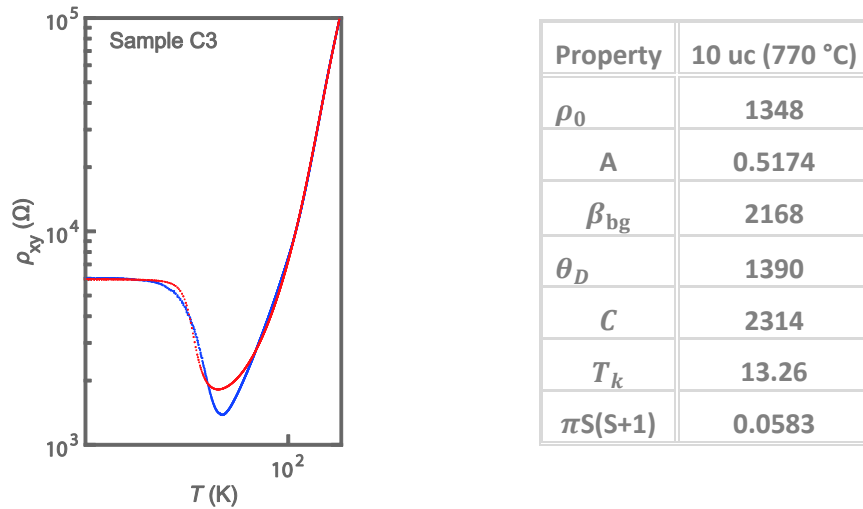| Property	10 uc (770 °C)
ρ_0	1348
A	0.5174
β_{bg}	2168
θ_D	1390
C	2314
T_k	13.26
$\pi S(S+1)$	0.0583

Figure 5.5: The sheet resistivity as a function of the temperature for sample C3 showing a low temperature resistivity upturn. The red line present the fit of the experimental data to the total sheet resistivity given by equation 5.6. Table 2 presents the parameters for the fitting of the sheet resistivity (equation 4.5) for sample C3 (10 uc with growth temperature 770 °C).

5.3 Temperature dependent magnetotransport

In this section, we study the magnetotransport at different temperature with an out-of-plane applied magnetic field for two different samples, namely sample C3 (10 uc, 770 °C) and sample D2 (9 uc, 840 °C) (for more details see appendix C.2). The Hall effect measurements provide information about the temperature dependence of the sheet carrier density and the electron mobility while the magnetoresistance reveals the presence of weak anti-localisation.

Figure 5.6 shows the two-dimensional Hall resistivity (equation 3.4) versus the magnetic field at different temperatures for sample C3 and sample D2. The Hall resistivity is anti-symmetrized in order to reduce the influence of inhomogeneities. The applied magnetic field, varying from -5 T to +5 T,

results in a linear response of the Hall resistivity at all temperatures considered, indicating the presence of one type of charge carrier in the system. The magnitude of the resistivity in sample C3 (10 uc) with an applied field of ± 5 T at 1.5 K is twice as large as the magnitude of the resistivity in sample D2 (9 uc). In LAO/STO(111) heterostructures, the interface conductance peaks at 9 uc (i.e., the critical thickness) and decays rapidly with increasing thickness, indicating that the film thickness can be origin for the difference in sheet resistivity for the two samples under investigation.[5] Furthermore, sample C3 is the sample with the lower growth temperature resulting in a higher density of defects, increasing the resistivity.
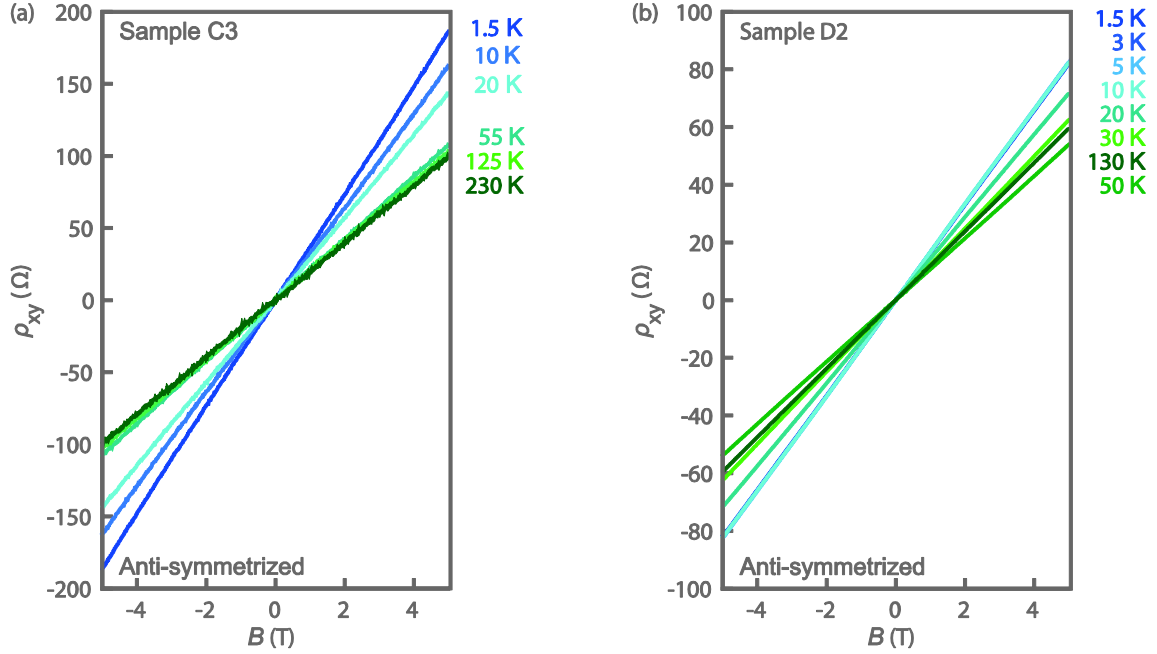

Figure 5.6: The temperature dependent Hall resistivity as a function an out-of-plane applied magnetic field. The applied magnetic field varies from -5 T to 5 T. a) Sample C3 grown at 770 °C with a 10 uc thick film. b) Sample D2 grown at 840 °C with a 9 uc thick film.

The slope of the Hall resistivity and applied magnetic field defines the Hall coefficient (equation 2.5). Subsequently, the sheet carrier density can be determined using $n_{2D} = -1/eR_H$ (equation 2.6). Figure 5.7a shows the evolution of the sheet carrier density for sample C3 and sample D2 where the Hall coefficients are extracted from the Hall measurement presented in figure 5.6. Both samples show a monotonous decrease in sheet carrier density while decreasing the temperature to 1.5 K. Sample C3 has an average sheet carrier density, $n_{2D} \sim 2 \times 10^{13}$ cm^{-2} whereas the average sheet carrier density of sample D2 is $n_{2D} \sim 4.5 \times 10^{13}$ cm^{-2}, both are comparable to sheet carrier densities previously reported in {100} and {110}-oriented LAO/STO systems.[1,5] The overall carrier density of sample C3 is lower than the carrier density of sample D2. Fête et al.[89] performed a study on the influence of the PLD growth temperature on the electronic properties in the LAO/STO(100) system. They observed that samples grown at 650 °C obtain a lower sheet carrier density than samples grown at 800 °C and 900 °C, i.e., higher growth temperature yield higher sheet carrier density. The measured sheet carrier density presented in figure 5.7a shows the same behaviour.

The electron mobility can be obtained from the sheet carrier density and the sheet resistivity. Since the systems contains one type of mobile carriers equation 2.7, i.e., $\mu = 1/n_{2D}e\rho_{xy}$, can be used to determine the electron mobility. Figure 5.7b shows the measured evolution of the electron mobility with temperature. An increase in the electron mobility is observed upon cooling. This behaviour is

expected because at high temperatures the electron scattering is dominated by acoustical phonon vibrations whereas at lower temperatures the phonon vibration freeze out such that the impurity and charged defect scattering become important. The electron mobility dominated by acoustical phonon scattering is proportional to $T^{-3/2}$.[93] The red lines in figure 5.7b give the fit ($\mu \propto T^{\alpha}$) in the high temperature range for both samples. The exponents are α_{C3} = -1.66 and α_{D2} = -1.38 for sample C3 and sample D2, respectively. These values are reasonably close to the theoretical value.

At low temperatures, the mobility saturates at $\mu_{C3} = 670$ cm^2/Vs and $\mu_{D2} = 960$ cm^2/Vs for sample C3 and sample D2, respectively. Fête et al.[89] observe an electron mobility which changes from 600 to 8000 cm^2/Vs as the growth temperature is reduced from 900 to 650 °C at 1.5 K, , i.e., the lowest growth temperature induces the highest electron mobility. This disagrees with our observations. However, Thiel et al.[94] studied the influence of dislocations cores on the electrical transport properties of the 2DES in LAO/STO(100) heterostructures and discussed that the electron mobility is mostly affected by imperfections at the interface rather than the sheet carrier density. Their experiments reveal that a reduction of the dislocation density will enhance the conductivity and the mobility of the 2DES. The number of dislocations is related to the microstructural quality of the STO substrates and to the misfit dislocations caused by strain relaxation. If the quality of the samples measured by Fete et al.[89] is significantly different from the quality of the samples under investigation in this study, different behaviour for the electron mobility can be observed.
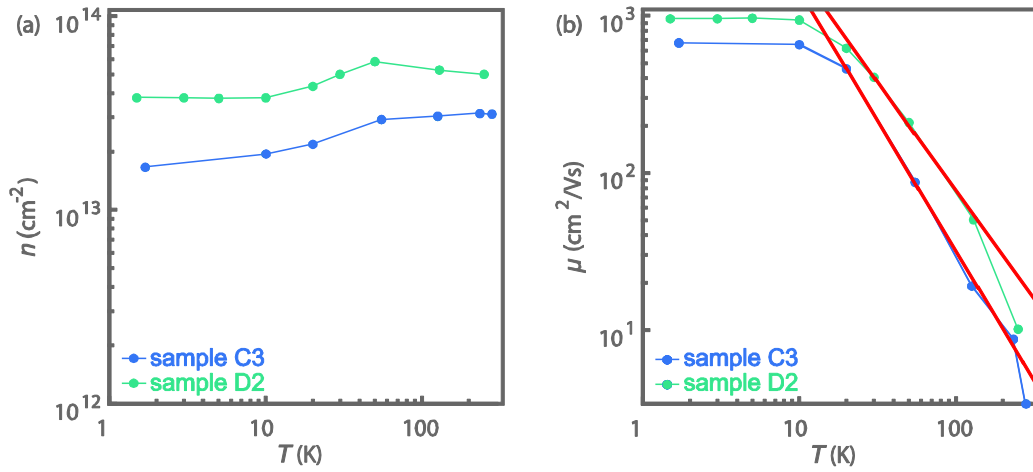

Figure 5.7: a) The sheet carrier density (n_{2D}) as a function of temperature extracted from the Hall measurements presented in figure 5.6 for sample C3 and sample D2. b) The temperature dependence of the electron mobility (μ) for sample C3 and sample D2. The red line presented the T^{α} fit with α_{C3}= -1.66 and α_{D2}= -1.38, indicating the freeze out of acoustic phonon vibrations.

The magnetoresistance is defined as $MR(B) = (\rho_{xx} - \rho_0)/\rho_0$ and the sheet resistivity is given by $\rho_{xx}(B) = \rho_0(1 + \omega_c^2\tau^2) = \rho_0(1 + B^2\mu^2)$ where the latter results from $\omega_c = eB/m^*$ and $\tau = \mu m^*/e$ (see section 2.3.2). Figure 5.8 shows the response of the symmetrized magnetoresistance for an out-of-plane applied magnetic field at different temperatures for sample C3 and sample D2. The different noise level result from the measurement modes, the measurements on sample C3 are performed in DC mode whereas the measurements on sample D2 are obtained in AC mode.

We have seen that the mobility at high temperatures is supressed by the acoustical phonon scattering (see figure 5.7b), which is reflected in the magnetoresistance. At high temperatures, the electron mobility is very small such that $B^2\mu^2 \ll 1$, resulting in a constant sheet resistivity (ρ_0) and

the magnetoresistance is negligible. Figure 5.8 shows that the magnetoresistance tends to zero above 55 K and 30 K for sample C3 and sample D2, respectively. As the temperature is lowered, the electron mobility increases hence the $B^2\mu^2$-term is not negligible anymore and the resulting magnetoresistance is non-zero. For a given magnetic field, a gradual increase in the magnitude of the magnetoresistance is observed due to the increasing mobility, e.g. considering the applied magnetic field of 3 T, the magnetoresistance in both samples is increased when the temperature is reduced. At the lowest temperature, the mobility saturates (see figure 5.7b) and a B^2-dependence become apparent as can be clearly observed for temperatures below 20 K. Furthermore, a positive contribution to the B^2-dependence becomes prominent at small magnetic fields. The inset of figure 5.8 displays the magnetoresistance of sample D2 from -5 to 5 T at 1.5 K. The red line is the fit of the B^2-component at the higher magnetic fields, where the positive deviation to the B^2-dependence at lowest applied magnetic fields can be distinguished. This contribution is due to weak anti-localization which will be discussed in more detail in the next section when the gate tunability of the magnetoresistance in the 2DES is considered.
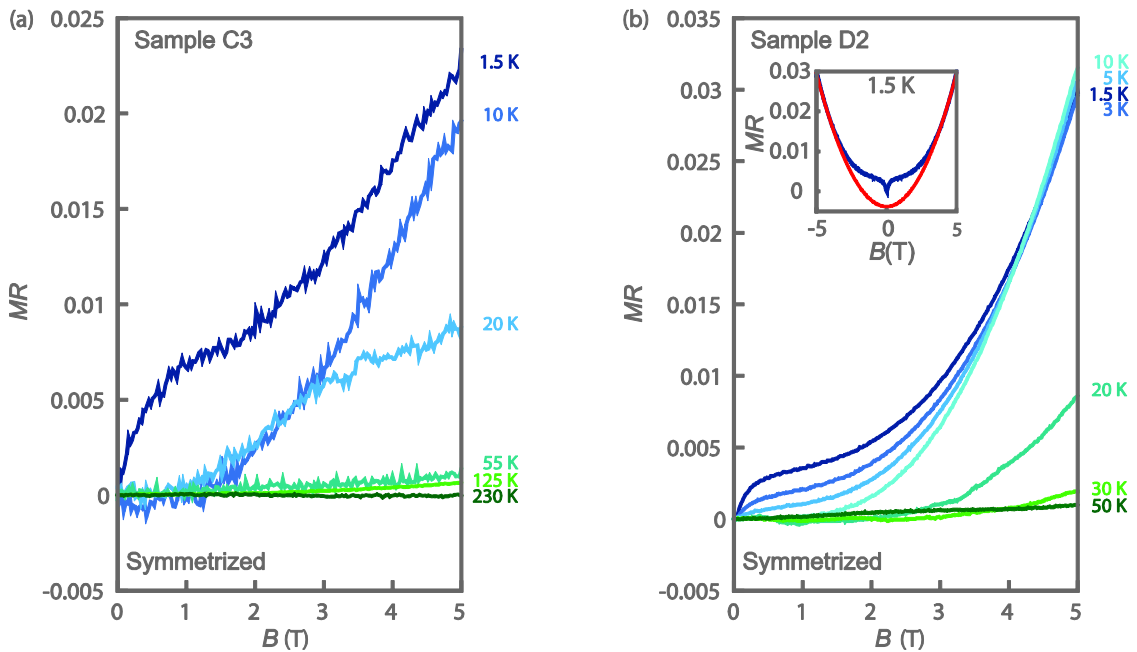

Figure 5.8: The temperature dependence of the out-of plane magnetotransport. a) The magnetoresistance as a function of the magnetic field for sample C3 with the temperature ranging from 1.5 K to 230 K. b) The evolution of the magnetoresistance with magnetic field for sample D2 while the temperature ranging from 1.5 K to 50 K. The inset displays the MR from -5 to 5 T at 1.5 K with the red line emphasizing the B2-dependence at the highest magnetic field and the positive contribution to the B2-dependence at low magnetic field, indicating weak anti-localisation.

5.4 Gate tunability of the 2DES

The field-effect is a powerful tool that has enabled the investigation of many exotic properties of LAO/STO heterostructures. Without changing the interface structure, an effective control of the electronic transport properties of the interface can be achieved. The most common technique is a back-gate configuration. In this geometry, an electrode is placed at the back of the STO substrate, taking advantage of the high dielectric constant of the STO. This system can be considered as a parallel plate capacitor where the plates are the back-gate and the 2DES. The measurements conducted in this section are performed at 1.5 K where the dielectric constant of STO is ~20000.[95] The transport properties of the LAO/STO heterostructures develop a large hysteresis during the first

gate voltage sweep. Therefore, a sweep to the maximum back-gate voltage is performed before studying the influence of different gate voltages on the electronic transport properties. The samples under investigation are sample C3 (10 uc, 770 °C) and sample D2 (9 uc, 840 °C) (more growth details are presented in appendix C.2). The magnetic field during the experiments is applied out-of-plane with respect to the conducting interface.

5.4.1 Zero-field sheet resistivity

Figure 5.9 shows the zero-field sheet resistivity as a function of the different applied back-gate voltages for sample C3 and sample D2, measured at 1.5 K. Both samples display a decrease in resistivity upon an increasingly larger positive voltage on the back-gate. In other words, accumulation of charge carriers due to a positive back-gate voltages (in the range of voltages considered) enhances the conductance at the interface of these samples. An increase of the gate voltage from 4 V to 10 V in sample C3 and from 5 V to 45 V in sample D2 results in a modulation of 850 Ω to 300 Ω and 680 Ω to 100 Ω, respectively. Note that the zero-field sheet resistivity does not saturate indicating that the maximum electrostatic doping has not been achieved. Transport measurements with higher applied back-gate voltages can provide the maximum attainable conductivity.
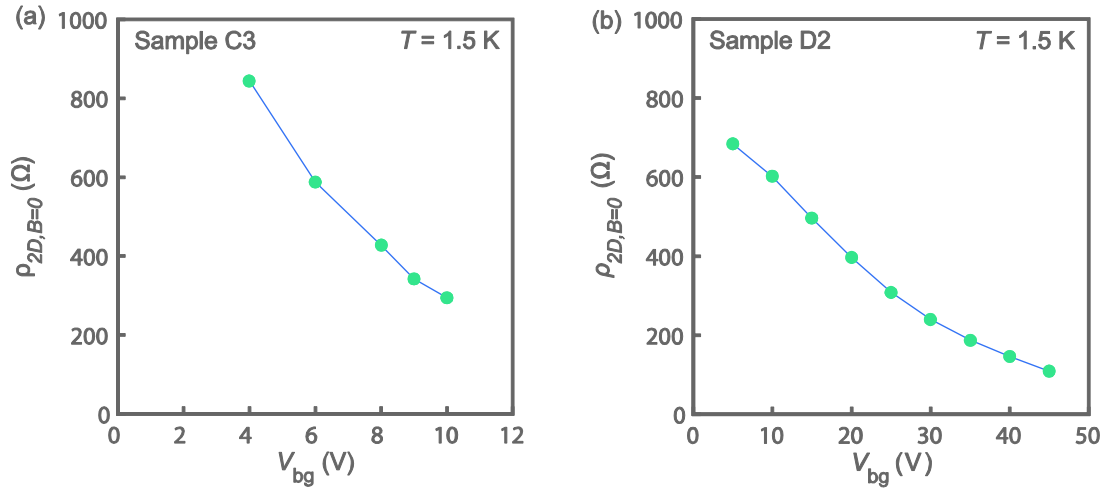

Figure 5.9: The evolution of the zero-field sheet resistivity with varying back gate voltage at 1.5 K for a) Sample C3 with a back-gate voltage ranging from 4 to 10 V and b) Sample D2 with a back-gate voltage varying from 5 to 45 V.

A similar modulation of sheet resistance is achieved while the range of applied back-gate voltages is noticeably smaller in sample C3 with respect to sample D2. The dimension of the Hall bar channel of sample D2 is 100 x 200 μm whereas the dimension of the Hall bar channel of sample C3 is 25 x 50 μm. The capacitance between the back gate and the 2DES is influences influenced by the size of the channel while the capacitance has a direct dependence on the surface area of the conducting plates, i.e., $C = \frac{\varepsilon_0 \varepsilon_r A}{d}$. This indicates that an increase in the interface area of the Hall bar channel results in a larger capacitance. The gate voltage is related to the capacitance as: $C = q/V_{bg}$ such that for a larger area, a lower gate voltage has to be applied to achieve the same charge, i.e., for larger Hall bar channels a lower gate voltage is needed to achieve the same conductivity in the channel by electrostatic doping. This parallel plate capacitor model predicts the reverse of what is observed in our resistivity measurements.

Rakhmilevitch et al.[96] studied, with electron transport measurements and electrostatic model calculations, the effect of the dimension of the Hall bar channel on the capacitance when applying a back-gate voltage. They observed that when the distance between the back gate and the 2DES is significantly larger as the size of the Hall bar, the geometrical capacitance dominates, resulting in a substantially different capacitance as predicted by the parallel plate capacitor model. In the case that the geometrical capacitance dominates, the capacitance is inversely proportional to the width of the Hall bar channel. This indicate that a stronger electric field effect is induced in narrow Hall bar channels which is in agreement with the results presented in figure 5.9, knowing that the channel width of sample C2 is four times smaller than the channel width of sample D2.

5.4.2 Hall effect

In order to study the influence of the back-gate in more detail, Hall measurements are performed. Figure 5.10a displays the Hall effect of sample C3 for different back-gate voltages at 1.5 K. The Hall resistivity is linear for all applied back-gate voltages in the magnetic field range from -5 T to 5 T, indicating the presence of one type of carrier, hence electrostatic doping with 10 V does not populate a higher energy conduction bands. Figure 5.10b shows the Hall effect of sample D2 for a back-gate voltage range of 15 to 45 V and an applied magnetic field up to 10 T. Although, the applied back-gate voltage is higher than the back-gate voltage applied to sample C3, figure 5.9 shows that this range of voltages result in a similar modulation of the zero-state resistivity. Now back to sample D2, from the lowest back-gate voltage up to 35 V, the Hall resistivity is linear with a varying magnetic field. Above 35 V, the resistivity demonstrates a change in slope at high magnetic field, indicating multi-carrier transport.
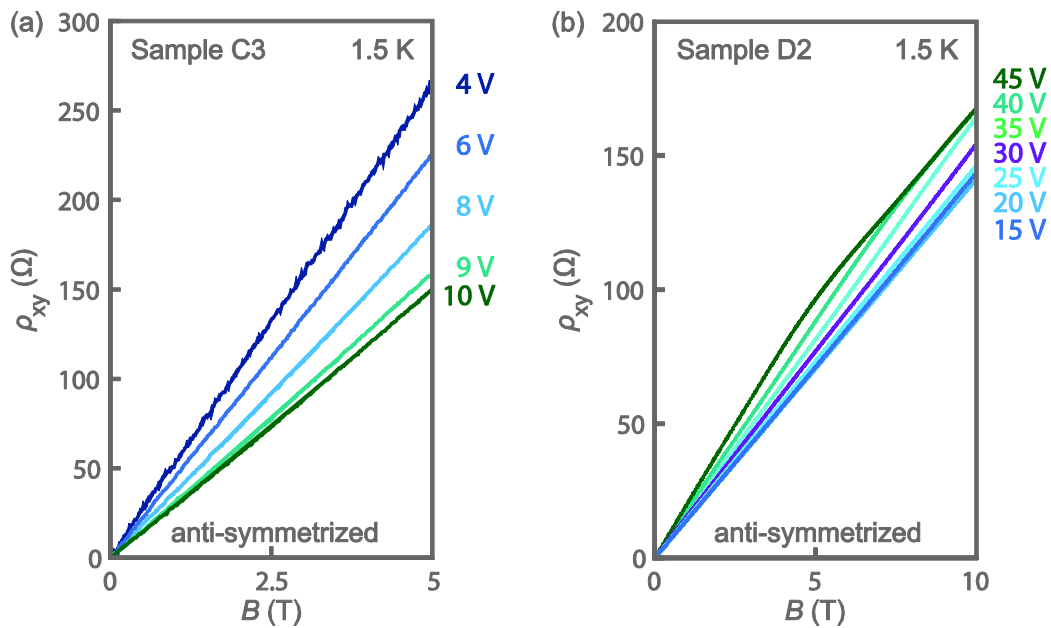

Figure 5.10: The anti-symmetrized Hall resistivity as a function of the applied magnetic field for different back-gate voltages at 1.5 K with a) sample C3 (grown at 770 °C with a 10 uc thick film) studied in the back-gate voltage range of 4 V to 10 V whereas b) sample D2 (grown at 840 °C with a 9 uc thick film) is measured with the applied back-gate voltage ranging from 15 V to 45 V.

First, we will consider the linear Hall effect, where the slope determines the sheet carrier density via equation 2.6. Figure 5.11a shows the evolution of the sheet carrier density and the electron mobility with the back-gate voltage ranging from 4 V to 10 V for sample C3. The sheet carrier density is fairly constant, namely 1.5×10^{13} electrons/cm^2 whereas the mobility displays an increase from 700 to 1000 cm^2/Vs. Figure 5.11b displays the sheet carrier density for sample D2 in the linear Hall effect regime,

i.e., in the range of back-gate voltages from 15 V to 35 V. In this voltage range, the inverse of the Hall resistance shows a slight decrease with increasing voltage. Furthermore, the overall sheet carrier density in sample D2 is higher than the ones obtained for sample C3, as observed for the temperature dependent sheet carrier density presented in figure 5.7a. The electron mobility is determined with use of the measured zero-field resistivity and the sheet carrier density (equation 2.7) and displays a changes from 200 cm^2/Vs to 880 cm^2/Vs when increasing the back-gate voltage from 15 V to 35 V.

Liu et al.[97] performed magnetotransport measurements on LAO/STO(100) heterostructure modulating the electronic transport properties with a back-gate and a side-gate configurations. They observed that the back-gate strongly modifies the electron mobility whereas the sheet carrier density remains almost unaffected while the top-gate mainly varies the sheet carrier density. According to them, the increase in electron mobility suggests that a positive back-gate voltage results in a less confined 2DES due to (1) electrons which are trapped more deeply in the STO substrate and (2) the population of higher conduction bands allows additional states (d_{xz}/d_{yz}) to become accessible and play a more prominent role in the electronic transport. This behaviour of the carrier density and mobility at the interface of sample C3 is not observed for the magnetic fields and back-gate voltages considered. However, sample D2 displays, in line with the results of Liu et al.[97], a slightly decreasing sheet carrier density and an significant increase in carrier mobility with an increasing back-gate voltage.
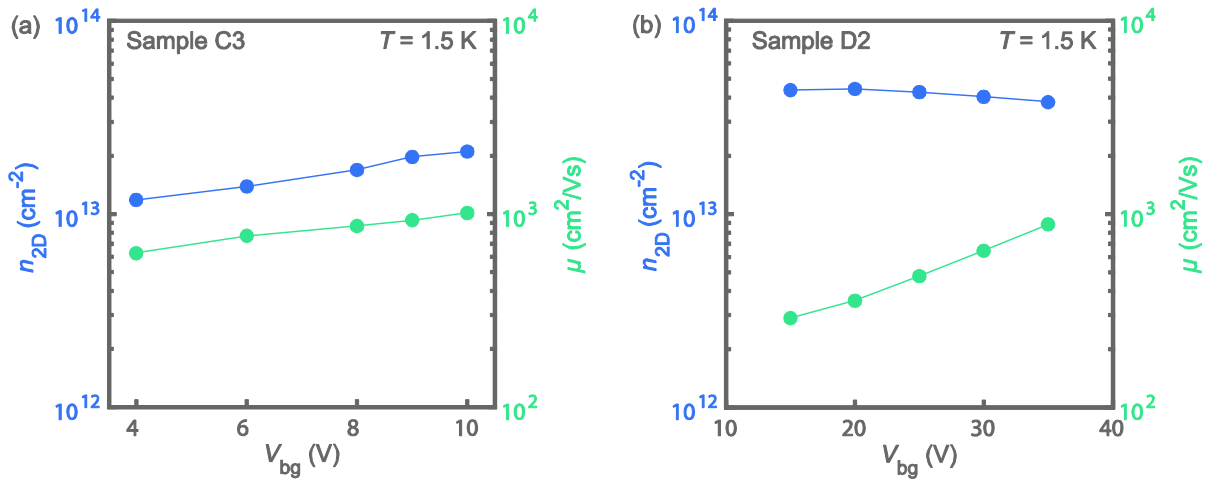

Figure 5.11: The sheet carrier density and the electron mobility for different applied back gate voltages at 1.5 K for a) sample C3 and b) sample D2

Coming back to the non-linear Hall effect observed in sample D2 at back-gate voltages 40 V and 45 V. The shape of the non-linearity in the Hall effect can be explained by a two carrier transport model, which considers an increase in the back-gate voltage raises the Fermi level, resulting in the occupation of a higher energy conduction band by a second type of carrier which consequently contribute to the electronic transport. The two-band model gives the resistivity as a function of magnetic field,

$$\rho_{xy} = \frac{(\sigma_{2D,1}^0 \mu_1 + \sigma_{2D,2}^0 \mu_2) + (\sigma_{2D,1}^0 \mu_2 + \sigma_{2D,2}^0 \mu_1)\mu_1\mu_2 B^2}{(\sigma_{2D,1}^0 + \sigma_{2D,2}^0)^2 + (\sigma_{2D,1}^0 \mu_2 + \sigma_{2D,2}^0 \mu_1)^2 B^2} B \tag{5.7}$$

where μ is the mobility and $\sigma_{2D}^0 = ne\mu$ is the zero-field conductivity.[42] Figure 5.12a shows the best fit for the two-band model with the carrier densities $n_1 = 1.73 \times 10^{13}$ cm^{-2} and $n_2 = 3.22 \times 10^{13}$ cm^{-2} and the carrier mobilities $\mu_1 = 2444$ cm^2/Vs and $\mu_2 = 580$ cm^2/Vs, indicating a high electron mobility in the low energy band whereas the second band obtain a lower electron mobility but a higher carrier density.
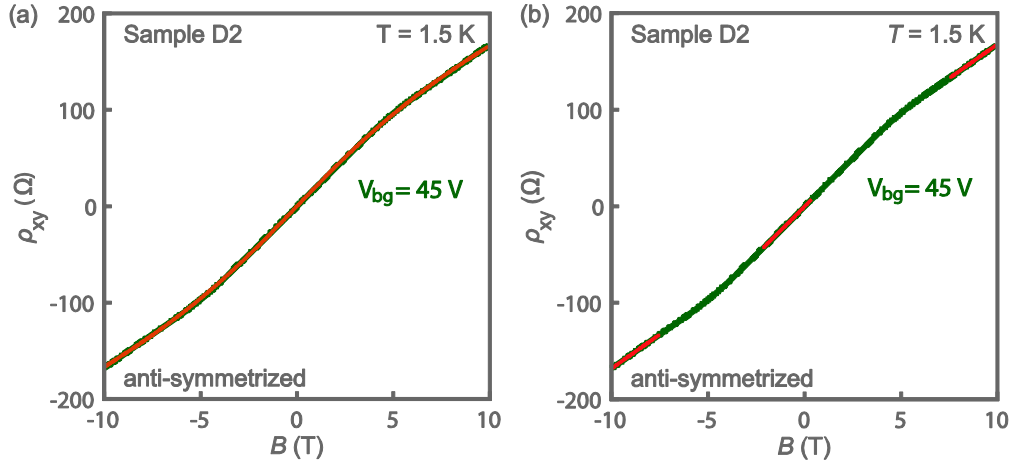

Figure 5.12: The Hall resistivity with varying magnetic field for a back-gate voltage of 45 V at a temperature of 1.5 K is presented by the blue line. a) The red line represents the fit to the two-band model for the mobility being $\mu_1 = 2444$ cm^2/Vs and $\mu_2 = 580$ cm^2/Vs and the carrier density $n_1 = 1.73 \times 1013$ cm^{-2} and $n_2 = 3.22 \times 1013$ cm^{-2}. b) The red line presents the linear fit for high and low magnetic fields where the slope, i.e., the Hall coefficient, gives an estimate of the sheet carrier density for the high mobility carriers (n_1) and total carriers (n_{tot}), respectively.

However, Joshua et al.[98] discuss the assumption of the two-carrier transport model that the carrier density and electron mobility are independent of the magnetic field to be in inaccurate because their magnetotransport measurements on LAO/STO(100) heterostructures show differently. Therefore, they state that the two-band model is inadequate for extracting the carrier mobility, but can reliably determine the carrier densities. The model they introduce considers the slope at zero magnetic field to determine by the sheet carrier density (n_1) in the low energy conduction band while the slope at high magnetic gives the total sheet carrier density (n_{tot}) of both conduction bands contributing to the electronic conduction. Figure 5.12b shows the Hall effect at an applied back-gate voltage of 45 V where linear fits for the low and high magnetic field region are indicated by the red lines. The slope of these red lines, i.e., the Hall coefficient (R_H), determines the sheet carrier density as $n_1 = \dfrac{1}{eR_H(B=0)}$ and $n_{tot} = \dfrac{1}{eR_H(B=|10|)}$.

Figure 5.13 shows the sheet carrier density for the single band conduction (n_1) as well as the carrier density for the total band conduction (n_{tot}) in the range of the back-gate voltages from 15 V to 45 V. At the lowest back-gate voltages (15 V to 35 V), the single band carrier density and the total band carrier density are similar while at the applied back-gate voltage of 40 V and 45 V, the total carrier density displays a clear deviation from the single band carrier density. This indicates an additional contribution from a different type(s) of carrier(s) to the carrier density. The evolution of the two types of carrier densities with the back-gate voltage is comparable to the one observed in previous report.[98] However, Joshua et al.[98] observed a saturation of the carrier density for the single band conduction (n_1) when reaching the so-called critical density which is defined as the carrier density where the total carrier density starts deviating from the single band carrier density. Figure 5.13

shows that the critical carrier density, $n_c \approx 3.73 \times 10^{13}$ cm^{-2}. Additionally, it is observed that the single band carrier density does not saturate after the critical current density is reached, indicating that the effective contribution to the electron transport of the carriers in the lowest conduction band is continuously reduced. The sheet carrier densities in the lowest conduction band is measured to be $n_1 = 1.73 \times 10^{13}$ cm^{-2} for the two-band model and $n_1 = 3.1 \times 10^{13}$ cm^{-2} for the model introduced by Joshua et al.[98]. This indicates that the two methods clearly result in different sheet carrier densities hence predict different behaviour of the electronic transport.
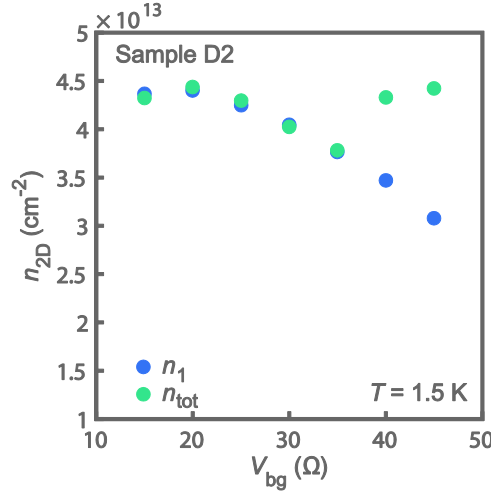

Figure 5.13: The sheet carrier density n_1, and n_{tot}, where n_1 and n_{tot} are obtained from the Hall coefficient around B = 0 T and B = 10 T, respectively (as presented in figure 5.12b).

The change in the sheet carrier density and the carrier mobility with the back-gate can be related to the band structure. The interfacial electrons of LAO/STO heterostructures, reside in the t_{2g} conduction bands of STO. In bulk STO, the three t_{2g} conduction bands are degenerate at the Γ-point in the high symmetry phase. However, the low temperature tetragonal distortion and quantum confinement result in non-degenerate conductions bands at the Γ-point where the d_{yz} and d_{xy} bands form a low energy doublet while the d_{xy} band is higher in energy (see section 2.4.1).[21] Therefore, non-ohmic behaviour is expected in such a heterostructure, when increasing the Fermi level by means of a gate voltage. At low gate voltages, i.e., low carrier density, all the conduction electrons reside in the d_{xy} band while an increase in the carrier density with a gate voltage can populate the d_{xz} and d_{yz} bands, introducing a different type of carriers into the system.[98] The band structure of LAO/STO(111) is relative unexplored. However, Rödel et al.[24] performed ARPES measurement on cleaved STO(111) substrates where a two-dimensional electron system is formed at the interface and remains as long as the STO is kept in vacuum such that reconstruction is prevented. Because the band structure of the 2DES in LAO/STO is dominated by the t_{2g} conduction bands of STO an interpretation for the band structure of LAO/STO(111) can be made. Rödel et al.[24] measured within their measurement limit, the band structure of LAO/STO(111) to be degenerate, indicating that higher energy t_{2g} conduction bands are not accessible for the electron such that the origin of the non-linear Hall effect is unclear. However, calculations of the band dispersion along the high-symmetry directions, K-Γ-K and M-Γ-M (see figure 2.6f), of the LAO/STO(111) interface performed by Walker et al.[25] show the presence of a non-degenerate conduction bands. The band calculations display an energy gap ~10 meV which creates a possibility of populating a second conduction band with a different symmetry, resulting in the non-linearity of the Hall resistivity.

5.4.3 Gate tunable magnetoresistance

In this section, the evolution of the magnetoresistance for different levels of electrostatic doping is studied in sample C3 (9 uc, T_g =770 °C) and sample D2 (10 uc, T_g = 840 °C). Figure 5.14 shows the magnetoresistance as a function of magnetic field, recorded at 1.5 K with the back-gate voltage ranging from 4 to 10 V and 10 V to 45 V for sample C3 and sample D2, respectively. The voltage ranges are relatively different however as shown in figure 5.9, they roughly yield the same zero-field resistivity because the electric field modulation of the zero-field resistivity is related to the width of the Hall bar channel (see section 5.4.1).
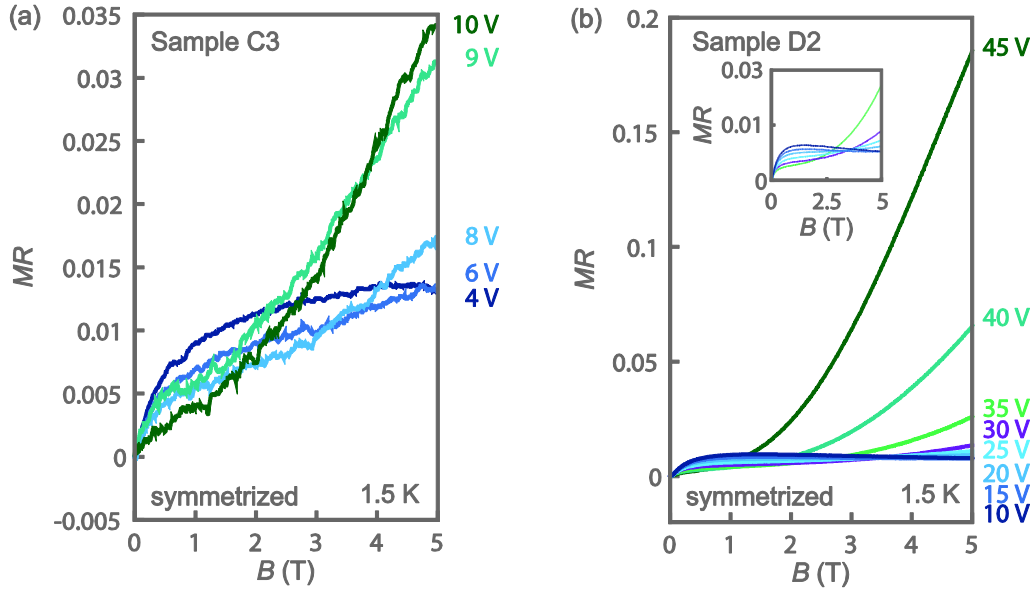

Figure 5.14: The evolution of the magnetotransport as a function the out-of plane magnetic field for different levels of electrostatic doping at LAO/STO(111) interfaces. a) The magnetoresistance for sample C3 with the applied back gate ranging from 4 V to 10 V. b) The magnetoresistance for sample D2 with the applied back gate voltage ranging from 10 V to 45 V. The inset shows a zoom for the back-gate voltage range from 10 V to 35 V.

Sample C3 displays a small positive increase in magnetoresistance of 3.5 % by a variation of the applied magnetic field from 0 T to 5 T at a fixed back-gate voltage of 10 V. Sample D2 shows a positive increase of 18 % for the largest applied back-gate voltage in the magnetic field range from 0 T to 5 T. Even though the back-gate modulation of zero-field sheet resistivity is similar, the difference in the magnitude of the magnetoresistance of sample C3 and sample D2 is relatively large. The inset in figure 5.14 displays the magnetoresistance in sample D2 up to 35 V. In this range of applied back-gate voltages, corresponding to single band conduction, the variation in the magnetoresistance comparable to the one observed in sample C3.

As the back-gate voltage is increased, the evolution of the magnetoresistance changes from a rather flat curve at low back-gate voltages to a distinct B^2-dependence at the highest applied back-gate voltages. The magnetoresistance is defined by $MR \propto B^2 \mu^2$ (see section 5.3). The electric field modulation of the carrier mobility displayed in figure 5.11 shows an increase of magnitude when the back-gate voltage is increased such that the magnetoresistance will go to zero when the mobility approaches zero at small applied back-gate voltages. Upon increase of the applied back-gate voltage, the carrier mobility increases and the classical B^2-component becomes more and more pronounced.

More specifically, in the linear regime of the Hall effect, the evolution of the carrier mobility as a function of the back-gate voltage was determined from the Hall effect (figure 5.11). An increase in the carrier mobility from 627 cm²/Vs to 1010 cm²/Vs is observed when the back-gate voltage in increased from 4 V to 10 V for sample C3 while the carrier mobility in sample D2 displays an increase from 288 cm²/Vs to 880 cm²/Vs when increasing the back-gate voltage from 15 V to 35 V. The electric field modulation of the carrier mobility in the linear regime of the Hall effect in sample C3 and sample D2 is similar, consequently the response of the magnetoresistance as a function of the magnetic field is similar.

However, the magnitude of the magnetoresistance in sample D2 is increased significantly for an applied back-gate voltage of 40 V and 45 V. The Hall effect is observed to be non-linear above 35 V, indicating a contribution of a second type of carrier. According to the two-band model, the mobility in the second conduction band ($\mu_2 = 580$ cm²/Vs) is four times lower than the mobility in the low energy conduction band ($\mu_1 = 2444$ cm²/Vs). The magnetoresistance is inversely proportional to the carrier mobility such that a reduction of the carrier mobility can cause a serious increase in the magnetoresistance. Furthermore, the presence of a second type of carrier hinders the motion of the mobile carriers at the interface due to interaction between the two types of carriers which adds to the increase in the magnetoresistance. Finally, comparing these observations with the results for the magnetoresistance at different temperatures (figure 5.8) shows that the influence of an decreasing temperature or increasing back-gate voltage is observed to result in similar modulation of the magnetoresistance.

Thereafter, figure 5.14 displays a small positive contribution to the B^2-dependence of the magnetoresistance at low magnetic fields, also observed in the temperature magnetoresistance (see inset figure 5.8b). Previous reports ascribe this positive contribution to weak (anti-) localization and spin orbit coupling.[46,99] In two dimensional system, the variation in conductivity ($\Delta\sigma/\sigma_0$ with $\sigma_0 = e^2/\pi h$) caused by an applied magnetic field, due to either weak localization or weak anti-localization can be described by the Maekawa-Fukuyama (MF) formula:

$$\frac{\Delta\sigma}{\sigma_o} = \Psi\left(\frac{H}{H_i + H_{so}}\right) + \frac{1}{2\sqrt{1-\gamma^2}}\Psi\left(\frac{H}{H_i + H_{so}(1 + \sqrt{1-\gamma^2})}\right) - \frac{1}{2\sqrt{1-\gamma^2}}\Psi\left(\frac{H}{H_i + H_{so}\left(1 - \sqrt{1-\gamma^2}\right)}\right)$$

(equation 2.15 in section 2.3.2). This MF-formula gives an estimate of the inelastic and spin orbit characteristic fields, H_i and H_{so}, which are related to the inelastic and spin-orbit scattering times as $\tau_{i,so} = \hbar/4eDH_{i,so}$, where D is the diffusion constant. The spin-orbit scattering time is related to fluctuations in the internal magnetic field after each scattering event and gives information about the spin splitting. The inelastic scattering time is associated with the loss of phase coherence of the wavefunction caused by electron-electron or electron-phonon interactions.

In order to obtain the scattering times, the diffusion constant needs to be determined which is defined as $D = \hbar^2\pi\sigma_{2D}^0/e^2m^*$.[46] The zero-field sheet conductance (σ_{2D}^0) is the inverse of the zero-field resistance presented in figure 5.9 (section 5.4.1). In the MF theory, the effective mass is average effective mass of the carriers at the interface. In the {111} orientation, the effective mass of the charge carriers is strongly anisotropic. Rödel et al.[24] measured the light and heavy bands in the ground state of the 2DES to be degenerate at the Γ-point. The effective masses in the <110> and

<11$\bar{2}$> directions are determined by means of a tight-binding model and the experimentally obtained Fermi surface maps. The resulting effective mass of the light and heavy band in the <110> direction are $m_L^* = 0.27\ m_e$ and $m_H^* = 1.08\ m_e$ and in the <11$\bar{2}$> direction are $m_L^* = 0.33\ m_e$ and $m_H^* = 8.67\ m_e$, respectively, where m_e is the free electron mass. The diffusion constant is determined by an effective mass considering all the conduction bands in the [111] plane. To the best of our knowledge, there is no report on the overall effective mass in the {111} orientation. An attempt to estimate the inelastic and spin-orbit scattering times is made, considering an effective mass of $3m_e$ which is the same as the effective mass used by Caviglia et al.[45] when performing a similar analysis on the LAO/STO (001)-oriented interface.
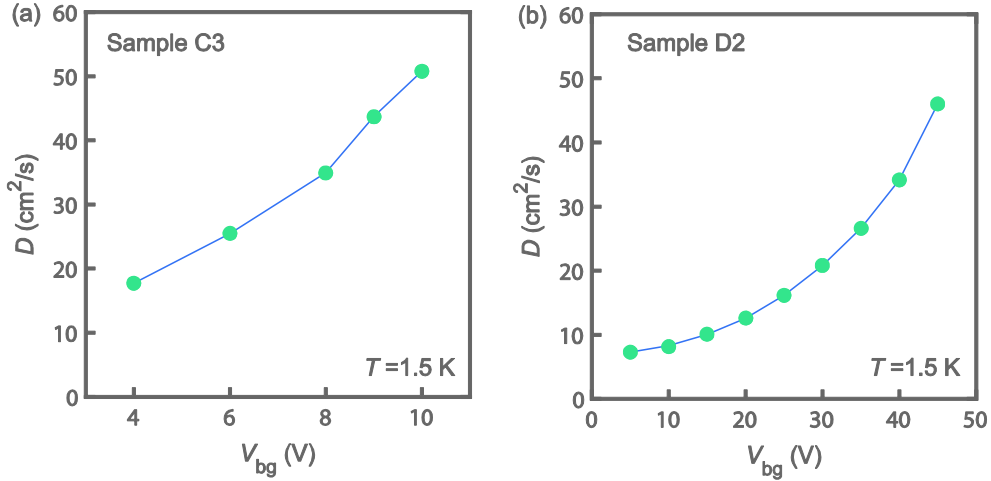

Figure 5.15: The estimated field effect modulation of the diffusion constant at the interface of a) sample C3 and b) sample D2 at 1.5 K. The diffusion constant is determined from equation 2.17 where the effective mass is considered to be $3m_e$ and the zero-field sheet conductivity is extracted from figure 5.9.
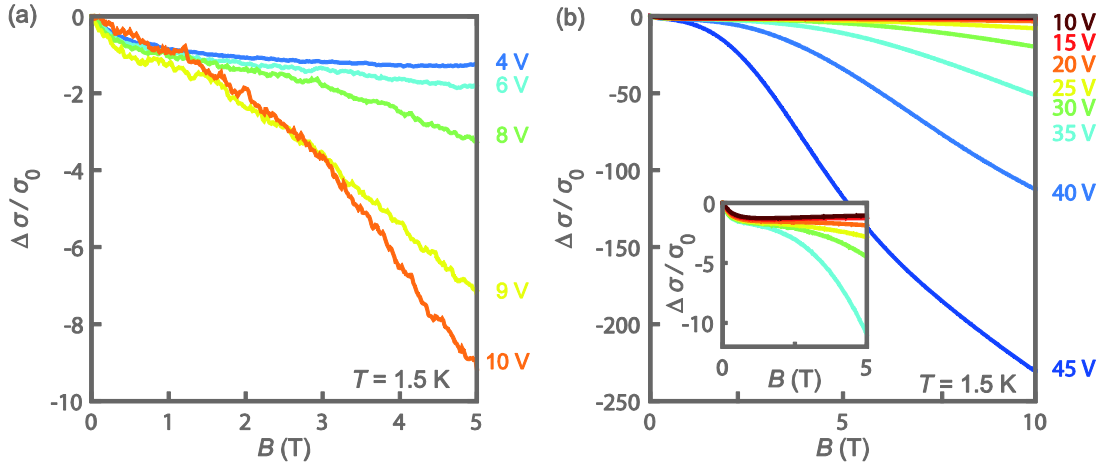

Figure 5.16: The normalized variation of the magnetoconductivity with a varying magnetic field from 0 T to 5 T at different applied back gate voltages at 1.5 K for a) sample C3 and b) sample D2. The inset in b) displays the magnetoconductivity for sample D2 with the applied back-gate voltage range from 10 V to 35 V and a magnetic field up to 5 T, in order to show the similarities in the magnetoconductivity for sample C3 and sample D2.

Figure 5.15a and b displays the evolution of the estimated diffusion constant with an increasing back-gate voltage for sample C3 and sample D2 at 1.5 K. As the diffusion constant is related to the inverse of the zero-field resistance, which in both cases displays a monotonic decrease with an increasing back-gate voltage, the diffusion constant increases monotonically for both samples. Furthermore, the

electric field modulation of the diffusion constants in sample C3 and sample D2 is similar within the back-gate voltages considered.

The experimental magnetoresistance presented in figure 5.14 is converted to a normalized variation in magnetoconductivity such that the data can be related to the MF-formula. Figure 5.16a shows the evolution of the change in conductivity in units of $\sigma_0 = e^2/\pi h$ within the magnetic field range of 0 T to 5 T at different applied gate voltages for sample C3. Figure 5.16b displays the normalized conductivity for sample D2 at different applied back-gate voltages with the magnetic field ranging from 0 T to 10 T. In both cases, a positive applied back-gate voltage induces a negative variation in magnetoconductivity.

The MF-theory is used to fit the experimental data of the magnetoconductance presented in figure 5.16. Since the effective mass is considered to be one or two order of magnitude larger than the corresponding of typical semiconductors, the diffusive regime does not hold in the complete range of magnetic fields.[99] The magnetic field at which the diffusive regime exactly disappears is not precisely known. Therefore three different magnetic field ranges are considered, namely 0 to 0.5 T, 0 to 1.5 T and 0 to 3 T. Figure 5.17a, b and c show the results for sample C3 with a fixed back-gate voltage of 8 V at 1.5 K. Clearly, the fit with the magnetic field up to 3 T does not adequately fit to the experimental data. In the magnetic field regimes up to 0.5 T and 1.5 T, the MF-fit are in good agreement with the data. Figure 5.17d, e and f display the MF-fits for the magnetoconductivity in sample D2 with a fixed back-gate voltage of 25 V at 1.5 K for the magnetic fields ranging up to 0.5 T, 1.5 T and 3 T, respectively. The best fits in sample D2 are found to be in the magnetic field range from up to 1.5 T. Appendix D presents the fits with the MF-theory for all the back-gate voltages considered in figure 5.16.
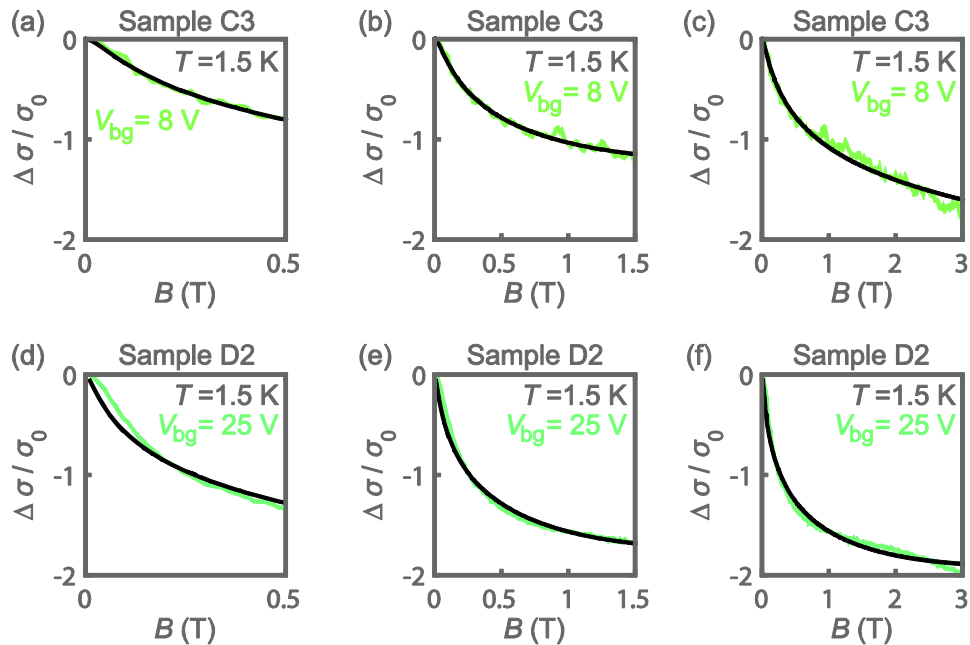

Figure 5.17: The Maekawa-Fukuyama fit to the experimental data at 1.5 K of sample C3 and sample D2 at a fixed back-gate voltage of 8 V and 25 V, respectively. The MF-fit is executed in the applied magnetic field range in a) and d) from 0 T to 0.5 T, b) and e) from 0 T to 1.5 T and c) and f) from 0 T to 3.0 T.

As mentioned before, sample C3 is measured in DC mode whereas the measurement in sample D2 are performed in AC mode. This is the origin of the different noise levels in the signals. The noise in sample C3 is such that a reliable estimate of the scattering times is not feasible. For further analysis, sample D2 in the magnetic field range from 0 T to 1.5 T is considered. Figure 5.18 shows the magnetoconductivity in sample D2 with the back-gate voltage ranging from 10 V to 45 V at 1.5 K. The MF-fits are observed to be in good agreement with the experimental results up to an applied back-gate voltage of 35 V. Above 35 V, the MF fit does not match with the behaviour of the experimental data because the MF theory considers a single parabolic conduction band. Concomitantly, the Hall measurements showed that for 40 V and 45 V displays a non-linear behaviour hence additional conductions band(s) contribute to the electronic transport. The MF-theory therefore cannot adequately describe the data above 35 V. For the remainder of this analyses, the back-gate voltages which result in a linear Hall effect will be considered, providing the scattering times in the low energy conduction band.
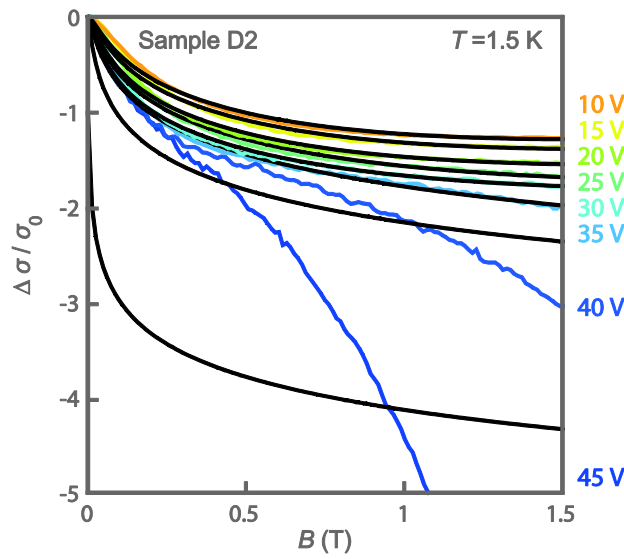

Figure 5.18: The variation in the magnetic conductance in units of $\sigma_0 = e^2/(\pi h)$ in sample D2 for different applied back-gate voltages at 1.5 K. The black lines present the fit with the MF theory.

The MF-fits give an estimate of the relaxation parameters (τ_i and τ_{so}) and the Zeeman correction (γ) can be obtained. The Zeeman correction is defined as $\gamma = g\mu_B H / 4eDH_{so}$. Figure 5.19a shows the effective g-factor of the Zeeman correction as a function of the back-gate voltage. The electric field modulation from 5 V to 30 V results in an increasing g-factor. The inset displays the g-factor up to an back-gate voltage of 45 V where a rapid decrease of the g-factor above 30 V is observed. While for 40 V and 45 V the MF theory did not properly fit with the experimental data, the fit for the data obtained with the back-gate voltage at 35 V seemed to be consistent. However, the g-factor obtains a value which is similar to the values where the second conduction band plays a role indicating that the spin and orbital magnetic moment might already be influenced by a second conduction band. The typical value for the g-factor of a bare electron at positive back-gate is 2. The g-factors estimated from the fit with the experimental data are all higher than 2. Caviglia et al.[99] performed an MF analysis on the magnetoconductivity at the LAO/STO(100) interfaces at 1.5 K. They observed an electric field modulation of the g-factor from 0.2 at -300 V to 2.5 at 100 V. At back-gate voltages above 35 V, the data cannot be explained by the MF theory due to the presence of a second conduction band but the effective g-factor can be studied for negative applied back-gate voltages in future research.

Additionally, the fits provide an estimate of the inelastic scattering time and the spin-orbit scattering time. Figure 5.19b displays the electric field modulation of the scattering times in sample D2 at 1.5 K. The inelastic scattering time remains fairly constant with increasing back-gate voltage while the spin-orbit scattering time is decreasing from 0.2 ps to 0.05 ps when the back-gate voltage is increased from 5 V to 30 V. In the considered range of applied back-gate voltages, the inelastic scattering time is always longer than the spin-orbit scattering time, indicating that the inelastic scattering is weak compared to the spin-orbital coupling. Hence, the low field positive contribution to the B^2-dependence in the magnetoconductivity is due to weak anti-localization characterized by strong spin-orbit coupling. Furthermore, the obtained scattering times are in the same order of magnitude as previous reports.[46,99] Caviglia et al.[99] studied the scattering times in LAO/STO(100) interfaces with use of the MF theory. They also observed a rather constant inelastic scattering time while the spin-orbit scattering time shows a sharp decrease with increasing back-gate voltage. At applied negative back-gate voltages, the spin-orbit scattering time was revealed to be longer than the inelastic scattering time, indicating weak localization. For future studies on the LAO/STO(111), the localization at interfaces can be studies more in depth by exploring the evolution of the inelastic and spin-orbit scattering at negative back-gate voltages.
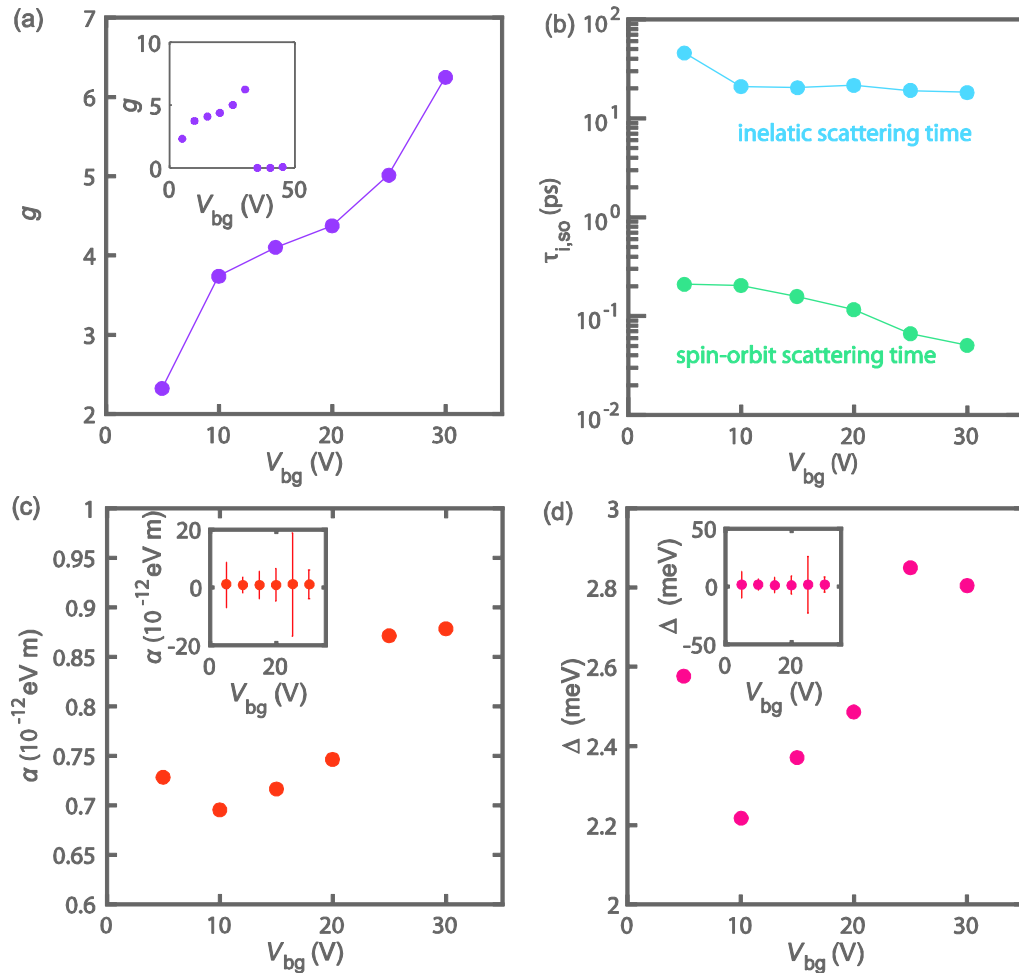

Figure 5.19: a) The evolution of the Zeeman correction factor (*g*) as a function of the applied back-gate voltage of sample D2 at 1.5 K. The inset shows the g-factor up to an applied back-gate voltage of 40 V. b) The back-gate voltage dependence of the inelastic scattering time (τ_i) and the spin-orbit scattering time (τ_{so}) of sample D2 at 1.5 K.

Lastly, the Rashba coupling constant and the spin splitting are determined from the spin-orbit scattering time. The Rasba effect is the splitting of the spin bands in two-dimensional systems induced by a combined effect of spin-orbit coupling and the symmetry breaking at the interface. The Rashba Hamiltonion is given by $H_R = \alpha(\boldsymbol{\sigma} \times \boldsymbol{p})\hat{z}$ where α is the Rashba spin-orbit coupling constant and $\boldsymbol{\sigma}$ and $\boldsymbol{p}$ are the Pauli matrix and the momentum, respectively. The Rashba spin-orbit coupling constant is related to the spin-orbit scattering time as $\alpha = \sqrt{\hbar^4/4\tau_{so}m_e^2 2D}$ where m_e is the effective mass, D is the diffusion constant, $\hbar$ is the reduced Planck constant and τ_{so} is the spin-orbit scattering time. The resulting electric field modulation of the Rashba coupling constant is presented in Figure 5.19c which shows an increase in the Rashba coupling constant when increasing the back-gate voltage from 10 V to 30 V. In the weak-anti localization regime, Caviglia et al.[99] also measured an increasing Rashba coupling constant. However, the inset shows the same data with the corresponding uncertainty indicating that the evolution could actually be constant. The corresponding spin splitting is related to the Rashba coupling constant as $\Delta = 2\alpha k_F$ where the Fermi wavevector (k_F) can be rewritten in term of the sheet carrier density: $k_F = \sqrt{2\pi n_{2D}}$. With use of the sheet carrier density extracted from the Hall effect measurements (figure 5.11b) the spin splitting is determined. Figure 5.19d displays the back-gate voltage dependent spin splitting which shows a similar evolution as the Rashba coupling constant. But also here the uncertainty is such that the data might just as well be presented by a constant. Therefore, no real statements about the ability to control the Rashba coupling constant and the Rashba spin splitting by means of an back-gate voltage can be made. In order to appreciate the real trend of these parameters a wider range of applied back-gate voltages has to be considered, which is an interesting topic for future studies.

6. Superconductivity

Reyren et al.[4] were the first to discover that the 2DES of the LAO/STO(100) interface condenses into a superconducting phase below 200 mK. Later, Caviglia et al.[54] showed that the ground state of the LAO/STO(100) interface can be driven through a quantum phase transition from an insulation to a superconducting phase by electric field modulation. Recently, Herranz et al.[5] reported on high mobility conduction at the LAO/STO interface in the {110} and {111} crystallographic orientations, which provides new opportunities for uncovering the origin of the high mobility 2DES in LAO/STO heterostructures and the realization of new electronic properties, e.g., graphene-like properties in the multi-layer LAO/STO(111) heterostructures.[88]

In this study, the properties of the superconducting ground state at the LAO/STO(111) interface are explored. The presence of the superconducting phase is investigated for two different growth temperatures, namely 770 °C and 840 °C. Evidence for the modulation of the superconducting phase with the electric field effect is presented and the evolution of the superconducting critical current with varying magnetic field is discussed. Furthermore, the BKT analysis implies a superconducting-to-metal transition that is consistent with a two-dimensional character of the superconducting phase. The samples under investigation are sample C3 (770 °C) and sample D1 (840 °C) both with a 10 uc LAO film. Appendix C.2 gives more details about the growth conditions and the surface structure of these two samples. The electronic transport measurements are performed in a Hall bar geometry, described in section 3.6 and 3.7. As the phase transition to a superconducting state was expected to occur at a few mK, the measurements are performed in a dilution refrigerator (section 3.5).

6.1 Electric field control of the superconducting phase

The sheet carrier density plays an important role in defining the ground state of LAO/STO systems. Caviglia et al.[54] explored the phase diagram of the LAO/STO(100) heterostructure by varying the sheet carrier density by means of a back-gate. They showed that electrostatic tuning of the carrier density drives an insulating-to-superconducting phase transition. As discussed before, the LAO/STO system with a back-gate and a 2DES can be considered as a coupled capacitor where the capacitance of the STO is dependent on the back-gate voltage. It is observed that reversible and reproducible capacitance characteristics can be obtained by applying a voltage sweep to the highest back-gate voltage, named training.[54] In this study, the samples display linear *VI*-characteristics upon cooling down to 50 mK in the untrained state, i.e., no superconducting ground state is observed. The back-gate is used to apply an electric field and possible uncover a superconducting ground state at values of the sheet carrier density different from the values in the native state.

Figure 6.1a shows the *VI*-characteristics of sample C3 where the back-gate voltage ranges from 0 to 20 V at 50 mK. The curves display a linear behaviour for all applied back-gate voltages (no zero state resistance plateau is observed) indicating the sample is in a resistive state. The *VI*-characteristics of sample D1 for different applied back-gate voltages are shown in figure 6.1b from 20 V and 35 V and in figure 6.1c from 35 V and 80 V at a temperature of 50 mK. Below 20 V, the contacts were insulating and no electronic transport measurements were possible. In this sample a zero-resistance state plateau, the signature of a superconducting state, is present.

The *VI*-characteristics show that for the considered range of applied back-gate voltages at 50 mK, sample C3 is in a resistive state whereas sample D1 obtains a superconducting ground states. The difference in the electronic properties of the 2DES is can be attributed to the growth conditions. As explained by Chen et al.[100] for YBCO films on STO substrates, lower growth temperatures induce more dislocations and disorder at the interface of a system such that the amount of vortex pinning cores is increased. The enhancement of vortex pinning will subsequently raise the critical current density. This study shows the opposite, sample C3 with a growth temperature of 770 °C, i.e., in theory higher defect density, is resistive while sample D1 which was grown at 840 °C shows a superconducting ground state.
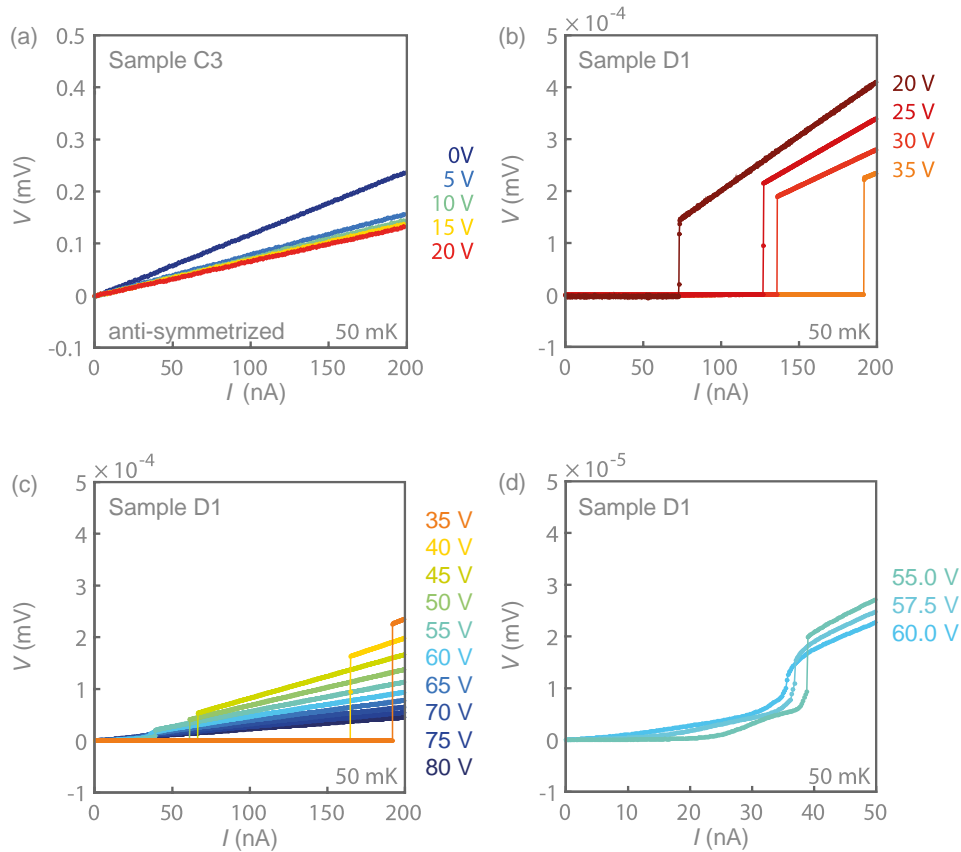
Figure 6.1: a) linear *VI*-characteristic for sample C3 for different applied back-gate voltages ranging from 0 V to 20 V at 50 mK. b) *VI*-characteristics for sample D1 for applied voltages between 20 V and 35 V and c) *VI*-characteristics for sample D1 for applied voltages between 35 V and 80 V at 50 mK. The *VI*-characteristics for sample D1 shows a superconducting zero-resistance plateau for the back-gate voltages below ~57.5 V. Above ~57.5 V, a finite-resistance state appears at low currents. d) The *VI*-characteristics for a back-gate voltage ranging from 55 V to 60 V, showing the transition from a zero-resistance plateau to a finite-resistance at low currents.

The *VI*-characteristics in sample D2 are split up in two regions depending on the response of the zero-resistance state plateaus. The zero-resistance state plateaus become wider as the back-gate voltage is increased up to 35 V (figure 6.1b). For larger values of the back-gate voltage, the zero-resistance state plateaus become smaller again (figure 6.1c). However, taking a closer look at zero-resistance state plateau in the back-gate voltage range of 55 V to 60 V (figure 6.1d), the zero-resistance state disappears at 57.5 V. Above 57.5 V, a finite-resistance state is observed at low bias currents, although a resistive transition can still be identified.

The evolution of the superconducting critical current with the applied back-gate voltage of sample D1 is studied in order to investigate this behaviour and the properties of superconducting ground state in more detail. The superconducting critical current is obtained from *VI*-characteristics as presented in figure 6.1 but with a smaller back-gate voltage step. The differential resistance (d*V*/d*I*) is determined from the *VI*-characteristics and the critical current is defined as the current where the differential resistance reaches a maximum. Figure 6.2 shows the superconducting critical current as a function of the applied back-gate voltage at 50 mK. The critical current presents the cross-over from a superconducting to a resistive state. Below the critical current, indicated by the blue and green areas, the system is in a superconducting state while above the critical current the system is in a normal resistance state, as indicated in the figure.

The variation of the back-gate voltage induces a modulation of the superconducting critical current. At the lowest applied gate voltage (~20 V), corresponding to the smallest carrier density, a critical current of ~110 nA is measured. As the back-gate voltage is increased, an increase in the critical current is induced until it reaches a maximum at 33 V where the critical current is ~200 nA. For larger voltages, the critical current decreases again. The electrostatic doping until ~55 V results in a dome shaped evolution of the critical current. For a back-gate voltage above ~55 V, the influence of the electric field on the critical current seems to change, i.e., the effected of the back-gate voltage on the critical current appears to be less prominent.
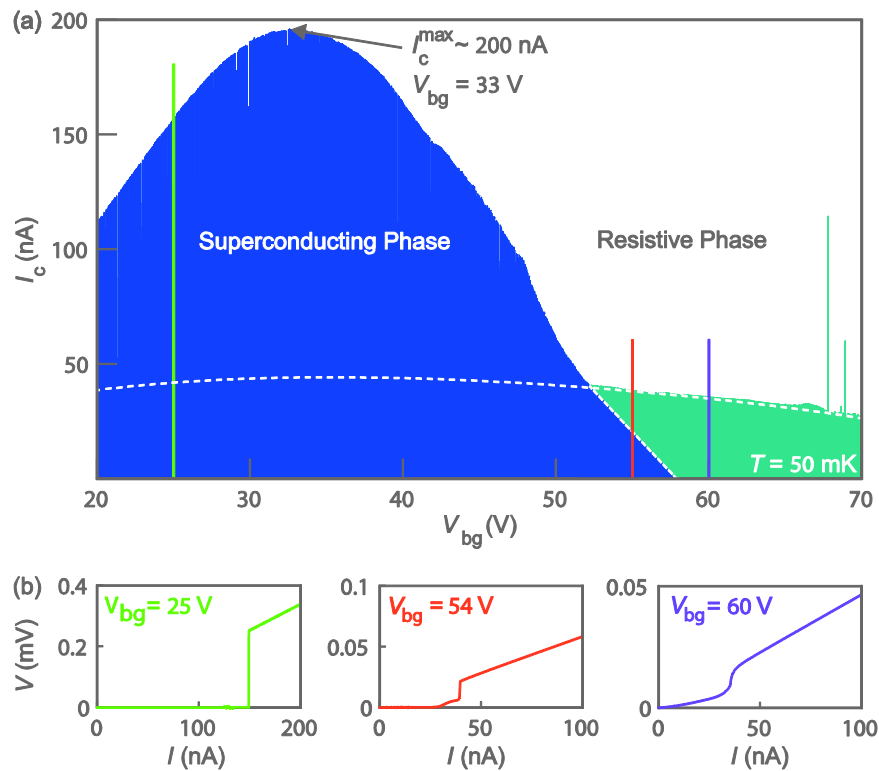

Figure 6.2: a) The evolution of the superconducting critical current with the back-gate voltage of the LAO/STO(111) (sample D1) interface at 50 mK, indicating the superconducting phase (blue area) and two resistive phases (green and white area). b) Three *VI*-characteristics at specific applied back-gate voltages, namely 25 V, 54 V and 60 V. The colour of the curves correspond to the lines in (a) with the same colour.

In the range of back-gate voltages considered, the superconducting state was never completely suppressed but the modulation of the sheet carrier density allows for a remarkable tuning of the superconducting critical current. In order to elucidate the response of the critical current, *VI*-

characteristics at three applied back-gate voltages are considered. The positions of the *VI*-characteristics are highlighted in figure 6.2a where green, red and purple correspond to 25 V, 54 V and 60 V, respectively. At a back-gate voltage of 25 V, the *VI*-curve shows abrupt switching between the superconducting and resistive state while at 60 V the switching is observed to be gradual. When applying a back-gate voltage of 54 V, a peculiar *VI*-curve is measured. The change from the superconducting phase to the resistive phase starts gradual and is followed by a sudden switch. This switching behaviour seems to be a combination of the former two curves, suggesting the presence of two superconducting phases, accompanied by a dome shaped modulation of the critical current.

Figure 6.2a shows two white dashed lines which illustrate the possible shape of the two superconducting domes. One dome with a higher critical current that is sensitive to electrostatic doping and shows abrupt switching from the superconducting to the resistive state. The second dome is identified by a lower critical current, the electrostatic doping is much less effective and the transition from the superconducting to the resistive state is gradual. Figure 6.3 shows the same graph presented in figure 6.2a where exact values of the superconducting critical current are displayed by the green dots. This graph shows that besides the overall trend of the critical current, stochastic switching is observed for back-gate voltages between 20 V and 50 V. Note that the data points are quite dense and the stochastic switching observed is a small percentage of the total amount of data points.
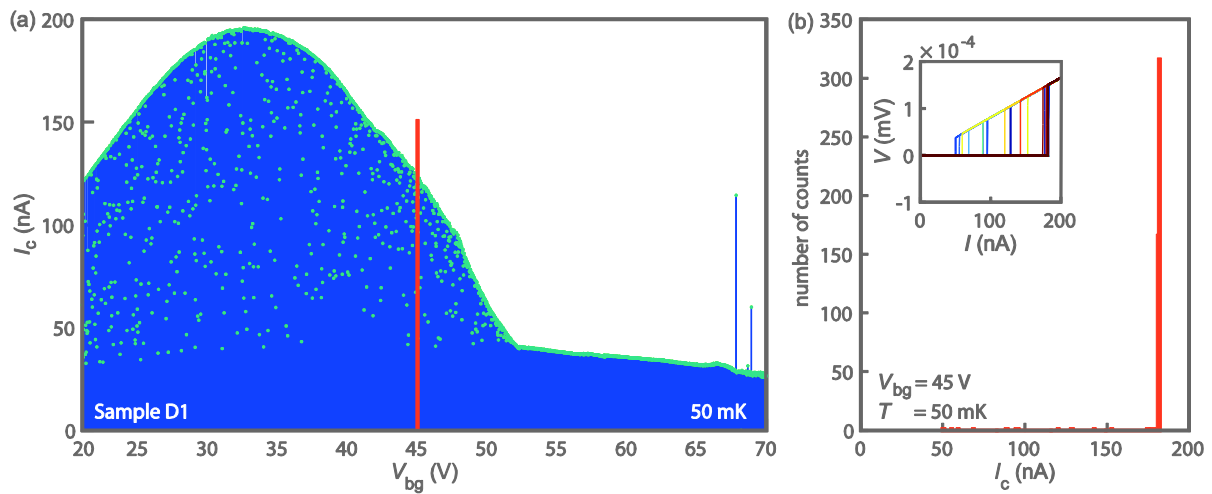

Figure 6.3: a) The evolution of the superconducting critical current as a function of applied back-gate voltage of sample D1 at 50 mK (similar to the graph presented figure 6.2) where the green dots present the exact values of the critical current showing stochastic switching for back-gate voltages between 20 V and 50 V. b) A histogram presenting the stability of the critical current with 45 V applied to the back-gate shows a sharp peak at ~182 nA. The inset shows the (500) *VI*-characteristics which define the superconducting critical current at 45 V.

In view of this stochastic switching, a stability check of the critical current is performed. The VI-characteristics, displayed in the inset of figure 6.3b, are taken repeatedly at 50 mK and a fixed back-gate voltage of 45 V. Figure 6.3b shows a histogram presenting the number of times a specific critical current is measured. The average superconducting critical current is ~181.87 nA and from the total amount counts, i.e., 500, 96,4 % result in a critical current ~(182 $\pm$ 1) nA, indicating a fairly stable critical current. Furthermore, all the observed superconducting critical current are measured in a range from ~50 nA to ~183 nA. The distribution obtains a maximum observed critical current ~183 nA, after which it reduces rapidly with decreasing critical current until it reaches the lowest measured critical current ~50 nA. Although the cause for the stochastic switching remains unclear,

this measurements show clearly that the switching only occurs above a certain critical current, emphasizing the existence of two superconducting domes (see figure 6.3a), i.e., two different superconducting phases.

With this in mind, the origin of two superconducting phases in the system is discussed. The electronic properties of bulk STO can be modified by controlled electrostatic doping, cation substitution or oxygen vacancies. The introduction of n-type carriers can result in a metallic state in the STO. Gross et al.[101] studied the influence of argon ion-milling on the conductivity of single-crystal STO substrates. They observed that argon ion-milling drives an insulator-to-metal transition due to the creation of oxygen vacancies which donate two mobile electron to the system. A highly conducting surface layer, deeper than the penetration depth of the argon ions is observed which is present at room temperature and cryogenic temperatures.

The Hall bar channels in this study are defined by an argon ion-milling process (see section 3.7). As explained, this process can introduce a metallic state in the STO owing to n-type carrier doping. In order to investigate the finite resistance state at high electrostatic doping (green area in figure 6.2), electronic measurements between electronic contacts from two different Hall bars are performed (each sample contains five Hall bars see figure 3.16). The STO is measured to be insulating even with an applied back-gate voltage of 100 V, indicating conduction in the bulk STO cannot explain the appearance of two superconducting phases in the LAO/STO(111) heterostructure.

Prawiroatmodjo et al.[102] report on gate-tunable superconductivity at the interface of an amorphous LAO film on top of an STO(100) substrate. They present *VI*-characteristics at different temperatures which show similar behaviour as the *VI*-curves presented in figure 6.2b. At low temperatures, the system switches abruptly from the superconducting to the resistive state when the bias current in increased. As the temperature is increased, the bias current drives a transition where the switching changes from sharp to gradual with a transition region that shows a combination of both types of switching. This behaviour of the electronic transport is explained by considering superconducting puddles imbedded in a matrix, which form a random array of coupled Josephson junctions.
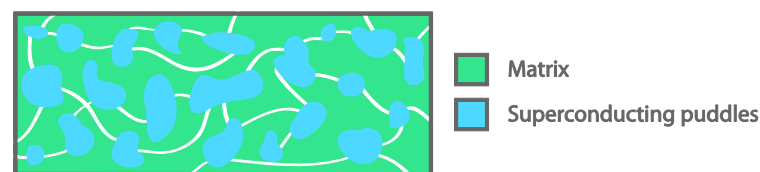

Matrix
Superconducting puddles

Figure 6.4: A schematic representation of an inhomogeneous interface consisting of a random array of superconducting puddles embedded in a matrix forming weakly coupled Josephson junctions. The Josephson junctions are S-I-S, S-N-S or S-s-S depending on the electronic nature of the matrix. The white line present the percolative paths between the superconducting puddles.

A Josephson junction is a system which consists of two superconductors coupled by a weak link. The weak link can consist of an insulator, normal metal or a superconductor creating S-I-S, S-N-S, S-s-S Josephson junctions, respectively. Figure 6.4 shows a random array of superconducting puddles enclosed in a matrix, where the blue areas are the superconducting puddles and the green area is the matrix. The white lines present possible paths the electrons can follow. The coupling between the superconducting puddles is determined by the conductance of the matrix. A back-gate voltage modulates the carrier density, i.e., the conductance at the interface of the heterostructure (as shown in figure 5.9). Consequently, the back-gate voltage allows for tuning of the coupling between the

Josephson junctions. Thereafter, the back-gate voltage also affects the sheet carrier density in the superconducting puddles, thereby changing their distribution.[103] This allows for the possibility that the dimensions of the superconducting puddles in a resistive matrix varies with applied back-gate voltage such that between 20 V and 55 V, the Josephson junction coupling is the strongest. Whereas above 55 V, the size of the superconducting puddles remains fairly constant with increasing back-gate resulting in a rather fixed coupling which induces a smaller variation in the critical current.

Caprara et al.[103] explain the superconductivity in inhomogeneous oxide systems (LTO/STO and LAO/STO(100)) by a multiband conduction scenario considering different types of carriers, namely low mobility carriers (LMC) and high mobility carriers (HMC). They discuss that considering the multiband structure, the carriers in the lowest states have a more two-dimensional character which accounts for a low mobility whereas carriers occupying the higher subbands are less confined along the interface and more mobile. Caprara et al.[103] state that superconductivity seems to be triggered by the HMC. The whole set of lower bands is considered as one subband collecting all the LMC with vanishingly small T_c, while the occupation of the upper subband(s) by HMC give rise to a finite T_c. According to them, this scenario can be related to the inhomogeneous structure of the system by assuming that the superconducting puddles are regions with the HMC which are locally filled and the weakly localized resistive matrix correspond to regions where the HMC subbands are empty.

However, the lowest energy band in the band structure of the LAO/STO(100) (figure 2.6a) is conduction band with the HMC whereas the LMC reside in a higher energy band. Experiments show that the superconducting phase arises when the electric field modulation reaches a certain energy level.[54] Moreover, an increase in sheet carrier density induced by a gate voltage will raise the Fermi level. This means that at low doping levels only the lowest energy band with HMC are occupied and by increasing the doping level, higher energy bands will get filled such that LMC will contribute to the conduction. In contrast to what Caprara et al.[103] state, this indicates that the superconducting phase goes together with the presence of LMC.

The type of carriers contributing to the conduction will play an important role in the superconducting phase. Unfortunately, the band structure of the LAO/STO(111) has not been studied thoroughly. However, Rödel et al.[24] measured the band structure of STO(111) by performing ARPES on in-site cleaved STO(111) substrates. The energy-momentum maps show that the ground state of the 2DES constitutes dispersion of one heavy and one light band. In the resolution of their measurement the heavy and light bands are observed to be degenerate at the Γ-point. Additional subbands are not observed, implying that the band bending at the surface is too low to populate upper subbands. On the other hand, calculations performed by Walker et al.[25] reveal a non-degenerate ground state at the Γ-point with an energy difference of ~10 meV. They discuss that the higher subbands show a progressively more bulk-like character where the energy of the second subband is located just below the Fermi level.

No magnetotransport measurements are performed on sample D1. However, such measurements are conducted on a different sample with the same growth temperature and layer thickness, i.e., sample D2. The Hall effect measured in sample D2 (LAO/STO(111)) shows non-linear behaviour above a back-gate voltage of 35 V, indicating the presence of multiband conduction (see figure 5.12). Note, that the applied back-gate voltage in sample D2 does not directly relate to the applied back-

gate voltage in sample D1. However, the electron properties can be considered in terms of low and high levels of electrostatic doping. The electronic transport is dominated by one conduction band containing HCM when the electrostatic doping is low. Above a certain level of electrostatic doping, a second conduction band with LMC comes into play. For example in sample D2, a back-gate voltage of 45 V results in an electron mobility of 2444 cm^2/Vs below the inflection point while above the inflection point the electron mobility is 580 cm^2/Vs according to the two band model. HMC are sensitive to gate tuning which could indicate that the electric field modulation of the critical current between 20 V and 55 V in sample D2 is dominated by HMC. Furthermore, sample D2 shows that the corresponding carrier densities for the HMC and LMC are given by 1.73×10^{13} cm^{-2} and 3.22×10^{13} cm^{-2}, respectively. A reduction in carrier density will emphasize the disorder at the interface consequently the coupling between the Josephson junctions will weaken and fluctuations of the local superconductivity increase. This could be related to the stochastic switching observed in the critical current.[103] However, to make real statements about the influence of the electron mobility and the carrier density, the electronic transport properties should be determined in sample D1. This will test if the electronic properties measured in sample D2 are representative for 10 uc LAO/STO(111) heterostructures. Thereafter, the evolution of the critical current below 20 V needs to be uncovered.
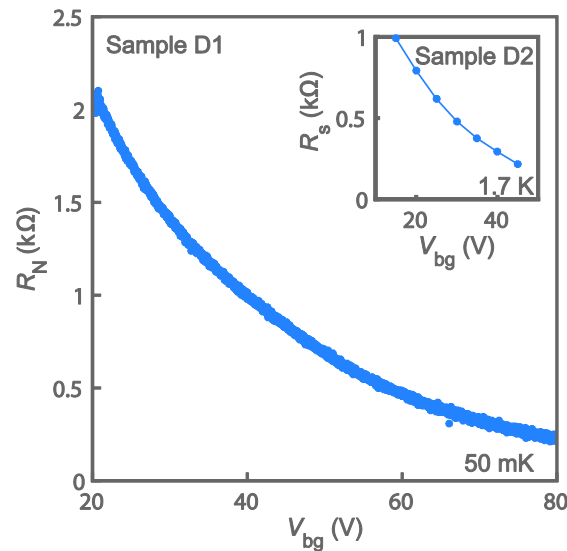

Figure 6.5: The normal-state resistance of sample D1 (10-uc with T_g = 840 °C) obtained from the same *VI*-characteristics from which the critical current is determined at 50 mK which follows the same trend as the zero-field sheet resistance in sample D2 (9 uc with T_g = 840 °C) at 1.7 K as shown in the inset.

Furthermore, the normal state resistance with varying back-gate voltage is extracted from the same *VI*-characteristics used to determine the superconducting critical current. Figure 6.5 displays the back-gate voltage dependence of the normal state resistance. As a reference, the zero-field sheet resistance of sample D2 at 1.7 K is shown in the inset. The overall trend of the resistance is the same, i.e., the resistance decreases with increasing back-gate voltage and both show a resistance which is in the same order of magnitude. A further comparison cannot be made due to the difference in the film thickness and the temperature at which the measurements are performed. What can be seen is that the normal state resistance does not show distinct features as was demonstrated for the superconducting critical current.

6.2 Temperature dependence the superconducting phase

In order to determine the superconducting critical temperature, electronic measurements at different temperatures are performed. The dilution refrigerator used in this study, does not allow for automated control of the temperature. The temperature of the sample is adjusted by manually applying a fixed current to a heater in thermal contact with the mixing chamber. The temperature in the mixing chamber will increase due to the applied current. Once the current is set to the preferred value, the stabilisation of the temperature is monitored. However, the temperature sensor is positioned between the mixing chamber and sample such that the temperature sensor reaches a stable temperature before the sample does. In order to observe the thermalization of the sample, *VI*-characteristics are taken repeatedly. The saturation of the critical current determine completely thermalization of the sample. The waiting time before starting the electronic measurement is approximately one and a half hour.

Figure 6.6a shows the *VI*-characteristics of the LAO/STO(111) heterostructure (sample D1) obtained from a four-probe Hall bar geometry by ranging the temperature from ~43 mK to ~82 mK. A fixed back-gate voltage of 33 V is applied which corresponds to the optimal doping conditions, i.e., the highest critical current observed in figure 6.2a. At the highest temperatures, the *VI*-characteristics display linear ohmic behaviour whereas upon cooling the characteristics are non-linear and a zero-resistance state plateau appears, which becomes increasingly wider as the temperature is further decreased. The appearance of a zero-resistance state provides evidence for superconductivity.
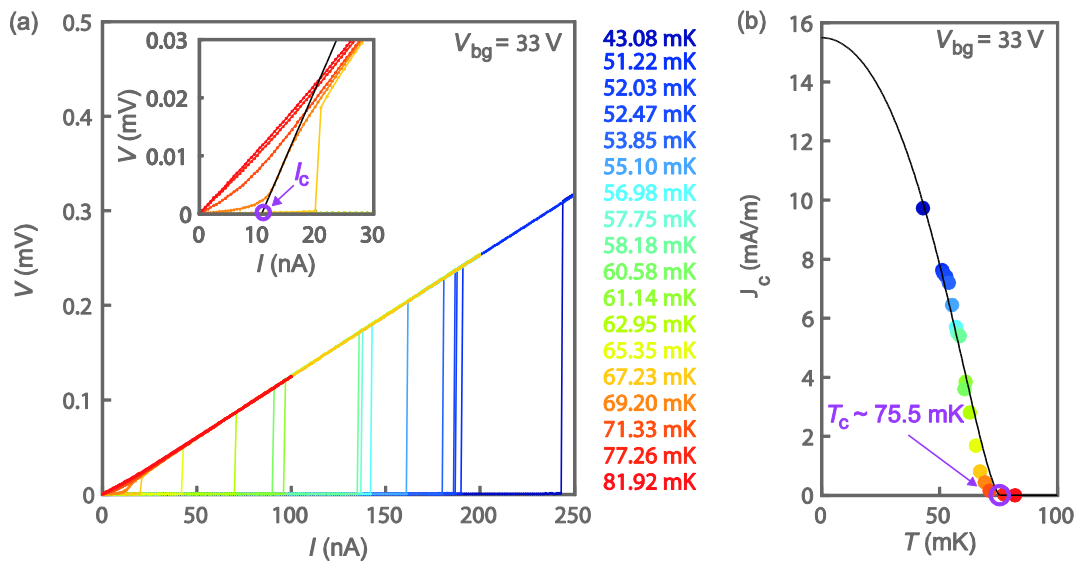

Figure 6.6: a) *VI*-characteristics of sample D1 at different temperatures ranging from ~43 mK to ~82 mK at a back gate voltage of 33 V, showing a superconducting-to-metal transition. The inset shows the critical current at ~69 mK, defined by the linear extrapolation of the transition region between the ohmic regime and the zero state resistance plateau b) The critical current density ($J_c = I_c / 25 \mu$m) as a function of the temperature where the black line is the fit to the Ginzburg-Landau mean field theory, indicating a superconducting transition temperature of (75.5±0.9) mK.

At the lowest temperatures, Figure 6.6a displays a well-defined critical current while at the higher temperatures the transition gets rounded. The critical current at each temperature is determined by a linear extrapolation of the slope between the ohmic regime and zero state resistance plateaus, as indicated for ~69 mK in the inset of figure 6.6a. Figure 6.6b displays the critical current density as a function of the temperature. The critical current density is defined as the critical current divided by

the width of the Hall bar channel. The dimension of the Hall bar channels on sample D1 is 25 μm x 50 μm, resulting critical current density $J_c = I_c/\,25\ \mu$m. The critical current density is maximum at 43 mK, being ~9.7 mA/m whereas it is reduced to ~0 mA/m at 82 mK, exhibiting a similar shape as previous reports on the evolution of the critical current density with temperature in (100) and (110) orientated LAO/STO heterostructures. At 50 mK, the heterostructures with the (100) and the (110) orientations possess a critical current density of ~9.8 mA/m and ~2.6 mA/m, respectively.[4,50] The magnitude of the measured critical current density for sample D1 at 50 mK is comparable , i.e., ~7.7 mA/m.

In a homogeneous superconducting thin film, the critical current density is described by the Ginzburg-Landau mean field as:[102]

$$J_c^{\mathrm{GL}} \propto J_c^0 \left(1 - \left[\frac{T}{T_c}\right]^2\right)^{\frac{3}{2}} \left(1 + \left[\frac{T}{T_c}\right]^2\right)^{\frac{1}{2}}, \tag{6.1}$$

where $J_c^0 = H_c^0 t/3\sqrt{6}\pi\lambda_0$ with the superconducting film thickness t and the zero temperature critical magnetic field and penetration depth H_c^0 and λ_0, respectively.[104] Figure 6.6b displays the temperature dependence of the critical current density. The fit with the Ginzburg-Landau mean field theory presented by the black line, gives a maximum critical current density of J_c^0~15.4 mA/m at 0 mK and the superconducting transition temperature is T_c~(75.5$\pm$0.9) mK. It is observed that the fit does not completely agree with the experimental data at higher temperatures. The Ginzburg-Landau mean field does not hold when the interface is inhomogeneous and should be consider as an array of coupled Josephson junctions. We will come back to this point once the zero temperature critical magnetic field is determined.

However, the critical current indicates that the superconducting critical transition temperature T_c~(75.5$\pm$0.9) mK. In contrast, the superconducting transition temperature in LAO/STO(100) and (110) heterostructures are observed to be ~200 mK.[4,50] The reason for the difference can be related to inhomogeneities at the interface possibly creating superconducting puddles in a resistive or superconducting matrix, as discussed before (figure 6.4). In a homogeneous sample, the entire interface will be characterized by a superconducting state, while an inhomogeneous interface is dependent on the coupling between the superconducting puddles. At temperatures below 1 K, the driving mechanism for the transition between superconducting and resistive puddles is given by the competition between the Josephson coupling (E_J) and the charging energy (E_C). The Josephson coupling is related to the resistivity of the matrix and tends favours the superconductivity. The charging energy is the energy required to charge the junction with one elementary charge and favours insulating behaviour. The charging energy is defined as $e^2/2C$ where C is the capacitance which is determined by the size of the puddles. When the resistivity in the matrix is such that the coupling between the puddles is very weak and or the size of the superconducting puddles is large meaning large E_C, the superconducting interface conduction is easier to suppress. In this scenario it can be expected that the critical parameters, like temperature and magnetic field, are lower in comparison to the critical parameters in the superconducting phase at a homogeneous interface.[105,106]

6.2.1 Berezinskii - Kosterlitz –Thouless (BKT) phase transition

The two-dimensional character of the superconducting phase can be indicated with the BKT theory of 2D superconductivity (explained in section 2.4.1). In two-dimensional systems, the transition from the superconducting towards the normal state is a BKT phase transition, characterized by a transition temperature (T_{BKT}) at which vortex-antivortex pairs unbind. The BKT phase transition results in a $V \propto I^{a(T)}$ power law dependence with a = 3 at the BKT transition temperature. The *VI*-characteristics in figure 6.6a show signatures of a BKT phase transition, namely a gradual change in the transition from the superconducting to the resistive state. The inset of figure 6.7a displays the same *VI*-characteristics as in figure 6.6a on a logarithmic scale for the complete range at temperatures considered, being ~43 mK to ~82 mK. Figure 6.7a shows the *VI*-curves for temperatures between ~69 mK and ~82 mK, where the onset of the superconducting phase is more clearly visible. The resulting fits for the power law dependence ($V \propto I^{a(T)}$) are indicated by the black lines while the purple coloured line corresponds to $V \propto I^3$ showing that 69.20 mK < T_{BKT} < 71.33 mK.

Figure 6.7b displays the temperature dependence of the exponent for temperatures between ~69 mK and ~82 mK. Below 69 mK, the magnitude of the exponent increases rapidly. As the temperature is increased, the value of the exponent converges towards 1, indicating ohmic behaviour. The evolution of the exponent reveals the BKT transition temperature to be ~70 mK as the exponent approaches 3. The BKT transition temperatures in (100) and (110) orientated LAO/STO interfaces are determined to be 190 mK and 184 mK, respectively.[4,50] These values are twice as high as the BKT transition observed in sample D1. The reduction in the BKT transition temperature could be related to an inhomogeneous interface suggesting superconducting puddles in a matrix where the interface conduction is dependent on the coupling and charging energy.
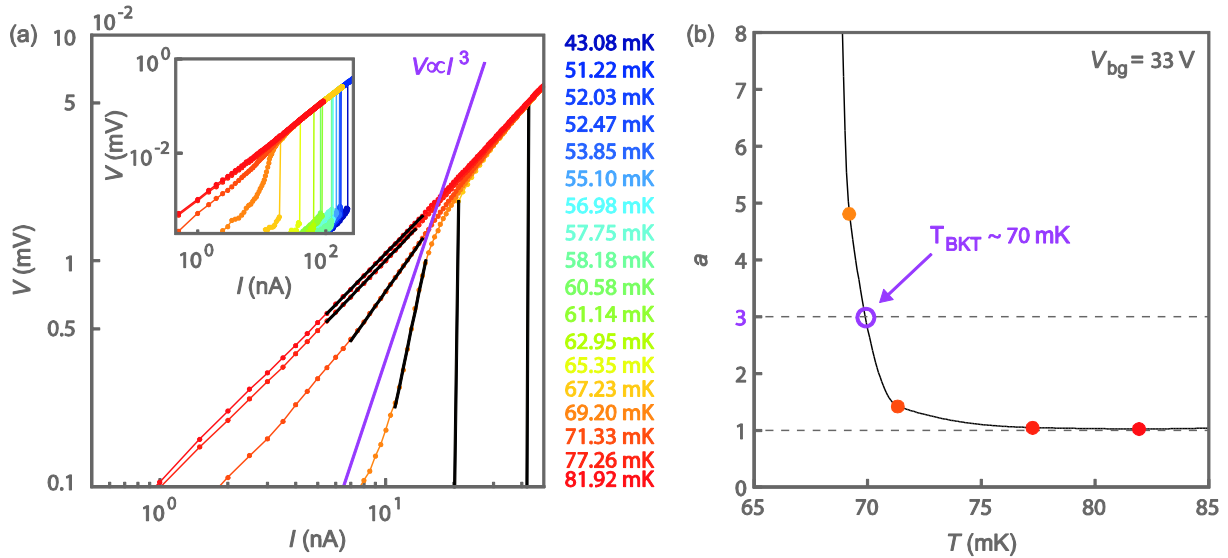

Figure 6.7: a) The inset shows *VI*-characteristics of sample D1 at different temperatures ranging from ~43 mK to ~82 mK and a back gate voltage of 33 V as presented in figure 6.6 but on a logarithmic scale. The graph displays a zoom-in of the inset where only the *VI*-curves for ~65 mK to ~82 mK are presented. The black lines indicate the fit for the BKT with $V \propto I^a$ and the purple line presents $V = I^3$, indicating that the BKT transition temperature lies between 69 mK and 71 mK. b) The exponent as a function of the temperature where the BKT transition temperature is defined to be the temperature where the exponent is 3 which is ~70 mK.

In order to fully confirm the superconducting transition to be consistent with a two-dimensional superconducting film, the resistance needs to be studied with varying temperatures. The BKT theory predicts the resistance to follow the relation: $[\mathrm{d}\ln R / \mathrm{d}T]^{-\frac{2}{3}} = (2/b_R)^{\frac{2}{3}}(T - T_{BKT})$ with $b_R =$

$\left(4\pi T_{\mathrm{BKT}}^{\frac{1}{2}}\right)/b$ (see section 2.4.1). Automated control on the temperature is not possible with the dilution refrigerator used for this study, therefore it was not feasible to perform high resolution temperature dependent resistivity measurements. In future work, such a measurement would be valuable, beside confirming the two-dimensional character of the superconducting state, it also provides an estimate of the correlation length, which is the same as the vortex core radius.

6.3 Magnetic field dependence of the superconducting phase

A superconductor-to-metal state transition can be induced by means of an externally applied magnetic field. The magnetic field can be used to further assess the dimensionality of the superconducting state. In two-dimensional superconductors, like LAO/STO, the response to an applied magnetic field is highly anisotropic, the critical magnetic field of the in-plane field is typically higher as the out-of-plane critical magnetic field. In this study, the electronic transport measurements are performed with an the magnetic field applied perpendicular to the interface of a 10 uc LAO/STO(111) heterostructure (sample D1) at 50 mK.

Electronic measurements with an in-plane applied magnetic field are not performed, due the limitations of the dilution refrigerator. The dilution refrigerator used in this study has a rigid sample position and the magnetic field induced by the superconducting magnet can only be applied in one specific direction. Furthermore, the measurements with an in-plane magnetic field can only be performed in a narrow range of rotational angles while the resistivity peaks sharply when the applied magnetic field is precisely aligned with the interface.[107] The accurate position of the in-plane magnetic field can be achieved with a three-dimensional vector magnet which allows for automated rotation of the magnetic field. Unfortunately, such a machine was not at our disposal.

Figure 6.8 displays the superconducting critical current as a function of the back-gate voltage for different applied magnetic fields ranging from 0 mT to 4 mT. The evolution of the critical current with the back-gate voltage at zero magnetic field, is the same as presented in figure 6.2a. As a general trend, the externally applied magnetic field is responsible for the suppression of the superconducting critical current. However, the evolution of the superconducting critical current with applied magnetic field is not uniform across the range of back-gate voltages considered. The magnetic field seems to be most drastic within the back-gate voltage range from 20 V to ~57.5 V where the maximum superconducting critical current at 33 V is reduced from ~200 nA at 0 mT to ~50 nA at 4 mT. Above 57.5 V, the influence of the magnetic field on the critical current is less prominent, emphasizing the different nature of the two regions.

Note, the stochastic switching is more clearly visible in domes constructed for the superconducting critical current with a magnetic field applied. This is related to the lower resolution in the applied back-gate voltage, no physical conclusions can be taken from comparing the zero field critical current with the critical current obtained with an magnetic field applied. However, the resolution of the back-gate voltage is the same for all the data obtained with a magnetic field applied. Figure 6.8 seems to display a reduction in the stochastic switching when the applied magnetic field is increased

from 0.4 mT to 4 mT. Additionally, the stochastic switching disappears completely for applied back-gate voltages above 57.5 V for each of the applied magnetic fields considered.
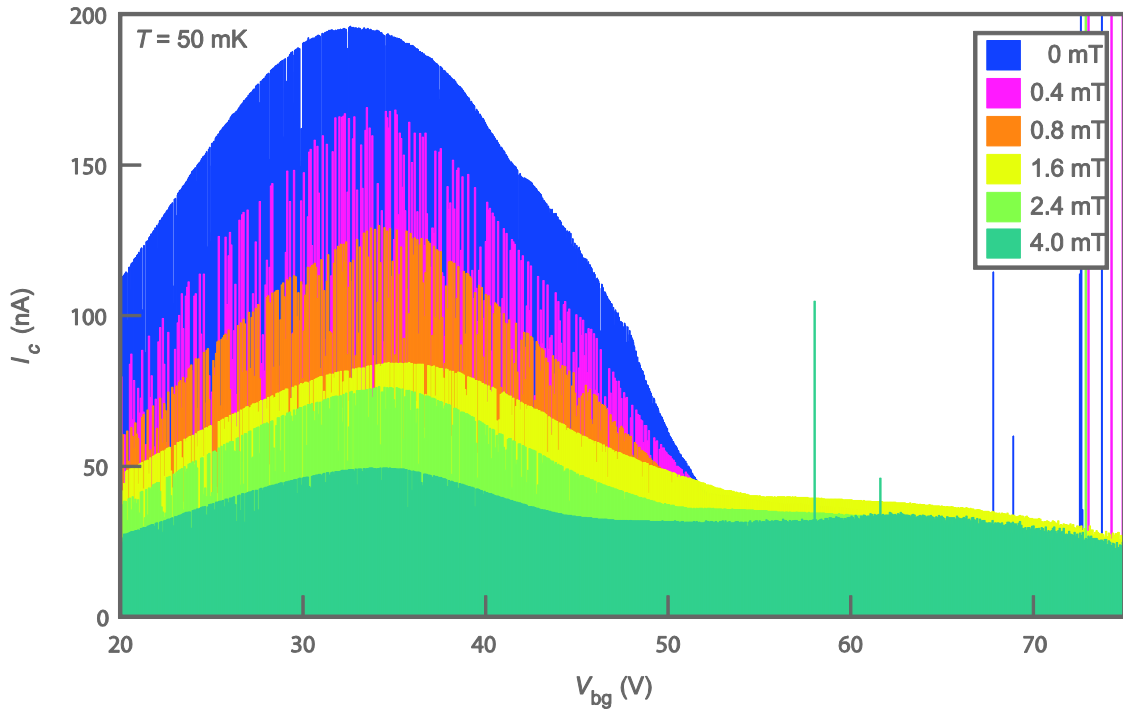

Figure 6.8: The superconducting critical current as a function of the back-gate voltage at the LAO/STO(111) interface (sample D1) for various out-of-plane applied magnetic fields at 50 mK. The dome shape evolution of the critical current for the applied back-gate voltages between 20 V and 55 V is clearly suppressed by an increase of the applied magnetic field from 0 mT to 4 mT whereas above 55 V, the effect of the magnetic field on the critical current is noticeably reduced.

In order to find the out-of-plane critical magnetic field of the superconducting state, the *VI*-characteristics of sample D1 are investigated for different values of the applied magnetic field at 50 mK. Figure 6.9a and b shows the *VI*-characteristics for the applied magnetic fields ranging from 0 mT to 47 mT at fixed back-gate voltages 33 V and 60 V, respectively. These back-gate voltages represent the two different regimes identified in the evolution of the critical current with the back-gate voltage (figure 6.8). In both cases, the magnetic field supresses the superconducting critical current, driving a phase transition from the superconducting to resistive state. Figure 6.9c and d display the differential resistance, d*V*/d*I,* obtained from the *VI*-curves, as a function of the bias current. The inset of figure 6.9c displays the behaviour of the *VI*-characteristics at low bias current. At low magnetic fields and low bias currents, the differential resistance goes to zero for the back-gate voltage of 33 V, corresponding to the zero-resistance state plateau hence superconducting state. At a back-gate voltage of 60 V, the resistance does not show a zero-resistance state plateau but an superconducting transition can be identified. However, for both applied back-gate voltages, the d*V*/d*I* increases as the bias current is increased until it reaches a maximum where after the critical current drops down and saturates at 150 nA to 1.30 kΩ and 0.48 kΩ at 33 V and 60 V, respectively. This saturation point $(\mathrm{d}V/\mathrm{d}I)_{I=150\,\mathrm{nA}}$ corresponds to the normal state.
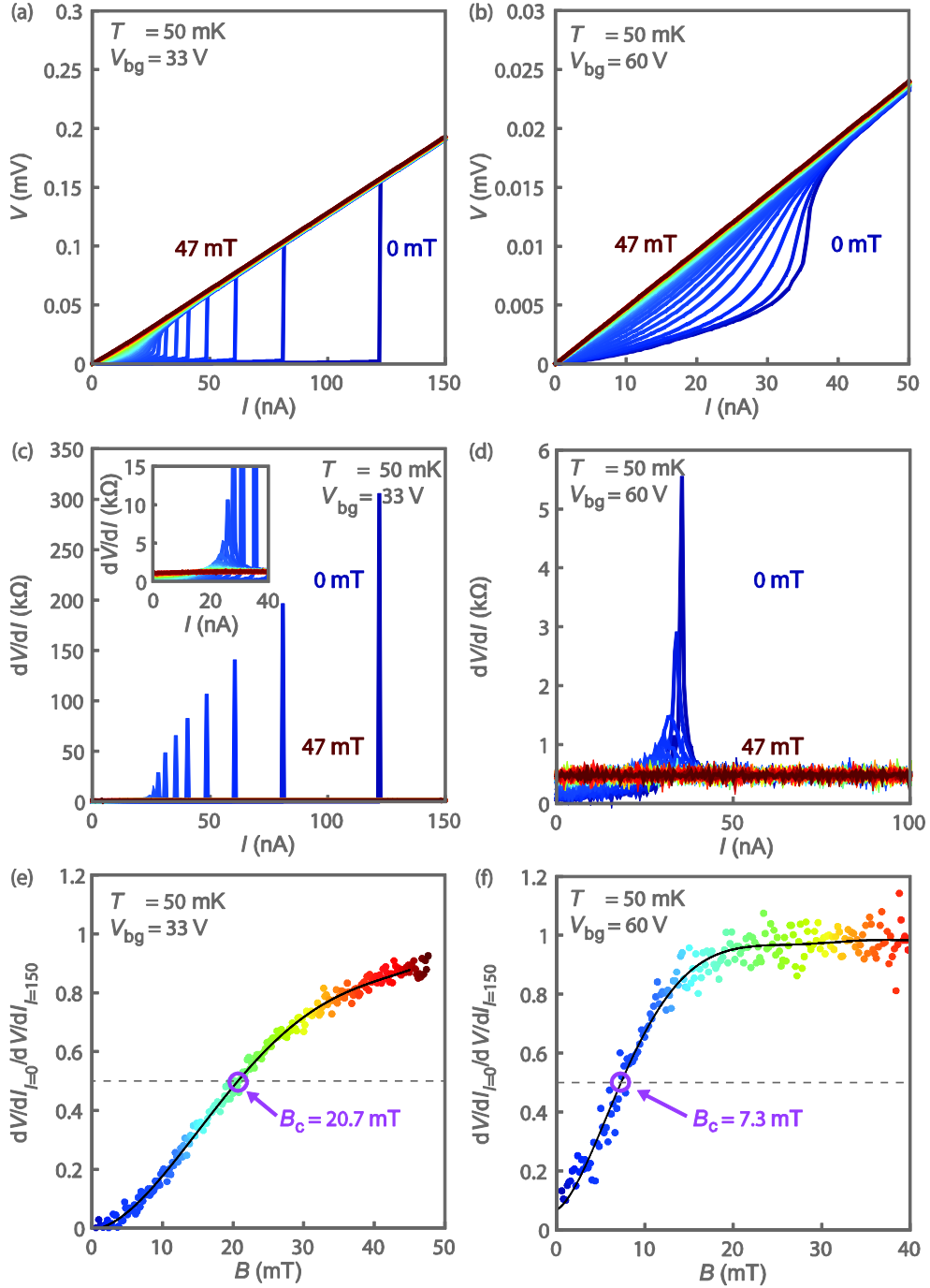
Figure 6.9: a) and b) The *VI*-characteristics of sample D1 for different out-of-plane applied magnetic fields ranging from 0 mT to 47 mT recorded at *T* = 50 mK and a fixed back-gate voltage of 33 V and 60 V, respectively. c) and d) Numerical d*V*/d*I*-*I* curves obtained from the *VI*-characteristics presented in (a) and (b), respectively. The inset in d) shows a zoom in of the low bias current region. e) and f) The zero bias current differential resistance (d*V*/d*I*$_{I=0 nA}$) as a function of the magnetic field normalized by the differential resistance of the normal state at a bias current of 150 nA (d*V*/d*I*$_{I=150 nA}$). The critical magnetic field (*B*$_c$) is defined as d*V*/d*I*$_{I=0 nA}$ / d*V*/d*I*$_{I=150 nA}$ = 0.5. At an applied back-gate voltage of 33 V, the critical out-of-plane magnetic field *B*$_c$ = 20.7 mT while at 60 V, *B*$_c$ = 7.3 mT. The black line are an guide to the eye.

The normalized differential resistance, (d*V*/d*I*)$_{I = 0 nA}$/(d*V*/d*I*)$_{I = 150 nA}$, allows for the determination of the superconducting critical field. Figure 6.9e and f plot the normalized differential resistance as a function of the applied magnetic fields. For the back-gate voltage at 33 V, the normalized differential resistance is observed to be zero at zero magnetic field. Upon increase of the applied magnetic field, the normalized differential resistance increases. The superconductivity is totally suppressed when the normalized differential resistance is 1 such that the interface has returned to the normal state in

the whole range of applied bias currents. A magnetic field of 47 mT, is not resulting in a complete saturation of the normalized differential resistance at 33 V, indicating normal state is not reached. On the other hand, when the back-gate voltage is set to 60 V, the normalized differential resistance is observed to saturate at 1 showing that a magnetic field of ~20 mT is enough to attain the normal state.

Han et al.[108] performed the same analysis on LAO/STO(110) heterostructures. They define the critical magnetic field as the field at which the resistance at I = 0 nA recovers to half of the value of the resistive state, i.e., $(dV/dI)_{I=0 \text{ nA}}/(dV/dI)_{I=150 \text{ nA}}$= 0.5. The out-of-plane critical magnetic field for LAO/STO(110) heterostructures was observed to be ~104 mT at 50 mK. Reyren et al.[51] showed, following the same criteria, that the out-of-plane critical magnetic field is ~100 mK for the LAO/STO(100) interface at 50 mK. Figure 6.9e and f shows that the critical magnetic fields of LAO/STO(111) at 50 mK are lower as the ones observed in the (100) and (110) orientations, namely ~20.7 mT and ~7.3 mT for the applied back-gate voltages 33 V and 60 V, respectively. The difference between the critical magnetic field of the back-gate voltages 33 V and 60 V emphasizes once more the difference in the superconducting phases above and below an applied back-gate voltage of ~57.5 V.

The in-plane coherence length can be determined with use of the critical magnetic field at the zero temperature, $\varepsilon = \left(\Phi_0/2\pi\mu_0 H_{c\perp,0}\right)^{1/2}$ (see section 2.4.2). According to the Ginzburg-Landau theory, the critical magnetic field at 0 K can be related to the temperature as:

$$H_{c,0} = H_{c,T}\left[1 + \left(\frac{T}{T_c}\right)^2\right] \Big/ \left[1 - \left(\frac{T}{T_c}\right)^2\right], \tag{6.2}$$

where $H_{c,T}$ is the critical field at a specific temperature T.[50] In section 6.2, the critical transition temperature for sample D1 is observed to be 75.5 mK at a fixed back-gate voltage of 33 V. This allows for the determination of the in-plane superconducting coherence length at a back-gate voltage of 33 V. The superconducting critical temperature at 60 V is not measured, therefore this analysis cannot be performed for the this back-gate voltage. The out-of-plane magnetic field at 50 mK is $\mu_0 H_{c\perp,50}$ (33 V) = 20.7 mT. Subsequently, equation 6.2 determines the zero temperature critical magnetic field $B_{c,0} = \mu_0 H_{c\perp,0} \approx 53.04$ mT at 33 V. With use of this zero temperature critical magnetic field the in-plane superconducting coherence length is estimated to be $\varepsilon \approx 78.8$ nm for an applied back-gate voltage of 33 V. In the LAO/STO(100) heterostructures, the in-plane superconducting coherence length is ~70 nm[51,55] while in LAO/STO(110) it is ~52 nm[50], indicating that the magnitude of the observed in-plane coherence length for the LAO/STO(111) heterostructure is reasonable.

The analysis is proceeded by a note on the superconducting film thickness determined by the in-plane critical magnetic field (equation 2.22) in LAO/STO heterostructures. The superconducting layer thickness in LAO/STO (100) and (110) oriented systems are observed to be ~12 nm[51] and ~18 nm[108], respectively. Unfortunately, in this study no in-plane magnetic field measurements are performed because of the limitations of the dilution refrigerator mentioned before. Therefore an estimate for the superconducting layer thickness is not possible. For future experiments, transport measurements with an in-plane applied magnetic field would be very useful for full characterization of the superconducting phase.

In section 6.2, the superconducting critical temperature was determined from the temperature dependence of the critical current density and the Ginzburg-Landau mean field theory (equation 6.1). The zero temperature critical current density is defined as $J_c^0 = H_{c,0}t/3\sqrt{6}\pi\lambda_0$. The fit of the Ginzburg-Landau mean field theory with the experimental data results in a zero temperature critical current density of 15.4 mA/m. By now, an estimate of the critical magnetic field and the superconducting film thickness at zero temperature are obtained such that we can test if the theory holds for our system. The superconducting film thickness (t) is taken to be 15 nm and the zero temperature critical magnetic field, $H_{c\perp,0}$= 1.65 × 10^4 A/m. The Pearl length (Λ) for LAO/STO heterostructures is ~8 mm.[109] The penetration depth (λ_0) can be related to the Pearl length using $\Lambda = 2\lambda^2/t$,[110] which results in λ_0 = 7.75 μm. Implementing these values in the equation for the zero temperature critical current density gives J_c^0= 1.38 A/m. This is two order of magnitude larger as the zero temperature critical current density predicted by the Ginzburg-Landau mean field theory, indicating that the superconducting interface cannot be considered as an homogeneous superconducting thin film and the Ginzburg-Landau mean field theory does hold anymore.

An inhomogeneous interface can be modelled by superconducting puddles imbedded in a matrix forming Josephson junctions. The total critical current density of an array of resistively coupled Josephson junctions is expected to follow the same function as an individual weak link which is $J_{JJ} = \frac{\pi}{2e}\Delta(T)/R_{JJ}\tanh(\Delta(T)/2k_BT)$ where $\Delta(T)$ is the superconducting gap.[102] The measurements performed during this study do not allow for determination of the superconducting gap or its temperature dependence. For future research, this would be a good test to see if the temperature dependence of the critical current density can be related to an inhomogeneous interface creating a Josephson-coupled array of superconducting puddles. Additionally, it possibly provides a better understanding for the observed behaviour of back-gate dependent critical current density.

Returning back to the critical magnetic field of the superconducting phase. There is a certain limit above which the force of the magnetic field breaks up the cooper pair, which is called the Pauli paramagnetic limit. The paramagnetic field gives the upper critical field at which the singlet superconductivity is destroyed by the Zeeman splitting of the electron spins.[111] The paramagnetic limiting field is defined by the Bardeen-Cooper-Schrieffer formula: $\mu_0 H_c^p = \frac{1.76k_BT_c}{\sqrt{2}\mu_B} = 1.84\,T_c$.[112] In LAO/STO(100) and (110) systems, it is observed that the limit is exceeded for the in-plane critical magnetic field while the out-of-plane critical magnetic field is well below the limit. Considering the critical transition temperature T_c = (75.5±0.9) mK, the Pauli paramagnetic limit is $\mu_0 H_c^p$ = (138.9±1.7) mT. The estimated out-of-plane magnetic field at a fixed applied back-gate voltage of 33 V does not violate the Pauli paramagnetic limit.

Hereafter, the critical current is extracted from the *VI*-curves, presented in figure 6.9a and b, by linear extrapolation of the transition region between the normal state and the superconducting state. Figure 6.10 displays monotonic decrease of the critical current density as a function of the applied magnetic field for 33 V and 60 V applied to the back-gate at 50 mK. Prawiroatmodjo et al.[102] discuss the evolution of the critical current with a varying magnetic field for an inhomogeneous interface by considering a random array of coupled Josephson junctions. The response of the critical current density for an individual uniform rectangular Josephson junction with an applied magnetic field follows a Fraunhofer pattern, $J_c \propto |\mathrm{sinc}(\pi\Phi/\Phi_0)|$ where Φ is the magnetic flux and $\Phi_0 = h/$

$2e$, the superconducting magnetic flux quantum.[112] However, for an random array of Josephson junctions the critical current density will result from a superposition of Fraunhofer patterns, such that no oscillations will be observed. The expected evolution of the critical current density with magnetic field for an array of coupled Josephson junctions is,

$$J_c \propto 1/(1 + B/B_0)^\beta \qquad (6.3)$$

where $1 \leq \beta \leq 2$ depends on the geometry of the junction and $B_0 = \Phi_0/\pi A_0$.[102,113] The average size of the junction area, A_0, can be obtained using equation 6.3 to fit the experimental data.

The black lines, in figure 6.10 display the fits of equation 6.3, relating the magnetic field to the critical current density for an array of Josephson junctions with the data. Considering the critical current density with a fixed back-gate voltage of 33 V, the fit shows a good overall agreement yielding $\beta = 1.4$ and an average junction size, $A_0 \approx 0.34 \ \mu m^2$. At an applied back-gate of 60 V (figure 6.10b), the fit and the experimental data do not to agree perfectly. For this back-gate voltage, the fitting parameters are $\beta = 1.82$ and $A_0 \approx 0.14 \ \mu m^2$. The size of the Hall bar channel on sample D1 is 25 μm x 50 μm = 1250 μm^2 which is much larger as the estimated average junction sizes such that this system allows for a distribution of superconducting puddles at the interface. Assuming the fitting parameters are correct for both back-gate voltages, then it is observed that the average size of the junction area and the geometrical factor change as the back-gate voltage is increased from 33 V to 60 V. This suggests that the geometry and the size of the Josephson junction, i.e., the superconducting puddles are affected by the magnitude of the applied back-gate voltage. This might explain earlier observation such as the behaviour of the critical current above and below the applied back-gate voltage of 57.5 V.
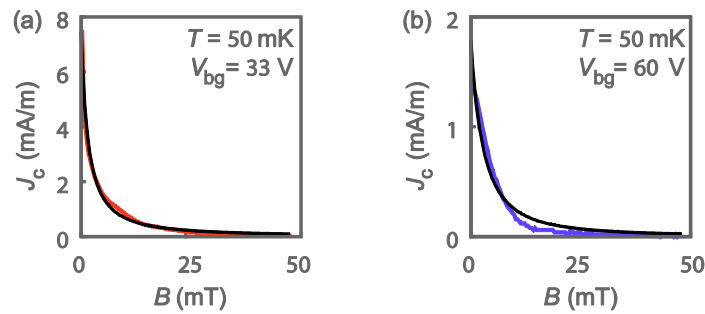
Figure 6.10: The magnetic field dependence of the superconducting critical current at 50 mK. The red and purple line corresponds to an applied back-gate voltage of 33 V and 60 V, respectively. The black line presents the fit with $J_c(B) \propto 1/(1 + B/B_0)^\beta$ [(102)].

As shown in section 6.2, the sample temperature changes the properties of the superconducting phase. Next, the temperature dependence of the critical magnetic field at an fixed back-gate voltage of 33 V is investigated. The temperature of the sample, i.e., the mixing chamber is set by a manual heater to a specific temperature. Once the sample temperature is stabilized, the applied magnetic field is varied from 0 to 7 mT in steps of 0.5 mT with a magnetic field sweep rate of 1.55 mT/s. The sweep rate of the magnetic field has to be chosen carefully. A fast changing magnetic flux will induce eddy currents in metal components of the dilution refrigerator with a finite resistance. Subsequently, this can induce an increase in the temperature of the mixing chamber hence the sample temperature. In order to allow changes caused by the changing magnetic flux to stabilize, the *VI*-characteristic are taken 22 seconds after the stabilization of magnetic field. After each step in the applied magnetic field step, the temperature as well as *VI*-characteristic are measured.

Figure 6.11a shows the temperature after each magnetic field step at a fixed back-gate voltage of 33 V. It displays a fairly stable temperature and determines the average temperature of this specific measurement to be (51.17±0.17) mK. The critical current is obtained from the *VI*-curves, i.e., the maximum of the d*V*/d*I*, while ramping the magnetic field up and down. Figure 6.11b displays the results for the magnetic field sweep at ~51 mK. The blue data is recorded during the ramp up of the magnetic field and the red data is measured while ramping down. The critical current shows a monotonic decrease when ramping up. During the ramp down, the critical current displays the same trend with a slight increase of the magnitude. Overall, the critical current display a similar trend while ramping up and ramping down at all considered temperatures between 43 mK and 61 mK, indicating that the magnetic field sweeps do not significantly influence the magnetic field response of the superconducting critical current. Above 61 mK, the differential resistance does not properly define the critical current.
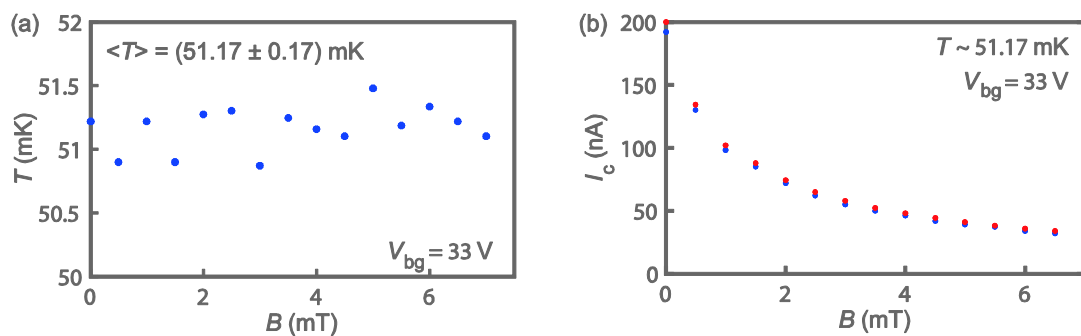
Figure 6.11: a) The temperature as a function of the magnetic field. The average temperature of the measurement is determined from the specific temperature at each magnetic field determining the average temperature to be (51.17±0.17) b) The variation of the superconducting critical current with a varying magnetic field ramping up (blue) and ramping down (red), considering the temperature ~51 mK at an applied back-gate of 33 V.
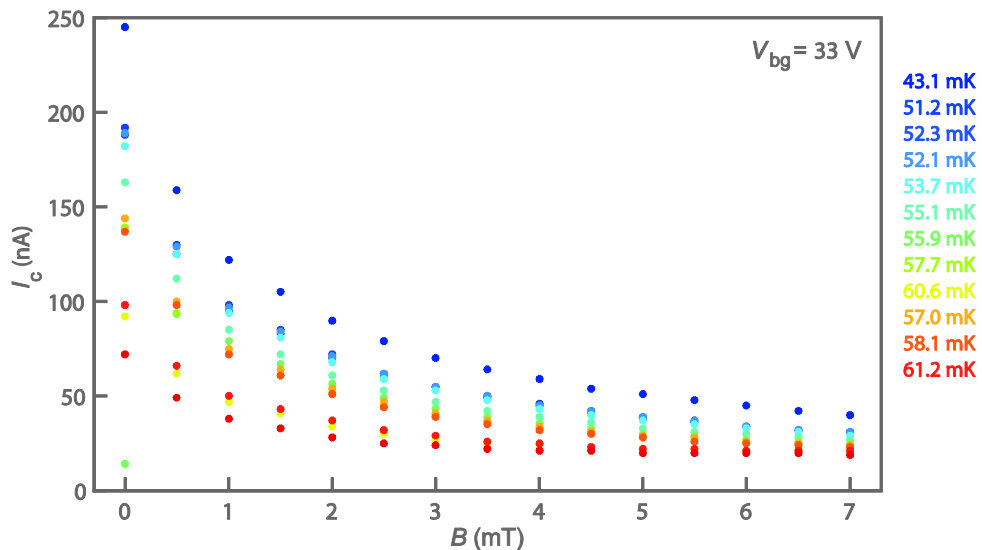
Figure 6.12: The critical current as a function of the magnetic field at different temperatures ranging from 43 mK to 61 mK. at an applied back-gate voltage of 33 V.

Figure 6.12 displays superconducting critical current as a function of the magnetic field at different temperatures for a fixed back-gate voltage of 33 V. Besides the monotonous decrease in superconducting critical current with increasing magnetic field, the critical current is clearly suppressed by an increasing temperature. Furthermore, it observed that the in influence of the temperature is more drastic at lower applied magnetic fields in comparison to the higher magnetic

field. Moreover, the critical current seems to saturate around 20 nA at the highest applied magnetic fields. Overall, the magnetic field range of 0 mT to 7 mT does not allow for completely suppression of the superconducting phase for the considered temperatures indicating that the magnitude of the magnetic field is not sufficient to determine the critical magnetic field. It was observed that the critical magnetic field at 50 mK is ~20 mT such that in order to obtain the temperature dependence of the critical magnetic field, the maximum applied magnetic field during the voltage sweep has to be larger than 20 mT.

7. Conclusions

7.1 Summary

Since its discovery, the 2DES hosted at the LAO/STO(100) interface has been studied extensively. Only a reduced number of interfaces has been observed to display a 2DES, which challenges the understanding of these emerging properties that do not exist in bulk. Recent observation of a 2DES at the interface of (110) and (111) oriented LAO/STO heterostructures opens up new possibilities for unravelling the nature of the 2DES as well as novel electronic properties. Furthermore, the existence of a gate-tunable superconducting ground state in the LAO/STO(100) interface is already well established and its presence in LAO/STO(110) heterostructure has been observed. However, superconductivity in LAO/STO(111) heterostructures has not been reported on.

In this work, a magnetotransport study on the 2DES of LAO/STO(111) heterostructures at different temperatures and applied back-gate voltages is performed in order to investigate its electronic and superconducting properties. The heterostructures are prepared by depositing LAO thin films on single Ti-rich terminated STO(111) substrates using PLD. Subsequently, the interfaces are patterned into Hall bar geometries by means of electron beam lithography. The magnetotransport measurements are performed in a flow cryostat with a base temperature of 1.5 K whereas the measurements on the superconducting phase are conducted in a dilution refrigerator with a base temperature of 40 mK. Both refrigerators are equipped with a superconducting magnet.

Firstly, an attempt to single terminate the STO(111) substrates by means of BHF etching and heat treatment in an oxygen environment has been made. A wide range of different etching times, annealing temperatures, annealing times and the oxygen flows have been explored, however not yielding single terminated STO(111) substrates. At first, contamination of the substrates surface was observed to originate from the quartz tube. A clean tube allows for successful termination of STO(100) substrates. However, single termination of the STO(111) substrates was not achieved, possible due to a poor quality of the substrates.

LAO/STO(111) heterostructures display a thickness dependent sheet conductivity. The critical film thickness is experimentally observed to be 9 uc. Modelling the structure of charged atomic planes as a series of coupled parallel plate capacitors predicts the critical film thickness of 11 uc. However, including the non-linearity of the polar discontinuity, the critical film thickness is estimated to be 8 uc. The mismatch between the proposed models and the experiments is analysed by considering the assumptions made on the physical parameters used for modelling the potential in the thin film.

The sheet resistivity in LAO/STO(111) heterostructures as a function of the temperature showed that higher growth temperatures result in a higher conductivity due to the enhancement of the diffusivity during the growth, which reduces the inhomogeneities at the interface. Furthermore, the samples with a 9 uc LAO film are metallic down to 1.6 K while the sample with 10 uc LAO film displays a low temperature resistivity upturn which can be attributed to the Kondo effect.

Furthermore, the temperature dependent Hall resistance for samples in the native state displays a linear Hall effect down to 1.5 K, indicating that the electronic transport is dominated by single band conduction in the magnetic field range considered. The sheet carrier density is determined to be $\sim 2 \times 10^{13}$ cm^{-2} and $\sim 4.5 \times 10^{13}$ cm^{-2} for the samples with growth temperatures of 770 °C and 840 °C, respectively. The magnitude of the electron mobility is observed to rapidly increase when the temperature is reduced due to freeze out of the acoustical phonon vibrations. At the lowest temperatures, the mobility saturates at $\mu_{770\,°C} = 670$ cm^2/Vs and $\mu_{840\,°C} = 960$ cm^2/Vs. The evolution of the electron mobility reflects in the magnetoresistance where the magnetoresistance becomes negligible at high temperatures while the classical B^2-component is apparent at low temperatures. Additionally, low temperatures also reveal quantum corrections at small magnetic fields.

We have shown that the back-gate voltages allows for the modulation of the electronic conduction at the interface. It is observed that by adding carriers to the interface, the sheet resistivity decreases. Electrostatic tuning of the sheet resistivity is observed to be strongly dependent on the width of the Hall bar channel. Furthermore, the Hall effect displays non-linearity above a certain level of electrostatic doping, indicating the presence of a second type of carrier with a low mobility. The origin of the second conduction band is discussed considering the band structure of LAO/STO(111) heterostructures. The presence of a second low mobility carrier is clearly visible in the magnetoresistance. The single band conduction results in a magnetoresistance of $\sim$ 3 %, while the existence of a second conduction band raises the total magnetoresistance to $\sim$ 18 % in the considered magnetic field range.

Furthermore, the electrostatic modulation of the inelastic and spin-orbit scattering times is determined using the Maekawa-Fukuyama formula. The inelastic scattering time was fairly constant while a decrease in the spin-orbit scattering time is observed with an increasing back-gate. However, in the whole range of back-gate voltages, the inelastic scattering time is significantly longer compared to the spin-orbit scattering time, indicating that the quantum correction is due to weak anti-localization characterized by a strong spin-orbit interaction. The spin-orbit scattering time determines the energy of the spin splitting to be $\sim 2.2 - 2.8$ meV.

Lastly, we have demonstrated that the two-dimensional electron system of an LAO/STO(111) heterostructure condenses into a superconducting state. At optimal electrostatic doping, the maximal critical current density at 50 mK is observed to be 8 mA/m, the superconducting BKT transition temperature is $\sim$70 mK and the in-plane coherence length is $\sim$78.8 nm. The back-gate voltage shows remarkable tuning of the critical current, indicating the presence of two different superconducting phases. One phase, at low levels of electrostatic doping, that displays sharp switching between the superconducting and resistive phase and which is sensitive to electrostatic tuning. Above a certain level of doping, a second phase becomes apparent. This phase shows a lower critical current, gradual switching and the response to electrostatic field is less prominent. The normal state resistance shows a monotonic decrease with increasing back-gate voltage. Furthermore, the magnetic field modulation results in out-of-plane critical magnetic fields of 20.7 mT and 7.3 mT in the low and high levels of electrostatic doping, respectively.

The peculiar behaviour of the superconducting phase in the LAO/STO(111) is possible related to an inhomogeneous interface. This interface can be considered as superconducting puddles embedded in a matrix such that the interface conduction can be modelled as an random array of Josephson junctions. The magnetic field dependence of the critical current density shows a monotonous decrease in magnitude. By modelling the evolution of the critical current as an array of Josephson junction, an average junction size of 0.34 μm^2 and 0.14 μm^2 is obtained for low and high electrostatic levels of doping, respectively. Furthermore, the model indicates differences in the geometry of the superconducting puddles in the two regions, which again indicates the existence of two different phases.

7.2 Perspectives

The electronic and especially the superconducting properties in LAO/STO(111) heterostructures are relatively unexplored. In this work, we have paved the way by investigating the interface conduction with *VI*-characteristics using Hall bar geometries. However, more research has to be conducted to provide a better understanding of the physics at play at the interface of this heterostructure.

In view of the surface treatment, I would suggest to performed a similar treatment on unterminated STO(111) substrates from a different batch because the treatment seems to be unsuccessful due to the quality of the substrates. X-ray spectroscopy on the substrates used in this study can confirm this assumption.

Thereafter, we have seen that the sheet conductance peaks at the critical thickness which is consistent with literature. The interface of the sample with an 11 uc film is determined to be insulating while previous research showed metallic behaviour. The conductivity of such an 11 uc heterostructure needs to be confirmed on a new sample.

The temperature dependent Hall effect has been investigated for a magnetic field range of $\pm$ 5 T. However, the back-gate dependent Hall effect showed the presence of a second conduction band at a magnetic field of 5 T. I would suggest to conduct additional temperature dependent Hall effect measurements in a wider range of applied magnetic fields in order to see if features of a second conduction band become apparent. Furthermore, it would be interesting to conduct magnetotransport measurements as a function of temperature at the different doping levels, e.g., at doping levels that can present the two different superconducting phases. As mentioned, the back-gate dependent Hall effect displays non-linearity above a certain back-gate voltage. Applying a higher back-gate voltage will provide more information on the sheet carrier density and electron mobility of the second conduction band. Furthermore, a saturation of the slope above the deflection point is not reached such that a larger magnetic field range is necessary to obtain accurate electronic properties.

Additionally, we have demonstrated that the magnetoresistance contains in a low temperature quantum correction due to weak anti-localization. When including magnetoresistance measurements at negative back-gate voltage, it is expected to observe a transition from weak-anti localization to a weak localization regime. Furthermore, this would allow for better understanding of the evolution of the spin splitting with applied back-gate voltage.

All the magnetotransport measurements presented in this section, are performed on two samples with different LAO film thickness and different dimensions of the Hall bar channels. New samples need to be fabricated with similar film thickness or Hall bar channel size, to investigate the influence of the individual parameters on the electronic transport.

The superconducting phase of the LAO/STO(111) heterostructure is investigated in a sample with a 10 uc thick film. While this is the first observation of the superconducting phase in this crystallographic orientation, the performed measurements should be repeated in a different sample to confirm that the observed physics of the superconducting phase are representative for LAO/STO(111) heterostructures. Furthermore, it would be interesting to explore the superconducting phase of a sample with a 9 uc LAO film since the conductivity peaks at this thickness.

The results acquired from this study can be improved. A larger range of applied back-gate voltages will allow for observations of the complete evolution of the critical current with electrostatic doping. Because of the limitation of the dilution refrigerator, only a limited number of temperatures are used to investigate the temperature dependence of the critical current. Automated control of the temperature will allow for a high resolution resistivity and critical current measurements such that a more accurate estimation of the superconducting transition temperature can be determined.

Additional magnetic field studies can be used to acquire more information on the behaviour of the two different superconducting phases that have been distinguished. An in-plane magnetic field study should be performed such that the critical magnetic field can be obtained which determines the superconducting layer thickness. Furthermore, the dome-shaped evolution of the critical current is not completely suppressed by the out-of-plane magnetic field range under consideration. Similar experiments could be carried out with a wider range of magnetic fields showing a full transition to the resistive state could be executed. Thereafter, we have determined the out-of-plane critical magnetic field at two different levels of electrostatic doping. *VI*-measurements with a varying magnetic field at additional back-gate voltages can provide the electric field dependence of the critical magnetic field which allows for the investigation of the characteristics of the superconducting puddles from the magnetic field dependent critical current density. Finally, the measurements regarding the evolution of the critical magnetic field as a function of the temperature should be redone in a wider range of magnetic field such that the magnetic field completely suppresses the superconducting phase.

Acknowledgements

First of all, I would like to thank Dr. Andrea Caviglia for the opportunity to do this exciting research in the stimulating environment of his group. One of the main reasons for performing my master project in this group was his drive and enthusiasm which inspired me. I would like to extend my gratitude to my mentor Mafalda Monteiro, who provided me with a lot of support and guidance. During the months of my thesis, she thought me almost everything I needed to know to make this thesis a success from the sample growth and fabrication to how to conduct electronic measurement in cryogenic devices. I am also thankful for the support of Prof. Dr. Barend Thijsse. Furthermore, I would like to thank the other graduate students and the postdoc of the group Emre, Giordano, Dirk and Nicola for the fruitful discussions and of course for playing beach volleyball with me whenever the sun was out. Lastly, I would like to say thanks to all the people from MED who make me feel welcome and made the experience even more pleasant.

Appendix A: Cryostat Cooldown Manual

December 8, 2015

The Navy Beach Cooldown Manual
CavigliaLAB

The Navy Beach is an Oxford Instruments Spectromag series low loss cryostat, equipped with a superconducting magnet system. It is an all metal construction with vacuum insulation and intermediate temperature radiation shielding. Figure 1 shows a schematic of the cryostat highlighting the nitrogen jacket(pink), helium jacket(purple), sample space(green) and the magnetic coils (yellow). A vacuum jacket (white) separates the sample space, helium and nitrogen jacket, serving as isolation.
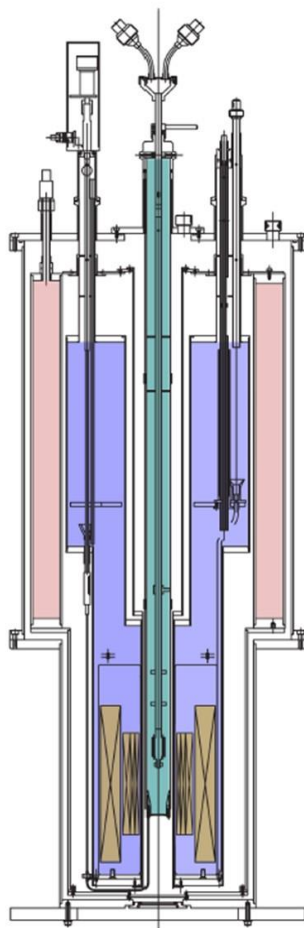
Figure   1: Schematic representation of the cross-section of the flow cryostat. Different colors highlight the main areas: the nitrogen jacket (pink), the helium jacket (purple), the sample space (green, the superconducting magnet coils (yellow) and the vacuum jacket (white).

LEGEND.		
1	N2 SAFETY VALVE.	
2	EYE BOLTS (2 OFF)	M8
3	WIRING FOR HELIUM LEVEL PROBE.	
4	VTI AUTO NEEDLE VALVE	
5	S/SPACE EXAUST & VAC VALVE(NW16)	NW25
6	SAMPLE SPACE Ø37.0 REF.	NW40
7	WIRING FOR VTI.	
8	O.V.C. 3/4 VAC VALVE & SAFETY	NW25
9	WIRING FOR SWITCH & A/B°S.	
10	120amp CO-AX CURRENT LEAD	
11	SYPHON ENTRY	Ø9.5
12	WIRING FOR NEEDLE VALVE.	
13	QUENCH VALVE 2 OFF	NW25
14	HELIUM RECOVERY MANIFOLD.	NW25
15	N2 STACKS FILL/VENT.	
16	SAMPLE ROD WITH 2x18 PIN FISCHER	NW40
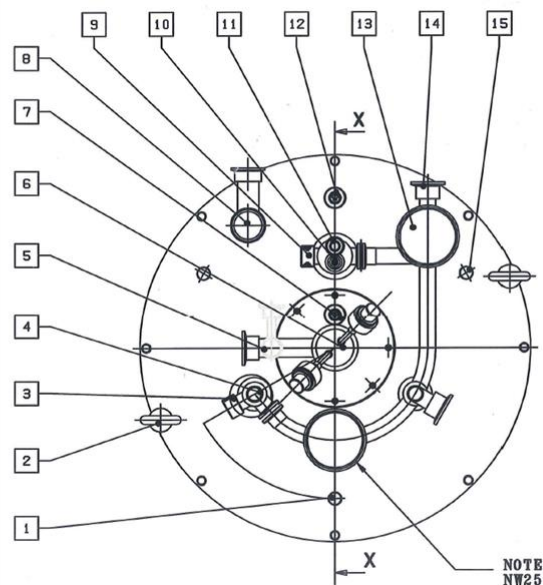
Figure 2: *Schematic representation of the topview of the cryostat. The legend referes to the numbers in the schematic which identify the different inlets, outlets, motors etc.*
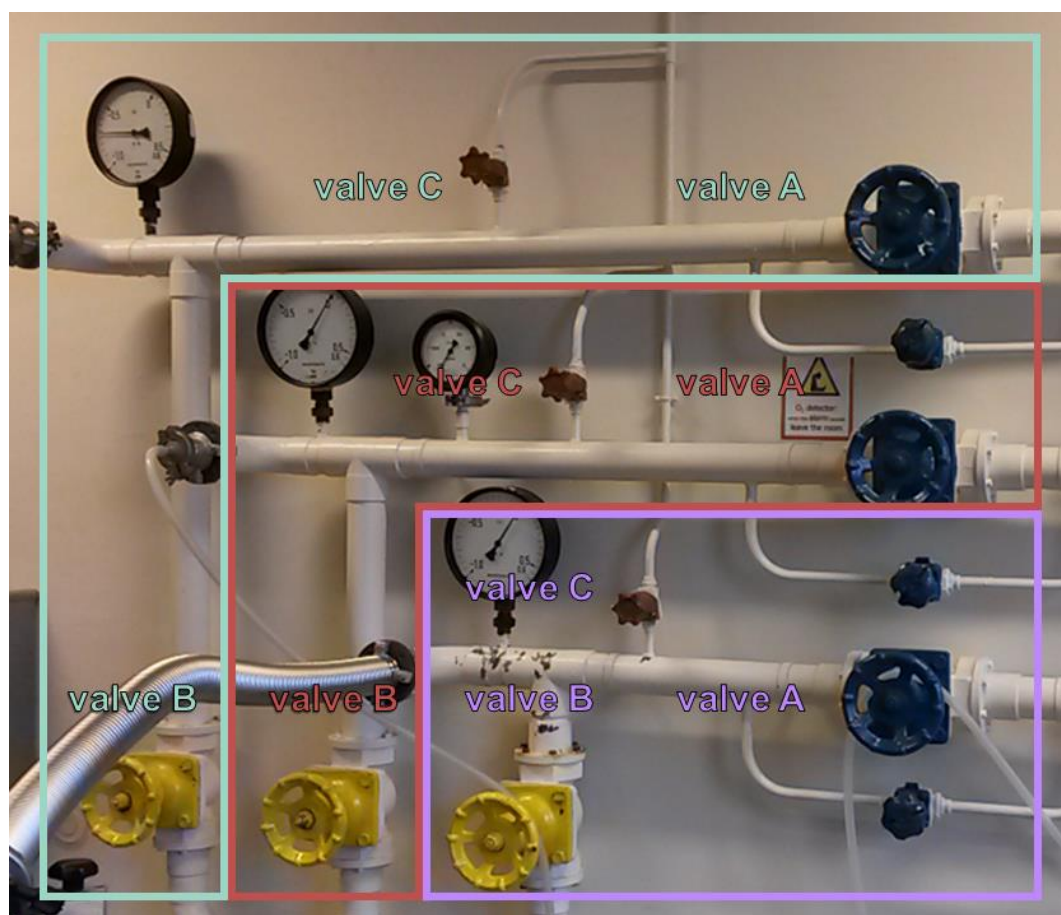
Figure 3: *Image of the wall where three block are drawn each containing a pump line (big blue knobs), helium recovery (yellow knobs), helium supply (brown knobs) (indicated by valve A, valve B and valve C, respectively) and the respective pressure meters. The green lock (g) is connected to the sample space, the purple block (p) is connected to the helium jacket and the red block (r) is normally not connected.*

Figure 2 shows the topview of the cryostat. The numbers represent the different components which are identified in the legend. Figure 3 displays the wall next to the cryostat. Each of the coloured valves is connected to a different line, as follows:

- Blue: valve of the pump line (**valve A**)
- Yellow: valve of the helium recovery line (**valve B**)
- Brown: valve of the helium supply (**valve C**)

Nitrogen vessel and Helium dewars

The nitrogen vessels should be picked up from the basement in the hallway near room B-04 Before taking the vessel to the lab, check to amount of nitrogen with the meter at the top of the vessel. Furthermore make sure there is a nozzle attached to the outlet of the vessel. When a nitrogen vessel is empty and has to be returned, the vessel should brought inside room B-04.

The helium dewar can be picked up at the ground floor from room B008 On the touch screen in the room it can be checked which dewars are filled. Here, one has to indicate which dewar is going be taken and on who's name. In order to take a dewar, close the exhaust valve of the dewar first. Subsequently, disconnect the exhaust from the helium recovery line. Finally, close the valve of the helium recovery line. In the lab the exhaust of the helium dewar need to be connected with a rubber tube to the free helium recovery line (**Br**) on the wall. This done by closing the rubber tube of the recovery line by folding it and open the valve of the recovery line (**valve Br**). Thereafter, connect the rubber tube to the exhaust of the dewar and open the exhaust.

The transport of the nitrogen vessels and helium dewars has to be done with the left elevator in the C wing close to the head entrance. An authorised campus card can block the elevator for other users to provide save transportation. Swipe the card for the sensor and read "voorkeur" (preference) above the elevator. Swipe the card for the sensor in the elevator (within 30 seconds) and the display outside the elevator will read "TU transport" on all floors. Put the vessel or dewar inside the elevator. Continue by pressing the button of the floor number you need to go to. Get out of the elevator hence do not travel with the same elevator as the vessel/dewar. Hold you card again in front of the sensor in the hall way and the elevator will transport the vessel or dewar to the preferred floor. The elevator will not open until your card is swiped in front of the sensor at the preferred floor. Take the vessel or dewar out when the doors are opened. Finally, the elevator needs to be unblocked by swiping the cards for the sensor inside the elevator. Now, you should read the current floor number above the elevator.

Steps for cooling down the system from room temperature

The first step of a cool down of the system from room temperature, is pumping down vacuum jacket. This is followed by filling the helium jacket with nitrogen to pre-cool it down to 77 K. Thereafter the nitrogen in the helium jacket is transferred to the nitrogen jacket. Subsequently, the nitrogen jacket is completely filled with nitrogen from a nitrogen vessel. At this stage the system will be at 77 K. Finally, helium will be transferred from a helium dewar to the helium jacket. In short, the steps that need to be performed are the following:

1. Pump the vacuum jacket

2. Pre-cooling of the Helium jacket with Nitrogen

3. Transfer of Nitrogen from Helium to Nitrogen jacket

4. Transfer of Nitrogen from the vessel to the jacket

5. Frozen needle valve check

6. Transfer of Helium to the Helium jacket

1. Pump the vacuum jacket

A Hicube (Pfeiffer) turbopumping station is used to pump the vacuum jacket. When the pump is connected to the Navy Beach there are three important valves. Valve1 is located at the beginning of the vacuum line at the pump side. Furthermore on top of the system there are two more valves represent by no. 8 in figure 2. These valves are labelled valve2 (outer valve) and valve3 (inner valve).

1. Connect the pump to the valves (2 and 3) on top of the system with use of the vacuum line.

2. Make sure valve2 and valve3 are closed.

3. Open valve1 and turn on the pump (there is an ON/OFF button at the back and a menu button at the front.

4. Wait until the pressure sensor reads $\sim 10^{-5}$ mbar (see display on the pump)

5. Open valve2

6. Read the pressure variation from the display on the pump

   o if the pressure is increasing (a tiny bit): open valve3
   o if the pressure is **not** increasing: check if valve1 is open

7. Wait until the pressure reads $\sim 10^{-7}$ mbar (dynamic pressure)

8. Read the static pressure in the following way:

- o Close valve3
- o Wait 10 min.
- o Open valve3
- o Check if the pressure < ~10^{-6} mbar
  - if yes: close first valve3 and subsequently valve2.
  - if no: pump for a longer time and repeat the procedure described above until the static pressure is at the desired value.

9. If the desired static pressure is reached, valve3 and thereafter valve2 are closed. In order to detach and turn off the pump follow the next procedure:

   - o Close the valve1
   - o Turn of the vacuum pump (with the menu button at frontside of the pump, below the display)
   - o Wait for the pump to be vented (the venting will be done automatically by the station)
   - o When the pressure is above 300 mbar, disconnect the pump from the Navy by decoupling of the vacuum line at the Navy side (close to valve2)
   - o Close the end of the line with a (plastic cap or an O-ring and a metal cap)
   - o Turn off the pump at the backside of the station
   - o Return the pump to the second floor

2. Pre-cooling of the Helium jacket with Nitrogen

The temperature of liquid nitrogen is 77 K whereas the temperature of liquid helium is 4 K. Because the complete system is at room temperature, the helium jacket will be pre-cooled to 77K with liquid nitrogen in order to minimize the evaporation of helium.

1. Check if the needle valve is closed such that no nitrogen can leak away into the sample space. This should be done as follows:

   - o Turn off the ITC4 (which is located in the rack)
   - o Wait for a few seconds
   - o Turn on the ITC4 (during the start-up, the program automatically closes the needle valve)
   - o Check if the motor of the needle valve is rotating. (see figure 2 no. 4)

If the motor is not rotating hence the needle valve does not close, go to section 5. Frozen needle valve check. If the motor is rotating, the needle valve is being closed. Continue by releasing the vacuum in the helium jacket and create a slight overpressure inside. The overpressure will prevent surrounding air or dust from going inside the jacket. Subsequently, disconnect the helium jacket from the helium recovery line.

2. Close the connection between the helium recovery line and the helium jacket (figure 3, **valve Bp**)

3. Open the helium supply (figure 3, **valve Cp**) of the helium jacket until you read 1.2 bar (this will create an overpressure)

4. Disconnect the (silver) exhaust line of the helium jacket (no.14) from the recovery line and close the end of the recovery line with a cap

5. Open the helium jacket by removing the cap from the transfer tube valve (no.11)

6. Bring the metal tube (which is hanging in the blue locker close to the window) inside the helium jacket with the grooves pointing downwards

7. In order to make sure the lower part of the Navy, which contains the superconducting magnet, is also filled with nitrogen and cooled down, the tube has to be connected at bottom of the upper part of the system. This can be done by screwing the tube in a hole at the bottom.

8. Tighten the (black) ring at the opening of the helium jacket to seal the space

9. Make sure the pressure in the nitrogen vessel is around 1.25 bar

10. Connect the metal tube to the nitrogen vessel with a transparent rubber tube

11. Open the nitrogen vessel

12. Hold the rubber tube until it freezes

13. If the pressure in the nitrogen vessel is to low (< 1 bar), open a bit the pressure valve on the vessel

    There is no meter to read out the amount of nitrogen inside the helium jacket. Therefore the jacket needs to be filled until the nitrogen is spraying out of the exhausts of the helium jacket. To stop the transfer continue with the following steps.

14. Close the nitrogen vessel

15. Defrost the rubber tube with use of a heat gun

16. Decouple the nitrogen vessel and the helium jacket by removing the rubber tube

17. Leave the metal tube inside the helium jacket

3. Transfer of Nitrogen from Helium to Nitrogen jacket

1. Connect the metal tube in the helium jacket (no.11) to the opening of the nitrogen jacket (no.15) with a transparent rubber tube

2. Take the cap of the recovery line of the helium jacket and connect it again (do not open the recovery valve yet)

3. Open the helium supply (**valve Cp**), if necessary, in order to create an overpressure in the helium jacket (to accelerate the transfer to the nitrogen jacket)

4. Keep track of the gas outlet of the second exhaust of the nitrogen jacket (no.1). When the gas outlet is minimal the transfer is completed.

5. Defrost the rubber tube with a heat gun

6. Decouple the tube and unscrew the stick when the tube is defrosted

7. Remove the metal tube and close the helium jacket with the dust cap

8. Turn on the pump connected to the pump line by pressing "aan" in the pump room

9. Open the valve between the pump line and helium jacket (**valve Ap**)

10. Check if the helium jacket does not contain any nitrogen by reading the pressure

   o If pressure is -1: all nitrogen is gone.
   o If pressure is > -1 (i.e. the N_2 vapour pressure): there is still nitrogen inside the vessel! reconnect the jackets and increase the helium pressure in the helium jacket (**valve Cp**)

11. Flush the helium jacket (twice)

   o Close the valve between the pump line and helium jacket (**valve Ap**)
   o Inject helium (**valve Cp**) until the pressure reads 1 bar
   o Close the helium inlet (**valve Cp**)
   o Open the pump line again (**valve Ap**)

12. Keep pumping on the helium jacket for a while (overnight if possible)

4. Transfer of Nitrogen from the vessel to the jacket

After transferring the nitrogen from the helium jacket to the nitrogen jacket the percentage of nitrogen in the jacket will be around 28%. To reach 100%, more nitrogen has to be added to the jacket using a nitrogen vessel.

1. Connect the nitrogen vessel to the inlet of the nitrogen jacket with the transparent rubber tube

2. Make sure the pressure in the vessel is sufficiently high

3. Open the nitrogen vessel

4. The nitrogen meter on the computer (GIO level monitor) can be used to monitor the amount of nitrogen inside the jacket

5. The transfer can be accelerated by increasing the pressure in the nitrogen vessel

6. When the jacket is filled, close the vessel

7. Defrost the rubber tube with use of the heatgun and disconnect the jacket and the vessel

8. Close of the inlet and outlet of the nitrogen jacket

5. Frozen needle valve check

During the filling of the jackets, the needle valve is in principle closed. To control the temperature of the sample during measurements the needle valve should be able to open and close. If the valve is frozen this movement will be blocked. Therefore a check needs to be performed, to see if the valve is frozen. If the valve is blocked, the valve needs to be defrosted. The valve can be controlled with the gas flow using the program called GIO temperature monitor. Open reads 99% gas flow, closed is 0% gas flow.

1. Make sure the valves between the pumps and the sample space (**valve Ag**) and the helium jacket (**valve Ap**) are closed

2. Needle valve should be closed (gas flow is 0%)

3. Open the helium supply line (**valve Cp**) to let helium gas in the helium jacket

4. Open the needle valve (set gas flow to 20%)

5. Check if the pressure in the sample space is increasing when opening the needle valve and check if the motor (no. 4) is rotating

6. If the pressure does not change and/or the motor is not rotating the valve is blocked

7. In order to remove the blockade (e.g. ice) the valve can be gently heated

8. Make sure the sensor in the rack is at the position "needle valve"

9. Turn on the heater near the needle valve by applying 15V with the power supply in the rack

10. Read the resistance which can be converted to temperature with the sheet on the wall

11. The resistance should decrease when warming up

12. Try to open the valve once in a while to see if the valve defrosts

13. To check if the valve is open:

    - Check if the valve between the pump and helium jacket (**valve Ap**) is closed
    - Open the helium supply line to the helium jacket (**valve Cp**)
    - Check the pressure on the vacuum jacket (if the valve is open it should increase)
    - Close the valve of the helium supply (**valve Cp**) if the pressure increases

14. Turn off the power supply for the heater when the valve can be controlled again

15. Open the valve between the pump line and sample space (**valve Ag**)

16. Close the needle valve

17. Open the valve between the pump line and the helium jacket (**valve Ap**)

18. After a while close the valve between the pump line and the helium jacket (**valve Ap**)

19. Open the valve between the helium recovery line and the helium jacket (**valve Bp**)

6. Transfer of Helium in the Helium jacket

In the end, the helium jacket needs to be filled with helium from a helium dewar.

1. Close valve between the exhaust of the helium dewar and recovery line (**valve Br**)

2. Open the top bore of the helium dewar

3. Put the helium transfer line with one leg into the helium dewar

4. **Do not** put the other leg of the transfer line in the cryostat yet

5. Slowly push the leg inside the dewar (make sure the orange balloon keeps a normal size)

6. Wait until a white plume of helium comes out of the second leg

7. Remove the cap form the transfer tube valve (no. 11) on top of the cryostat

8. Put the second leg of the helium transfer line in the transfer tube valve of the helium jacket (no. 11)

9. Seal this connection with the black ring around the (second) leg

10. Turn the helium reading to "high". The helium meter on the computer, GIO levels monitor can be used to monitor the amount of helium inside the jacket.

11. The transfer can be accelerated by increasing the pressure in the helium vessel by connecting an aquarium pump between the recovery line and the exhaust of the helium dewar

    o Connect the helium recovery line to the "in" connection of the aquarium pump with a rubber tube
    o Open the valve between the recovery line and the aquarium pump (**valve Br**)
    o Turn on the aquarium pump and check if there is a helium flow coming out of the "out" connection
    o If there is a flow, turn the pump off
    o Connect the "out" connection of the aquarium pump to the exhaust of the helium dewar with a rubber tube
    o Open the exhaust of the helium dewar

12. When the jacket is at 90%, disconnect the aquarium pump as follows:

    o Turn the aquarium pump
    o Close the exhaust of the helium dewar
    o Disconnect the aquarium pump and the helium dewar
    o Disconnect the aquarium pump and the helium recovery line (keep the rubber tube close by folding it)
    o Connect the helium recovery line to the helium dewar
    o Open the exhaust of the helium dewar

13. When the jacket is at 95%, pull up the "first leg" of the transfer line, which goes into the helium dewar

14. Take the "second leg" of the transfer line out of the helium jacket

15. Close the transfer tube valve of the helium jacket

16. Turn the helium reading rate to "low"

DONE!

Appendix B: Schematic of Cleanroom Processing

Legend

- STO
- LAO
- PMMA A3 495
- PMMA A6 950
- Aquasave
- Titanium
- Gold

Step 1: Contacts & Markers

Plane sample

Spinning

E-beam exposure
(gold pads location)

Removal of Elektra
(with H$_2$0)

Removal of e-beam
exposed area
(with MIBK)
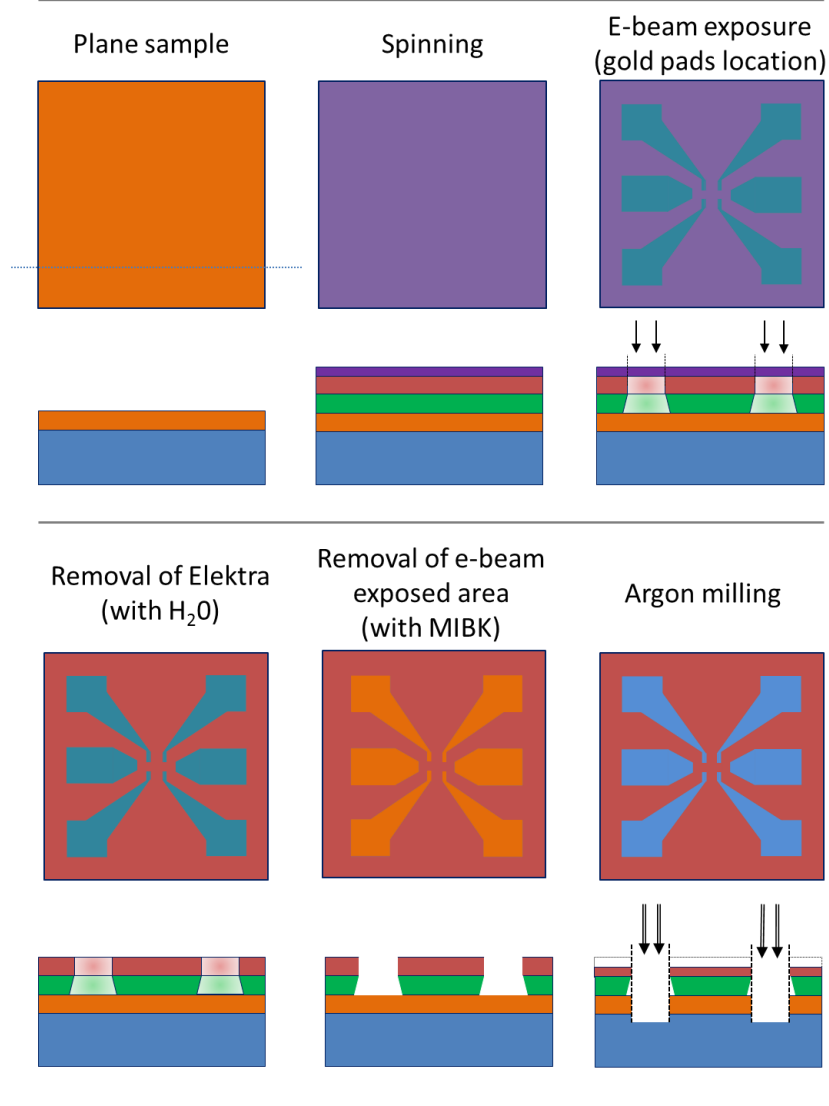
Argon milling

Titanium deposition
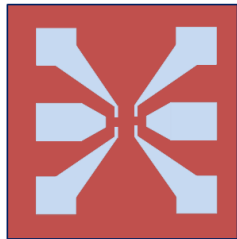
Gold deposition
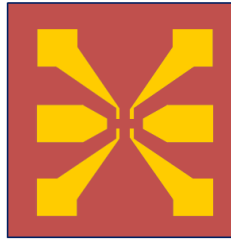
Lift-off

Step 2: Hall bar channels

Spinning
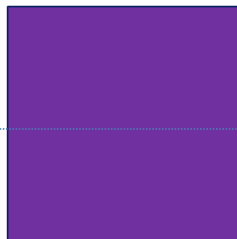
E-beam exposure
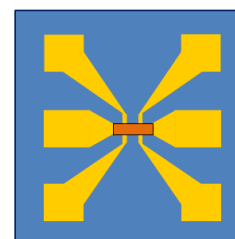(of the area around
the hall bar)
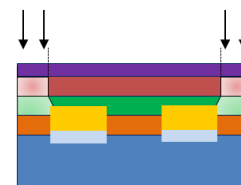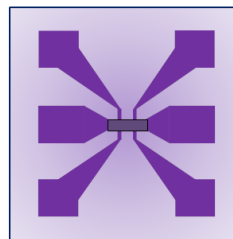
Removal of aquasave
(with H_2O)
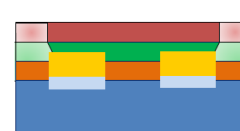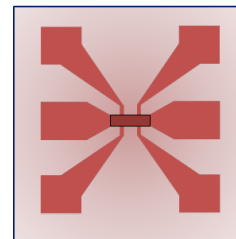
Removal of exposed
area
(with MIBK)
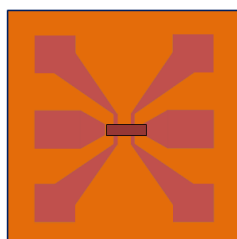
Argon milling
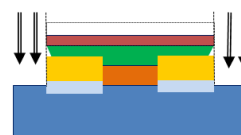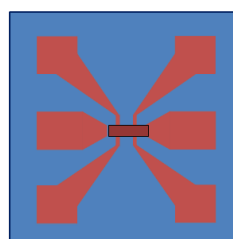
Lift-off

Appendix C: Sample catalog

C.1 Sample catalog of the surface treatment

Sample	Pre-annealing			BHF etching	Post-annealing		
	temperature	time	oxygen flow	time	temperature	time	oxygen flow
STO(100)							
A1$_a$	-	-	-	30 sec.	950 °C	1.5 hours	0 L/hour
A1$_b$	-	-	-	30 sec.	-	-	-
A2$_a$	-	-	-	30 sec.	950 °C	1.5 hours	2 L/hour
A2$_b$	-	-	-		950 °C	1.5 hours	2 L/hour
A3	-	-	-	30 sec.	950 °C	1.5 hours	10 L/hour
A4	950 °C	1.5 hours	8 L/hour	30 sec.	950 °C	1.5 hours	8 L/hour
STO(111)							
B1$_a$	-	-	-	30 sec.	1000 °C	2 hours	2 L/hour
B1$_b$	-	-	-	30 sec.	1000 °C	5 hours	2 L/hour
B2$_a$	-	-	-	30 sec.	1000 °C	6 hours	2 L/hour
B2$_b$	-	-	-	30 sec.	1000 °C	6 hours	2 L/hour
B3	-	-	-	30 sec.	1100 °C	6 hours	2 L/hour
B4	-	-	-	30 sec.	1100 °C	12 hours	2 L/hour
B5	-	-	-	30 sec.	1100 °C	24 hours	2 L/hour
B6	-	-	-	30 sec.	950 °C	6 hours	2 L/hour
B7$_a$	-	-	-	30 sec.	-	-	-
B7$_b$	-	-	-	60 sec.	-	-	-
B7$_c$	-	-	-	90 sec.	-	-	-
B7$_d$	-	-	-	180 sec.	-	-	-
B7$_e$	-	-	-	300 sec.	-	-	-
B8	-	-	-	30 sec.	950 °C	1.5 hours	8 L/hour
B9$_a$	950 °C	1.5 hours	8 L/hour	30 sec.	950 °C	1.5 hours	8 L/hour
B9$_b$	-	-	-	30 sec.	-	-	-
B10	950 °C	1 hour	8 L/hour	30 sec.	-	-	-

C.2 Sample catalog of the PLD growth of LaAlO$_3$/SrTiO$_3$(111) heterostructures

Sample	Deposition			Post-annealing		
	temperature	Oxygen pressure	# unit cell	temperature	time	oxygen pressure
C1	770 °C	6x10^{-5} mbar	8	600 °C	1 hour	300 mbar
C2	770 °C	6x10^{-5} mbar	9	600 °C	1 hour	300 mbar
C3	770 °C	6x10^{-5} mbar	10	600 °C	1 hour	300 mbar
C4	770 °C	6x10^{-5} mbar	11 (275 pulses)	600 °C	1 hour	300 mbar
D1	845 °C	6x10^{-5} mbar	10	600 °C	1 hour	300 mbar
D2	845 °C	6x10^{-5} mbar	9 (211 pulses)	600 °C	1 hour	300 mbar
D3	845 °C	6x10^{-5} mbar	9	600 °C	1 hour	300 mbar

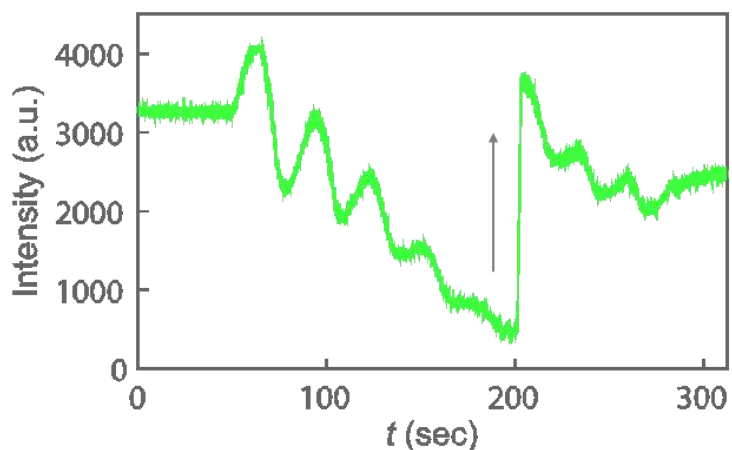* The arrows indicate a manual increase of the intensity

Sample C1
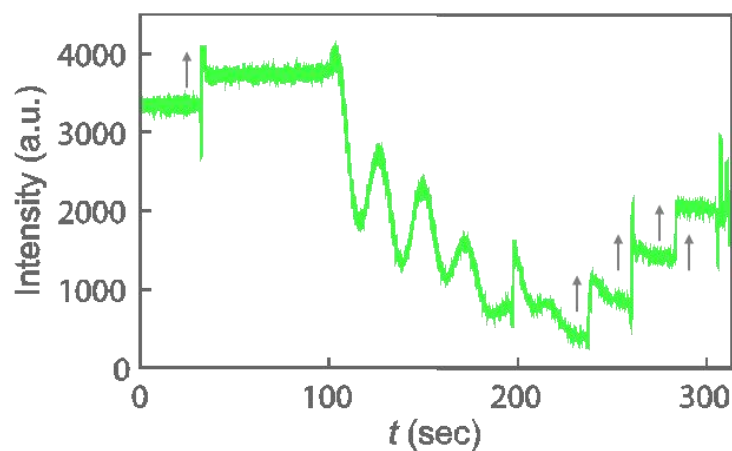
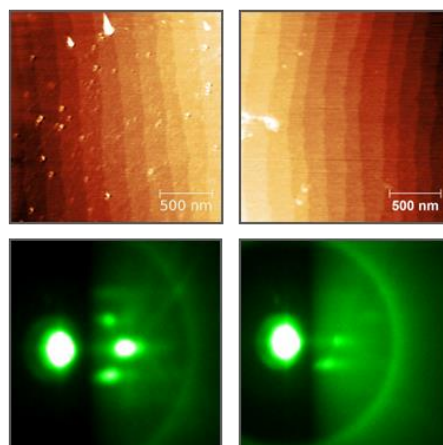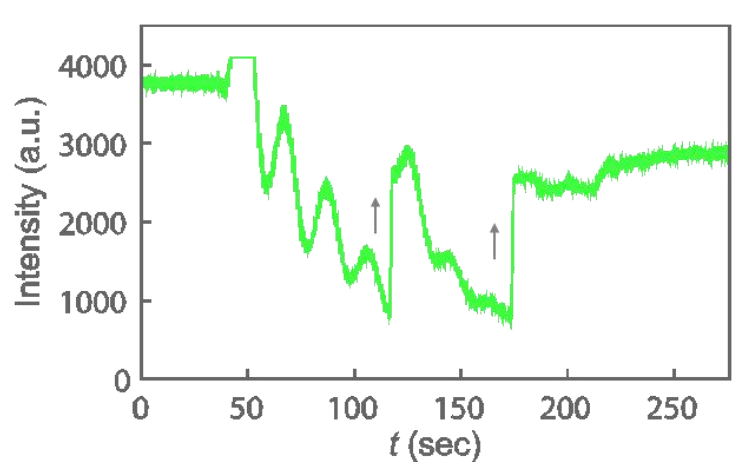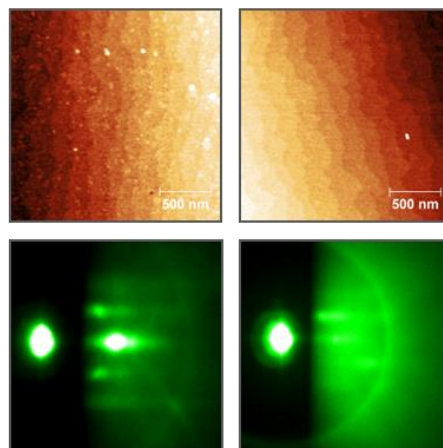Before deposition   After deposition
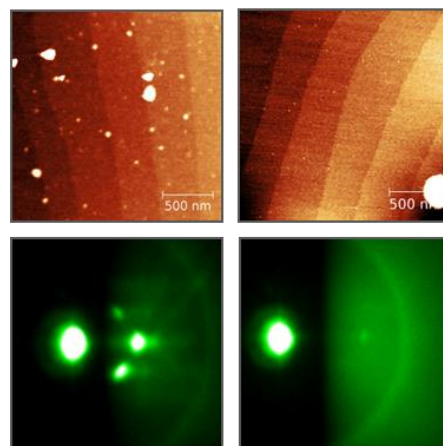
Sample C2
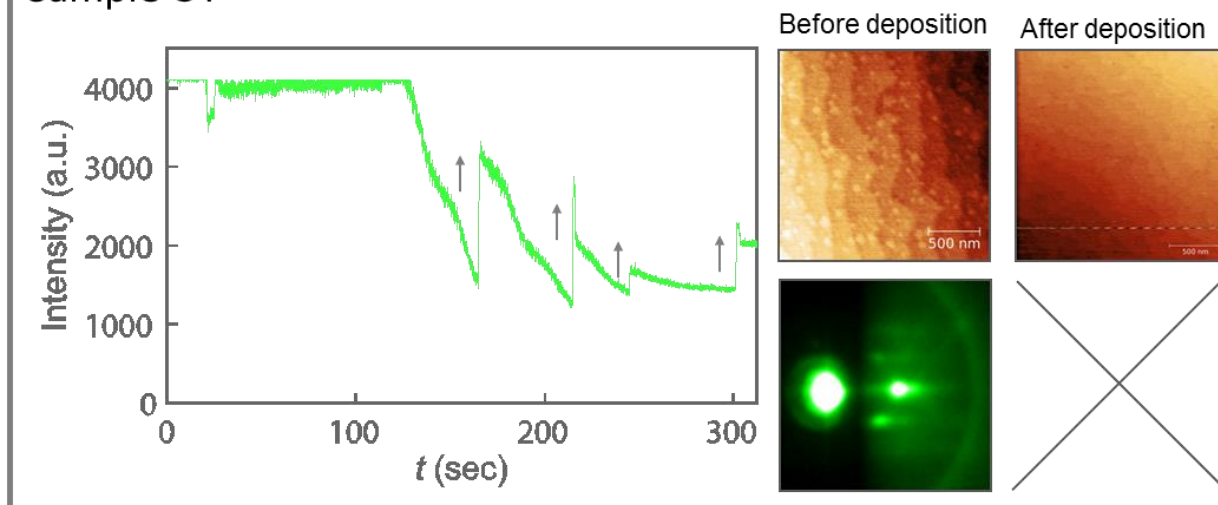

Before deposition   After deposition

Sample C3
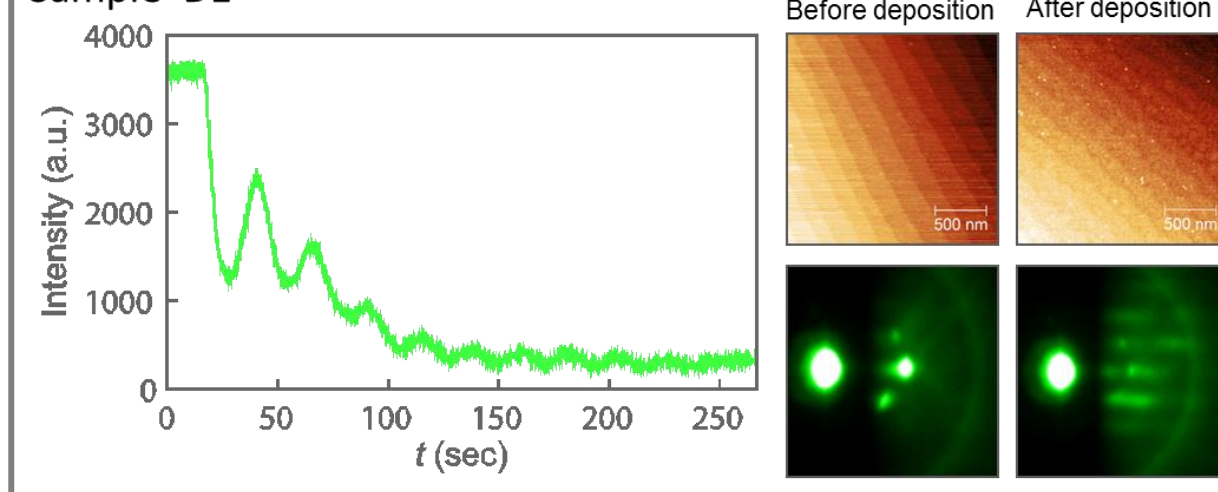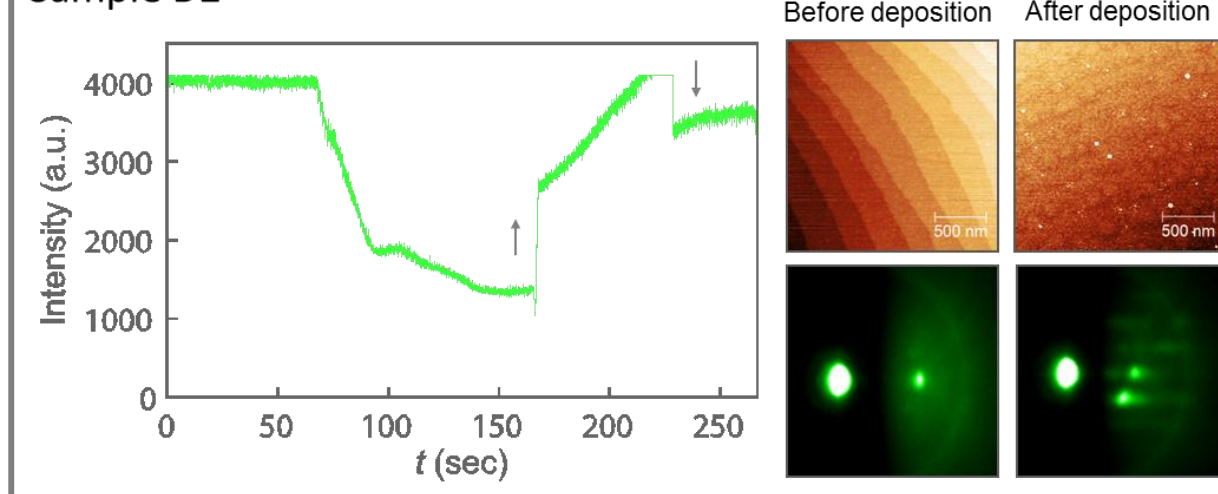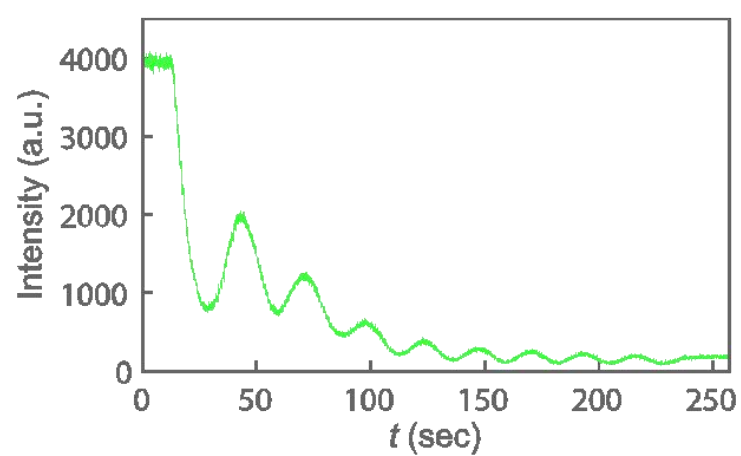

Before deposition   After deposition

Sample C4

Before deposition   After deposition

Sample D1

Before deposition   After deposition
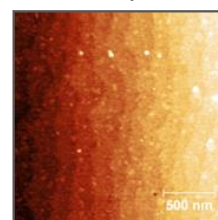

Sample D2

Before deposition   After deposition

Sample D3

Before deposition   After deposition
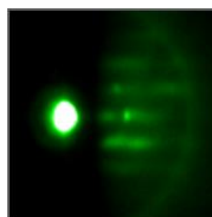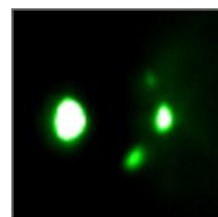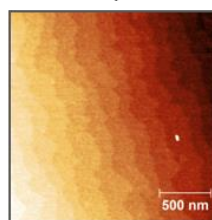
Appendix D: Maekawa-Fukuyama fit

The Maekawa-Fukuyama formula:

$$\frac{\Delta\sigma}{\sigma_o} = \Psi\left(\frac{H}{H_i + H_{so}}\right) + \frac{1}{2\sqrt{1-\gamma^2}}\Psi\left(\frac{H}{H_i + H_{so}(1+\sqrt{1-\gamma^2})}\right) - \frac{1}{2\sqrt{1-\gamma^2}}\Psi\left(\frac{H}{H_i + H_{so}\left(1-\sqrt{1-\gamma^2}\right)}\right),$$

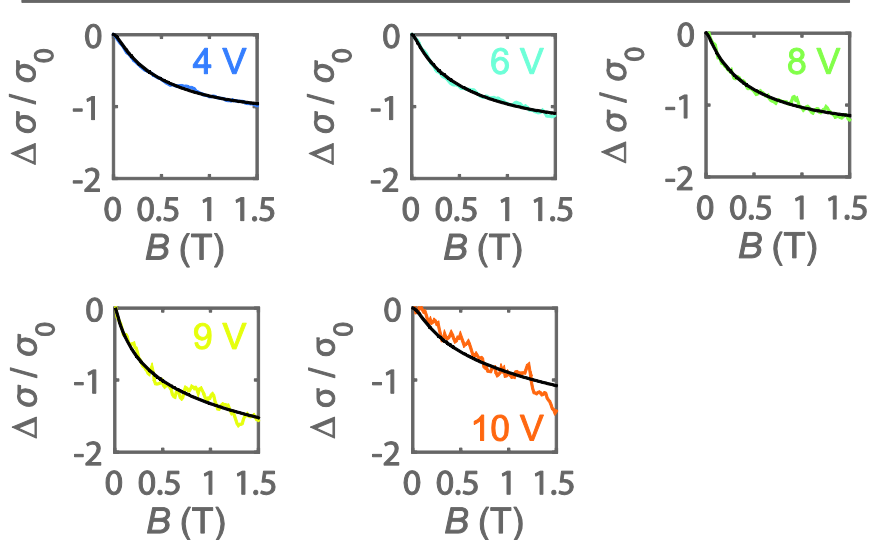with: $\Psi(x) = \ln(x) + \psi\left(\frac{1}{2} + \frac{1}{x}\right)$ (ψ is the digamma function)

$\gamma = g\mu_B H/4eDH_{so}$ (Zeeman correction)

$H_{i,so} = \hbar/4eD\tau_{i,so}$ (τ_i and τ_{so} are the inelastic and spin-orbit scattering time)
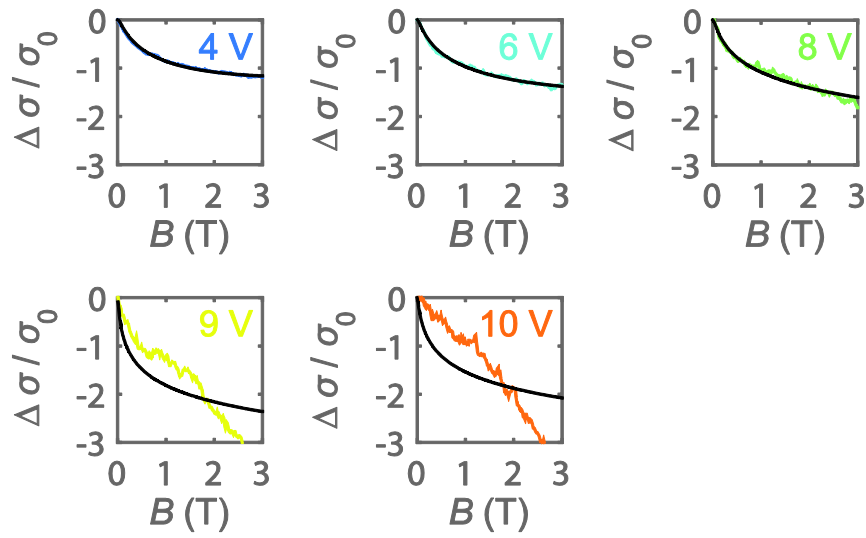
Sample C3: MF-fit up to a magnetic field of 0.5 T
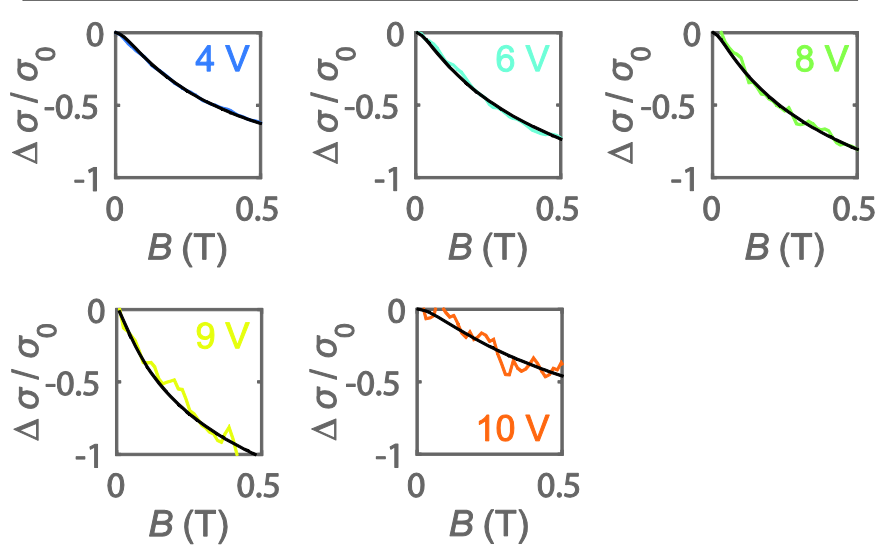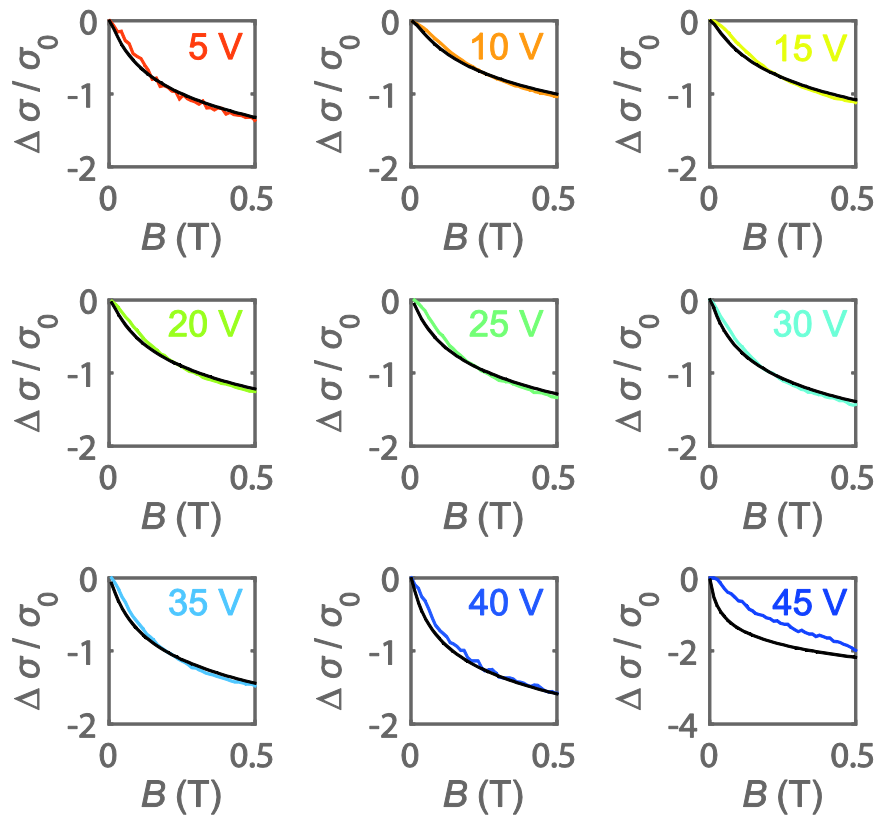

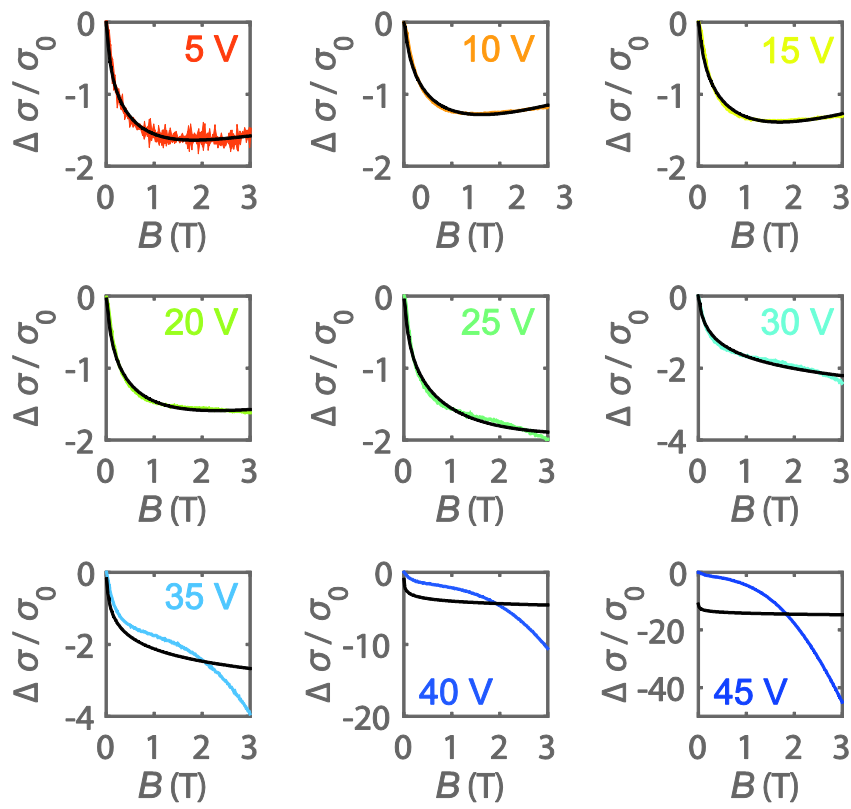**Sample C3**: MF-fit up to a magnetic field of 1.5 T

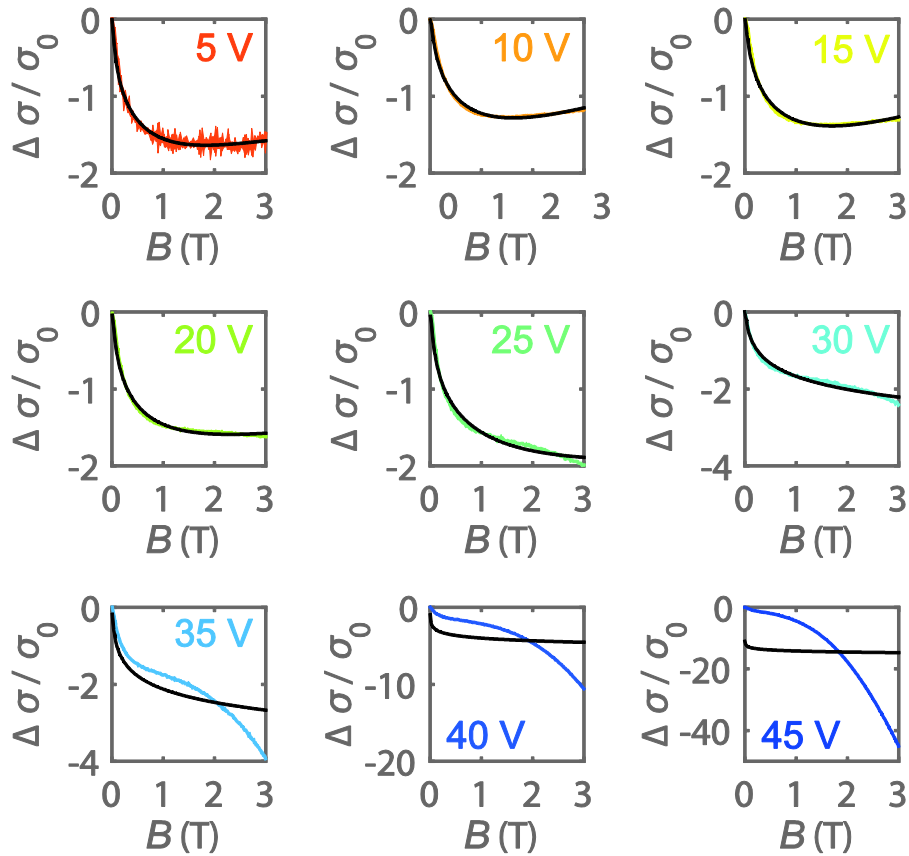**Sample C3**: MF-fit up to a magnetic field of 3 T

Sample D2: MF-fit up to a magnetic field of 0.5 T

Sample D2: MF-fit up to a magnetic field of 1.5 T

Sample D2: MF-fit up to a magnetic field of 3 T

Appendix E: Poster presented at Physics at FOM in Veldhoven

Nomenclature

2DES   : Two-Dimensional Electron System
AES   : Auger Electron Spectroscopy
AFD   : Anti-Ferro-Distortive
AFM   : Atomic Force Microscopy
Ar   : Argon
ARPES: : Angle Resolved Photoemission Spectroscopy
BKT   : Berezinskii-Kosterlitz-Thouless
HMC: : High Mobility Carriers
LAO   : $LaAlO_3$ (Lanthanum Aluminium Oxide)
LMC   : Low Mobility Carriers
MF   : Maekawa-Fukuyama
MIBK   : Methyl Isobutyl Ketone
MR   : MagnetoResistance
PL   : Photoluminescence
PLD   : Pulsed Laser Deposition
PMMA   : Polymethyl Methacrylate
PVD   : Physical Vapour Deposition
RHEED   : Reflection High-Energy Electron Diffraction
SPM   : Scanning Probe Microscopy
STM   : Scanning Tunnelling Spectroscopy
STO   : $SrTiO_3$ (Strontium Titanium Oxide)
TMO   : Transition Metal Oxide
uc   : unit cell
WAL   : Weak Anti-Localisation
WL   : Weak Localisation

References

1. Ohtomo, A. & Hwang, H. Y. A high-mobility electron gas at the $LaAlO_3/SrTiO_3$ heterointerface. *Nature* **427,** 423–426 (2004).
2. Lee, J. *et al.* Titanium dxy ferromagnetism at the $LaAlO_3/SrTiO_3$ interface. *Nat. Mater.* **12,** 703–706 (2013).
3. Diez, M. *et al.* Giant Negative Magnetoresistance Driven by Spin-Orbit Coupling at. *Phys. Rev. Lett.* **115,** 1–5 (2015).
4. Reyren, N. *et al.* Superconducting interfaces between insulating oxides. *Science.* **317,** 1196–1200 (2007).
5. Herranz, G., Sánchez, F., Dix, N., Scigaj, M. & Fontcuberta, J. High mobility conduction at (110) and (111) $LaAlO_3/SrTiO_3$ interfaces. *Sci. Rep.* **2,** 1–5 (2012).
6. Howard, C. J. *et al.* Space-group symmetry for the perovskite $Ca_{0.3}Sr_{0.7}TiO_3$. *J. Phys. Condens. Matter* **17,** L459–L465 (2005).
7. Peña, M. A. & Fierro, J. L. G. Chemical structures and performance of perovskite oxides. *Chem. Rev.* **101,** 1981–2017 (2001).
8. Tokura, Y. & Nagaosa, N. Orbital Physics in Transition-Metal Oxides. *Science.* **288,** 462–467 (2000).
9. Salehi, H. First Principles Studies on the Electronic Structure and Band Structure of Paraelectric $SrTiO_3$ by Different Approximations. *J. Mod. Phys.* **02,** 934–943 (2011).
10. Goldschmidt, V. M. Die Gesetze der Krystallochemie. *Naturwissenschaften* **21,** 477–485 (1926).
11. Koonce, C. S., Cohen, M. L., Schooley, J. F., Hosler, W. R. & Pfeiffer, E. R. Superconducting Transition Temperatures of Semiconducting $SrTiO_3$. *Phys. Rev.* **163,** 380–390 (1967).
12. Jarlborg, T. Tuning of the electronic screening and electron-phonon coupling in doped $SrTiO_3$ and WO_3. *Phys. Rev. B* **61,** 9887–9890 (2000).
13. Russell, B. C. & Castell, M. R. ($\sqrt{13}$X$\sqrt{13}$)R13.9° and ($\sqrt{7}$X$\sqrt{7}$)R19.1° reconstructions of the polar $SrTiO_3$ (111) surface. *Phys. Rev. B* **75,** 1–7 (2007).
14. Marks, L. D., Chiaramonti, A. N., Tran, F. & Blaha, P. The small unit cell reconstructions of $SrTiO_3$ (111). *Surf. Sci.* **603,** 2179–2187 (2009).
15. Russell, B. & Castell, M. Reconstructions on the polar $SrTiO_3$ (110) surface: Analysis using STM, LEED, and AES. *Phys. Rev. B* **77,** 1–9 (2008).
16. Kahn, A. H. & Leyendecker, A. J. Electronic energy band in strontium titanate. *Phys. Rev.* **135,** 447–450 (1964).
17. Janotti, A., Steiauf, D. & Van de Walle, C. G. Strain effects on the electronic structure of $SrTiO_3$: Toward high electron mobilities. *Phys. Rev. B* **84,** 1–4 (2011).
18. Monteiro, A.M.R.V.L. Fundamental aspects of the two-dimensional electron system found. (2014).
19. El-Mellouhi, F., Brothers, E. N., Lucero, M. J., Bulik, I. W. & Scuseria, G. E. Structural phase transitions of the metal oxide perovskites $SrTiO_3$, $LaAlO_3$, and $LaTiO_3$ studied with a screened hybrid functional. *Phys. Rev. B - Condens. Matter Mater. Phys.* **87,** 1–11 (2013).
20. Joshua, A., Pecker, S., Ruhman, J., Altman, E. & Ilani, S. A universal critical density underlying the physics of electrons at the $LaAlO_3/SrTiO_3$ interface. *Nat. Commun.* **3,** 1129 (2012).
21. Salluzzo, M. *et al.* Orbital reconstruction and the two-dimensional electron gas at the $LaAlO_3/SrTiO_3$ interface. *Phys. Rev. Lett.* **102,** 1–4 (2009).
22. Noland, A. Optical Properties and Band structure of $SrTiO_3$ and $BaTiO_3$. *Phys. Rev.* **140,** 651–655 (1965).
23. Hwang, H. Y. *et al.* Emergent phenomena at oxide interfaces. *Nat. Mater.* **11,** 103–13 (2012).
24. Rödel, T. C. *et al.* Orientational Tuning of the Fermi Sea of Confined Electrons at the $SrTiO_3$ (110) and (111) Surfaces. *Phys. Rev. Appl.* **1,** 1–5 (2014).

25. McKeown Walker, S. *et al.* Control of a Two-Dimensional Electron Gas on SrTiO$_3$ (111) by Atomic Oxygen. *Phys. Rev. Lett.* **113,** 1–5 (2014).

26. Nakagawa, N., Hwang, H. Y. & Muller, D. A. Why Some Interfaces Cannot be Sharp. *Nat. Mater.* **5,** 204–209 (2005).

27. Nishimura, J., Ohtomo, A., Ohkubo, A., Murakami, Y. & Kawasaki, M. Controlled Carrier Generation at a Polarity-Discontinued Perovskite Heterointerface. *Jpn. J. Appl. Phys.* **43,** L1032–L1034 (2004).

28. Thiel, S., Hammerl, G., Schmehl, A., Schneider, C. W. & Mannhart, J. Tunable Quasi–Two-Dimensional Electron Gases in Oxide Heterostructures. *Science.* **313,** 1942–1945 (2006).

29. Reinle-Schmitt, M. L. *et al.* Tunable conductivity threshold at polar oxide interfaces. *Nat. Commun.* **3,** 932 (2012).

30. Siemons, W., Koster, G., Yamamoto, H. & Harrison, W. A. Origin of charge density at LaAlO$_3$ on SrTiO$_3$ heterointerfaces ; possibility of intrinsic doping. *Phys. Rev. Lett.* **98,** 1–14 (2007).

31. Herranz, G. *et al.* High Mobility in LaAlO$_3$/SrTiO$_3$ Heterostructures: Origin, Dimensionality, and Perspectives. *Phys. Rev. Lett.* **98,** 216803 (2007).

32. Kalabukhov, A. *et al.* Effect of oxygen vacancies in the SrTiO$_3$ substrate on the electrical properties of the LaAlO$_3$/SrTiO$_3$ interface. *Phys. Rev. B* **75,** 1–4 (2007).

33. Popović, Z., Satpathy, S. & Martin, R. Origin of the Two-Dimensional Electron Gas Carrier Density at the LaAlO$_3$ on SrTiO$_3$ Interface. *Phys. Rev. Lett.* **101,** 256801 (2008).

34. Huijben, M. *et al.* Defect engineering in oxide heterostructures by enhanced oxygen surface exchange. *Adv. Funct. Mater.* **23,** 5240–5248 (2013).

35. Liu, Z. Q. *et al.* Origin of the Two-Dimensional Electron Gas at LaAlO$_3$/SrTiO$_3$ Interfaces: The Role of Oxygen Vacancies and Electronic Reconstruction. *Phys. Rev. X* **3,** 1–9 (2013).

36. Cancellieri, C. *et al.* Influence of the growth conditions on the LaAlO$_3$/SrTiO$_3$ interface electronic properties. *EPL Europhys. Lett.* (2010). doi:10.1209/0295-5075/91/17004

37. Chambers, S. a. *et al.* Instability, intermixing and electronic structure at the epitaxial LaAlO$_3$/SrTiO$_3$(001) heterojunction. *Surf. Sci. Rep.* **65,** 317–352 (2010).

38. Willmott, P. *et al.* Structural Basis for the Conducting Interface between LaAlO$_3$ and SrTiO$_3$. *Phys. Rev. Lett.* **99,** 155502 (2007).

39. Ohtomo, A., Muller, D. A., Grazul, J. L. & Hwang, H. Y. Artificial charge-modulation in atomic-scale perovskite titanate superlattices. *Nature* **419,** 3–5 (2002).

40. Mukunoki, Y., Nakagawa, N., Susaki, T. & Hwang, H. Y. Atomically flat (110) SrTiO$_3$ and heteroepitaxy. *Appl. Phys. Lett.* **86,** 1–3 (2005).

41. Annadi, A. *et al.* Anisotropic two-dimensional electron gas at the LaAlO$_3$/SrTiO$_3$ (110) interface. *Nat. Commun.* **4,** 1–7 (2013).

42. Fete, A. Magnetotransport Experiments at the LaAlO$_3$/SrTiO$_3$ interface. (UNIVERSITÉ DE GENÈVE, 2014).

43. Guduru, V. K. *et al.* Multi-band conduction behaviour at the interface of LaAlO$_3$/SrTiO$_3$ heterostructures. *J. Korean Phys. Soc.* **63,** 437 (2013).

44. Gariglio, S., Reyren, N., Caviglia, A. D. & Triscone, J.-M. Superconductivity at the LaAlO$_3$/SrTiO$_3$ interface. *J. Phys. Condens. Matter* **21,** 164213 (2009).

45. Caviglia, A. D. *et al.* Tunable Rashba Spin-Orbit Interaction at Oxide Interfaces. *Phys. Rev. Lett.* **104,** 126803 (2010).

46. Stornaiuolo, D. *et al.* Weak localization and spin-orbit interaction in side-gate field effect devices at the LaAlO$_3$/ SrTiO$_3$ interface. *Phys. Rev. B* **90,** 235426**,** 1–6 (2014).

47. Schooley, J. F., Hosler, W. R. & Cohen, M. L. Superconductivity in semiconducting SrTiO$_3$. *Phys. Rev.* **12,** 474–475 (1964).

48. Medvedyeva, K. Characteristic properties of two-dimensional superconductors close to the phase transition in zero magnetic field. *Solfjärden Offset AB* (Umeå University, 2003).

49. Schneider, T., Caviglia, A. D., Gariglio, S., Reyren, N. & Triscone, J.-M. Electrostatically-tuned superconductor-metal-insulator quantum transition at the LaAlO$_3$/SrTiO$_3$ interface. *Phys. Rev. B* **79,** 184502 (2009).

50. Han, Y.-L. *et al.* Two-dimensional superconductivity at (110) LaAlO$_3$/SrTiO$_3$ interfaces. *Appl. Phys. Lett.* **105,** 1–4 (2014).

51. Reyren, N. *et al.* Anisotropy of the superconducting transport properties of the LaAlO$_3$/SrTiO$_3$ interface. *Appl. Phys. Lett.* **94,** 112506 (2009).

52. Shalom, M. Ben, Sachs, M., Rakhmilevitch, D., Palevski, A. & Dagan, Y. Tuning spin-orbit coupling and superconductivity at the SrTiO$_3$/LaAlO$_3$ interface: a magneto-transport study. *Phys. Rev. Lett.* **105,** 1–5 (2010).

53. Gariglio, S. & Triscone, J. M. Oxide interface superconductivity. *Comptes Rendus Phys.* **12,** 591–599 (2011).

54. Caviglia, A. D. *et al.* Electric field control of the LaAlO$_3$/SrTiO$_3$ interface ground state. *Nature* **456,** 624–627 (2008).

55. Herranz, G. *et al.* Orientational tuning of the 2D-superconductivity in LaAlO3/SrTiO3 interfaces. *arXiv* 5 (2013). at <http://arxiv.org/abs/1305.2411>

56. Koster, G., Kropman, B. L., Rijnders, G. J. H. M., Blank, D. H. A. & Rogalla, H. Quasi-ideal strontium titanate crystal surfaces through formation of strontium hydroxide. *Appl. Phys. Lett.* **73,** 2920 (1998).

57. Chang, J., Park, Y.-S. & Kim, S.-K. Atomically flat single-terminated SrTiO$_3$ (111) surface. *Appl. Phys. Lett.* **92,** 152910 (2008).

58. Kawasaki, M. *et al.* Atomic control of the SrTiO$_3$ crystal surface. *Science* **266,** 1540 – 1542 (1994).

59. Leca, V. *Heteroepitaxial growth of copper oxide superconductors by Pulsed Laser Deposition*. (2003).

60. Lippmaa Laboratory; http://lippmaa.issp.u-tokyo.ac.jp/sto/substrate/. (2015).

61. Chambers, S. A., Droubay, T. C., Capan, C. & Sun, G. Y. Unintentional F doping of SrTiO$_3$ (001) etched in HF acid-structure and electronic properties. *Surf. Sci.* **606,** 554–558 (2012).

62. Hatch, R. C. *et al.* Surface electronic structure for various surface preparations of Nb-doped SrTiO$_3$ (001). *J. Appl. Phys.* **114**, 103710 (2013).

63. Kareev, M. *et al.* Atomic control and characterization of surface defect states of TiO$_2$ terminated SrTiO$_3$ single crystals. *Appl. Phys. Lett.* **93,** 061909, 1–3 (2008).

64. Zhang, J. *et al.* Depth-resolved subsurface defects in chemically etched SrTiO$_3$. *Appl. Phys. Lett.* **94,** 1–3 (2009).

65. Biswas, A. *et al.* Universal Ti-rich termination of atomically flat SrTiO$_3$ (001), (110), and (111) surfaces. *Appl. Phys. Lett.* **98,** 051904 (2011).

66. Woo, S. *et al.* Surface properties of atomically flat poly-crystalline SrTiO$_3$. *Sci. Rep.* **5,** 8822 (2015).

67. Connell, J. G., Isaac, B. J., Ekanayake, G. B., Strachan, D. R. & Seo, S. S. a. Preparation of atomically flat SrTiO$_3$ surfaces using a deionized-water leaching and thermal annealing procedure. *Appl. Phys. Lett.* **101,** 1–3 (2012).

68. Kowalski, C. *NanoScope Software Version 5 Document Revision History : MultiMode SPM Instruction Manual*. (2004).

69. Montanari, S. http://gorgia.no-ip.com/phd/html/thesis/phd_html/node5.html. chapter 4.1 (2005).

70. Eason, R. *Pulsed Laser Deposition of Thin Films*. *Pulsed Laser Deposition of Thin Films* (2006).

71. Willmott, P. & Huber, J. Pulsed laser vaporization and deposition. *Rev. Mod. Phys.* **72,** 315–328 (2000).

72. Wang, K. Laser Based Fabrication of Graphene. *Advances in Graphene Science* 77–95 (2013).

73. Atenrok. https://en.wikipedia.org/wiki/Reflection_high-energy_electron_diffraction. (2016).

74. Koster, G. . & Rijnders, G. In Situ Characterization of Thin Film Growth. (Woodhead Publishing Series in Electronic and Optical Materials, 2011). doi:10.1533/9780857094957.1.3

75. Ichimiya, A. & Cohen, P. I. Reflection High-Energy Electron Diffraction. (Cambridge University Press, 2004).

76. Charles, K. *Introduction to Solid State Physics*. (2005).

77. Institute fur Elektrische Messtechnik und Grundlagen der Elektrotechnik. http://www.emg.tu-bs.de/forschung/analytik/rheed_e.html. (2015).

78. Ingle, N. J. C. Inelastic scattering techniques for in situ characterization of thin film growth: Backscatter Kikuchi diffraction. In Situ Characterization of Thin Film Growth (Woodhead Publishing Limited, 2011).

79. Huijben, M. *et al.* Structure-Property Relation of $SrTiO_3$/$LaAlO_3$ Interfaces. *Adv. Mater.* **21,** 1665–1677 (2009).

80. http://cdms.berkeley.edu/UCB/75fridge/inxsrc/dilution/. (2015).

81. Adwaele. https://en.wikipedia.org/wiki/File:Cold_part_of_dilution_refrigerator.jpg. (2016).

82. Cheng, G. *et al.* Anomalous Transport in Sketched Nanostructures at the $LaAlO_3$/$SrTiO_3$ Interface. *Phys. Rev. X* **011021,** 1–8 (2013).

83. Smink, S. E. M. Electrostatic tuning of the $LaAlO_3$/$SrTiO_3$ interface devices. (2014).

84. Lippmaa, M. *et al.* Atom technology for Josephson tunnel junctions : $SrTiO_3$ substrate surface. *Mater. Sci. Eng. B* **56,** 111–116 (1998).

85. Sánchez, F., Ocal, C. & Fontcuberta, J. Tailored surfaces of perovskite oxide substrates for conducted growth of thin films. *Chem. Soc. Rev* **43,** 2272–2285 (2272).

86. Chang, J., Park, Y.-S. & Kim, S.-K. Atomically flat single-terminated $SrTiO_3$ (111) surface. *Appl. Phys. Lett.* **92,** 152910 (2008).

87. Konaka, T., Sato, M., Asano, H. & Kubo, S. Relative permittivity and dielectric loss tangent of substrate materials for high-Tc superconducting film. *J. Supercond.* **4,** 283–288 (1991).

88. Doennig, D., Pickett, W. E. & Pentcheva, R. Massive symmetry breaking in $LaAlO_3$/$SrTiO_3$ (111) quantum wells: a three-orbital, strongly correlated generalization of graphene. *Phys. Rev. Lett.* **111,** 128604, 2–6 (2013).

89. Fete, A. *et al.* Growth-induced electron mobility enhancement at the $LaAlO_3$/$SrTiO_3$ interface. *Appl. Phys. Lett.* **106,** (2015).

90. Hsu, W.-C. *et al.* Metallic conduction and large electron-phonon-impurity interference effect in single TiSi nanowires. *Nanoscale Res. Lett.* **7,** 500 (2012).

91. De Luca, G. M. *et al.* Transport properties of a quasi-two-dimensional electron system formed in $LaAlO_3$/$EuTiO_3$/$SrTiO_3$ heterostructures. *Phys. Rev. B - Condens. Matter Mater. Phys.* **89,** 1–6 (2014).

92. Ramaneti, R., Lodder, J. C. & Jansen, R. Kondo effect and impurity band conduction in $Co:TiO_2$ magnetic semiconductor. *Phys. Rev. Appl.* **76,** 1–5 (2007).

93. Ibach, H. & Luth, H. *Solid-state physics : an introduction to principles of materials science*. (2009).

94. Thiel, S. *et al.* Electron Scattering at Dislocations in $LaAlO_3$/$SrTiO_3$ Interfaces. *Phys. Rev. Lett.* **046809,** 1–4 (2009).

95. Muller, K. A. & Burkard, H. SrTiO3: An intrinsic quantum paraelectric below 4 K. *Phys. Rev. B* **19,** (1979).

96. Rakhmilevitch, D. *et al.* Anomalous response to gate voltage application in mesoscopic $LaAlO_3$/$SrTiO_3$ devices. *Phys. Rev. B* **87**, 125409, 1–5 (2013).

97. Liu, W. *et al.* Magneto-transport study of top- and back-gated $LaAlO_3$/$SrTiO_3$ heterostructures. *Appl. Mater.* **3**,062805**,** (2016).

98. Joshua, A., Pecker, S., Ruhman, J., Altman, E. & Ilani, S. A universal critical density underlying the physics of electrons at the $LaAlO_3$/$SrTiO_3$ interface. *Nat. Commun.* **3,** 1129 (2012).

99. Caviglia, A. D. *et al.* Tunable Rashba spin-orbit interaction at oxide interfaces - Supplementary Information. 1–5 (2010).

100. Chen, Z. *et al.* Influence of growth temperature on the vortex pinning properties of pulsed laser deposited $YBa_2Cu_3O_{7-x}$ thin films. *J. Appl. Phys.* **103**, 043913, 1–7 (2008).

101. Gross, H., Bansal, N., Kim, Y.-S. & Oh, S. Metal-insulator transition on $SrTiO_3$ surface induced by ionic-bombardment. *J. Appl. Phys.* **110,** (2011).

102. Prawiroatmodjo, G.E.D.K. *et al.* Gate-tunable superconductivity at the amorphous $LaAlO_3$/$SrTiO_3$ interface. 1–6 (2015): arXiv:1510.01199v1

103. Caprara, S. *et al.* Multiband superconductivity and nanoscale inhomogeneity at oxide interfaces. *Phys. Rev. B* **88,** 020504, 1–5 (2013).

104. Skocpol, W. J., Beasley, M. R. & Tinkham, M. Self-heating hotspots in superconducting thin-film microbridges Self-heating hotspots in superconducting thin-film. *J. Appl. Phys.* **45,** 4045–4066 (1974).

105. Agren, P. Charging effects in small capacitance Josephson junction circuits. (Royal Institute of Tehcnology, 2002).

106. Feigel'man, M. V., Larkin, A. I. & Skvortsov, M. A. Quantum Superconductor-Metal transition in a Proximity Array. *Phys. Rev. Lett.* **86,** 1869–1872 (2001).

107. Wang, X. *et al.* Magnetoresistance of two-dimensional and three-dimensional electron gas in LaAlO$_3$/SrTiO$_3$ heterostructures : Influence of magnetic ordering , interface scattering , and dimensionality. *Phys. Rev. B* **84,** 3–6 (2011).

108. Han, Y.-L. *et al.* Two-dimensional superconductivity at (110) LaAlO$_3$/SrTiO$_3$ interfaces. *Appl. Phys. Lett.* **105,** 192603 (2014).

109. Bert, J. a. *et al.* Direct imaging of the coexistence of ferromagnetism and superconductivity at the LaAlO$_3$/SrTiO$_3$ interface. *Nat. Phys.* **7,** 767–771 (2011).

110. Bert, J. A. *et al.* Gate-tuned superfluid density at the superconducting LaAlO$_3$/SrTiO$_3$ interface. *Phys. Rev. B* **84,** 060503, 1–5 (2012).

111. Zuo, F., Brooks, J. S., Mckenzie, R. H., Schleuter, J. A. & Williams, J. M. Paramagnetic limiting of the upper critical field of the layered organic superconductor k- (BEDT-TTF)$_2$Cu(SCN)$_2$. *Phys. Rev. B* **61,** 750–755 (2000).

112. Tinkham, M. *Introduction to superconductivity*. (McGraw-Hill, Inc, 1996).

113. Matthews, D. N. & Driver, R. Critical current density of ceramic high-temperature superconductors in a low magnetic field. *Physica C* **191,** 339–346 (1992).